

1225-0767(ISSN Print)
2287-6715(ISSN Online)
한국연구재단 우수등재학술지

Journal of Ocean Engineering and Technology

Vol. 34, No. 3 (Serial Number 154)

June 2020

한국해양공학회지



www.joet.org



The Korean Society of Ocean Engineers

Editorial Board

■ Editor-in-Chief

Joonmo Choung Inha University, Korea

■ Manuscript Editors

Hyeongsik Choi Korea Maritime and Ocean University, Korea

Joon-Young Kim Korea Maritime and Ocean University, Korea

Seokhwan Ahn Jungwon University, Korea

Sungwon Shin Hanyang University, Korea

Woo Dong Lee Gyeongsang National University, Korea

■ Editorial Board Members

Ahmet Ergin Istanbul Technical University, Turkey

Atila Incecik University of Strathclyde, UK

Beom-Seon Jang Seoul National University, Korea

Bo Woo Nam Seoul National University, Korea

Chang Yong Song Mokpo National University, Korea

Chong Hyun Lee Jeju National University, Korea

Do Kyun Kim Newcastle University, UK

Dongho Jung Korea Research Institute of Ships & Ocean Engineering, Korea

Erkan Oterkus University of Strathclyde, UK

Geoffrey Lyons BPP-TECH, UK

Gökhan Tansel Tayyar Istanbul Technical University, Turkey

Gyusung Cho Tongmyong University, Korea

Hee Jin Kang Korea Research Institute of Ships & Ocean Engineering, Korea

Hooi-Siang Kang Universiti Teknologi Malaysia, Malaysia

Hyeon Kyu Yoon Changwon National University, Korea

Hyun-Sik Kim Tongmyong University, Korea

Jinwhan Kim Korea Advanced Institute of Science and Technology, Korea

Jong Chun Park Pusan National University, Korea

Kangsu Lee Korea Research Institute of Ships & Ocean Engineering, Korea

Kookhyun Kim Tongmyong University, Korea

Kwang-Jun Paik Inha University, Korea

Masashi Kashiwagi Osaka University, Japan

Moo Hyun Kim Texas A&M University, USA

Narakorn Srini Newcastle University, UK

Norimi Mizutani Nagoya University, Japan

Se-Min Jeong Chosun University, Korea

Seongim Choi Virginia Tech, USA

Seung Min Park Hyein Engineering & Construction, Co., Ltd., Korea

Soonchul Kwon Pusan National University, Korea

Sungnam Hong Gyeongsang National University, Korea

Sung-Woong Choi Gyeongsang National University, Korea

Taemin Ha Kangwon National University, Korea

Taeseong Kim Loughborough University, UK

TaeSoon Kang GeoSystem Research Corp., Korea

Tak Kee Lee Gyeongsang National University, Korea

Weoncheol Koo Inha University, Korea

Yeon-Joong Kim Inje University, Korea

Yong Uk Ryu Chonnam National University, Korea

Younghun Kim Kyungnam University, Korea

Youngsub Lim Seoul National University, Korea

Yun Hae Kim Korea Maritime and Ocean University, Korea

Research Ethics Board

■ Chief

Sung-Bu Suh Dongeui University, Korea

■ Research Ethics Board Members

Han Koo Jeong Kunsan National University, Korea

Jinwhan Kim Korea Advanced Institute of Science and Technology, Korea

Yong Uk Ryu Chonnam National University, Korea

Published on June 30, 2020

Published by The Korean Society of Ocean Engineers (KSOE)

Room1302, 13, Jungang-daero 180beon-gil, Dong-gu, Busan, 48821, Korea

TEL: +82-51-759-0656 FAX: +82-51-759-0657 E-mail: ksoehj@ksoe.or.kr URL: http://www.ksoe.or.kr

Printed by Hanrimwon Co., Ltd., Seoul, Korea E-mail: hanrim@hanrimwon.co.kr

ISSN(print) 1225-0767 ISSN(online) 2287-6715

This journal was supported by the Korean Federation of Science and Technology Societies (KOFST) grant funded by the Korean government.

© 2020 by The Korean Society of Ocean Engineers (KSOE)

This is an open access article distributed under the terms of the creative commons attribution non-commercial license (<http://creativecommons.org/licenses/by-nc/4.0>) which permits unrestricted non-commercial use, distribution, and reproduction in any medium, provided the original work is properly cited.

Journal of Ocean Engineering and Technology

한국해양공학회지

CONTENTS

Volume 34, Number 3

June, 2020

<Original Research Articles>

- Punching Fracture Experiments and Simulations of Unstiffened and Stiffened Panels for Ships and Offshore Structures
Sung-Ju Park and Joonmo Choung 155
- Prediction of Barge Ship Roll Response Amplitude Operator Using Machine Learning Techniques
Jae Hwan Lim and Hyo Jae Jo 167
- Trajectory Tracking Performance Analysis of Underwater Manipulator for Autonomous Manipulation
Junbo Chae, Taekyeong Yeu, Yeongjun Lee, Yoongeon Lee and Suk-Min Yoon 180
- Experimental Study of Load Characteristics of Buried and Exposed Large-Diameter Pipelines Using Fiber-Optic Strain Sensor
Joseph Chul Chung, Michael Myung-Sub Lee and Sung Ho Kang 194
- Estimation of Penetration Depth Using Acceleration Signal Analysis for Underwater Free Fall Cone Penetration Tester
Jung-min Seo, Changjoo Shin, OSoon Kwon, In Sung Jang, Hyoun Kang and Sung Gyu Won 202

<Technical Research Article>

- A Review of IOSS Design Standardization Technology for Aluminum Alloy Handrail of Offshore Platform
Yeon-Ho Kim, Joo-Shin Park, Hyun-Chang Shin, Sung-Jun Kim, Dae-Kyeom Park,
Yeon-Chul Ha and Jung-Kwan Seo 208
- Study on System Support for Offshore Plant Piping Process Using 3D Simulator
Hyun-Cheol Kim and Gyu-Hong Lee 217

<Review Article>

- Underwater Acoustic Research Trends with Machine Learning: Passive SONAR Applications
Haesang Yang, Keunhwa Lee, Youngmin Choo and Kookhyun Kim 227

GENERAL INFORMATION

“Journal of Ocean Engineering and Technology” is the official journal published by “The Korean Society of Ocean Engineers (KSOE)”. The ISO abbreviation is “J. Ocean Eng. Technol.” and acronym is “**JOET**”. It contains original research articles, technical articles, review articles, and brief communications on technical issues.

JOET published the first issue in 1987 and has been publishing bimonthly since 2002. **JOET** is ranked the most influential journal with the longest history and largest membership around 1,000 people in the field of ocean engineering in Korea. **JOET** covers all topics in ocean engineering fields, and has five major research areas including ships/offshore platforms, coastal civil engineering, marine materials, ocean renewable energy platforms, marine robots, etc.

Ships and offshore platforms: Design of marine structures; Resistance and propulsion; Seakeeping and maneuvering; Experimental and computational fluid dynamics; Ocean wave mechanics; Fatigue strength; Plasticity; Optimization and reliability; Arctic technology and extreme mechanics; Noise, vibration, and acoustics; Concrete engineering; Thermodynamics and heat transfer; Hydraulics and pneumatics;

Coastal civil engineering: Coastal structures; Port and harbor structures; Soil mechanics; Drilling and exploration; Hydraulics of estuary; Seismic engineering; Coastal disaster prevention engineering;

Marine materials: Metallic materials; Organic materials; Ceramics; Composite materials; Materials properties; Corrosion and Anti-corrosion; Tribology;

Ocean renewable energy platforms: Offshore wind turbines; Wave energy platforms; Tidal current energy platforms; Floating photovoltaic energy platforms;

Marine robots: Robot sensor system; Autonomous navigation; Robot equipments; Spatial information and communications; Underwater network; Design of underwater vehicles;

Common areas: Design for safety; IT-based design; IT-based production engineering; Welding mechanics; Control engineering; GPS and GIS; Inspection and sensor; Port and logistics; Leisure boat and deep sea water; Offshore process systems engineering;

JOET is an open access journal currently published online. Therefore, all ocean engineers and researchers around the world can easily access all journal articles via the journal homepage (<http://www.joet.org>) and download the PDF-based original texts or view the web-based XML texts for free. Offline annual subscription fee is 100USD. **JOET** has a system where two or more peer reviewers must review each submitted paper and it is operated very strictly.

Full text is freely available from <http://www.joet.org> and <http://www.ksoe.or.kr> without sign-in. **JOET** is being indexed in some prominent database such as Korean Citation Index (KCI), Google Scholar, and Directory of Open Access Journals (DOAJ).

JOET is an open access journal distributed under the terms of the creative commons attribution non-commercial license (<http://creativecommons.org/licenses/by-nc/4.0>) which permits unrestricted non-commercial use, distribution, and reproduction in any medium, provided the original work is properly cited.

For correspondences concerning business matters, author needs to contact KSOE Secretariat by email or phone (e-mail: ksoehj@ksoe.or.kr or Tel: +82 51 759 0656). Correspondences for publication matters can be asked via email to the Editor-in-Chief (email: heroeswise2@gmail.com).

Punching Fracture Experiments and Simulations of Unstiffened and Stiffened Panels for Ships and Offshore Structures

Sung-Ju Park¹ and Joonmo Choung¹

¹Professor, Department of Naval Architecture and Ocean Engineering, Inha University, Incheon, Korea

²Postdoctoral researcher, Department of Naval Architecture and Ocean Engineering, Inha University, Incheon, Korea

KEY WORDS: Ductile fracture, Punch test, Structural steel, Stress triaxiality, Lode angle, Hosford-Coulomb model, DSSE model

ABSTRACT: Ductile fracture prediction is critical for the reasonable damage extent assessment of ships and offshore structures subjected to accidental loads, such as ship collisions and groundings. A fracture model combining the Hosford-Coulomb ductile fracture model with the domain of solid-to-shell equivalence model (HC-SDDE), was used in fracture simulations based on shell elements for the punching fracture experiments of unstiffened and stiffened panels. The flow stress and ductile fracture characteristics of JIS G3131 SPHC steel were identified through tension tests for flat bar, notched tension bar, central hole tension bar, plane strain tension bar, and pure shear bar specimens. Punching fracture tests for unstiffened and stiffened panels are conducted to validate the presented HC-DSSE model. The calibrated fracture model is implemented in a user-defined material subroutine. The force-indentation curves and final damage extents obtained from the simulations are compared with experimental results. The HC-DSSE fracture model provides reasonable estimations in terms of force-indentation paths and residual damage extents.

Nomenclature

A, ε_0, n	Material parameters of Swift constitutive model	$\bar{\varepsilon}_{HC}^{pr}$	Fracture strain of Hosford-Coulomb model
a, b, c, n_f	Hosford-Coulomb model parameters	$\bar{\varepsilon}_{DSSE}^{pr}$	Fracture strain of localization necking criterion
D	Damage indicator	$\bar{\varepsilon}_{DSSE}^{PST}$	Strain at the onset of localization under plane strain tension
D_{HC}	Damage indicator of Hosford-Coulomb model	$\bar{\varepsilon}_{p,f}$	Fracture strain
D_{DSSE}	Damage indicator of DSSE model	α	Least square error function
d	Dimension	$\bar{\varepsilon}_{plat}$	End of yield plateau
i	Number of experiments for fracture model calibration	σ	Caucy stress tensor
\mathbf{I}	Identity tensor	σ_m	Mean stress
I_1	First invariant of stress tensor	$\bar{\sigma}$	von Mises stress
J_2	Second invariant of the deviatoric stress tensor		
J_3	Third invariant of the deviatoric stress tensor		
l_e	Length of element		
R	Residual error		
\mathbf{s}	Deviatoric part of stress tensor		
t	Thickness of specimen		
f_1, f_2, f_3	Function of Lode angle parameters		
g_1, g_2	Function of stress triaxiality		
d, p	DSSE model parameter		
k	Flow stress		
η	Stress triaxiality		
$\bar{\theta}$	Lode angle parameter		
$\bar{\varepsilon}_p$	Equivalent plastic strain		

1. Introduction

In accidental scenarios related to ships and offshore structures that involve contact, such as collision and grounding, large deformation and fracture may occur occasionally. Damage assessment based on the numerical analysis of an accident can reduce the cost of physical experiments and reduce human, social, and environmental damages through the design of a structure that effectively responds to the accident load. Mild and high-tensile strength steels primarily used in the shipbuilding and offshore industry are considered as ductile materials. Therefore, information regarding the plasticity and fracture behavior of these steels is essential for an accurate structural behavior

Received 22 April 2020, revised 28 April 2020, accepted 29 April 2020

Corresponding author Joonmo Choung; +82-32-860-7346, jmchoung@inha.ac.kr

© 2020, The Korean Society of Ocean Engineers

This is an open access article distributed under the terms of the creative commons attribution non-commercial license (<http://creativecommons.org/licenses/by-nc/4.0>) which permits unrestricted non-commercial use, distribution, and reproduction in any medium, provided the original work is properly cited.

prediction through the numerical analysis of shipbuilding and offshore structures as well as material experiments.

In a phenomenological model, fracture initiation is defined as the point at which the damage indicator, which is expressed in terms of stress or strain, reaches a threshold. Researchers have used phenomenological models with stress triaxiality and lode angle as stress state parameters to predict ductile material failure (Johnson and Cook, 1985; Xue, 2007; Bai and Wierzbicki, 2008; Choung et al., 2015a; Choung et al., 2015b; Park et al., 2017; Cerik et al., 2019c; Park et al., 2019a; Park et al., 2020). Bai and Wierzbicki (2010) developed the modified Mohr–Coulomb model expressed by stress triaxiality and Lode angle parameter. Mohr and Marcadet (2015) proposed a Hosford–Coulomb (HC) fracture strain model expressed in terms of Mohr–Coulomb failure condition and the Hosford equivalent stress. The Mohr–Coulomb yield criterion-based fracture strain model has been demonstrated through theoretical/experimental studies to simulate the fracture prediction of ductile materials with high accuracy (Roth and Mohr, 2016; Algarni et al., 2017; Cerik et al., 2019a; Park et al., 2019b).

Researchers have attempted to quantitatively measure the extent of damage through failure tests on unstiffened/stiffened panels that are typically used in marine structures (Choung and Cho, 2008; Min and Cho, 2012; Park et al., 2016; Cho et al., 2018; Nho et al., 2018; Cerik et al., 2019b). Although plastic deformation problems accompanied by large strains such as impact and stranding generate complex loads, such as compression, shear, bending, and tension, the major damage mode is caused in the tensile region owing to the continued deformation of the thin-walled shell structure. In this tensile mode damage, localized necking usually occurs, resulting in a local thickness reduction. In other words, the stress state at the point where the local necking occurs changes from a plane stress to a triaxial stress. To accurately predict the local necking, fine solid element meshing is essential. Meanwhile, to reduce computational cost and enhance the simplicity of modeling, use of a shell element is inevitable. However, the existing phenomenological models significantly reduces the accuracy of fracture prediction in shell-element-based numerical analyses (Pack and Mohr, 2017; Park et al., 2019a; Cerik and Choung, 2020). Recently, researchers have attempted to improve the fracture prediction accuracy of a shell-element-based numerical analysis such that it is comparable to that of a solid-element-based numerical analysis. Pack and Mohr (2017) presented a domain of solid-to-shell equivalence (DSSE) model, where the thickness direction necking of a plate was defined as a fracture condition in the shell-element-based fracture simulation.

This study aims to obtain the plasticity and fracture behavior characteristics data of JIS G3131 SPHC, which is a thin structural steel material, and to perform a quantitative verification of the fracture model presented through structural experiments. Swift hardening law and HC–DSSE model material constants were obtained through tensile tests and numerical analysis of specimens of various fracture modes (flat bar, notched tension, central hole, plane strain, and pure shear). A user subroutine was developed to apply the proposed fracture model as

a fracture criterion for the commercial finite element program, Abaqus/Explicit. The quantitative verification of the proposed fracture model was performed by comparing the punching experiment of unstiffened/stiffened panels and the fracture stimulation.

2. Theoretical Background

2.1 Stress State Variable

The stress state of an isotropic material can be represented by the stress triaxiality (η) and Lode angle parameter ($\bar{\theta}$), which are expressed in terms of the stress invariant (Eqs. (1)–(2)). The stress triaxiality and lode angle are expressed in terms of the first invariant (I_1) of the stress tensor ($\boldsymbol{\sigma}$) and the second invariant (J_2) and third invariant (J_3) of the deviatoric stress tensor (\mathbf{s}) (Eqs. (3)–(6)). The range of the Lode angle parameter is $-1.0 \leq \bar{\theta} \leq 1.0$. The relationship between the stress triaxiality and Lode angle parameter is given in Eq. (7), and it can be represented in the plane stress state, as shown in Fig. 1.

$$\eta = \frac{I_1}{3\sqrt{3}J_2} = \frac{\sigma_m}{\sigma} \quad (1)$$

$$\bar{\theta} = 1 - \frac{2}{\pi} \arccos \left[\frac{3\sqrt{3}}{2} \frac{J_3}{(J_2)^{3/2}} \right] = 1 - \frac{2}{\pi} \arccos \left[\frac{27}{2} \frac{J_3}{\sigma^3} \right] \quad (2)$$

$$I_1 = \text{tr}[\boldsymbol{\sigma}] \quad (3)$$

$$J_2 = \frac{1}{2} \mathbf{s} : \mathbf{s} \quad (4)$$

$$J_3 = \det[\mathbf{s}] \quad (5)$$

$$\mathbf{s} = \boldsymbol{\sigma} - \frac{1}{3} I_1 \mathbf{I} = \boldsymbol{\sigma} - \sigma_m \mathbf{I} \quad (6)$$

$$\bar{\theta} = 1 - \frac{2}{\pi} \arccos \left[\frac{27}{2} \eta \left(\eta^2 - \frac{1}{3} \right) \right] \quad (7)$$

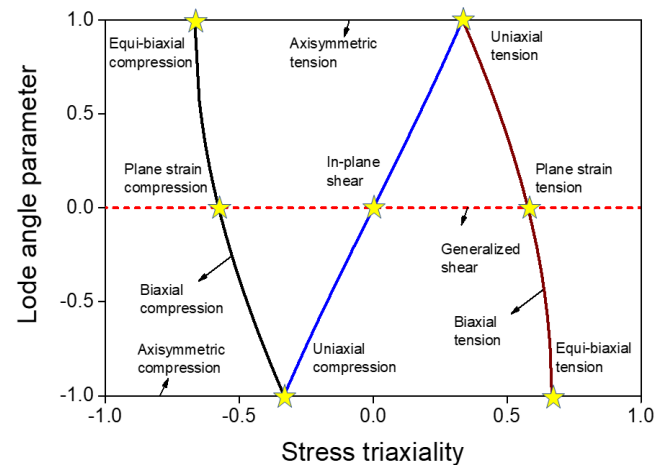


Fig. 1 Stress states on the plane of stress triaxiality and Lode angle parameter (Cerik et al., 2019a)

2.2 Fracture Model for Three-dimensional Stress State

Mohr and Marcadet (2015) presented the Hosford-Coulomb (HC) model as a fracture criterion for ductile materials and structures in a three-dimensional stress state under a proportional loading. In the HC model, the constant stress state parameter, $(\bar{\epsilon}_{HC}^{pr})$ is given as function of stress state parameters $\{\eta, \bar{\theta}\}$ and depends on material constants $\{a, b, c, n_f\}$ (Eq. (8)). Under proportional loading, if the equivalent plastic strain ($\bar{\epsilon}_p$) reaches the fracture strain, it is assumed that fracture has occurred. Roth and Mohr (2016) suggested $n_f = 0.1$ for general steel. Therefore, only material constants a, b , and c need to be determined in the HC model. The material constants a and c of the HC model represent the sensitivities of the stress triaxiality and Lode angle parameter, respectively. The material constant b determines the overall level of the fracture strain. Because the HC model has a small number of material constants, the material constants can be derived through a small number of experiments. Furthermore, the accuracy of the fracture prediction for ductile materials has been demonstrated and used by many researchers. On the other hand, a fracture model needs to consider the variability of the loading path during the deformation of materials and structures. Hence, a linear damage accumulation model, which is expressed as the accumulation of equivalent plastic strains, was used (Eq. (12)). In the accumulative damage model, failure occurs when the damage indicator (D) reaches 1.0.

$$\bar{\epsilon}_{HC}^{pr}(\eta, \bar{\theta}) = b(1+c)^{\frac{1}{n_f}} \left(\left\{ \frac{1}{2} \left((f_1 - f_2)^a + (f_1 - f_3)^a + (f_2 - f_3)^a \right) \right\}^{\frac{1}{a}} + c(2\eta + f_1 + f_3) \right)^{-\frac{1}{n_f}} \quad (8)$$

$$f_1 = \frac{2}{3} \cos\left(\frac{\pi}{6}(1 - \bar{\theta})\right) \quad (9)$$

$$f_2 = \frac{2}{3} \cos\left(\frac{\pi}{6}(3 + \bar{\theta})\right) \quad (10)$$

$$f_3 = -\frac{2}{3} \cos\left(\frac{\pi}{6}(1 + \bar{\theta})\right) \quad (11)$$

$$D = \int_0^{\bar{\epsilon}_{pr}} \frac{d\bar{\epsilon}_p}{\bar{\epsilon}_{HC}^{pr}} \quad (12)$$

2.3 Fracture Model for Plane Stress States

Ships and offshore structures are typical thin-walled shell structures, and shell-element-based modeling for the numerical analysis of these structures is essential for reducing time and simplifying modeling. The classical equivalent plastic-strain-based fracture model including the HC model shows a significantly reduced fracture prediction accuracy in shell-element-based fracture simulations. Park and Mohr (2017) presented a DSSE model as a fracture criterion for plane stress states through the Marciniak-Kuczynski (MK) analysis of a unit-size shell element model. The MK analysis is primarily used to theoretically

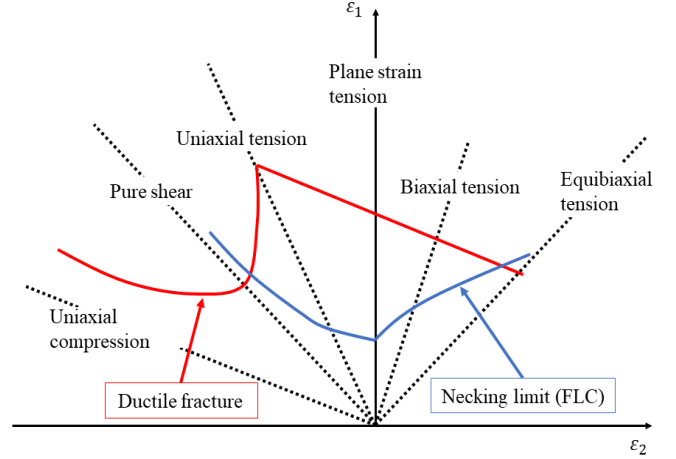


Fig. 2 A schematic curves of ductile fracture and necking limit

derive the forming limit curve of a material to avoid molding defects (necking, fracture, etc.) in the plate forming process. Therefore, the DSSE model considers the thickness direction necking to be a fracture criterion based on assuming that the difference between the local necking in the thickness direction and the point of occurrence of fracture is small based through MK analysis. In this study, for the fracture criterion in the shell-element-based fracture simulation, as shown in Fig. 2, the ductile fracture criterion (HC model) and the necking limit criterion (DSSE model) were applied. The application range of the DSSE model was $(1/3 \leq \eta \leq 2/3)$ for the biaxial tension regime, and the DSSE fracture strain ($\bar{\epsilon}_{DSSE}^{pr}$) comprised the stress triaxiality and material constants b, d , and p , as shown in Eq. (13). The material constant b was used in the HC model as well. Park and Mohr (2017) presented the DSSE model material constant $p = 0.01$ for ordinary steel through MK analysis. Therefore, only material constant d remained in the DSSE model.

Park and Mohr (2017) presented a Considère-assumption-based simplified equation to derive the material constant d of the DSSE model. In the Considère assumption, necking is defined as a plastic instability phenomenon. The flow stress ($k[\bar{\epsilon}_{DSSE}^{pr}]$) at the local necking plastic strain ($\bar{\epsilon}_{DSSE}^{pr}$) in the plane strain tensile (PST) state is shown in Eq. (16). Substituting the plane strain tensile state ($\eta = 1/\sqrt{3}$) into Eq. (13) yields Equation (17), which can be solved through numerical iterations. The linear damage accumulation model of the DSSE is expressed as Eq. (18).

$$\bar{\epsilon}_{DSSE}^{pr} = b \left[\left\{ \frac{1}{2} \left((g_1 - g_2)^d + g_1^d + g_2^d \right) \right\}^{\frac{1}{d}} \right]^{-\frac{1}{p}} \quad (13)$$

$$g_1 = \frac{3}{2}\eta + \sqrt{\frac{1}{3} - \frac{3}{4}\eta^2} \quad (14)$$

$$g_2 = \frac{3}{2}\eta - \sqrt{\frac{1}{3} - \frac{3}{4}\eta^2} \quad (15)$$

$$k[\bar{\epsilon}_{DSSE}^{-PST}] = \frac{2}{\sqrt{3}} \frac{dk[\bar{\epsilon}_{DSSE}^{-PST}]}{d\bar{\epsilon}_p} \quad (16)$$

$$(1 + 2^{d-1})^{\frac{1}{d}} = \sqrt{3} \left(\frac{\bar{\epsilon}_{DSSE}^{-PST}}{b} \right)^{-p} \quad (17)$$

$$D = \int_0^{\bar{\epsilon}_{DSSE}^{-PST}} \frac{d\bar{\epsilon}_p}{\bar{\epsilon}_{DSSE}^{-p}} \quad (18)$$

3. Obtaining Fracture Model Material Constants

3.1 Material Experiment

3.1.1 Steel type

Plates are primarily used in the manufacture of marine structures. Generally, a thick steel plate of thickness 6 mm or more is used as a laboratory specimen. In some cases, structural experiments are conducted using scale model of double hulls (Ehlers et al., 2008; Ringsberg et al., 2018; Cerik et al., 2019b), but large structural experiments are subject to constraints (experimental equipment capacity, cost issues, etc.). In this study, owing to these practical limitations, a damage evaluation study was conducted through a structural experiment of unstiffened/stiffened panels of a JIS G3131 SPHC hot-rolled thin plate with a thickness of 1.9 mm. The width of the target steel base plate was 1,530 mm, and the chemical composition is shown in Table 1. The longitudinal direction of the plate material was defined as a rolling direction.

3.1.2 Tensile tests

Fig. 3 shows the drawing and names of tensile specimens fabricated for the calibration of flow stress and fracture model material constants. The specimens were processed in the direction perpendicular to the steel processing direction, and the specimen thickness was 1.9 mm, which is the same as that of the base material. The dimensions of the flat smooth bars (FB) were in accordance with ASTM (2004) standards. A notched tension specimen (NT20) was used to verify the flow stress owing to its high elongation to fracture and excellent experimental reproducibility. The central hole specimen (CH) had a hole of radius of 4 mm at the center of the specimen, and it was designed to derive the stress state parameter in a pure tensile state at the fracture point. PST and pure shear (SH) specimens were designed to induce fracture states owing to PST and pure shear, respectively.

A tensile test was performed at room temperature through displacement control at a stroke speed of 0.5 mm/min using a universal material testing machine. In the experiment, the load of the lode cell and the displacement of the 50 mm extensometer were measured. The

Table 1 Chemical composition of JIS G3131 SPHC steel

Material	C	Si	Mn	P	S
JIS G3131 SPHC	0.0509	0.02	0.24	0.014	0.0062

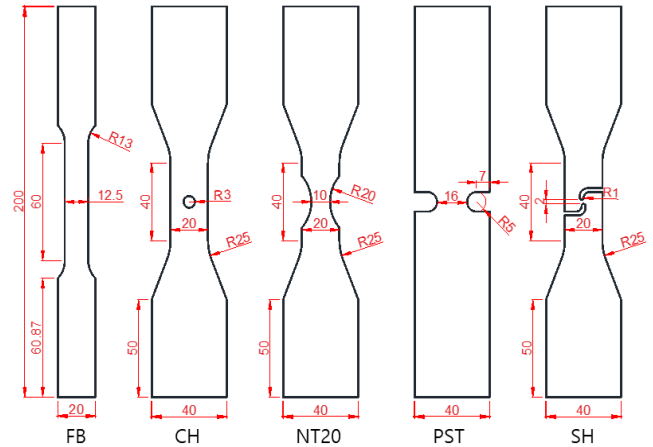


Fig. 3 Design of the specimens (unit: mm)

obtained load-displacement curve was used for the quantitative verification of the numerical analysis.

3.2 Numerical Analysis

3.2.1 Finite element modeling

A numerical analysis of each specimen is essential to derive the loading path at the fracture point. Fig. 4 shows the finite element model. CH, PST, and NT20 modeling was performed based on an 1/8 modeling by applying symmetrical conditions in the length, width, and thickness directions of the specimen. The shear specimens were modeled based on a 1/2 modeling through symmetrical conditions with respect to the thickness direction of the specimen. Each specimen was produced up to 50 mm, to which the extensometer was attached. In addition, by increasing the element size in regions far from the predicted fracture notch of the specimen, the time cost of numerical analysis was reduced. The size of the elements was determined by a sensitivity test according to the size of the elements. Finally, 10 elements were arranged in the thickness direction of the specimen.

3.2.2 Flow stress calculation

The true strain-true stress curve obtained through the tensile testing of smooth specimens is not valid beyond the ultimate strength, at which specimen non-uniformity occurs. In the numerical analysis of a fracture accompanied by a large strain, the flow stress is extrapolated

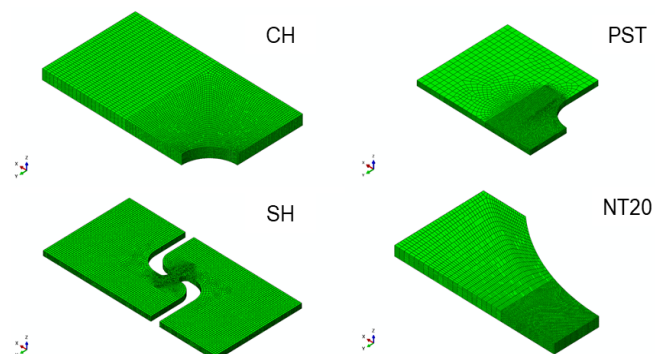


Fig. 4 Finite element models of the specimens

using the Swift constitutive equation. The Swift construction equation including the yield plateau where the initial yield stress is maintained comprises two parts: before and after $\bar{\epsilon}_{plat}$ where the yield plateau ends, as shown in Eq. (19).

$$k = f[\bar{\epsilon}_p] = \begin{cases} \sigma_0 & \text{if } \bar{\epsilon}_p \leq \bar{\epsilon}_{plat} \\ A(\epsilon_0 + \bar{\epsilon}_p)^n & \text{if } \bar{\epsilon}_p > \bar{\epsilon}_{plat} \end{cases} \quad (19)$$

The material constants of the Swift constitutive equation, $\{A, \epsilon_0, n\}$ were determined through a fit to the uniform-true-stress-uniform-true-strain curve obtained from the smoothing material experiment up to the ultimate strength. The flow stress is shown in Fig. 5, and it was used to compute the numerical analysis results and experimental results of NT20, which are shown in Fig. 6. It was confirmed from the numerical analysis results of NT20 that the flow stress, which was suggested from the numerical analysis, matched the experimental results accurately.

3.2.3 Loading path review

In this study, the time at which specimen fracture occurred was defined as the time at which the specimen suddenly lost its stiffness

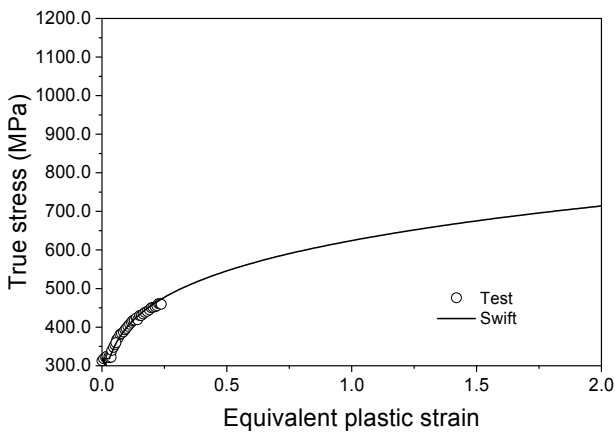


Fig. 5 Flow stress of JIS G3131 SPHC

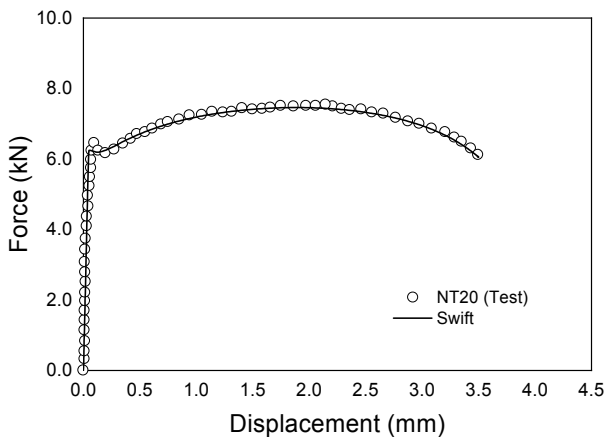
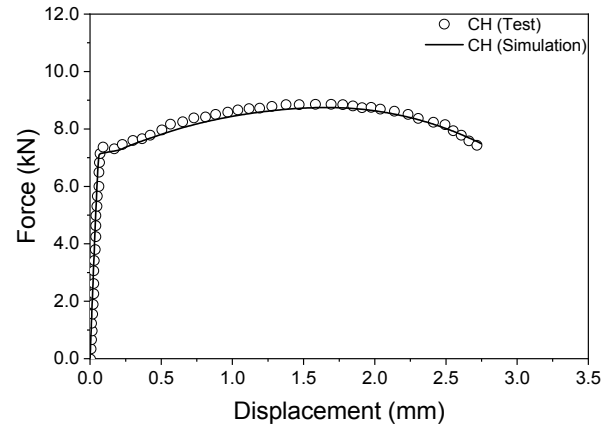
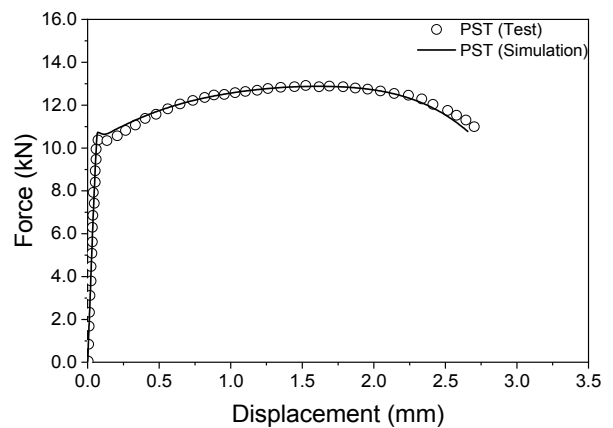


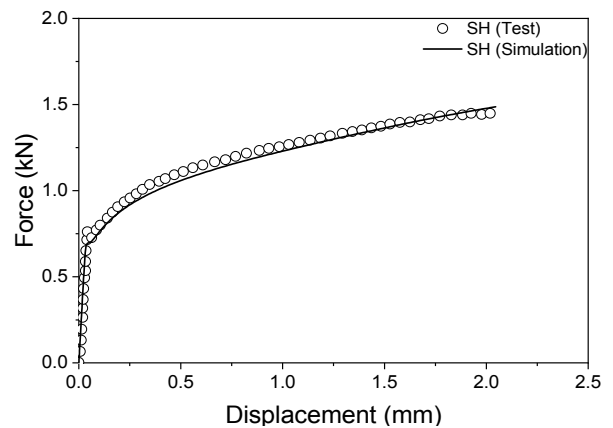
Fig. 6 Comparison of experimental and numerically predicted force-displacement curve of NT20



(a) CH



(b) PST



(c) SH

Fig. 7 Comparison of force-displacement between test and simulation

and the load rapidly decreased during the experiment. In the numerical analysis, the fracture initiation part was defined as the factor with the largest equivalent plastic strain at the time of fracture. Fig. 7 shows a load-displacement curve obtained from the experiments and numerical analysis of CH, PST, and SH until the point of failure. The numerical analysis results are consistent with the experiment results.

Fig. 8 shows the stress state parameter variability according to the equivalent plastic strain at the fracture point of each specimen. It was observed that CH exhibited a relatively small stress state variability. In

the case of PST, it was confirmed that the variability of the stress triaxiality was greater than that of the Lode angle because the initial notch radius did not maintain the shape as the specimen was subjected to a tensile force. In the case of SH, it was discovered that a tensile–shear combined load was applied in the initial pure tension as it approached the fracture point.

3.3 Determination of Fracture Model Material Constants

An optimization technique was applied to determine the material constants of the HC model. The design variables were set to the material constants of the HC model, the constraint to the range of the material constants, and the objective function to the minimum value of the error residual sum of squares (R^2) (Eq. (20)). The residual sum of squares of error means the sum of squares of the ratio of the loading path data to the corresponding predicted data, $\bar{\varepsilon}_{HC}^{pr}$, as shown in Eq. (21). The numerical analysis data of each specimen comprised at least 300 data points until failure occurred such that the error occurring in the entire loading path was minimized. i indicates the number of experiments conducted to calibrate the material constant. The material constants of the DSSE model were determined using Eqs. (16) and (17). Table 2 shows the material constants of the final version of the

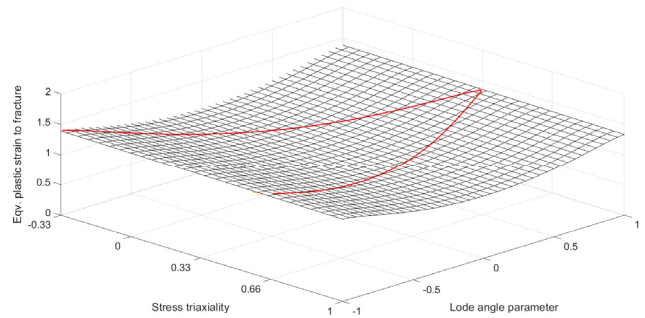
Table 2 Calibrated HC-DSSE model parameters

Constraint	HC model parameters			R^2	DSSE parameter
	a	b	c		d
$1.0 \leq a \leq 2.0$					
$0.1 \leq b \leq 2.0$	1.5979	1.3599	0.0012	0.0007	1.7027
$0.0001 \leq c \leq 0.2$					

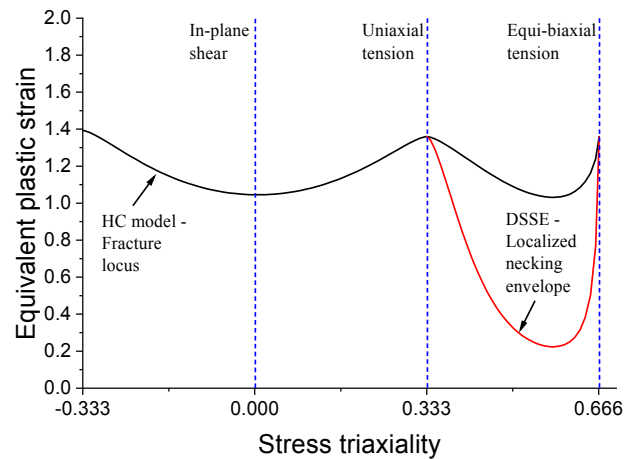
HC model as well as the design variables, constraints, residual sum of squares, and material constants of the DSSE model.

$$R^2 = \left\{ \left(\int_0^{\bar{\varepsilon}_{pr}} \frac{d\bar{\varepsilon}_p}{\bar{\varepsilon}_{HC}^{pr}} \right) - 1 \right\}^2 \tag{20}$$

$$\bar{\alpha} = \operatorname{argmin} \left\{ \sum_{i=1}^3 \left\{ \left(\int_0^{\bar{\varepsilon}_f} \frac{d\bar{\varepsilon}_p}{\bar{\varepsilon}_{HC}^{pr}} \right) - 1 \right\}^2 \right\} \tag{21}$$



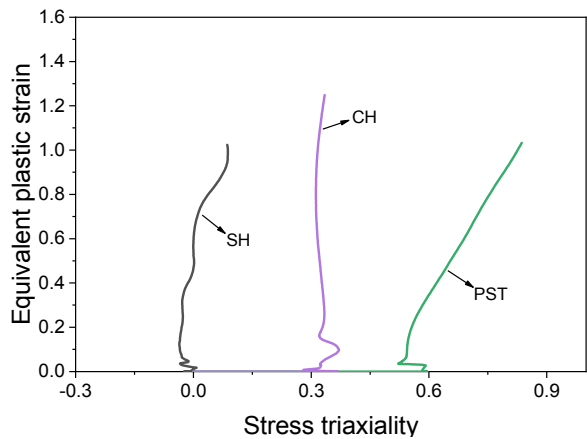
(a) 3D fracture surface



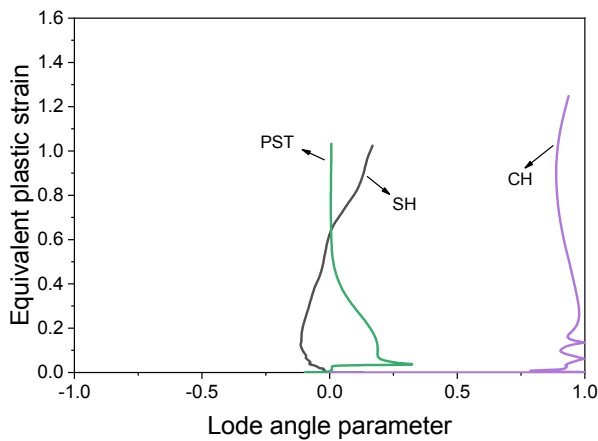
(b) Plain strain condition

Fig. 9 Fracture locus of JIS G3131 SPHC grade steel

Fig. 9(a) shows the HC model in a three-dimensional plane. It was observed that JIS G3131 SPHC steel was more sensitive to the volatility of the stress triaxiality than the lode angle. Fig. 9(b) shows the HC-DSSE model in the plane stress state. It was observed that the HC and DSSE models indicated the lowest strain in the PST, and that the necking condition of the DSSE was significantly lower than that of



(a) η



(b) $\bar{\theta}$

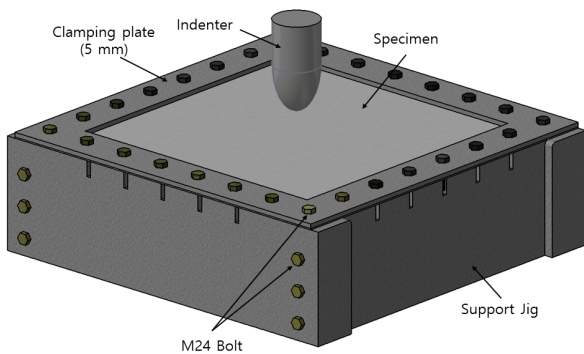
Fig. 8 Evolution of the equivalent plastic strain against stress state parameters

the HC model.

4. Semistatic Punching Experiment and Simulation

4.1 Experiment Summary

In this study, for the quantitative verification of the proposed HC-DSSE fracture model, an unstiffened and two stiffened panels punching fracture experiments of the same JIS G3131 SPHC steel and a shell-element-based fracture simulation were performed. The experimental setup is shown in Fig. 10, where the specimen was bolted to the jig to be fixed, to which a forced displacement of the indenter was applied. The indenter was manufactured in an ellipse shape of radii 50.0 and 25.0 mm in the major and minor axes, respectively (Fig. 11 (b)), and the major axis was in contact with the specimen. The drawings and names of the unstiffened and stiffened panels are shown in Fig. 11 (a). The unstiffened panel (0-FB) measured 800 mm × 800 mm × 1.9 mm, whereas the reinforcement measured 25.0 mm in height and 1.9 mm in thickness. For the stiffened panels, the stiffener was welded to the unstiffened panel, and depending on the number of reinforcing materials used, it was categorized into 1-FB for one reinforcing material, and 2-FB for two reinforcing materials. The thickness centerline of the reinforcing material of 1-FB coincided with that of the stiffened panels. Therefore, the indenter penetrated the stiffener. The centerline of the 2-FB reinforcing material was 100 mm off the centerline of the specimen, and an indenter penetrated between the stiffeners. It was single-pass welded using a TIG (tungsten inert-gas arc welding) arc welding machine. The welding speed was 5.0 mm/min, the rated output current was 50 A, and the load voltage is 70 V.



(a) Schematic of a punch test



(b) Photo of a punch test for un-stiffened panel

Fig. 10 Schematic and photo of a punch test

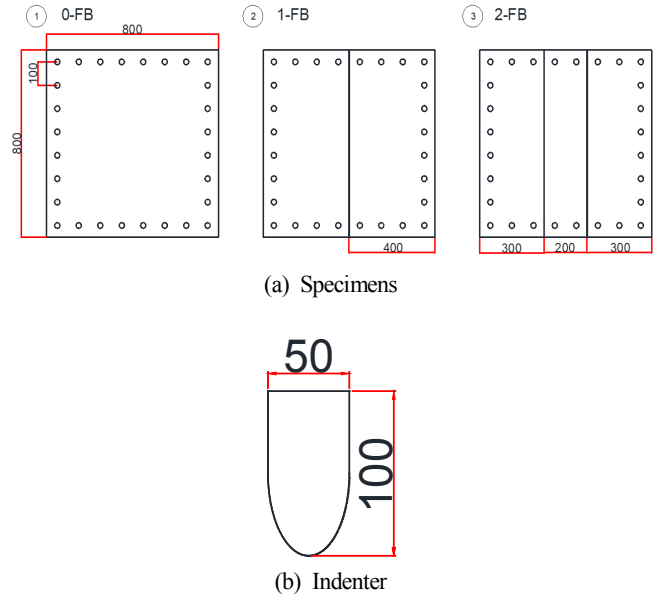


Fig. 11 Drawing of the test specimens and indenter (unit: mm)

The effective width excluding the specimen support was 600.0 mm × 600.0 mm. To evenly distribute the force to the fixed part of the specimen, a cover was separately manufactured. The forced displacement speed of the indenter was 10 mm/min. The stroke displacement and load were measured from the experiment.

4.2 User Subroutine Development

Through the development of the user subroutine of Abaqus/Explicit, a commercial finite element analysis program, the HC-DSSE model was applied as a fracture criterion. Fig. 12 shows the general algorithm of the material user subroutine, VUMAT. A single shell element has a section point in the component thickness direction. In this study, a

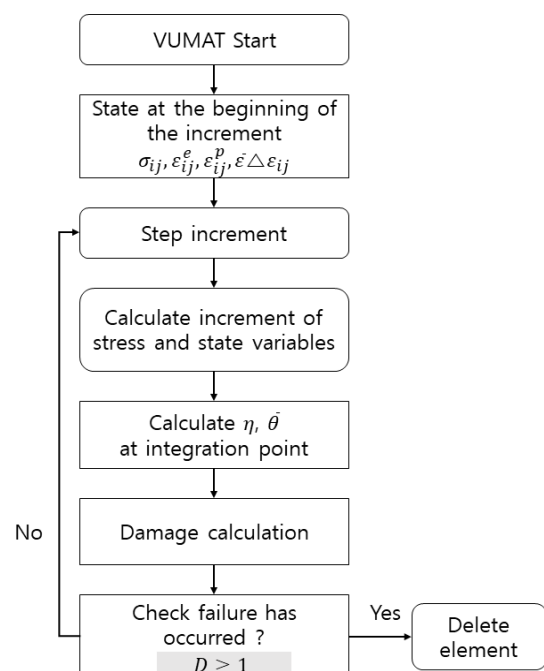


Fig. 12 Material user subroutine algorithm

four-node reduced integration (S4R) shell element with five integral thickness points, which is provided by Abaqus/Explicit, was used in the modeling. When one of the five-section points reached $D_{HC} = 1.0$ or all five integration points reach $D_{DSSE} = 1.0$, the integration point loses its stiffness and deleted. An element is deleted if all integration points lose their stiffnesses.

4.3 Numerical Analysis

4.3.1 Numerical analysis of unstiffened panel

The finite element model of the unstiffened panel specimen was generated using an S4R shell element. The indenter was modeled with a four-node rigid element. To verify the sensitivity of the element size, the element size of the unstiffened panel was modeled such that the ratio of the specimen thickness of 1.9 mm to the element length l_e was approximately 5.0 ($l_e = 10.0$ mm), 2.5 ($l_e = 5.0$ mm), and 1.25 ($l_e = 2.5$ mm). The modeling according to the boundary conditions and element size of the numerical analysis is shown in Fig. 13. The shell element was created for the entire width of the specimen (800 mm × 800 mm),

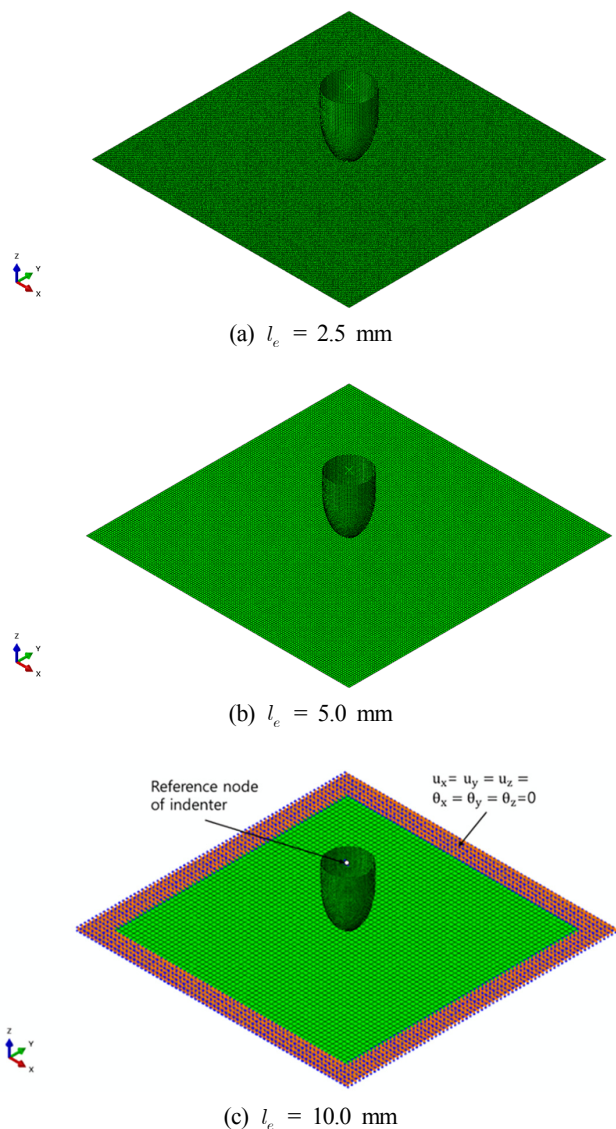


Fig. 13 Finite element models of un-stiffened panel

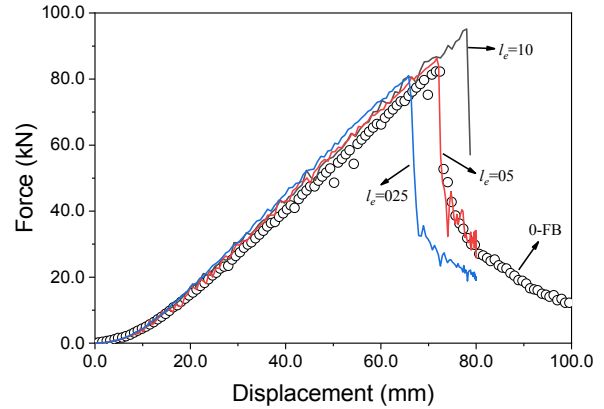


Fig. 14 Comparison of displacement-force curve between un-stiffened panel test and simulation

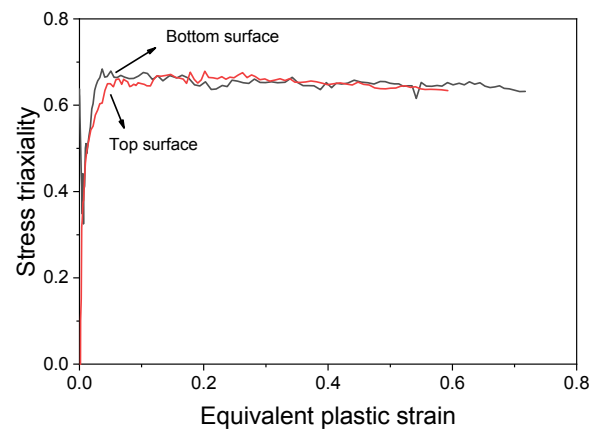
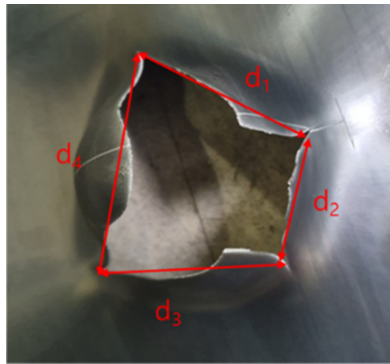


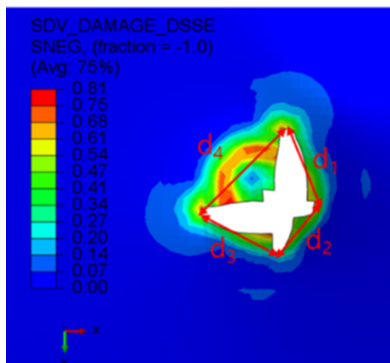
Fig. 15 Evolution of stress triaxiality in the fracture initiation element (mesh size: 5.0 mm)

and the six degrees of freedom of the specimen fixture, except for the effective width (600 mm × 600 mm), was fixed. The load was implemented by applying a forced displacement to the reference node of the rigid element (indenter). The speed of the indenter was 10 mm per minute, which was slow; hence, the analysis time was long. To address this problem, mass scaling and energy balance methods can be used. Because mass scaling can significantly induce the effect of inertia force at high-speed deformation during fracture, the analysis time was accelerated using energy balance. In other words, the simulation time was reduced by increasing the speed of the indenter such that the ratio of the kinetic energy to the total energy was maintained within 1.0%. After the speed was determined, the friction coefficient was determined such that the error rate of the load-displacement curve slope was the smallest in the experiment through repeated numerical analyses. According to numerical analysis, the friction coefficient was assumed to be 0.23.

Fig. 14 shows the load-stroke displacement curves from the unstiffened panel experiment and the numerical analysis. Based on the numerical analysis result, it was discovered that the fracture displacement differed according to the element size. In this study, the effect of the shell element size on the fracture strain was not considered, and because the shell element size that yielded the most accurate



(a) Test



(b) Simulation ($l_e = 5.0$ mm)

Fig. 16 Comparison of fracture propagation between un-stiffened panel tests and simulations

Table 3 Comparison of the experimentally measured and numerically predicted rupture size for un-stiffened panel test

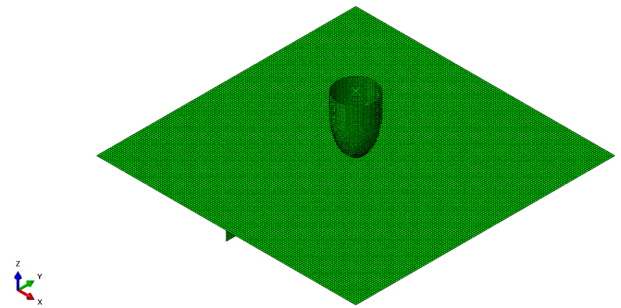
Case	d_1 (mm)	d_2 (mm)	d_3 (mm)	d_4 (mm)
0-FB (Test)	7.3	5.1	7.1	8.7
0-FB (Simulation)	7.32	5.2	6.63	8.04
Error	0.27	1.96	6.62	7.59

simulation result was 5.0 mm ($l_e/t = 2.5$), 5.0 mm was selected as the final element size. Fig. 15 shows the stress triaxiality according to the equivalent plastic strain increment of the indenter top surface and the bottom surface selection point of the fracture initiation point.

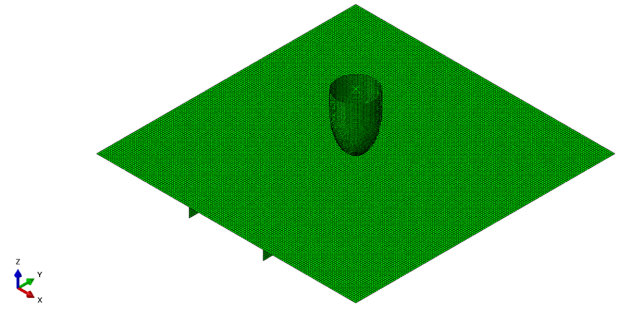
It was discovered that the stress states of the top (the indenter contact surface) and bottom surfaces of the specimen at the fracture point were highly strained under nearly equi-biaxial tension. Fig. 16 and Table 3 show the fracture extents of the final displacement results in the experiment and numerical analysis. From these results, it was discovered that the final fracture shape of the simulation analysis matched well with that of the experiment.

4.3.2 Numerical analysis of reinforcing plates

The element size of the stiffened panels in the modeling was $l_e = 5.0$, which was determined through the element size convergence test of the unstiffened panel. The FB-1 and FB-2 numerical analysis models are shown in Fig. 17. The boundary conditions and analysis conditions

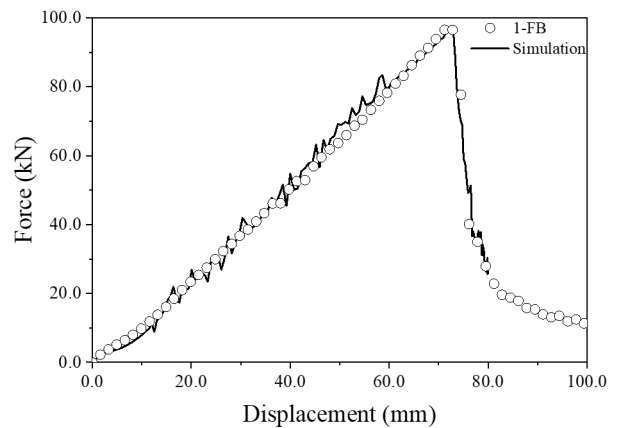


(a) FB-1

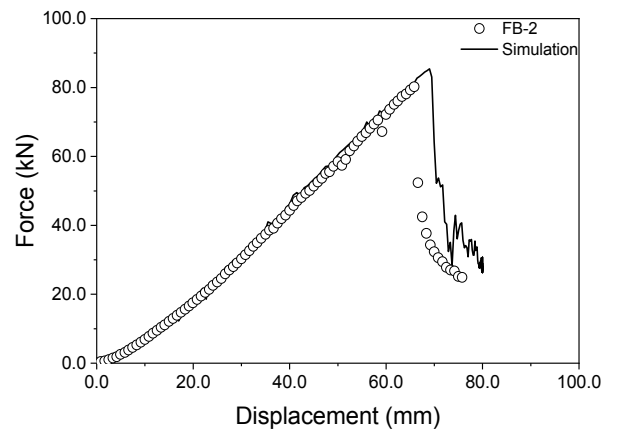


(b) FB-2

Fig. 17 Finite element models of stiffened panel



(a) FB-1



(b) FB-2

Fig. 18 Comparison of force-displacement curves obtained tests and simulation

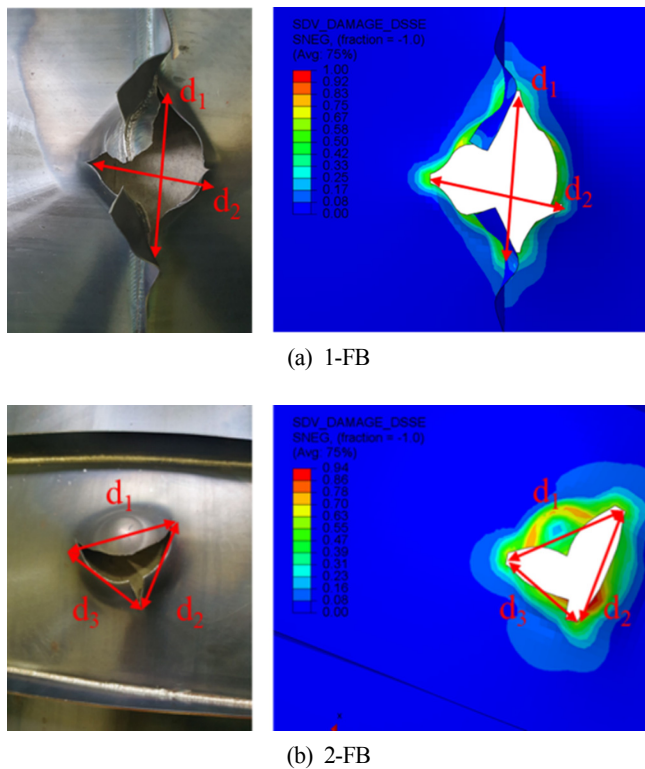


Fig. 19 Comparison of fracture propagation between stiffened panel test and simulations

Table 4 Comparison of the experimentally measured and numerically predicted rupture size for stiffened panel test

Case	d_1 (mm)	d_2 (mm)	d_3 (mm)
1-FB (Test)	12.0	9.9	-
1-FB (Simulation)	11.70	9.73	-
Error	2.50	1.72	-
2-FB (Test)	8.0	8.0	7.0
2-FB (Simulation)	7.9	7.3	6.7
Error	1.25	8.75	4.29

were the same as those for the unstiffened panel. Fig. 18 shows the numerical analysis results. It was observed that the fracture displacement and maximum load in the numerical analysis of 1-FB were similar to the experimental values. The error rates of the fracture initiation load and the fracture initiation displacement in the 2-FB numerical analysis were 6% and 8.4%, respectively. Fig. 19 shows the fractures of the specimens obtained from the experiments and numerical analyses of 1-FB and 2-FB. Table 4 shows a comparison of the fracture ranges from the experiments and numerical analysis, in which a relatively small error rate was observed.

5. Conclusion

Tensile specimens were fabricated using smooth bars for general structural steels and tested, in which nonlinear numerical analysis and

extrapolation were used to obtain the flow stress values up to the large strain section. To obtain the material constants for the HC fracture model and DSSE fracture model, various notched specimens were fabricated and tested on the same steel, and the flow stress results were applied to the nonlinear numerical analysis model to confirm the quantitative numerical analysis results. An optimization method was applied to the numerical analysis results of these material constant acquisition specimens to acquire the material constants of the HC and DSSE models.

A user subroutine was developed to apply the HC-DSSE fracture model as a fracture condition to a commercial finite element analysis program. Furthermore, to conduct a quantitative verification of the fracture model, a punching experiment of a unstiffened/stiffened panels and a fracture simulation based on a shell element were performed. The element size of the numerical model of the stiffened panels was determined by the sensitivity test of the shell element size for the numerical analysis of the unstiffened panel. Local necking occurred in the local area on the materials and structures, whereas dense elements simulated the exact necking point in the numerical analysis. Although the DSSE model considered necking and ductile fracture displacement to be closely related, it was difficult to ascertain exactly when the actual fracture occurred after the necking. Therefore, considering the exact necking point as a fracture using a dense element can underestimate the fracture displacement. This effect can be corrected by sufficiently enlarging the element size. It was confirmed in this study that the numerical analysis result predicted the fracture behavior of the structure the most accurately when the element size was approximately 2.5 times the thickness of the structure. In the future, it is necessary to solve the component sensitivity issue of the fracture model by conducting studies, such as the correction of fracture strain according to the element size. Furthermore, accidents such as the collision and stranding of the ship's offshore structures typically cause dynamic loads on the structures. To apply the ductile material fracture model to these problems, studies on the effect of strain rate on ductile fracture should be conducted in the future.

Acknowledgments

This work was supported by Korea Environment Industry & Technology Institute (KEITI) through Industrial Facilities & Infrastructure Research Program, funded by Korea Ministry of Environment(MOE)(146836). This research was funded and conducted under 「the Competency Development Program for Industry Specialists」 of the Korean Ministry of Trade, Industry and Energy (MOTIE), operated by Korean Institute for Advancement of Technology (KIAT). (No. N0001287, HRD program for Korea-UK Global Engineer Education Program for Offshore Plant)

References

Algarni, M., Choi, Y., & Bai, Y. (2017). A Unified Material Model for

- Multiaxial Ductile Fracture and Extremely Low Cycle Fatigue of Inconel 718. *International Journal of Fatigue*, 96, 162-177. <https://doi.org/10.1016/j.ijfatigue.2016.11.033>
- American Society for Testing and Materials (ASME). (2004). *Standard Test Methods of Tension Testing of Metallic Materials (ASTM E8)*. American Society for Testing and Materials.
- Bai, Y., & Wierzbicki, T. (2008). A New Model of Metal Plasticity and Fracture with Pressure and Lode Dependence. *International Journal of Plasticity*, 24(6), 1071-1096. <https://doi.org/10.1016/j.ijplas.2007.09.004>
- Bai, Y., & Wierzbicki, T. (2010). Application of Extended Mohr-Coulomb Criterion to Ductile Fracture. *International Journal of Fracture*, 161(1), 1-20. <https://doi.org/10.1007/s10704-009-9422-8>
- Cerik, B.C., & Choung, J. (2020). On the prediction of ductile fracture in ship structures with shell elements at low temperatures. *Thin-Walled Structures*, 151, 106721. <https://doi.org/10.1016/j.tws.2020.106721>
- Cerik, B.C., Lee, K., Park, S.J., & Choung, J. (2019a). Simulation of Ship Collision and Grounding Damage Using Hosford-Coulomb Fracture Model for Shell Elements. *Ocean Engineering*, 173, 415-432. <https://doi.org/10.1016/j.oceaneng.2019.01.004>
- Cerik, B.C., Ringsberg J.W., & Choung, J. (2019b). Revisiting MARSTRUCT Benchmark Study on Side-shell Collision with a Combined Localized Necking and Stress-state Dependent Ductile Fracture Model. *Ocean Engineering*, 187, 106173. <https://doi.org/10.1016/j.oceaneng.2019.106173>
- Cerik, B.C., Park, B., Park, S.J., & Choung, J. (2019c). Modeling, Testing and Calibration of Ductile Crack Formation in Grade DH36 Ship Plates. *Marine Structures*, 66, 27-43. <https://doi.org/10.1016/j.marstruc.2019.03.003>
- Choung, J., & Cho, S.R. (2008). Study on True Stress Correction from Tensile Tests. *Journal of Mechanical Science and Technology*, 22, 1039-1051. <https://doi.org/10.1007/s12206-008-0302-3>
- Choung, J., Park, S.J., & Kim, Y. (2015a). Development of Three Dimensional Fracture Strain Surface in Average Stress Triaxiality and Average Normalized Lode Parameter Domain for Arctic High Tensile Steel: Part I Theoretical Background and Experimental Studies. *Journal of Ocean Engineering and Technology*, 29(6), 445-453. <https://doi.org/10.5574/KSOE.2015.29.6.445>
- Choung, J., Park, S.J., & Kim, Y. (2015b). Development of Three-Dimensional Fracture Strain Surface in Average Stress Triaxiality and Average Normalized Lode Parameter Domain for Arctic High Tensile Steel: Part II Formulation of Fracture Strain Surface. *Journal of Ocean Engineering and Technology*, 29(6), 454-462. <https://doi.org/10.5574/KSOE.2015.29.6.454>
- Cho, S.R., Park, J.Y., Song, S.U., & Park, S.H. (2018). Scale Effects on the Structural Behavior of Steel Unstiffened Plates Subjected to Lateral Collisions, *Journal of the Society of Naval Architects of Korea*, 55(2), 178-186. <https://doi.org/10.3744/SNAK.2018.55.2.178>
- Ehlers, S., Broekhuijsen, J., Alsos, H.S., Biehl, F., & Tabri, K. (2008). Simulating the collision response of ship side structures: A failure criteria benchmark study. *International Shipbuilding Progress*, 55(1), 127-144. <https://doi.org/10.3233/ISP-2008-0042>
- Johnson, G.R., & Cook, W.H. (1985). Fracture Characteristics of Three Metals Subjected to Various Strain, Strain Rates Temperatures and Pressures. *Engineering Fracture Mechanics*, 21(1), 31-48. [https://doi.org/10.1016/0013-7944\(85\)90052-9](https://doi.org/10.1016/0013-7944(85)90052-9)
- Mohr, D., & Marcadet, S. (2015). Micromechanically-motivated Phenomenological Hosford-coulomb Model for Predicting Ductile Fracture Initiation at Low Stress Triaxialities. *International Journal of Solids and Structures*, 67-68, 40-55. <https://doi.org/10.1016/j.ijsolstr.2015.02.024>
- Min, D.K., & Cho, S.R. (2012). On the Fracture of Polar Class Vessel Structures Subjected to Lateral Impact Loads. *Journal of the Society Naval Architects of Korea*, 49(4), 281-286. <https://doi.org/10.3744/SNAK.2012.49.4.281>
- Nho, I.S., Park, M.J., & Cho, Y.S. (2018). Preliminary Structural Design of Blast Hardened Bulkhead (The 2nd Report : Scantling Formula for Curtain Plate Type Blast Hardened Bulkhead). *Journal of the Society Naval Architects of Korea*, 55(5), 379-384. <https://doi.org/10.3744/SNAK.2018.55.5.379>
- Pack, K., & Mohr, D. (2017). Combined Necking & Fracture Model to Predict Ductile Failure with Shell Finite Elements. *Engineering Fracture Mechanics*, 182, 32-51. <https://doi.org/10.1016/j.engfracmech.2017.06.025>
- Park, S.J., Lee, K., & Choung, J. (2016). Punching Fracture Simulations of Circular Unstiffened Steel Plates Using Three-dimensional Fracture Surface. *Journal of Ocean Engineering and Technology*, 30(6), 474-483. <https://doi.org/10.5574/KSOE.2016.30.6.474>
- Park, S.J., Park, B., & Choung, J. (2017). Ductile fracture predictions of High Strength Steel (EH36) Using Linear and Non-Linear Damage Evolution Models. *Journal of Ocean Engineering and Technology*, 31(4), 288-298. <https://doi.org/10.26748/KSOE.2017.08.31.4.288>
- Park, S.J., Lee, K., Cerik B.C., Kim, Y., & Choung, J. (2019a). Ductile Fracture of a Marine Structural Steel Based on HC-DSSE Combined Fracture Strain Formulation. *Journal of the Society of Naval Architects of Korea*, 56(1), 82-93. <https://doi.org/10.3744/SNAK.2019.56.1.082>
- Park, S.J., Lee, K., Cerik B.C., & Choung, J. (2019b). Ductile Fracture Prediction of EH36 Grade Steel Based on Hosford-Coulomb Model. *Ships and Offshore Structures*, 14, 68-78. <https://doi.org/10.1080/17445302.2019.1565300>
- Park, S.J., Cerik B.C., & Choung, J. (2020). Comparative Study on Ductile Fracture Prediction of High-tensile Strength Marine Structural Steels. *Ships and Offshore Structures*. <https://doi.org/10.1080/17445302.2020.1743552>
- Ringsberg, J.W., Amdahl, J., Chen, B.Q., Cho, S.R., Ehlers, S., Hu, Z., ... Zhang, S. (2018). MARSTRUCT Benchmark Study on Nonlinear FE Simulation of an Experiment of an Indenter Impact

with a Ship Side-shell Structure. *Marine Structures*, 59, 142-157.
<https://doi.org/10.1016/j.marstruc.2018.01.010>

Roth, C.C., & Mohr, D. (2016). Ductile Fracture Experiments with Locally Proportional Loading Histories. *International Journal of Plasticity*, 79, 328-354. <https://doi.org/10.1016/j.ijplas.2015.08.004>

Xue, L. (2007). Damage Accumulation and Fracture Initiation in Uncracked Ductile Solids Subject to Triaxial Loading. *International Journal of Solids and Structures*, 44(16), 5163-5181. <https://doi.org/10.1016/j.ijsolstr.2006.12.026>

Author ORCIDs and Contributions

Author name	ORCID	Contributions
Park, Sung-Ju	0000-0002-7129-8567	①②③④
Choung, Joonmo	0000-0003-1407-9031	⑤

- ① Conceived of the presented idea or developed the theory
- ② Carried out the experiment or collected the data
- ③ Performed the analytic calculations or numerical simulations
- ④ Wrote the manuscript
- ⑤ Supervised the findings of this study

Prediction of Barge Ship Roll Response Amplitude Operator Using Machine Learning Techniques

Jae Hwan Lim¹ and Hyo Jae Jo²

¹Graduate Student, Ocean Science and Technology, Korea Maritime and Ocean University, Busan, Korea

²Professor, Division of Naval Architecture and Ocean Systems Engineering, Korea Maritime and Ocean University, Busan, Korea

KEY WORDS: Machine learning, Barge type ship, Roll Motion, Response amplitude operator (RAO), Deep neural network (DNN), Root mean square error (RMSE), Standard deviation (SD)

ABSTRACT: Recently, the increasing importance of artificial intelligence (AI) technology has led to its increased use in various fields in the shipbuilding and marine industries. For example, typical scenarios for AI include production management, analyses of ships on a voyage, and motion prediction. Therefore, this study was conducted to predict a response amplitude operator (RAO) through AI technology. It used a neural network based on one of the types of AI methods. The data used in the neural network consisted of the properties of the vessel and RAO values, based on simulating the in-house code. The learning model consisted of an input layer, hidden layer, and output layer. The input layer comprised eight neurons, the hidden layer comprised the variables, and the output layer comprised 20 neurons. The RAO predicted with the neural network and an RAO created with the in-house code were compared. The accuracy was assessed and reviewed based on the root mean square error (RMSE), standard deviation (SD), random number change, correlation coefficient, and scatter plot. Finally, the optimal model was selected, and the conclusion was drawn. The ultimate goals of this study were to reduce the difficulty in the modeling work required to obtain the RAO, to reduce the difficulty in using commercial tools, and to enable an assessment of the stability of medium/small vessels in waves.

1. Introduction

Vessels located in a marine environment move in six degrees of freedom (6DOF). Among the 6DOF motions, the roll determines the boarding comfort, stability, and work environment of the passengers. Moreover, roll motions are associated with marine accidents such as ship overturn, which cause more material and human damage than ship engine failures. To prevent such marine accidents, there is a need for a process to identify the stability in waves in the ship design stage. As the stability of vessels is determined by the response amplitude operator (RAO) and wave energy spectrum of the floating body, it is critical to determine the RAOs of vessels. Existing methods to determine the RAO include experimental methods and computer analysis simulations. The determination of an RAO through experiments involves difficulties, owing to various constraints in the experimental model, equipment, and environment. To determine the RAO using computer simulations, the following three steps are required.

Step 1: A modeling process is conducted for the information of the vessel. This is a preliminary step for analysis and simulation, in which

the shape information of the ship is generated.

Step 2: The vessel conditions are set. For example, the center of gravity and radius of gyration are input, considering the loading conditions and shape information of the vessel.

Step 3: The motion responses are analyzed in the frequency domain. Then, the analysis results (such as the RAO per external force direction) can be obtained.

However, the shape information of vessels is not easy to obtain, and some small and medium vessels do not have detailed information (e.g., drawings). Furthermore, computer simulation methods have inefficient aspects, as the above three steps must be repeated when the shape of the vessel changes. In addition, users have different skill levels for the commercial tools used in simulation, affecting the reliability of the results.

In view of the rising interest in artificial intelligence (AI)-related research in various fields, the shipbuilding and marine industry is also conducting research using AI techniques. Ham (2016) predicted lead times by considering the specifications and supply routes of fittings in shipyards using data mining techniques. Kim (2018) verified and

Received 5 December 2019, revised 13 May 2020, accepted 21 May 2020

Corresponding author Hyo-Jae Jo: +82-51-410-4302, hjjo@kmou.ac.kr

© 2020, The Korean Society of Ocean Engineers

This is an open access article distributed under the terms of the creative commons attribution non-commercial license (<http://creativecommons.org/licenses/by-nc/4.0>) which permits unrestricted non-commercial use, distribution, and reproduction in any medium, provided the original work is properly cited.

discussed prediction models for production lead times by considering the properties of blocks and pipes among the data of shipyards. In terms of ship operations, Park et al. (2004) and Lee et al. (2005) evaluated stability to disturbances during the navigation of specific vessels using a 3D panel method and researched a system for evaluating an optimal sea route by setting the kinematic phenomena of the hull (such as excessive rolling phenomenon) as variables. Mahfouz (2004) defined parameters related to a nonlinear roll to predict a nonlinear roll time series for vessels, and measured the accuracy using a cross-validation function and applying a regression algorithm. Kang et al. (2012) used artificial neural network (ANN) techniques to predict, in real time, the responses of floating bodies to nonlinear waves. Kim et al. (2018) predicted the roll motions of 9600TEU container ships in operation using navigation variables. Kim (2019) developed a fuel consumption rate prediction model based on ship operation data and created and verified a decision support model for abnormal conditions of equipment on sailing ships. Kim et al. (2019) tested seakeeping performance by using the RAO at various incident angles. Jeon (2019) developed a meta-model by combining three machine learning models to predict the fuel consumption of vessels and validated the AI model.

Most studies combining the motions of vessels with AI techniques have investigated the optimal route, motion responses, and other topics regarding one specific vessel. However, this study aimed to predict the motion characteristics of specific vessels by learning the motion characteristics of barge-type ships with various specifications. First, information on barge-type ships registered with classification societies was collected. Then, the RAO data of each ship was generated using an in-house code, based on a 3D singularity distribution method. Thus, data sets of the specifications and RAOs were created for various barge-type ships. Using some of this data as training data, the RAOs of specific ships in the test data were predicted after a learning process. The ultimate goal of this study was to identify the roll RAOs of barge-type ships using AI techniques. The results of this study can

provide a means for assessing the stability of various barge-type ships. Furthermore, the method developed in this study has the advantage of minimizing the modeling process for analyzing the RAO and the dependence on skill level for commercial tools.

2. Research Process

2.1 Machine Learning

Machine learning can be defined as a science of programming computers to learn from data. As shown in Fig. 1, machine learning can be classified based on the existence or absence of labeled data, into supervised learning, unsupervised learning, and reinforcement learning. Among them, supervised learning consists of classification and regression depending on predictions from results. Unsupervised learning is a method of deriving a result by a computer alone, i.e., without human intervention. One representative example of unsupervised learning is clustering. Reinforcement learning is a learning method that reinforces actions in the direction of the current action or in the opposite direction, through reward or penalty. Thus, this learning method selects an action or measure that maximizes the reward for selectable actions, by recognizing the current condition. The present study used a supervised learning method (which provides an answer) from among the machine learning methods, and a regression method to predict the values.

2.2 Perceptron

The human brain consists of combinations of neurons, and signals and information are communicated and learned through synapses interconnecting the neurons. A mathematical model of this process is called perceptron. Similar to the brain's learning principles, perceptrons also have the ability to solve problems by adjusting weights through learning. Fig. 2 shows conceptual diagrams of the human brain and perceptrons. The operation sequence of a perceptron is described below. However, single-layer perceptrons have difficulty

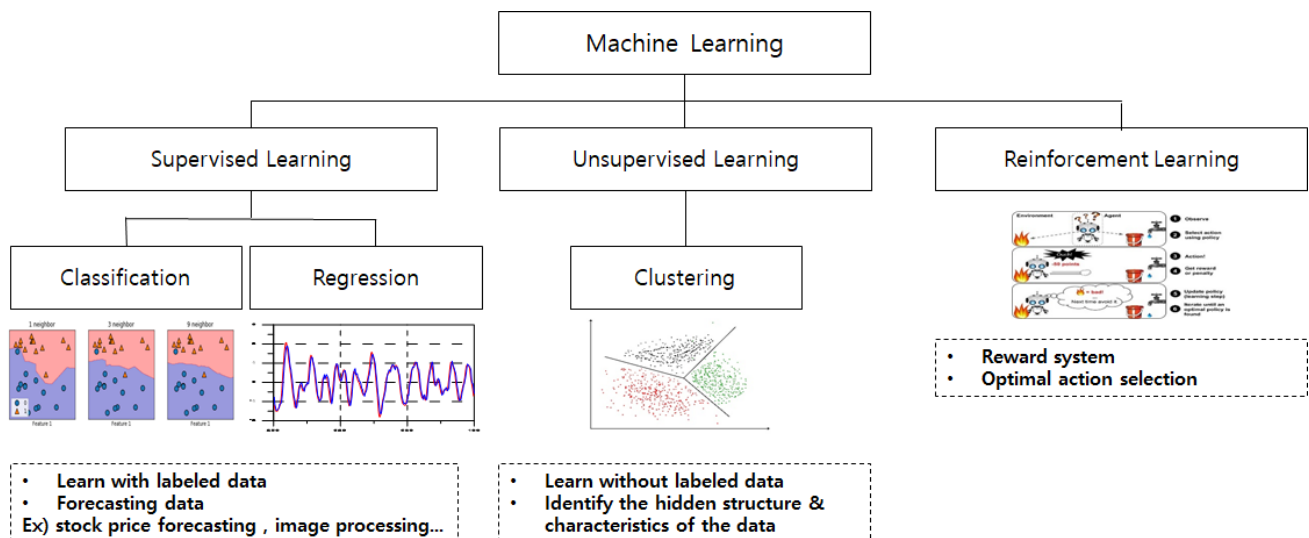


Fig. 1 Machine learning classification

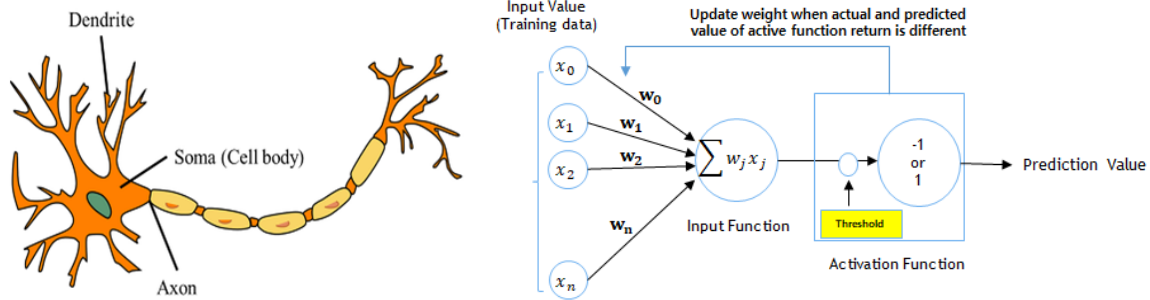


Fig. 2 Neuron concepts (Left) & Perceptron concepts (Right)

in learning non-linear models, as there is only one activation function.

- (1) Input of training data ($x_0, x_1, x_2 \dots x_n$);
- (2) Multiplication of the weights ($w_0, w_1, w_2 \dots w_n$) and input value;
- (3) Delivery of the sum of the multiplications to a net input function;
- (4) Returning a “1” if the prediction data of the net input function is larger than the threshold of the activation function, or a “-1” if the former is smaller than the latter; and
- (5) Updating the weight in the direction that minimizes the prediction and observation data.

2.3 Multi-Layer Perceptron (MLP)

Fig. 3 shows a concept diagram of a multi-layer perceptron (MLP). An MLP consists of multiple hidden layers between the input and output layers to compensate for the above-mentioned disadvantages of the single-layer perceptron. The complexity of the neural network is determined by the number of hidden layers. An ANN with two or more hidden layers is generally called a deep neural network (DNN). The operation principle of an MLP is similar to that of a single-layer perceptron, and its sequence is as follows.

- (1) Enter the training data ($x_0, x_1, x_2 \dots x_n$);
- (2) Randomly set the weights of each layer ($w_0, w_1, w_2 \dots w_n$);
- (3) Calculate the net input function value for each layer and the output value by the activation function;
- (4) Update the weights until the difference between prediction and observation data by the activation function of the output layer becomes the tolerance; and
- (5) Finish learning when the defined number of learning iterations for the training data is reached.

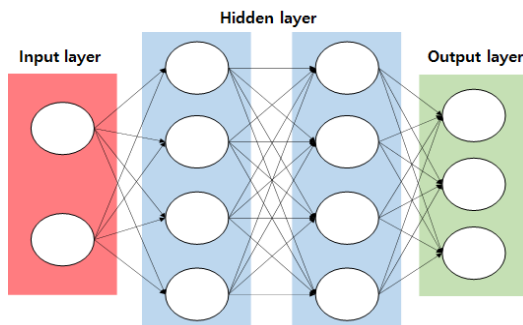


Fig. 3 Multi-Layer Perceptron concept

2.4 Data Collection

The length, breadth, and draft data of ships were collected from the specifications of barge-type ships registered with the Korea, Japan and Denmark-Germany register of shipping. In total, data were collected for 500 ships; ships with duplicate specifications were excluded from the data collection. In addition, eight input variables were generated for the learning model based on the collected ship data. The input variables were selected based on factors related to the roll motion, as shown in Table 1. The radius of gyration was set to 0.4 times the ship breadth, and the center of gravity was estimated under the assumption that the ship was on a free water surface.

Table 1 Input features

Features	Description	Range
L	Length (m)	14 ~ 183
B	Breadth (m)	6 ~ 76
D	Draft (m)	1.24 ~ 6
V	Volume (m ³)	169 ~ 89794
k_{44}	Radius of Gyration (m)	2.4 ~ 30.4
I_{44}	Mass moment of inertia of x-axis (kg·m ²)	102193.7 ~ 8.67×10 ⁹
C_{44}	Restoring coefficient of x-axis (kg/s ²)	62139.02 ~ 5.02×10 ⁹
GM_T	Transverse metacenter height (m)	0.083075 ~ 85.4

2.5 Structure of Artificial Neural Network (ANN)

The learning model was created using the Python language, and the ANN was configured using the TensorFlow library. The hyperparameters

Table 2 Hyper parameters

Parameter	Value
Input layer neurons	8
Hidden layer	Hidden layer: Variable Hidden layer neurons: Variable
Output layer neurons	20
Data ratio	Training data: 80 % Test data: 20 %
Learning rate	0.01
Epoch	10,000
Drop out	0.7
Batch size	80
Optimizer	Adam
Activation function	Sigmoid, Relu

used in this learning model are listed in Table 2. In addition, the numbers of hidden layers and hidden layer neurons were set as variables in this study. To prevent the overfitting of the ANN, the effects of the input variables were set identically through a normalization process of the input variables, and the range of normalization was set from 0 to 1. In addition, to prevent overfitting owing to the increased number of features during learning, the features of the learning model were reduced by applying the drop-out technique.

3. Learning Result and Discussion

3.1 Accuracy Assessment Indices

3.1.1 Random number change of the learning model

It was assumed that there would be a difference in the accuracy of the learning model depending on the training and test data, as data for a limited number of ships (500EA) was used. Thus, to consider various combinations of training and assessment data, the mean value of the accuracy was calculated for various training and assessment data, by changing the random number inside the learning model. In particular, the training and test data for the ANN were varied based on the seed number. Twenty random numbers from 0 to 19 were set, and the compositions of the assessment and test data were changed for each random number. Finally, the conclusion was derived by synthesizing the accuracy based on 20 random numbers.

3.1.2 Root mean square error (RMSE)

The root mean square error (RMSE), a general index for assessing a regression model, was used in this study. It can be expressed as shown in Eq. (1), where y_i denotes the RAO value obtained via simulation using an in-house code, and \hat{y}_i denotes the RAO value as predicted by the learning model.

$$RMSE = \sqrt{\frac{1}{n} \sum_{i=1}^n (y_i - \hat{y}_i)^2} \quad (1)$$

y_i : Original data

\hat{y}_i : Prediction data

n : Data number

3.1.3 Standard deviation (SD)

The standard deviation (SD), which represents the scatter, was used to reflect the fluctuations of each RMSE from the 20 random numbers. The SD can be expressed as shown in Eq. (2):

$$SD = \pm \sqrt{\frac{\sum (\hat{y}_i - \bar{y})^2}{n-1}} \quad (2)$$

\hat{y}_i : Prediction data

\bar{y} : Mean value of original data

n : Data number

3.1.4 Correlation coefficient

The scatter plots for two features were used to improve the accuracy of the learning model. To identify the relationships between the features in the scatter plots, the correlation coefficient (ρ) was used as an index to measure the direction and intensity of the linear relationship. The correlation coefficient can be expressed as shown in Eq. (3):

$$\rho = \frac{\sum_{i=1}^n (x_i - \bar{x})(y_i - \bar{y})}{\sqrt{\sum_{i=1}^n (x_i - \bar{x})^2} \sqrt{\sum_{i=1}^n (y_i - \bar{y})^2}} \quad (3)$$

x_i : Variable x

y_i : Variable y

\bar{x} : Variable x 's mean value

\bar{y} : Variable y 's mean value

n : Data number

3.2 Case Information

Data number: 100EA / 200EA / 300EA / 400EA / 500EA

Hidden layer number: 2/3/4 layers

Hidden layer neuron number: (256,256) / (200,200) / (100,100) / (115,95) / (18,18) / (14,14)

Table 3 shows the cases according to the variables. Each case is expressed in the form of 'DNdata number_L hidden layer number_NN (neuron number of layer 1, neuron number of layer 2...)'.

Table 3 Case table

Variable	Case
Data Number	DN100_L2_NN(256,256)
	DN200_L2_NN(256,256)
	DN300_L2_NN(256,256)
	DN400_L2_NN(256,256)
	DN500_L2_NN(256,256)
Hidden Layer Number	DN500_L2_NN(256,256)
	DN500_L3_NN(256,256,256)
	DN500_L4_NN(256,256,256,256)
Hidden Layer Neuron Number	DN500_L2_NN(256,256)
	DN500_L2_NN(200,200)
	DN500_L2_NN(115,95)
	DN500_L2_NN(100,100)
	DN500_L2_NN(18,18)
	DN500_L2_NN(14,14)

3.3 Learning Results by Data Number

The number of pieces of data was changed from 100 to 500, in 100 intervals. Fig. 4 shows the distribution plot for each data. Here, the x -axis represents the length in Fig. 4(a), breadth in Fig. 4(b), and draft in Fig. 4(c), and the y -axis represents the number. The purpose of using similar data distributions by data number was to preprocess the data

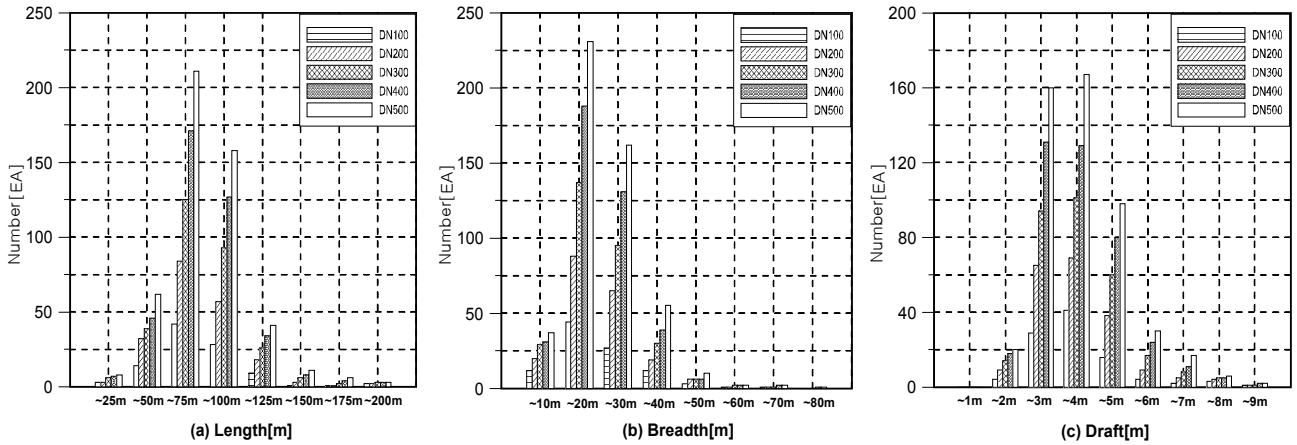


Fig. 4 Distribution plot by data number [(a) Length, (b) Breadth, (c) Draft]

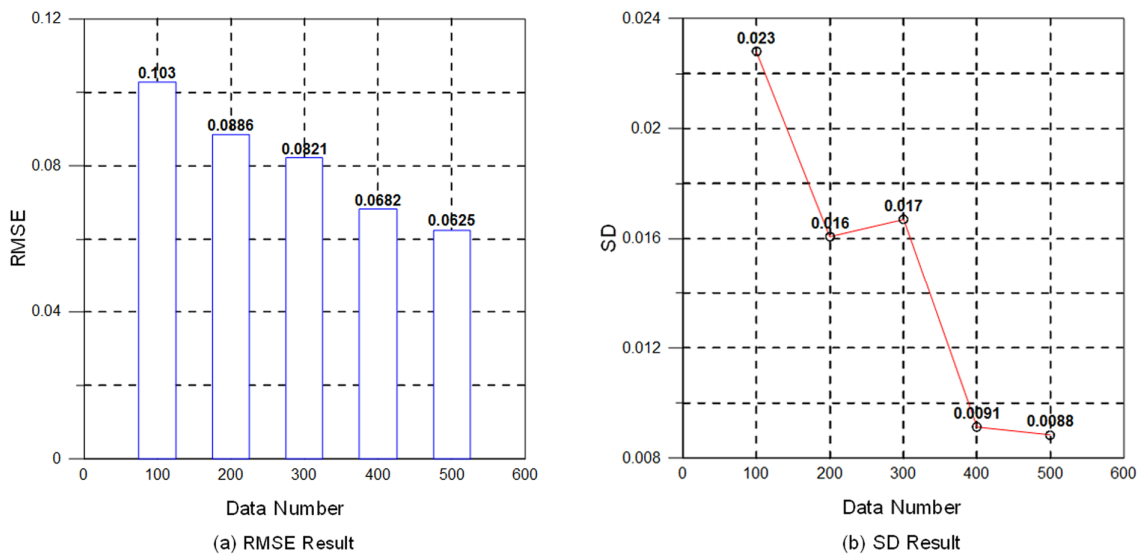


Fig. 5 (a) RMSE & (b) SD by data number

configurations before learning, as biased data can distort the accuracy of a learning model.

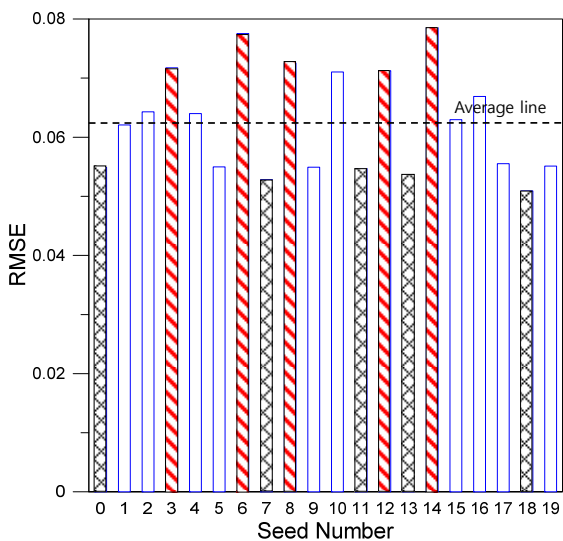


Fig. 6 DN500_L2_NN(256,256)'s RMSE

Fig. 5 shows the RMSE and SD values for 20 test data, according to the data number. In Fig. 5(a), it can be seen that the RMSE decreases with increasing data number. From Fig. 5(b), it can be seen that the variation of the accuracy also decreased.

Fig. 6 shows a graph with the seed number (0-19) as the x-axis and RMSE as y-axis for the case of DN500_L2_NN(256,256). In this case,

Table 4 RMSE of seed number

Seed number	RMSE	Mean
#3	0.0717	0.0743
#6	0.0775	
#8	0.0725	
#12	0.0712	
#14	0.0785	
#0	0.0548	0.0534
#7	0.0528	
#11	0.0547	
#13	0.0536	
#18	0.0509	

the data sets with the bottom 25% accuracies among the 20 seed numbers (3, 6, 8, 12, and 14) are indicated by red bars, whereas the data sets with the top 25% accuracies (0, 7, 11, 13, and 18) are indicated in black bars. Table 4 lists the values and means of the data with the bottom 25% and top 25% accuracies.

3.3.1 Seed number: 14

Seed number 14 is the data set with the highest RMSE, indicating that it has the lowest accuracy. However, the RMSE result of seed number 14 is derived as the mean RMSE for 100 ships, i.e., the test data. Considering that it is necessary to analyze the RMSE values for the 100 ships comprising the test data, a graph was generated for seed number 14, with the 100 ships of the test data on the x-axis, and the RMSE values of the ships on the y-axis (as shown in Fig. 7). A close examination of Fig. 7 reveals that the accuracy of the learning model for most of the ships is high, but the accuracy drops for some ships, owing to differences between the observed and predicted data.

Therefore, in this study, the RAOs of the bottom three ships and top three ships were compared as representative examples, and ships with a high RMSE were examined. For seed number 14, ships #21, #53, and #66 had low RMSEs, whereas ships #50, #63, and #80 had high RMSEs.

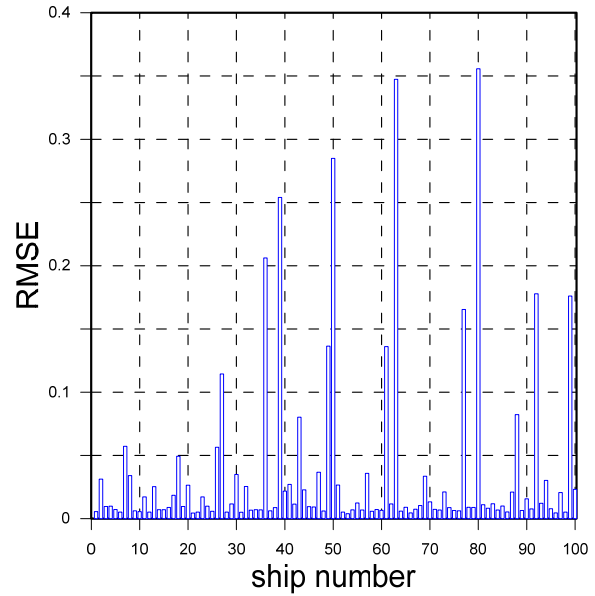


Fig. 7 Seed number 14's RMSE at each ship

Fig. 8 shows graphs for comparing the observed and predicted data of the RAOs for ships #21, #53, and #66. Although there were slight differences between the observed and predicted data in a specific

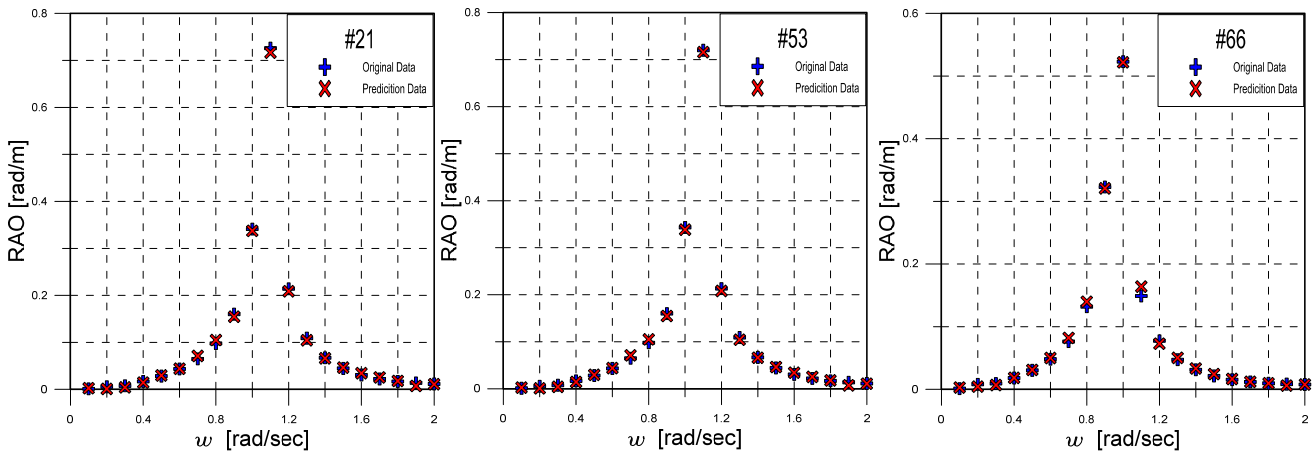


Fig. 8 #21, #53, and #66 RAO comparison

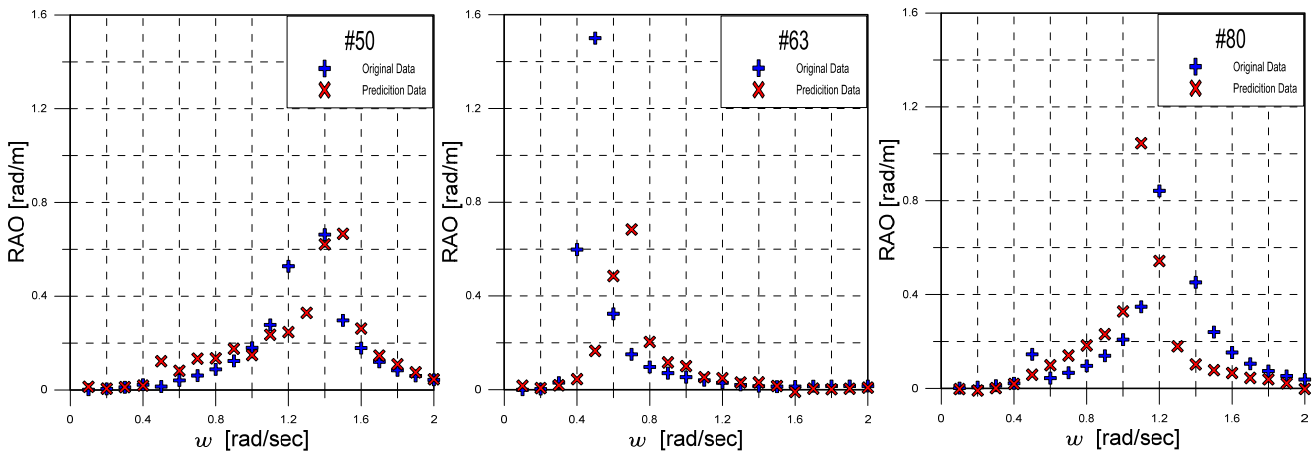


Fig. 9 #50, #63, and #80 RAO comparison

frequency range, the locations and sizes of the resonance points of the ships were predicted with high accuracy.

Fig. 9 shows graphs for comparing the observed and predicted data of the RAOs for ships #50, #63, and #80. It can be seen that ships #50, #63, and #80 have differences between the observed and predicted data at the locations of the resonance points. Furthermore, on the y-axis in Fig. 9, the size of the observation data at the resonance point is lower than 0.8 for ship #50, whereas the sizes at the resonance points of the observation data on the y-axis for ships #63 and #80 are approximately 1.2. This difference in the absolute values on the y-axis is another factor that increases the RMSE. Lastly, for ship #80, which has the lowest accuracy, there are differences in not only the location of the resonance point, but also in the size at the resonance point, as well as between the observed and predicted data over the entire frequency range.

3.3.2 Seed number: 18

Seed number 18 is the data set with the lowest RMSE, i.e., the data set showing the highest accuracy. The results were verified using the same method described for seed number 14 in Section 3.3.1. Fig. 10 shows a graph of 100 ships (the test data) on the x-axis, and the RMSE of each ship on the y-axis. A close examination of Fig. 10 reveals that

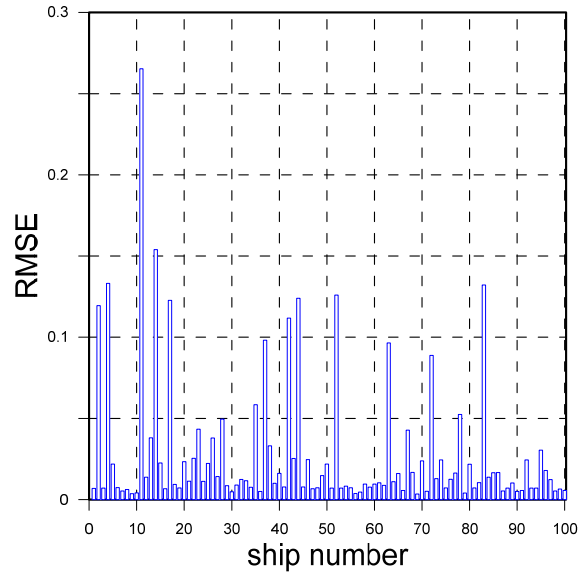


Fig. 10 Seed number 18's RMSE at each ship

although the accuracy of the learning model for most of the ships is high, the model's accuracy for some ships decreases, owing to differences between the observed and predicted data.

As in Section 3.3.1, the RAOs of top three and bottom three ships

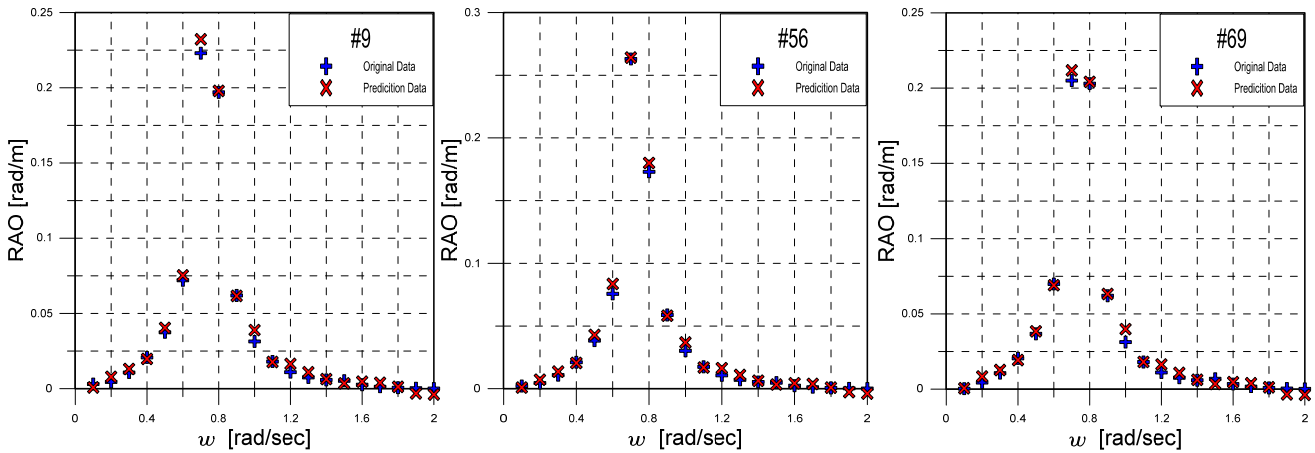


Fig. 11 #9, #56, and #69 RAO comparison

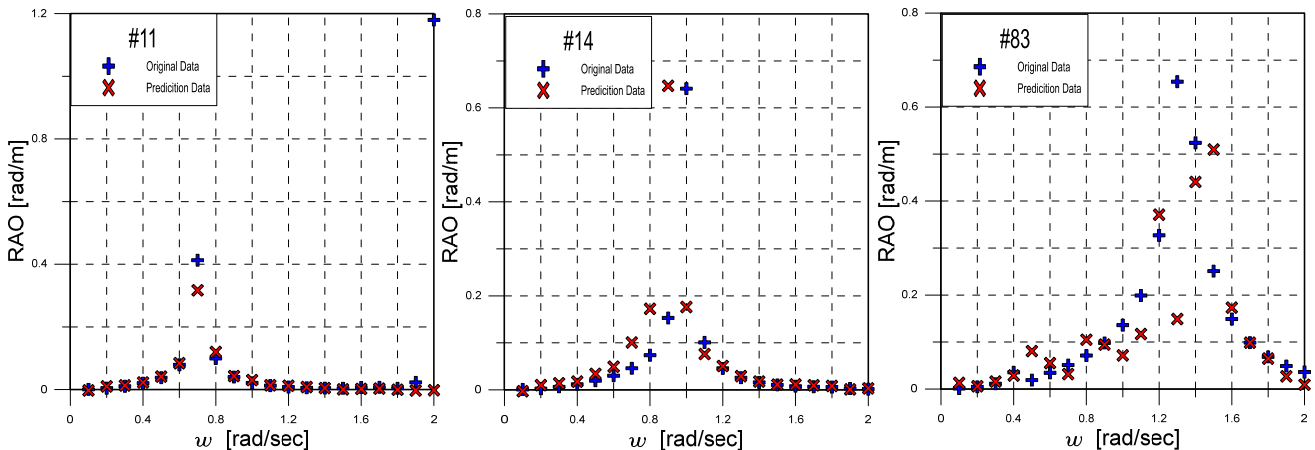


Fig. 12 #11, #14, and #83 RAO comparison

were compared for seed number 18, and they were selected as the data for examining the reasons for high RMSEs. Ships #9, #56, and #69 from seed number 18 showed low RMSEs, whereas ships #11, #14, and #83 showed high RMSEs.

Fig. 11 shows graphs comparing the observed and predicted data of the RAOs for ships #9, #56, and #69. Similar to ships #21, #53, and #66 of the above-mentioned seed number 14, there were slight differences between the observed and predicted data in a specific frequency range, but the locations and sizes of the ship’s resonance points were predicted with high accuracy.

Fig. 12 shows graphs comparing the observed and predicted data for the RAOs of ships #11, #14, and #83. The RMSE of ship #11 was measured as high, as the observation data were abnormal at 2 rad/s. This is considered to be a noise generated when the high-frequency region was analyzed using the in-house code; the prediction data is

considered to be the normal result. Thus, although ship #3 has the highest RMSE, data preprocessing for the abnormal result at 2 rad/s is expected to decrease the RMSE. In the case of ships #14 and #84, as mentioned above, a high RMSE is observed, owing to differences in not only the location of the resonance points, but also in the sizes at the resonance points, as well as between the observed and predicted data over the entire frequency range.

3.4 Learning Results with Different Numbers of Hidden Layers

The hidden layer calculates a weighted sum by receiving input values from the input layer and delivers this value to the output layer by applying it to an activation function. Regarding the number of hidden layers, one or two-layered neural networks are frequently used. Nevertheless, sometimes many hidden layers are required, owing to the purpose or complexity of the neural network. Therefore, to

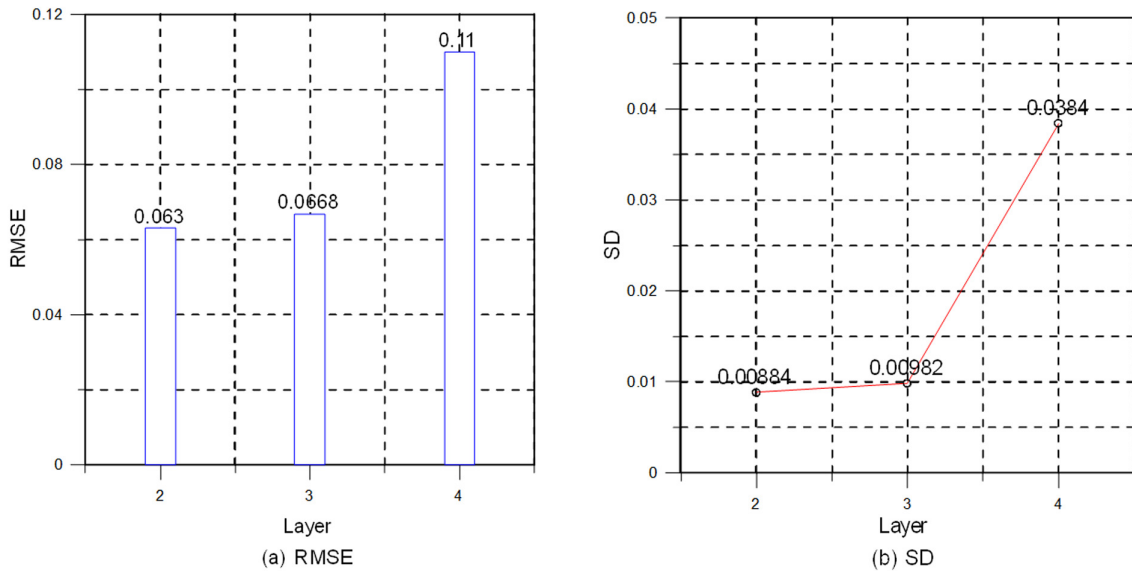


Fig. 13 (a) RMSE & (b) SD result with the change in the hidden layer number

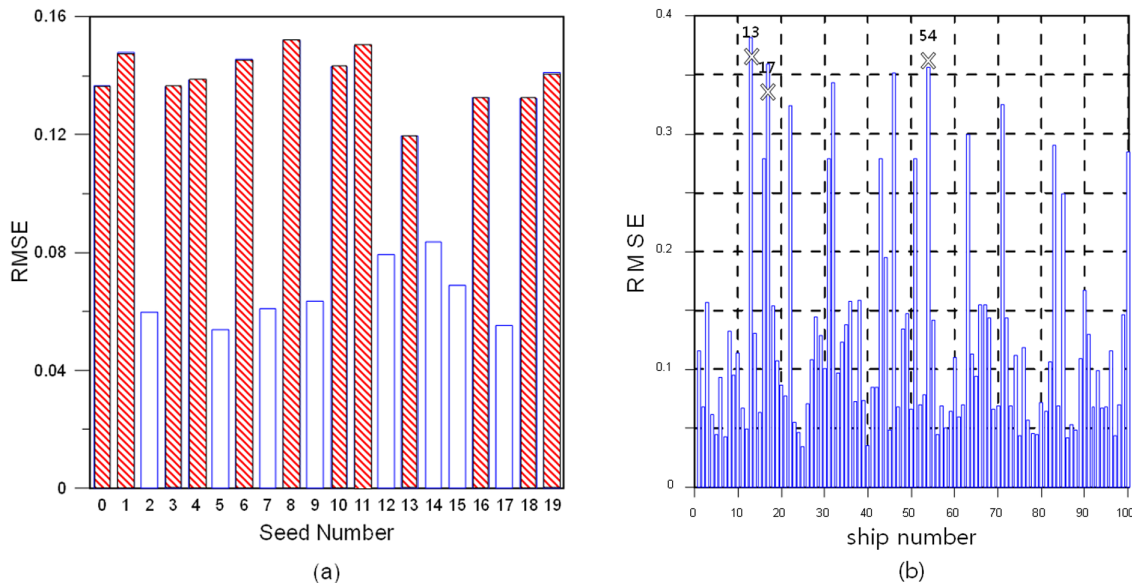


Fig. 14 (a) DN500_L4_NN(256,256)’s RMSE & (b) Seed number 8 RMSE

optimize the number of hidden layers in this study, the RMSE and SD values were obtained when increasing the number of hidden layers to two, three, and four.

Consequently, Fig. 13(a) shows a graph with the number of hidden layers on the x-axis and RMSE on the y-axis, and Fig. 13(b) shows a graph with the number of hidden layers on the x-axis and SD on the y-axis. An observation of these graphs reveals that when the number of hidden layers increased from two to three, the RMSE and SD increased slightly. When the number of hidden layers was four, the RMSE and SD increased sharply. Therefore, it was determined that two is the optimal number of hidden layers in this study.

Fig. 14(a) shows a graph with the seed number on the x-axis and RMSE on the y-axis for DN500_L4_NN(256,256). The 12 RMSEs higher than the mean are marked by red slashes. Fig. 14(b) shows a graph of the RMSEs for 100 ships in seed number 8, which has high RMSEs. In Fig. 14(b), ships #13, #17, and #54, which have high RMSEs, are marked with an 'X'.

An observation of the prediction data for the three ships in Fig. 15 reveals that all of the ships have the same RAO, even though their

specifications are different. Furthermore, a common phenomenon of predicting the same RAO is observed in the 12 seed numbers marked by red slashes, even though the 100 ships have different specifications. The cause of this phenomenon is considered to be the increased complexity of the system, owing to the increased number of hidden layers. In other words, it can be interpreted as a situation where the complexity increased, and the local minima was found in a certain part of the loss function instead of the global minima for the entire loss function, resulting in insufficient learning.

3.5 Learning Results with Different Numbers of Neurons in the Hidden Layer

In Sections 3.3 and 3.4, an intermediate conclusion was derived, i.e., that the optimal model is the case where there are data for 500 ships, and the number of hidden layer numbers is two. In this section, the learning results were analyzed according to different numbers of neurons in the hidden layer, to draw the final conclusions. During learning, there is difficulty in decision-making, as the number of neurons in the hidden layer depends on the user's experience, whereas

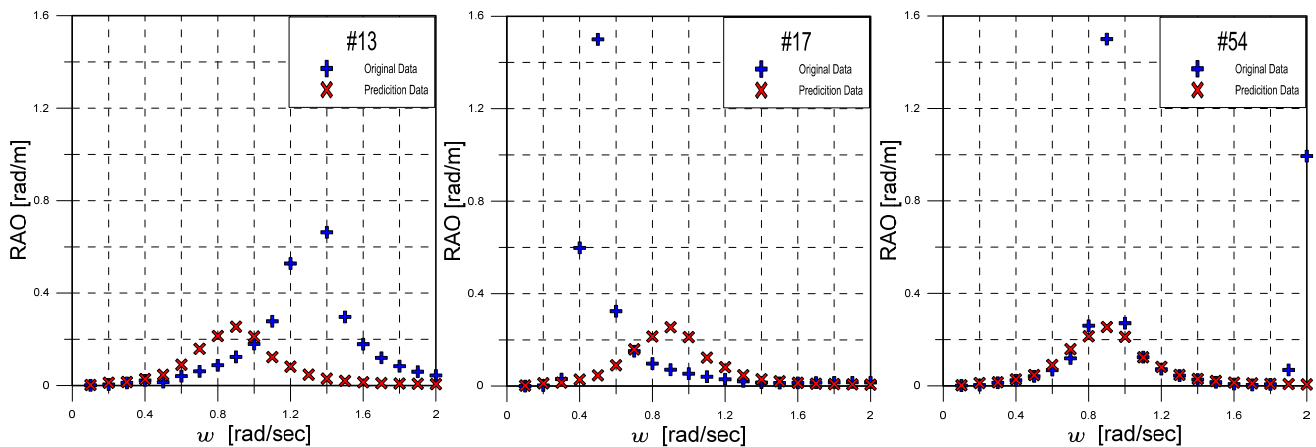


Fig. 15 #13, #17, and #54 RAO comparison

Table 5 Changes in the hidden layer number of neurons

Case	Name	Description	Etc
1	DN500_L2_NN(256,256)	First floor neuron : Random selection (256) Second floor neuron : Random selection (256)	-
2	DN500_L2_NN(200,200)	First floor neuron : Random selection (200) Second floor neuron : Random selection (200)	-
3	DN500_L2_NN(115,95)	First floor neuron: $\sqrt{(m+2)DN} + 2\sqrt{DN/(m+2)}$ Second floor neuron: $m\sqrt{DN/(m+2)}$	n : Input layer node number m : Output layer node number DN : Data number
4	DN500_L2_NN(100,100)	First floor neuron: Random selection (100) Second floor neuron: Random selection (100)	-
5	DN500_L2_NN(18,18)	First floor neuron: $\frac{2(n+m)}{3}$ Second floor neuron: $\frac{2(n+m)}{3}$	n : Input layer node number m : Output layer node number
6	DN500_L2_NN(14,14)	First floor neuron: $\frac{n+m}{2}$ Second floor neuron: $\frac{n+m}{2}$	n : Input layer node number m : Output layer node number

the neuron numbers of the input and output layers are fixed. Therefore, in this section, the RMSEs of the learning model were compared, by changing the numbers of neurons in the hidden layer in the cases of DN500_L2.

A backward approach was used to configure these cases, in which the neural network was learned and tested while reducing the number of neurons in the hidden layer step-by-step. Table 5 outlines each case using the neural network structure. For cases 1, 2, and 4, the number of neurons in the learning model was selected randomly. The number of neurons for case 3 was selected by referring to a previous study (Stathakis, 2009). For cases 5 and 6, a rule of thumb from a previous study (Kim, 2017) was used.

In Fig. 16(a), a tendency can be seen in that in general, as the number of neurons increased, the RMSE also increased. A close observation reveals that in case 3, the RMSE decreased somewhat, but the decrease was insignificant; moreover, in cases 5 and 6, the RMSEs increased sharply. In contrast, Fig. 16(b) shows that as the number of

neurons decreased, the SD also decreased. In short, cases 1, 2, 3, and 4 have low RMSEs on average, but the fluctuations of the RMSE were larger than those of cases 5 and 6, depending on the assessment data. In contrast, cases 5 and 6 have relatively high RMSEs, but the fluctuations of those RMSEs are small. Cases 1, 2, and 3 cannot be the optimal model because their SDs are excessively large, although their RMSEs are similar to that of case 4. Furthermore, cases 5 and 6 have low accuracy regarding the prediction data owing to high RMSEs, although their SDs are smaller than that of case 4. Therefore, case 4 is considered to be the optimal model, as an appropriate compromise between the RMSE and SD.

3.6 Analysis of the Optimal Model Learning Result and Discussion

Fig. 17(a) shows a graph of the RMSE based on assessment data of the case DN500_L2_NN(100,100). In Section 3.5, the SD of case 4 was found to have small fluctuations. In addition, the RMSE values for each seed number comprising case 4 show that seed number 14 has a

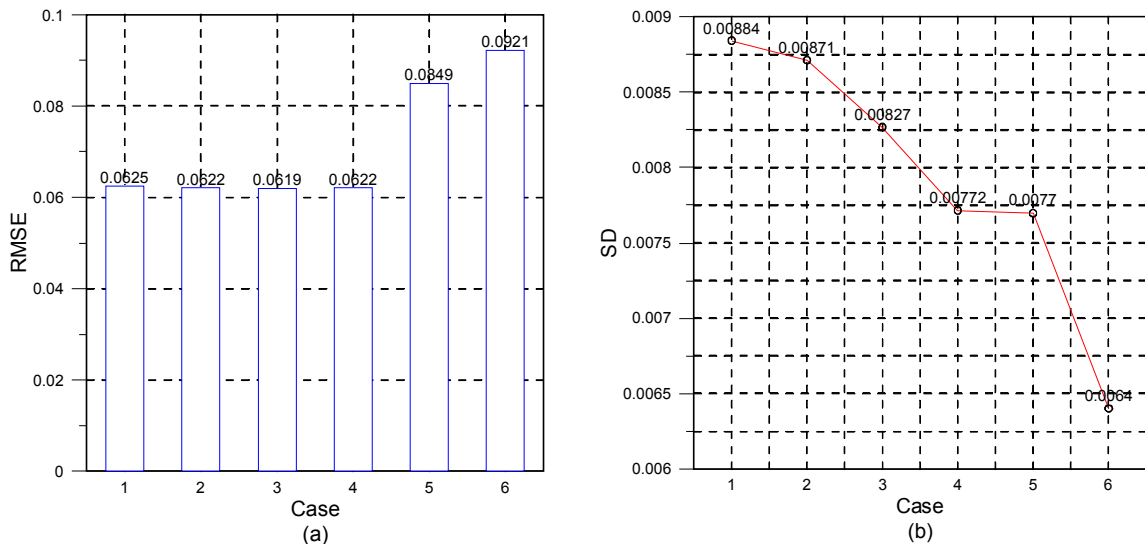


Fig. 16 (a) RMSE & (b) SD according to the number of neurons in the hidden layer

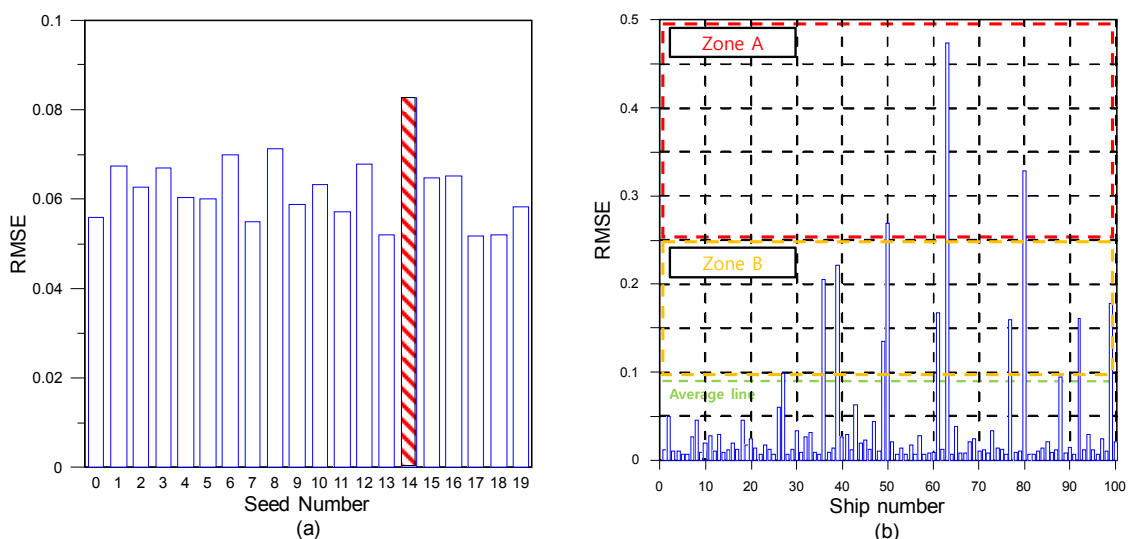


Fig. 17 (a) DN500_L2_NN(100,100)'s RMSE & (b) Seed number 14 RMSE

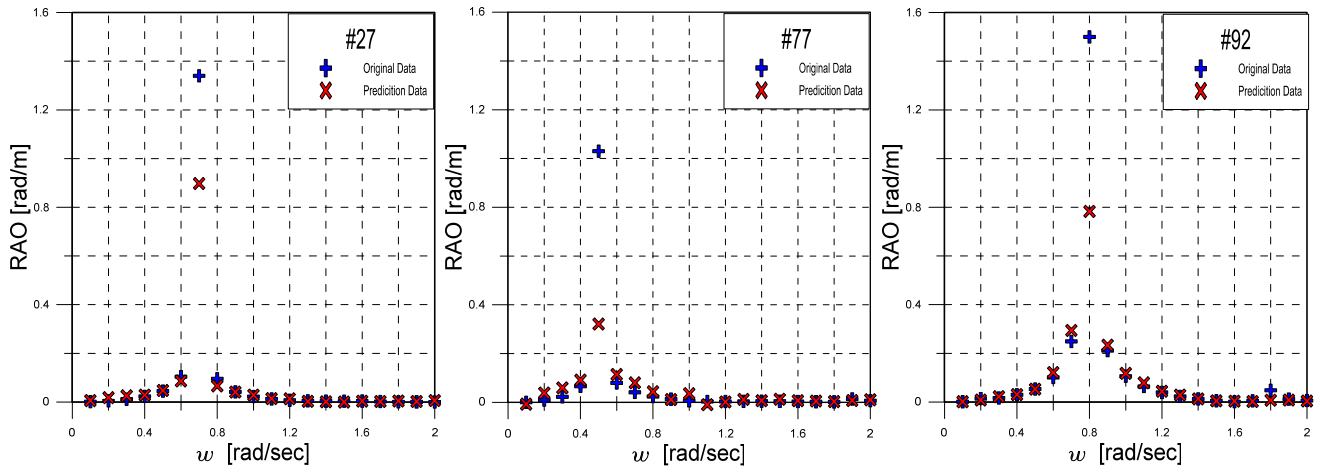


Fig. 18 RAO comparison (Zone B: #27, #77, and #92)

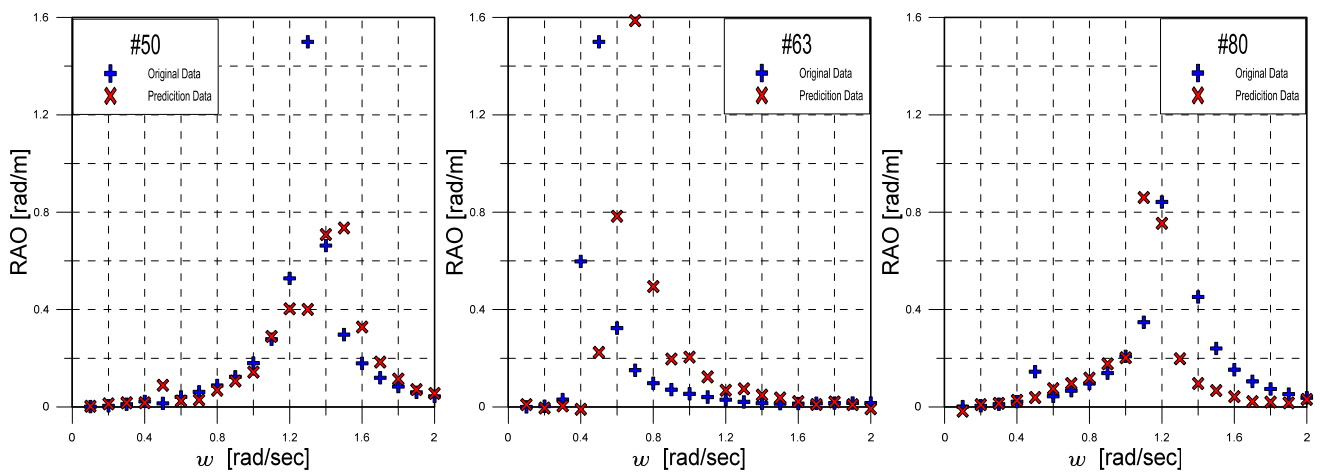


Fig. 19 RAO comparison (Zone A: #50, #63, and #80)

higher RMSE than those of the other test data.

Therefore, it is believed that an analysis of the test data for seed number 14 would improve the accuracy of the learning model, as well as the accuracy of learning results. Fig. 17(b) shows a graph of the RMSE for each ship in seed number 14. The results are analyzed by defining “Zone A” for $RMSE \geq 0.25$ and ≤ 0.5 , “Zone B” for $RMSE \geq 0.0826$ and < 0.25 , and “Below Average” for $RMSE < 0.0826$. The RAOs were initially compared for ships #50, #63, and #80, which belong to Zone A, and then for ships #27, #77, and #92, which belong to Zone B.

Fig. 18 shows a graph for comparing the RAOs of ships #27, #77, and #92, which belong to Zone B. These ships have somewhat lower accuracies than the mean, although higher than those of Zone A. Their RAO values over the entire frequency range are similar, and the location of the resonance is predicted with a high error. However, all three ships generated RMSEs, owing to differences in the sizes at the resonance point.

Fig. 19 shows a graph for comparing the RAOs of ships #50, #63, and #80, which belong to Zone A. Although they had the same general shape in the RAO, there were significant differences in the location and size of the resonance point, and between the observed and

predicted data over the low- and high-frequency ranges. From Fig. 19, it can be concluded that the difference between the observed and predicted data is the main cause of the RMSE for the ships with high RMSEs in each seed number.

It is believed that understanding the distribution characteristics of the data set by obtaining the correlation(s) between the training and test data can improve the accuracy for ships with a high RMSE. Therefore, in Table 6, the correlation coefficients of the input variables ($L, D, V, I_{44}, C_{44}, GM_T$) associated with the ship’s breadth in the assessment and test data of seed number 14 were determined and ranked. For example, the breadth (B) and volume (V) of the training

Table 6 Rank between training data and test data each feature

Feature	Coefficient_Train	Rank	Coefficient_Tests	Rank
L	0.740	3	0.660	5
D	0.719	4	0.609	6
V	0.839	2	0.737	4
I_{44}	0.658	6	0.759	3
C_{44}	0.715	5	0.874	1
GM_T	0.879	1	0.811	2

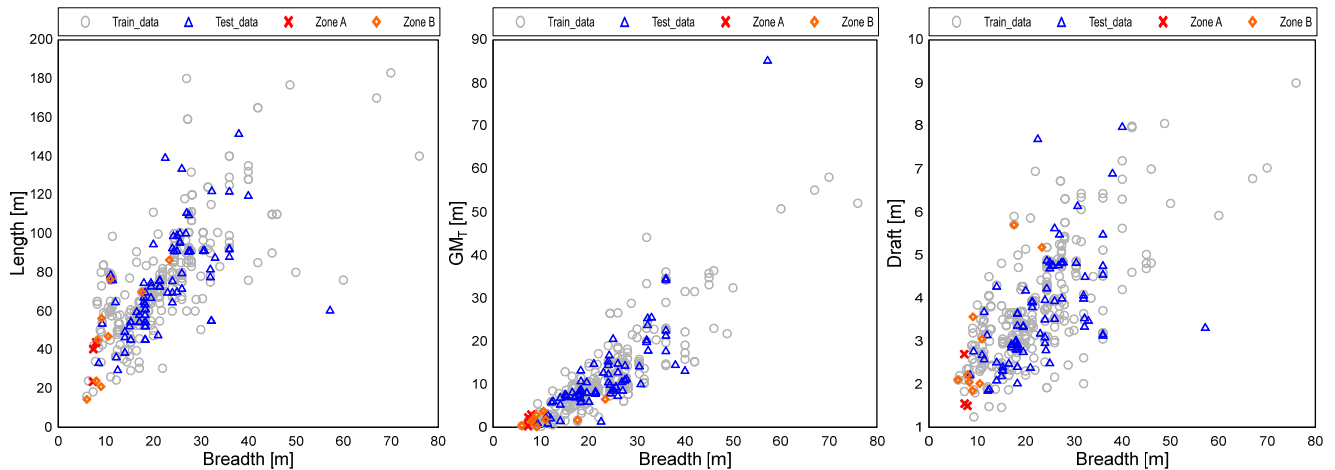


Fig. 20 Scatter plot (Breadth with length & draft & GMT)

data showed a high positive correlation of 0.839, but in the assessment data, it was 0.737, i.e., a lower correlation than in the training data. Moreover, the correlations for features such as the coefficient of restitution (which is directly related to the location of the resonance point) were different. This indicates that the low accuracy was caused by the differences between the trends of the training and assessment data.

Fig. 20 shows a scatter plots where the x-axis is set as the ship's breadth, and the y-axis is set as the length, draft, and transverse metacenter height. They shows the training data (gray circle), test data (blue circle), Zone A with high RMSEs (red cross mark), and Zone B with medium accuracy (orange diamond), as used in this study. Typically, when one specification of a ship (such as length) is determined, the other specifications, e.g., breadth and draft, have specific ranges. This means that the specifications of ships have certain correlations with one another, and these correlations can be also seen in the scatter plots.

The scatter plot in Fig. 20 indicates that the data are concentrated in a specific section, and that ships having a high RMSE (Zone A) are located in an area with a low data density. In other words, ships with specifications that have not been sufficiently trained have low data accuracy. Figs. 18–19 show that while the accuracy was somewhat insufficient for Zone A, the overall RAO trend for the ships belonging to Zone B was predicted, even though the RMSE was high. Furthermore, considering that only a difference in the size at the resonance point caused an RMSE for certain ships, it can be said that there are cases where the prediction data of the RAO is reliable, even in a region with low data density.

4. Conclusions

This study was conducted to predict the roll RAO of barge-type ships using machine learning. The input variables ($L, B, D, V, k_{44}, I_{44}, C_{44}, GM_T$) were generated using the specifications of 500 barge-type ships registered with classification societies. In addition, the values for the roll RAO were obtained by simulating the 500 ships using an

in-house code based on a 3D singularity distribution method, and the features and RAOs of the data sets were configured. Finally, the data were composed with the RAOs in the range of 0.1–2.0 rad/s, according to the major specifications of the barge-type ships. For the learning model, an ANN was created using Python's TensorFlow, and a DNN technique with two or more hidden layers was used. The accuracy of the learning results was determined by changing the number of datapoints, number of hidden layers, and node numbers in the hidden layer. The RMSE, SD, correlation coefficient, and scatter plot were used as accuracy indices. When the RMSE and SD were considered together, the optimal results were obtained in case 4 [DN500_L2_NN(100,100)]. Finally, the shortcomings of the learning model and possible improvements were examined through an analysis of the accuracy of Case 4.

The conclusions of this study can be summarized as follows.

- (1) The accuracy of the learning model can differ depending on the combination of training and test data. Therefore, the reliability of the learning results can be improved by collecting sufficient data.
- (2) The accuracy increases when there are more high-quality data following the statistical distribution.
- (3) Using many hidden layers can lower the accuracy, by increasing the complexity of the neural network model.
- (4) The optimal model in this study is DN500_L2_NN(100,100).
- (5) There are three main factors causing low accuracy in RAO prediction:
 - Failure to accurately predict the location of the resonance point;
 - An increase of RMSE owing to a difference in size between the observed and predicted data at the resonance point, and
 - Differences between the observed and predicted data over the entire frequency range.
- (6) The scatter plot showed that ships with low accuracy are located in an area with a low data density.
- (7) This study did not consider various data on the centers of gravity of the barge ships, which involves practical difficulties. Therefore, a study considering various centers of gravity should be conducted.

References

- Mahfouz, A.B. (2004). Identification of the Nonlinear Ship Rolling Motion Equation Using the Measured Response at Sea. *Ocean Engineering*, 31(17-18), 2139-2156. <https://doi.org/10.1016/j.oceaneng.2004.06.001>
- Park, G.I., Choi, K., Y., Lee, J.H., & Kim, M.S. (2004). Introduction of Optimum Navigation Route Assessment System Based on Weather Forecasting and Seakeeping Prediction. *Journal of Korean Navigation and Port Research*, 28(10), 833-841. <https://doi.org/10.5394/KINPR.2004.28.10.833>
- Lee, J.H., Park, G.I., Choi, K.Y., Kim, M.S., & Bang, C.S. (2005). Basic Research of Optimum Routing Assessment System for Safe and Efficient Voyage. *Journal of the Society of Naval Architects of Korea*, 42(1), 57-63.
- Stathakis, D. (2009). How Many Hidden Layers and Nodes. *International Journal of Remote Sensing*, 30(8), 2133-2147. <https://doi.org/10.1080/01431160802549278>
- Kang, M.S., Kim, Y.W., & Jung, H. (2012). Floating Body Motion Prediction System Using Artificial Neural Network. *Proceedings of The Korean Association of Ocean Science and Technology Societies*, 1041-1050.
- Ham, D.G. (2016). A Study of Data-Mining Methodology in Offshore Plant's Outfittings Procurement Management (Master's thesis). Korea Maritime and Ocean University, Busan, Korea.
- Kim, G.H. (2017). Artificial Neural Network for Short-Term Load Forecasting Algorithm Considering Temperature Characteristics (Master's thesis). Korea Maritime and Ocean University, Busan, Korea.
- Kim, J.H. (2018). A Study on Machine Learning for Prediction of the Shipbuliding Lead Time (Master's thesis). Korea Maritime and Ocean University, Busan, Korea.
- Kim, Y.R., Park, J.-B., & Moon, S.-B. (2018). Prediction of Ship Roll Motion Using Machine Learning-based Surrogate Model. *Journal of Korean Navigation and Port Research* 42(6), 395-405. <https://doi.org/10.5394/KINPR.2018.42.6.395>
- Jeon, M.Y. (2019). Development of Predictive Model of Ship's Fuel Consumption Using Machine Learning Method (Master's thesis). Pusan National University, Busan, Korea.
- Kim, Y.R., (2019). Development of a Fuel Consumption Prediction Model Based on Machine Learning Using Ship's Data (Master's thesis). Korea Maritime and Ocean University, Busan, Korea.
- Kim, Y.R., Park, J.-B., Park, J.-C., & Park, S.-K. (2019). Development of an Evaluation Procedure for Seakeeping Performance of High-speed Planing Hull Using Hybrid Method. *Journal of the Society of Naval Architects of Korea*, 56(3), 200-210. <https://doi.org/10.3744/SNAK.2019.56.3.200>

Author ORCIDs and Contributions

Author name	ORCID	Contributions
Lim, Jae Hwan	0000-0002-9687-3011	①②③④
Jo, Hyo Jae	0000-0002-7847-0462	①⑤

- ① Conceived of the presented idea or developed the theory
- ② Carried out the experiment or collected the data
- ③ Performed the analytic calculations or numerical simulations
- ④ Wrote the manuscript
- ⑤ Supervised the findings of this study

Trajectory Tracking Performance Analysis of Underwater Manipulator for Autonomous Manipulation

Junbo Chae¹, Taekyeong Yeu², Yeongjun Lee³, Yoongeon Lee⁴ and Suk-Min Yoon⁵

¹Researcher, Korea Research Institute Ship and Ocean Engineering, KRISO, Daejeon, Korea

²Principal Researcher, Korea Research Institute Ship and Ocean Engineering, KRISO, Daejeon, Korea

³Senior Engineer, Korea Research Institute Ship and Ocean Engineering, KRISO, Daejeon, Korea

⁴Researcher, Korea Research Institute Ship and Ocean Engineering, KRISO, Daejeon, Korea

⁵Senior Engineer, Hanwha Systems, Gumi-si, Korea

KEY WORDS: Remotely operated vehicle(ROV), 6-DOF Underwater manipulator, Autonomous underwater intervention, Closed loop inverse kinematics, End-effector tracking

ABSTRACT: In this study, the end-effector tracking performance of a manipulator installed on a remotely operated vehicle (ROV) for autonomous underwater intervention is verified. The underwater manipulator is an ARM 7E MINI model produced by the ECA group, which consists of six joints and one gripper. Of the six joints of the manipulator, two are revolute joints and the other four are prismatic joints. Velocity control is used to control the manipulator with forward and inverse kinematics. When the manipulator approaches a target object, it is difficult for the ROV to maintain its position and posture, owing to various disturbances, such as the variation in both the center of mass and the reaction force resulting from the manipulator motion. Therefore, it is necessary to compensate for the influences and ensure the relative distance to the object. Simulations and experiments are performed to track the trajectory of a virtual object, and the tracking performance is verified from the results.

1. Introduction

A manipulator can perform various tasks within a certain work space, and is used in a diverse range of applications in manufacturing and research. When a manipulator is fixed at a specific location to perform tasks, problems such as the constraints of the work space and the occurrence of singularity are encountered. To address these problems, a manipulator is mounted on a vehicle to perform mobile manipulation to interact with a target object. A robot with wheels and unmanned aerial vehicle such as drone are equipped with manipulators to perform the work (Kim et al., 2019; Korpela et al. 2012). Research is underway to carry out the work by installing a manipulator on a remotely operated vehicle (ROV) or an autonomy underwater vehicle operated not only on the ground and in the air but also on the ocean (Ribas et al. 2012, Kang et al. 2017).

Underwater manipulators installed on underwater vehicles have the following considerable differences from on-shore industrial manipulators: (1) the former structures can withstand deep-sea environments, (2) they are small and lightweight considering the nature of underwater vehicles,

and (3) their underwater intervention is diverse and complex (Ura and Takakawa, 1994/2015).

Since the deep sea environment is unique in that the pressure increases with the depth, the actuator of a manipulator must be manufactured to be pressure resistant and with a pressure equalization method capable of withstanding the pressure of the working depth. Owing to the characteristics of an underwater vehicle, there are constraints on the space and weight; therefore, its manipulator should be small and lightweight. In addition, an underwater manipulator must be able to respond to various operational scenarios occurring in a deep-sea environment; in comparison, the objective of an on-shore industrial manipulator is to perform a predetermined task repeatedly and accurately in a certain space. Therefore, an underwater manipulator is a man-machine system that requires operator judgment or manipulation of the manipulator control system. In this regard, studies have been conducted recently on autonomous manipulators that plan and execute intervention with simple instructions from an operator for pre-defined specific tasks.

The Korea Research Institute of Ship & Ocean Engineering (KRISO) has developed an underwater autonomous robot platform

Received 8 October 2019, revised 31 March 2020, accepted 10 April 2020

Corresponding author Suk-Min Yoon: +82-54-460-8727, smyoon@hanwha.com

© 2020, The Korean Society of Ocean Engineers

This is an open access article distributed under the terms of the creative commons attribution non-commercial license (<http://creativecommons.org/licenses/by-nc/4.0>) which permits unrestricted non-commercial use, distribution, and reproduction in any medium, provided the original work is properly cited.

equipped with a manipulator on a remotely operated vehicle (ROV). This underwater robot can automatically perform a series of tasks in which it recognizes the position of a target object, approaches the object, and grasps the object using a manipulator (Yeu et al., 2019).

In this study, the position tracking performance of the manipulator, ECA ARM 7E Mini model, is analyzed for autonomous intervention of underwater robots. For realizing the autonomous manipulation of underwater robots, forward and inverse kinematics are used to control the manipulator. The distance between an underwater robot body and the end-effector is obtained using forward kinematics, to determine the position of the end-effector according to the manipulator joint angle. In addition, the value of the joint angle to reach a target object for autonomous manipulation is calculated using inverse kinematics, which determines the position of the joint angle of the manipulator according to the position of the end-effector in arbitrary Cartesian coordinates. The ECA ARM 7E Mini manipulator consists of six degrees of freedom and one end-effector. Of the six joints, four are prismatic joints and two are revolute joints. The output of a prismatic joint of the manipulator in length units is converted into angular units using the kinematic correlation, and this was utilized in the calculation of the forward and inverse kinematics of the manipulator and for the velocity control algorithm.

When an underwater robot performs autonomous manipulation, disturbances, such as the reaction force from the manipulator operation, cable impacts, and external fluid force, arise. If these disturbances are not appropriately compensated owing to the lack of control performance or other reasons, the position and posture of the underwater robot will change, and a target point of the manipulator will vary continuously. For smooth autonomous manipulation by compensating for the constantly varying distance and the direction between the end-effector and a target object, an algorithm that allows the end-effector to track the target object is developed, and its performance is demonstrated.

The structure of this paper is as follows. Chapter 2 introduces the developed ROV for autonomous underwater manipulation. It also describes the manipulator specifications, kinematics, and inverse kinematics information. In addition, it presents the conversion method of the output information of the prismatic joints of the manipulator into angular information as well as the algorithm allowing the end-effector to track a target point. Chapter 3 presents the verification of the end-effector tracking algorithm using simulation. Chapter 4 describes the demonstration of the algorithm, verified by the simulation, using a manipulator installed on an underwater robot and analyzes the result of the underwater tracking of a target object. Chapter 5 presents the conclusion.

2. ROV for Autonomous Underwater Manipulation

2.1 Underwater Robot Platform

The underwater robot developed by KRISO for autonomous underwater manipulation is displayed in Fig. 1. The underwater robot for autonomous manipulation is primarily divided into upper and lower



Fig. 1 Underwater robot with ECA ARM 7E Mini

parts; the upper part is equipped with a thruster, electronic parts, and a buoyancy module, and the lower part comprises an ECA underwater manipulator ARM 7E Mini and related accessories. When operating for investigation and exploration purposes, the ROV function can be performed with the upper part alone, whereas for autonomous underwater manipulation, as presented in Fig. 1, autonomous manipulation is performed with both the upper and lower parts. The underwater robot measures the velocity and posture using an installed inertia measurement unit (IMU), a Doppler velocity log (DVL), and a depth sensor, and the position of the underwater robot is determined by these measurements. Subsequently, a target object and its position are identified using a camera and an underwater laser scanner.

2.2 Underwater Manipulator

The ARM 7E Mini model (Fig. 2), a manipulator for autonomous manipulation installed on the above underwater robot, is a commercial product that can operate up to 300 m underwater. Its weight on the ground and underwater weight are 50.8 kg, and 33.8 kg, respectively. Of the six joints of the ARM 7E Mini, four are prismatic joints and two are revolute joints.

2.2.1 Kinematic information

The output of the of a prismatic joint of the manipulator in length units was converted to angular units using the kinematic correlation, and this was applied to the forward and inverse kinematics of the manipulator. For the control of the manipulator, it was operated at 10 Hz, and the control input of the manipulator was the joint velocity. Table 1 summarizes the range of motion of each joint of the ECA ARM 7E Mini and the link length. In addition, when all joint angles



Fig. 2 ECA ARM 7E Mini

Table 1 Joint angle and link length information

Joint	Angle (°)		Link	Length (m)
	min	max		
q_1	-30	90	l_1	0.167
q_2	-20	100	l_2	0.685
q_3	-55	75	l_3	0.157
q_4	10	350	l_4	0.019
q_5	-30	90	l_5	0.436
q_6	$-\infty$	∞	l_6	0.042
			l_7	0.191

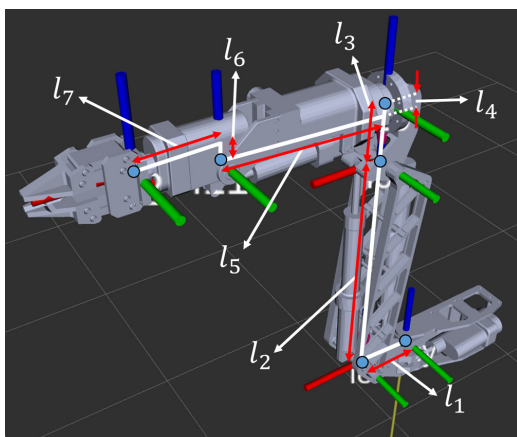


Fig. 3 Links of ECA ARM 7E Mini

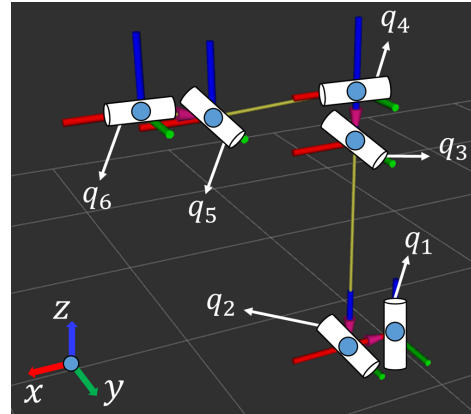


Fig. 4 Joint axes of the ECA ARM 7E Mini

are 0° , the length information of the link and the shape of the manipulator are as presented in Fig. 3, and the information of the joint coordinates and the rotational axis of the joints is as depicted in Fig. 4.

2.2.2 Prismatic joint–revolute joint transformation

Although the output of the manipulator is obtained in terms of the prismatic joints, the kinematics is described using the revolute joints, instead of the prismatic joints. This is because the manipulator is designed to rotate around the axis as a prismatic joint changes, so that it is easier to describe the kinematics with the revolute joints compared to when using the prismatic joints.

To control the manipulator based on the inverse kinematics, the position and velocity output of a prismatic joint are converted into angle and angular velocity, respectively. Here, the prismatic joints are denoted as $q_1, q_2, q_3,$ and $q_5,$ and the revolute joints are referred as q_4 and $q_6.$ To convert the length outputs of the four prismatic joints into rotational angles, we examine the relationship between a length output and a rotational angle.

The relationship between the length output and rotational angle for the second joint is as presented in Fig. 5. In the red triangle, the lengths

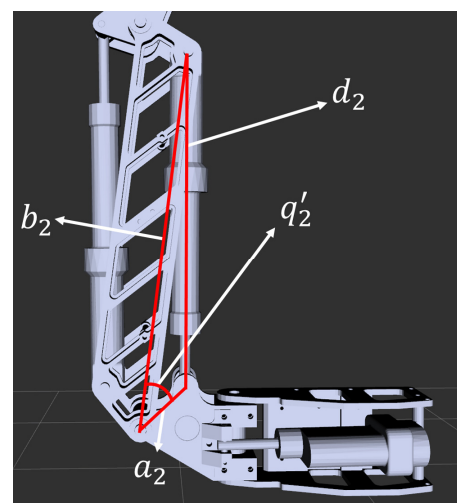


Fig. 5 Configuration of second prismatic joint $d_2,$ revolute joint $q_2',$ and constant b_2 and c_2

of the two sides, which are constants determined by the kinematic characteristics, are set as b_2 and c_2 , respectively; the angle between the two sides is q_2 , and the length of the other side is set as d_2 . Here, the included angle, q_2 , is specified according to the manipulator length output, d_2 . For using a joint angle as specified in Table 1 and Figs. 3 and 4, a constant, $q_{offset,2}$, is added to the specified q_2 to obtain the joint angle, q_2 .

Similarly, for joints $i = 1, 2, 3, 5$, which are the length outputs, position variable d_i , outputs of the prismatic joints, angular variable q_i of the revolute joints, and constants a_i and b_i corresponding to the two sides of the triangle, the relationship between d_i and q_i is described in Eq. (1) by the second cosine law.

$$d_i^2 = a_i^2 + b_i^2 - 2a_i b_i \cos(q_i) \quad (1)$$

Arranging Eq. (1) with respect to q_i , we obtain Eq. (2), and the angle of each joint output from the manipulator can be obtained. Here, the range of the variable, d_i , is typically within the range that satisfies the condition of a triangular formation with b_i and c_i . Therefore, under the condition that the sum of the lengths of two sides is greater than the length of the other side, $(a_i^2 + b_i^2 - d_i^2)/(2a_i b_i)$ typically has absolute value less than 1, and q_i is generally positive.

$$q_i = \arccos\left(\frac{a_i^2 + b_i^2 - d_i^2}{2a_i b_i}\right) \quad (2)$$

For the conversion into the joint angle as specified in Table 1 and Figs. 3 and 4, q_i is calculated by adding $q_{offset,i}$ to q_i as expressed in Eq. (3). Here, $q_{offset,i}$ is a constant determined according to the kinematic characteristics and kinematic description of each joint

$$q_i = \arccos\left(\frac{a_i^2 + b_i^2 - d_i^2}{2a_i b_i}\right) + q_{offset,i} \quad (3)$$

In addition, the relationship between the velocity variable, \dot{d}_i , of a prismatic joint and the angular velocity variable, \dot{q}_i , of a revolute joint can be obtained by differentiating Eq. (1).

$$\dot{q}_i = \frac{d_i}{a_i b_i \sin(q_i)} \dot{d}_i \quad (4)$$

Substituting Eq. (2) into Eq. (4), the angular velocity output from the manipulator is as follows.

$$\dot{q}_i = \frac{d_i}{a_i b_i \sin\left(\arccos\left(\frac{a_i^2 + b_i^2 - d_i^2}{2a_i b_i}\right)\right)} \dot{d}_i \quad (5)$$

2.3. Control Algorithm

To control the manipulator to reach a desired position, the position of the target joint angle for a given Cartesian position of the end-effector needs to be obtained. However, since a general method for solving inverse kinematics by analytical methods has not been identified, the inverse kinematics is solved using an inverse Jacobian matrix, a numerical method. \dot{q}_d is the target input velocity vector of the manipulator, \dot{x}_d is the target velocity vector of the end-effector in the rectangular coordinate system, and J is a Jacobian matrix that linearizes the relationship between the end-effector velocity vector and the manipulator joint velocity vector. Therefore, Eq. (6) can be obtained using the relationship of \dot{q}_d , J , and \dot{x}_d .

$$\dot{q}_d = J^{-1} \dot{x}_d \quad (6)$$

To improve the error in the joint velocity input resulting from the numerical integration in Eq. (6) and the tracking performance, closed loop inverse kinematics (Columé and Torras, 2014) is used to calculate the velocity input value of the manipulator, as expressed in Eq. (7).

$$\dot{q}_d = J^{-1} \dot{x}_d + k(q_d - q) \quad (7)$$

q is the angle vector of the current joint angle fed back from the manipulator, q_d is the target angle vector of the joint angle calculated based on inverse kinematics, and k is the gain value for the joint angle position error.

2.4. Tracking Algorithm

The position of an underwater robot changes under an arbitrary external force generated when the underwater robot performs autonomous manipulation. In this case, since the target for the interaction with the manipulator changes its position with reference to the underwater robot, the manipulator needs to continuously track the target. When the position vector of the end-effector is x in the Cartesian coordinate system, \dot{x}_d is defined as Eq. (8), the end-effector can continuously track the position vector, x_{obj} of the object to interact with.

$$\dot{x}_d = V \frac{(x_{obj} - x)}{|x_{obj} - x|} \quad (8)$$

If \dot{x}_d is set as in Eq. (8), the manipulator moves at velocity V in the direction of the target object in the Cartesian coordinate system.

$$V = \begin{cases} v_{max} & \text{if } |x_{obj} - x| dt \geq v_{max} \\ |x_{obj} - x| dt & \text{if } |x_{obj} - x| dt < v_{max} \end{cases} \quad (9)$$

Here, dt is defined as the time required for one control loop and v_{max} is defined as the maximum velocity that the end-effector requires

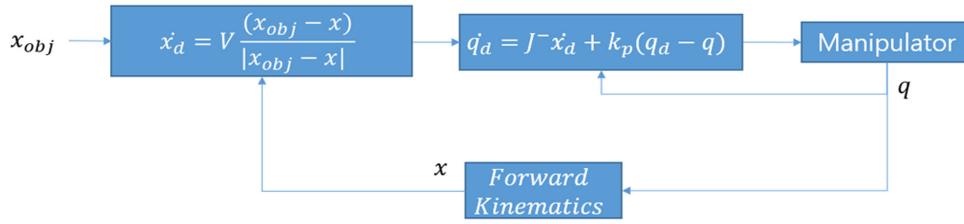


Fig. 6 Control loop of manipulator

for each control loop. When the velocity of the manipulator installed on the underwater robot is high, the subsequent fluid impact and an abrupt movement of the center of mass can adversely affect the position control of the underwater robot. Therefore, the movement velocity, V , of the end-effector is given as in Eq. (8). If the difference between the position of the target object and the end-effector is greater than v_{max}/dt , the velocity of the end-effector is set as v_{max} . If the difference is less than v_{max}/dt , it is set as $|x_{obj} - x|/dt$, proportional to the position difference between the object and the end-effector. Therefore, when the end-effector tracks the target object, it is moved with v_{max} at maximum. The controller of the manipulator is configured, as displayed in Fig. 6, using the inverse and forward kinematics. As presented in Fig. 6, the angle output, q , of a joint angle is obtained, and using the forward kinematics, the end-effector position, x , is obtained in the Cartesian coordinates system.

3. Tracking Algorithm Simulation

Prior to verifying the tracking performance of the manipulator, we aimed to verify the performance of the tracking algorithm by simulation. For the simulation environment, the open dynamics engine (ODE) of the open-source robotics foundation (OSRF) in Gazebo 7.15.0. ver. is used (Fig. 7). An ECA ARM 7E Mini model was fixed in the bottom of the Gazebo simulation environment, and the simulation was performed. Unlike the actual manipulator model, all the joints were assumed to be revolute joints in the simulation performance.



Fig. 7 Gazebo simulation with the ECA ARM 7E Mini

3.1 Linear Tracking Simulation

For the linear tracking simulation, from the initial position of the

end-effector, for tracking the trajectory of a point moving to a target ($X = 0.2$ m, $Y = 0$ m, $Z = 0$ m) positioned on a horizontal line, as depicted in Fig. 8, the trajectory of a point moving to a target ($X = 0.1$ m, $Y = 0$ m, $Z = -0.2$ m) positioned diagonally, as presented in Fig. 9, was determined.

The plots of the end-effector position and the position error of the horizontal tracking presented in Fig. 8 and of the diagonal tracking in Fig. 9 are indicated in Figs. 10 and 11, respectively. The two figures in the upper part of Fig. 10 display the position and position errors in the X and Z directions, respectively. In the X and Z directions, the maximum position errors are approximately 3.3 mm and 1 mm or less,

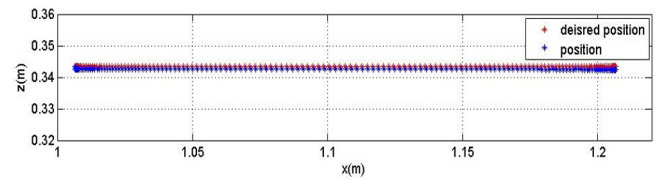


Fig. 8 End-effector trajectory of a horizontal movement obtained from the simulation

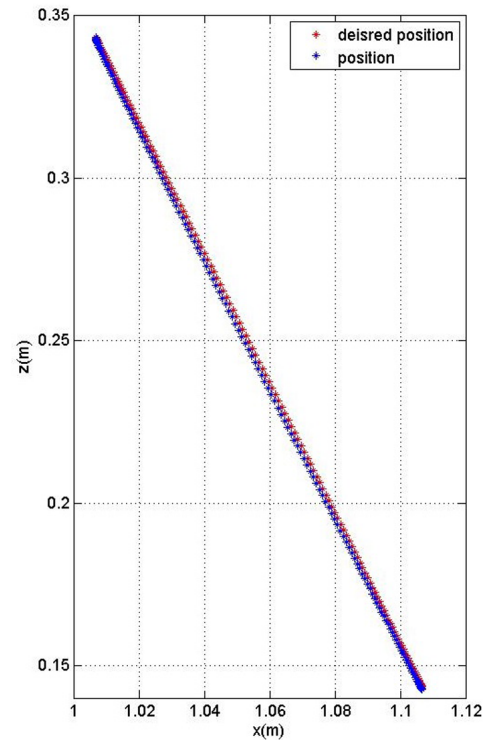


Fig. 9 End-effector trajectory of a diagonal movement obtained from the simulation

respectively. After the movement, the position error in the steady state is 0.1 mm in the X direction and 0.8 mm in the Z direction. The figures in the upper part of Fig. 11 display the position and position errors in the X direction and Z directions. The maximum position error in the X direction is approximately 2.3 mm, and it is 2 mm in the Z direction. After the movement, the position error in the steady state is 0.1 mm in the X direction and 0.8 mm in the Z direction. After completing the movement in both the horizontal and vertical directions, the error in the Z direction is greater than that in the X direction. As the

manipulator moves further away, the length of the moment arm increases at a particular gravity, and the torque loaded on the specific joint increases. With the increase in the torque, the position error of the joint increases. However, as expressed in Eq. (7), when there is an error in q_d , the target position of the joint, and q , the joint position. When the velocity input increases to compensate the error, the error becomes less than 1 mm in the steady state in the Z -direction. During the movement, the end-effector velocity is determined in proportion to the position and error of the point to be tracked by the manipulator, as

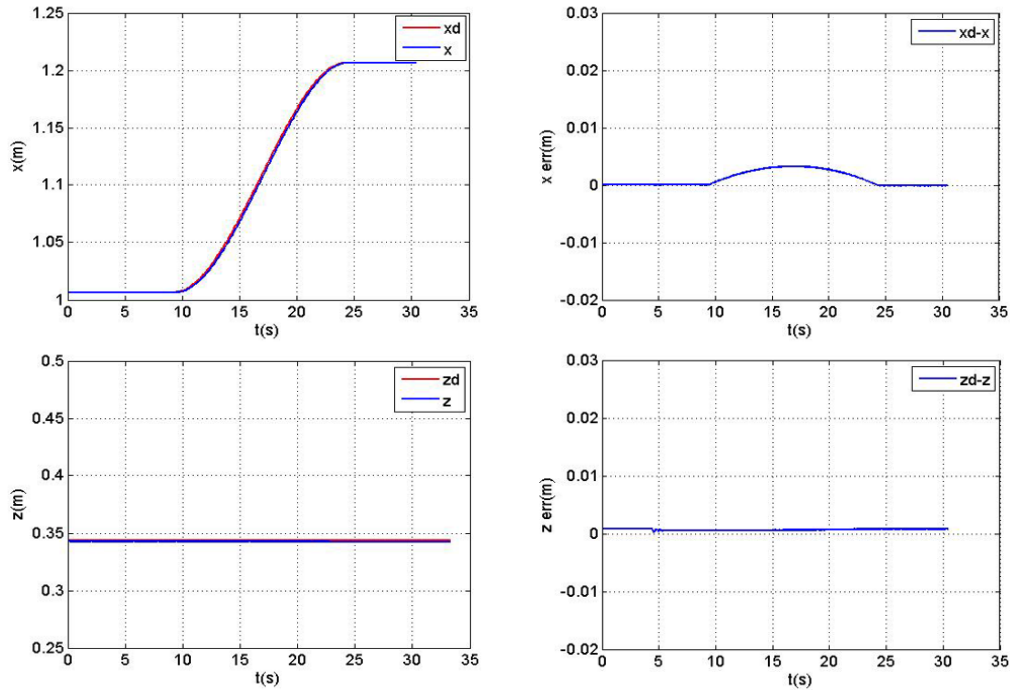


Fig. 10 Position and error for a horizontal movement obtained from the simulation

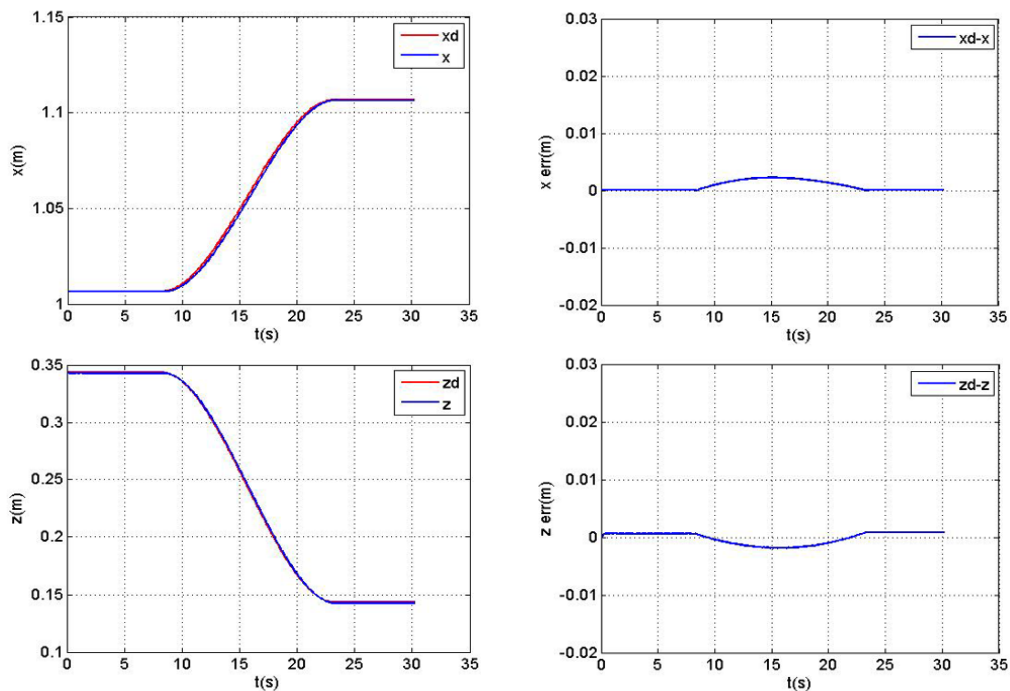


Fig. 11 Position and error for a diagonal movement obtained from the simulation

written in Eq. (9). Accordingly, it can be estimated that a position error will occur in proportion to the acceleration of the object to be tracked, which can be seen by comparing the position error variation in the X direction with acceleration and that in the Z direction without acceleration. Compared to the X direction position error graph, in the

Z direction position error graph, since there is no acceleration of the object, we can see that the position error is small.

3.2 Circular Tracking Simulation

In this section, we present the analysis of the simulation in which the

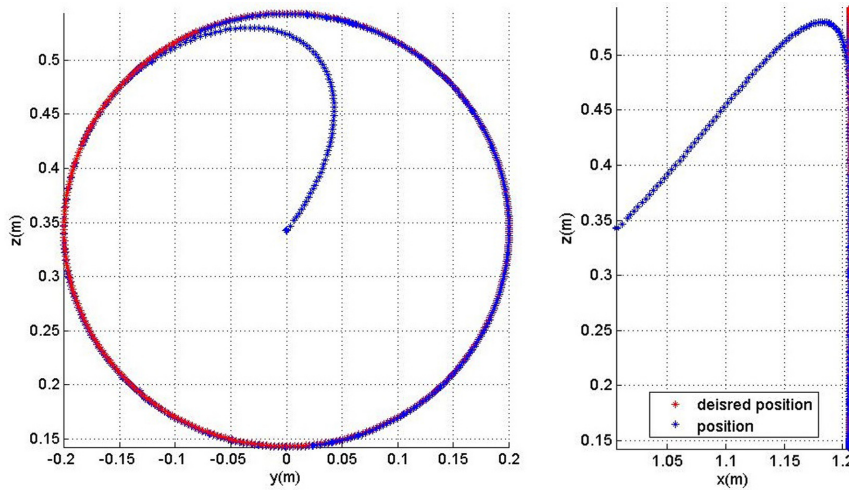


Fig. 12 End-effector trajectory for a circular movement obtained from the simulation

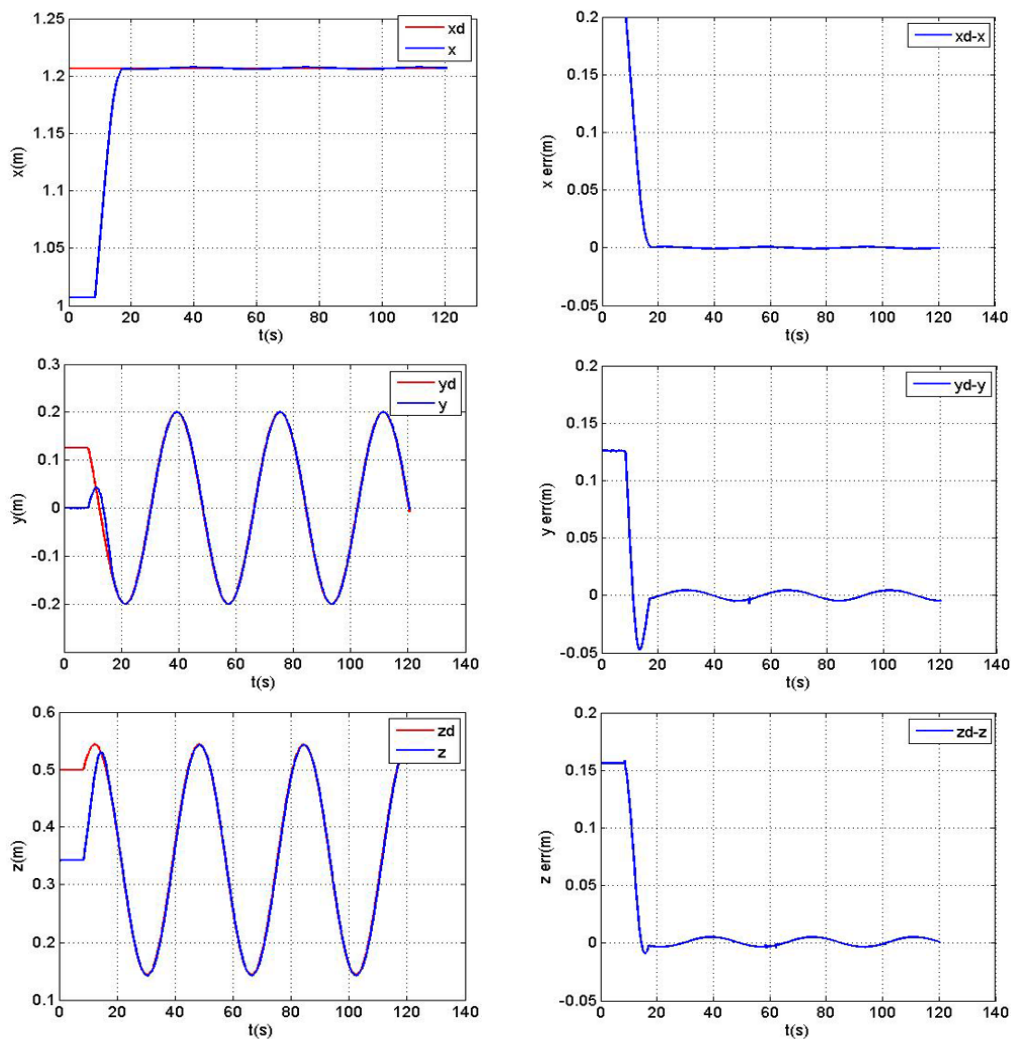


Fig. 13 Position and error for a circular movement obtained from the simulation

end-effector tracks the position of a point moving along the trajectory of a circle over time. A circular tracking simulation was performed (Fig. 12) to track the position of a target object moving along a circle with a radius of 20 cm, 20 cm away from the end-effector in the X direction

In Fig. 12, the red dot is the trace of the target object moving along the circle, and the blue dot is the trace of the end-effector position. At the beginning of the simulation, it can be seen that the manipulator end-effector moves to the front and the upper side where the target object exists. It then continues to track the path of the moving point after the target object position and end-effector are sufficiently close. Fig. 13 displays the position and position error graph, in which the left is the position graph, and the right is a position error graph. As soon as the movement starts, it can be noted that the blue line, which is the end-effector position, moves to the red line, which is the target position. Moreover, the red line continuously tracks, after the end-effector reaches the position near the moving point. In the position error graph, it can be seen that the position error decreases rapidly at the beginning of the operation, and over time, it tracks with an error of up to 5 mm in the Y and Z directions.

4. Tracking Performance Demonstration Experiment

This chapter describes the demonstration of the position tracking performance of the ECA ARM 7E Mini Manipulator by experiments. By applying the control and tracking algorithms used in the simulations, as discussed in Chapter 3, to an actual manipulator, we conduct experiments in which the end-effector performs linear

tracking and circular tracking. Finally, the manipulator is installed on an underwater robot, and an underwater tracking experiment of a target object is performed.

4.1 Linear Tracking Experiment

To verify the linear position tracking performance of the manipulator end-effector, an experiment was conducted as follows. After a grid paper was attached to a flat surface perpendicular to the $Y=$ axis, the end-effector was directed to grasp a pen. After keeping the pen and grid paper in contact at the initial position of the end-effector, horizontal tracking ($X=0.2$ m, $Y=0$ m, $Z=0$ m) and diagonal tracking ($X=0.1$ m, $Y=0$ m, $Z=-0.2$ m) experiments which were simulated as discussed in Chapter 3 were performed. Figs. 15 and 16 present the graph of the linear movement of the end-effector superimposed on the grid paper drawn with a pen. Here, the red dots are the target positions of the end-effector in Cartesian coordinates. The blue dots are the current position of the end-effector calculated using the forward kinematics based on the joint angle fed back from the manipulator. Here, there are parts where the initial control is unstable owing to the friction when the joint angle of the manipulator moves after stopping. In addition, there are errors from the kinematic modeling and tilting of the floor. However, overall, it can be confirmed that the trajectory of the end-effector and the trajectory drawn by the pen are similar.

The results of the horizontal tracking (Fig. 17) and diagonal tracking (Fig. 18) performed by the end-effector are examined according to the movement time. The upper left graph is a plot of the X -direction target position of the end-effector and the current position, and the upper

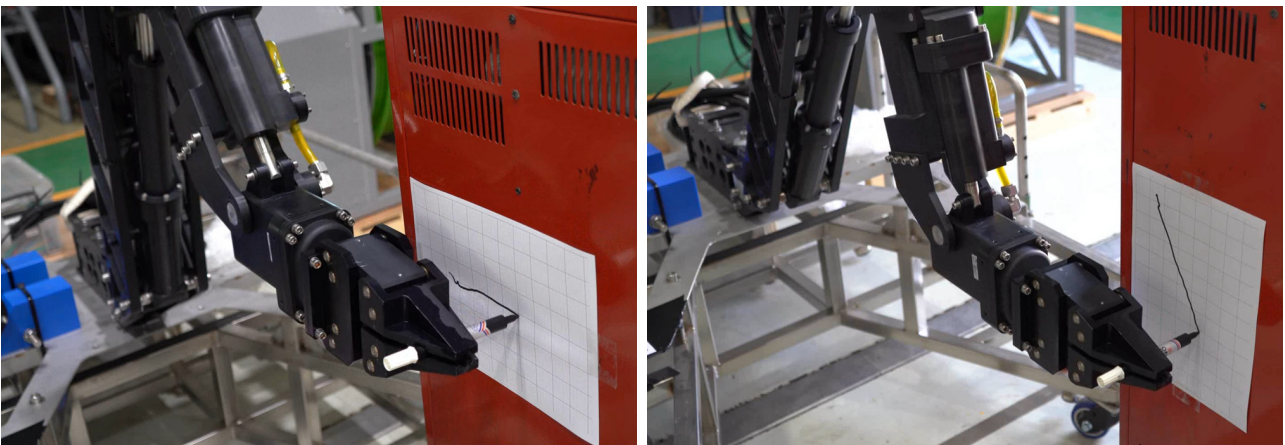


Fig. 14 Line drawing scenes using a pen held by end-effector

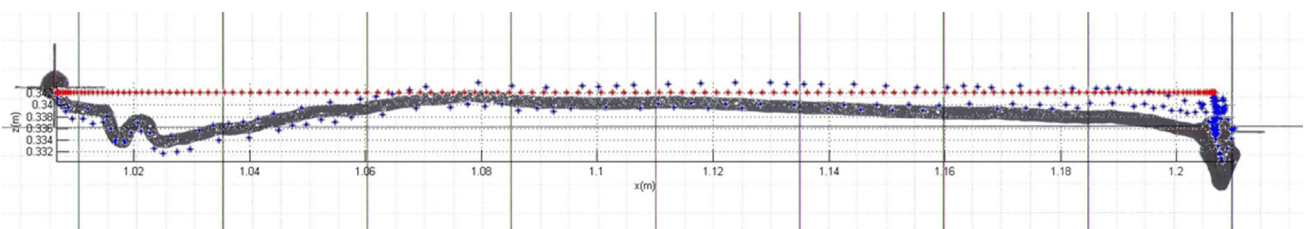


Fig. 15 Horizontal movement trajectory of the end-effector obtained from the experiment (Red: desired, Blue: measured, Black: drawn)

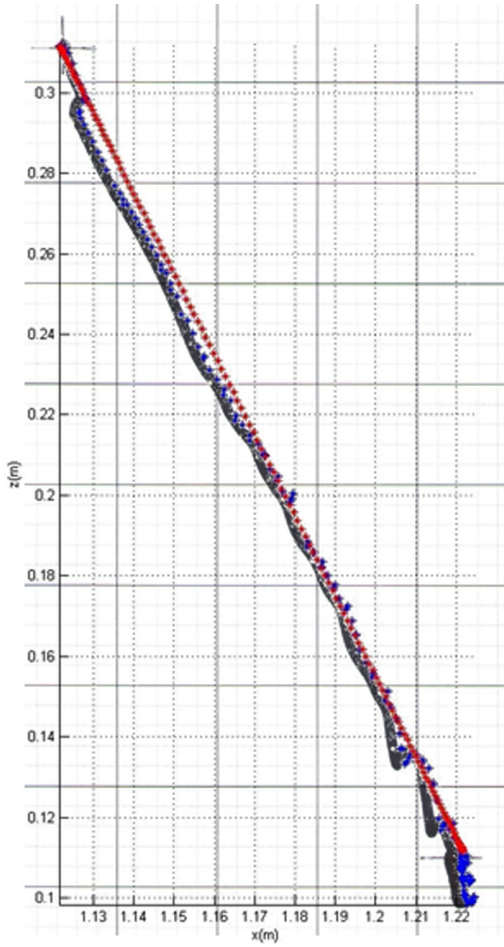


Fig. 16 Diagonal movement trajectory of the end-effector obtained from the experiment (Red: desired, Blue: measured, Black: drawn)

right graph is the X-direction position error plot. In the horizontal and diagonal tracking, when the manipulator starts to move for the first time, errors of up to 7 mm and 4 mm occur in the X-direction, respectively, and errors of less than 1 mm occur in the steady state after the manipulator completes the movement. The lower left graph displays the Z-direction target position of the end-effector and the current position, and the lower right graph presents the Z-direction position error. In the horizontal and diagonal tracking, during the movement of the end-effector, errors of up to 12 mm and 13 mm occur, respectively, and errors of approximately 4 mm and 1 mm occur, respectively, in the steady state after the manipulator arrives at the target point. It can be seen from the position error graph that the tracking error is relatively large in the low-velocity sections (10–15 s, 20–25 s) during the movement of the manipulator. The tracking error can be inferred as a decrease in the performance of the tracking of the position of the joint actuator when the joint is driven at a low velocity. Under the decreased tracking performance due to the low velocity, the position tracking performance of the joint angle is further deteriorated by the load, which emerges as a position error in the form of a deflection. Therefore, it can be confirmed that the position tracking error is larger than that obtained from the simulation.

4.2 Circular Tracking Performance Demonstration

Here, we present the experimental demonstration of the circular tracking performance verification, described using simulation in Chapter 3.2. The results of the experiment in which the end-effector of the manipulator tracks a continuously moving object in a circular motion are examined in this section. The left figure of Fig. 19 illustrates the manipulator tracking a virtual purple sphere, and it

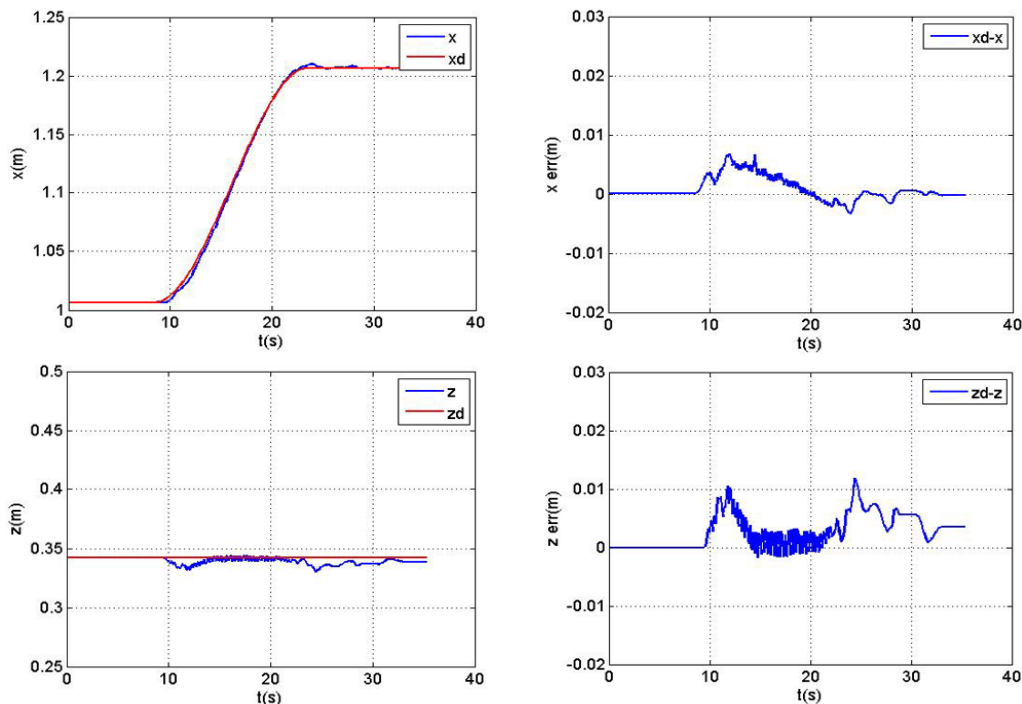


Fig. 17 Position and error for a horizontal movement obtained by the experiment

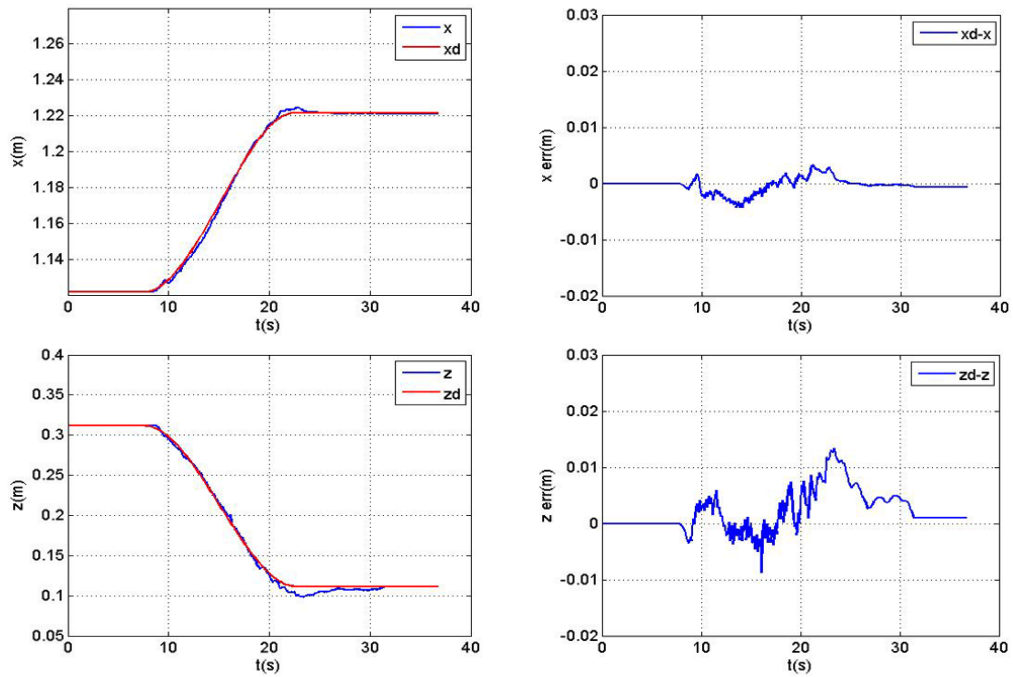


Fig. 18 Position and error for a diagonal movement obtained by the experiment

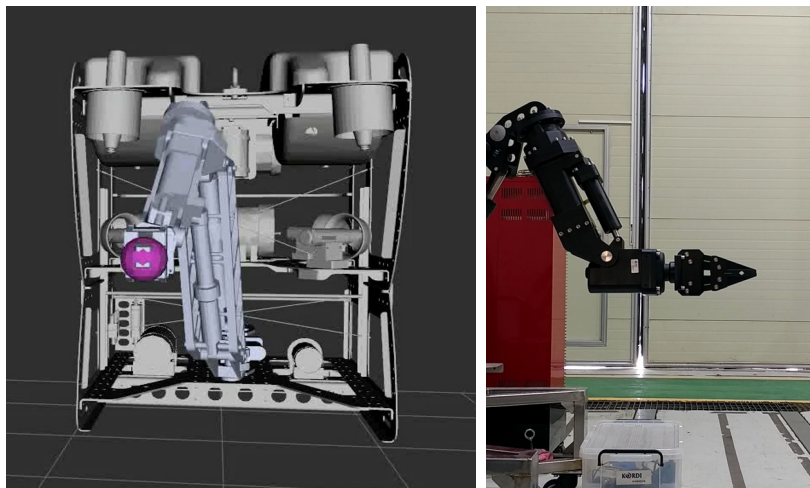


Fig. 19 Experimental tracking of a virtual sphere by the end-effector

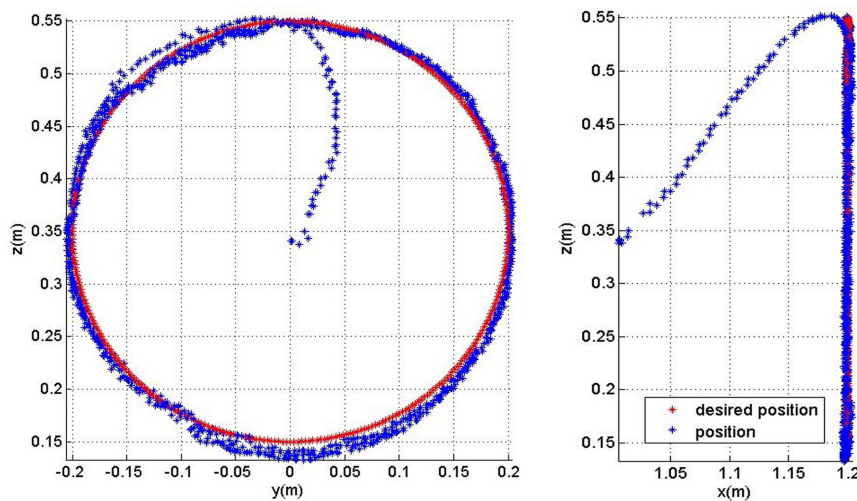


Fig. 20 End-effector trajectory for a circular movement obtained from the experiment

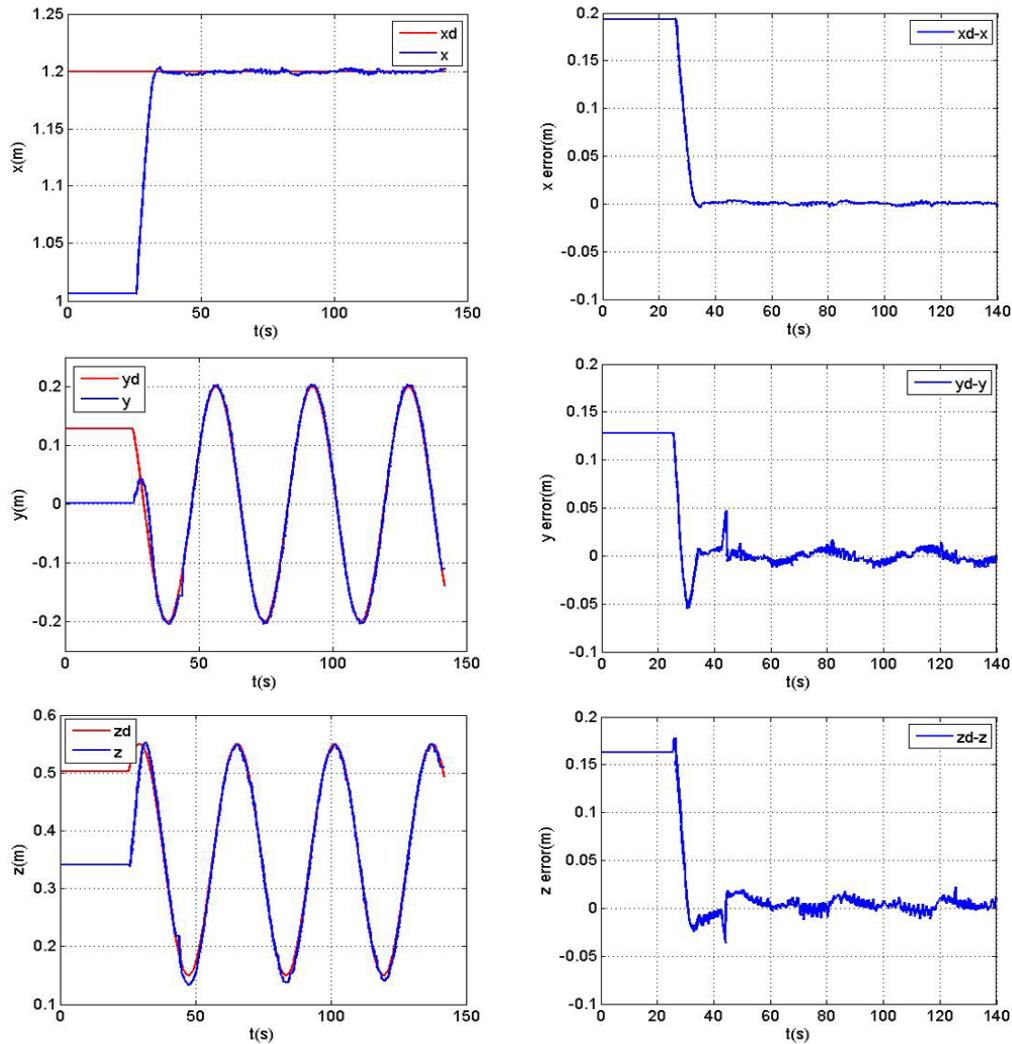


Fig. 21 Position and error for a circular movement obtained from the experiment

shows the shape of the manipulator based on the joint angle fed back from the manipulator. The picture on the left is that of the manipulator viewed from the side when the manipulator tracks the virtual sphere.

Fig. 20 displays a graph showing the trajectory of the end-effector tracking a virtual sphere moving in a circular motion in the Cartesian coordinate system. The left figure in Fig. 20 is the trajectory seen from the front of the manipulator, and this is a graph seen from the same viewpoint as the figure on the left of Fig. 19. The figure on the right in Fig. 20 is a trajectory seen from the side, and this is a graph seen from the same viewpoint as the figure on the right side of Fig. 19. The red dots represent the trajectory of the virtual sphere, and the blue dots represent the position of the end-effector calculated using the forward kinematics after the joint angle information is fed back from the manipulator.

Fig. 21 is a graph displaying the virtual sphere position and the end-effector position. In the initial stage of the tracking, the end-effector moves toward the front and the upper direction, which is the direction in which the virtual sphere exists. After the end-effector reaches sufficiently close to the virtual sphere, we can see that it continuously tracks the position of the virtual sphere. This can be

observed in more detail in Fig. 21 in which the position and position error graph are depicted. In the graph, when the virtual sphere faces downward, the end-effector has a maximum error of 19 mm in the Z direction with the virtual sphere. As in the case of the linear tracking experiment, deterioration of the actuator performance at a low velocity and a deflection due to the load are observed. Therefore, it is confirmed that the circular tracking experiment also has a larger error compared to the corresponding simulation. In particular, when the end-effector moves in the downward direction, it can be confirmed that the tracking performance of the joint actuator decreases under the action of gravity.

4.3 Underwater Tracking Performance Verification

In this section, an experiment of the underwater tracking of a target object with the manipulator installed on an underwater robot is discussed. The position of the target object is continuously obtained from the camera of the underwater robot, and the position of the target object is obtained from the base of the manipulator. At this time, an experiment is performed in which the position of the target object from the underwater robot is continuously changed and the end-effector of

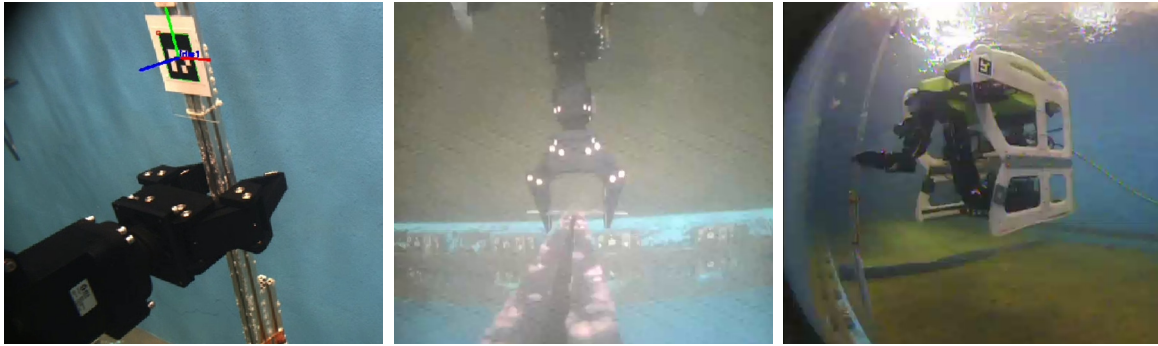


Fig. 22 Experimental tracking of an underwater object by the end-effector

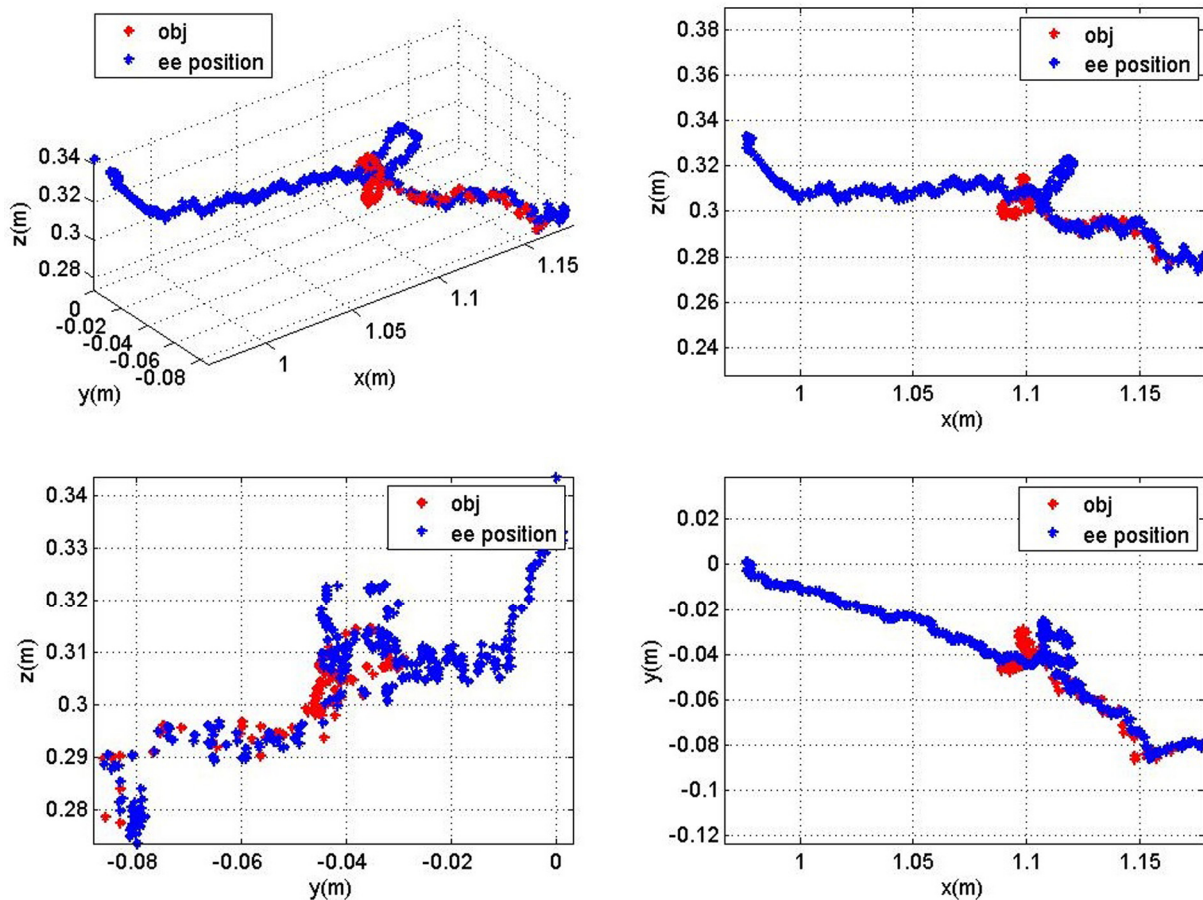


Fig. 23 End-effector trajectory for an underwater movement obtained from the experiment

the manipulator tracks the position of the target object, as shown in Fig. 22. Here, the target object is a square pipe equipped with a marker, and the position below 20 cm of the optical recognition marker is set as the position of the target object.

Fig. 23 illustrates a graph showing the position of the object from the underwater robot and the trajectory of the end-effector. The red dots denote the positions of the target object from the underwater robot, and the blue dots are the positions of the end-effector calculated based on the joint angle fed back from the manipulator. As in the previous experiments, the end-effector first approaches the position of the target object, and after the target object and the end-effector move sufficiently close, we can see that the end-effector continuously tracks

the target object as it moves. In the graph, it can be seen that the red dots are constantly moving owing to the navigation errors, which are the position control errors of the underwater robot due to the effect of the movement of the manipulator. It can be noted that the end-effector continuously tracks the change in the relative distance of the target object in underwater environment. Here, the graph in Fig. 23 presents the data in the state when the end-effector is sufficiently close to the target object, which is 10 s after the case in Fig. 14.

Fig. 24 depicts a graph of the end-effector position and the position error with the target object in underwater environment. In the initial stage of the tracking, we can observe that the end-effector moves toward the target object. During the end-effector tracking of the subject,

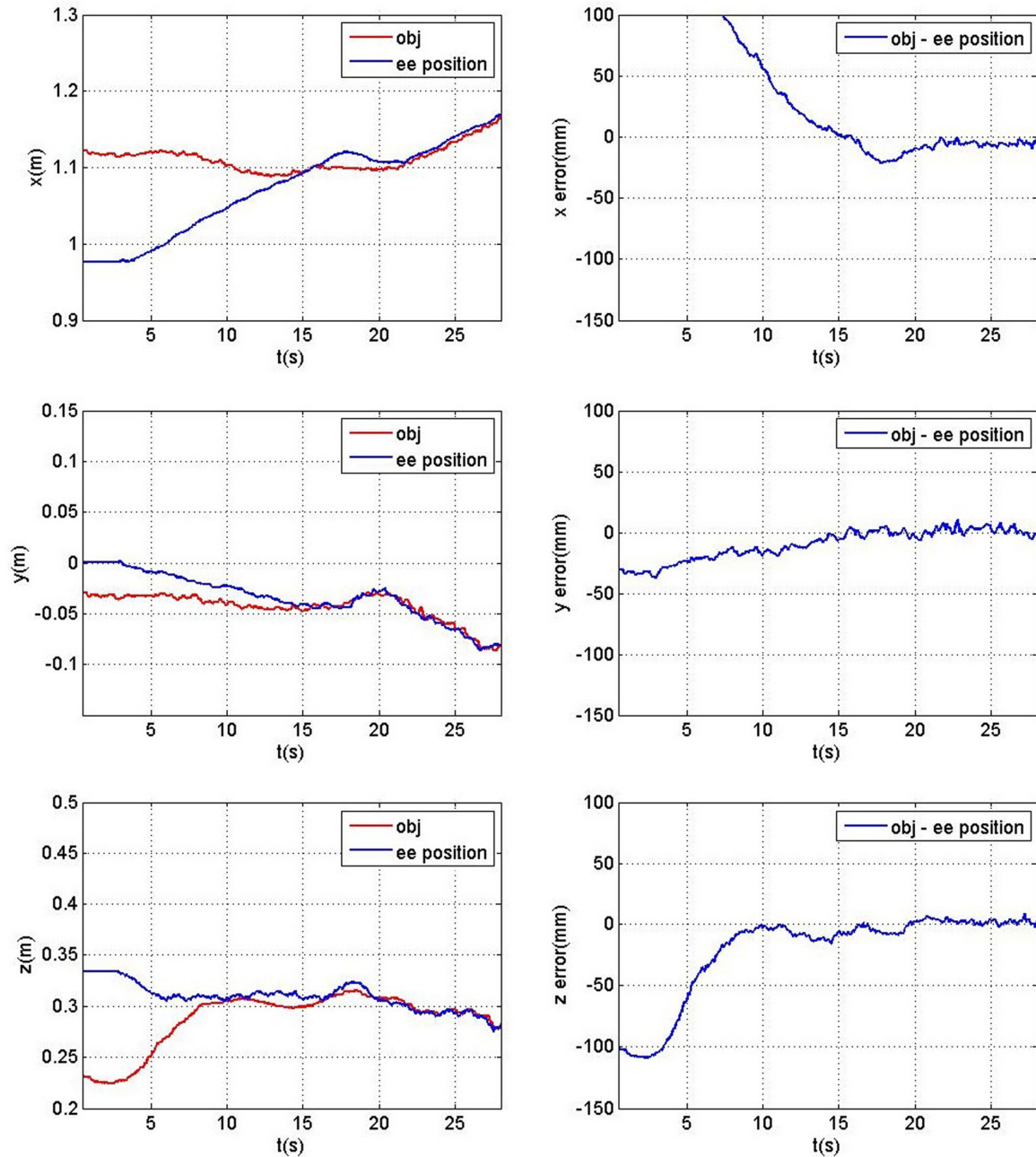


Fig. 24 Position and error for an underwater movement obtained from the experiment

an overshoot of approximately 20 mm occurs at approximately 17 s. Subsequently, it can be observed that the end-effector tracks stably according to the movement of the target object after approximately 20 s. At this time, an error of approximately 4 mm occurs in the X direction and of approximately 2 mm each occurs in the Y and Z directions. It can be confirmed that unlike the previous experiments on the ground, the effect of the control performance deterioration of the actuator by gravity is reduced.

5. Conclusion

In this study, the tracking performance of an ECA ARM 7E Mini model manipulator installed on an underwater robot for autonomous

manipulation was verified. For the kinematic description of the manipulator, a prismatic joint output was converted into a revolute joint output, and velocity control was performed based on closed-loop inverse kinematics. To respond to the changes in the position of the underwater robot due to disturbances, a manipulator control was implemented to track a target object. However, since rapid tracking of the manipulator adversely affects the position control performance of the underwater robot, it was ensured that the end-effector tracks the target object without exceeding the specified velocity. The performance of the tracking algorithm was verified by performing a simulation tracking a linear trajectory and a moving target object using the Gazebo simulator. The performance was further demonstrated using an actual manipulator and conducting an experiment the

identical to the simulation. Based on the tracking performance verification on the ground, the manipulator was installed on an underwater robot, to examine the underwater tracking performance. From the results of the experiment on the ground, it was confirmed that compared to the simulation result, an error was caused by the poor tracking performance of the end-effector, resulting from a lack of the control performance of the joint actuator under low velocity and load conditions. However, the results of an underwater experiment demonstrated that the tracking performance degradation of the actuator was reduced. A planned follow-up of this study is as follows. We aim to perform autonomous underwater manipulation by the manipulator by improving the tracking error of the target tracking algorithm of the manipulator used in this study. We aim to apply the results to autonomous decision-making for the movement of a manipulator in a work space and the movement of an underwater robot and the manipulator when the manipulator installed on the former interacts with a target object. Furthermore, to reduce the position error of the manipulator, we aim to apply dynamics-based control, such as a mass matrix

Acknowledgements

This study was conducted under the projects of “Development of 3D object recognition and robot-robot arm motion compensation control generic technology for autonomous underwater manipulation” and “Development of core technology on the cyber physical system of underwater robot (CPOS),” which were conducted as the institutional projects of KRISO.

References

- Colome, A., & Torras, C. (2014). Closed-loop Inverse Kinematics for Redundant Robots: Comparative Assessment and Two Enhancements. *IEEE/ASME Transactions on Mechatronics*, 20(2), 944-955. <https://doi.org/10.1109/tmech.2014.2326304>
- Kang, J.I., Choi, H.S., Jun, B.H., Nguyen, N.D., & Kim, J.Y. (2017). Control and Implementation of Underwater Vehicle Manipulator System Using Zero Moment Point. 2017 IEEE Underwater Technology(UT), At Busan, South Korea. <https://doi.org/10.1109/ut.2017.7890291>

- Kim, S.H., Jang, K.W., Park, S.H., Lee, Y.S., Lee, S.Y., & Park, J.H. (2019). Whole-body Control of Non-holonomic Mobile Manipulator Based on Hierarchical Quadratic Programming and Continuous Task Transition. In 2019 IEEE 4th International Conference on Advanced Robotics and Mechatronics (ICARM), Osaka, Japan, 414-419. <https://doi.org/10.1109/icarm.2019.8834269>
- Korpela, C.M., Danko, T.W., & Oh P.Y. (2012). MM-UAV: Mobile Manipulating Unmanned Aerial Vehicle. *Journal of Intelligent & Robotic Systems*, 65, 93-101. <https://doi.org/10.1007/s10846-011-9591-3>
- Ura, T., & Takakawa, S. (2015). All about Submersibles (W.S. Kim, D.S. Kim, Y.H. Choi, C.H. Park, J.S. Park, P.M. Lee, H.S. Jung, Trans.). Korea: CIR. (Original Work Published in 1994, Japan: Seizan-Shoten Publishing)
- OSRF(Open Source Robotics Foundation). (2019). Gazebo. Retrieved October 2019 from http://gazebosim.org/#collapseVersion7_1
- Ribas, D., Palomeras, N., Ridaio, P., Carreras, M., & Mallios, A. (2012). Girona 500 AUV: From Survey to Intervention. *IEEE/ASME Transactions on Mechatronics*, 17(1), 46-53. <https://doi.org/10.1109/tmech.2011.2174065>
- Yeu, T.K., Choi, H.T., Lee, Y.G., Chae, J.B., Lee, Y.J., Kim, S.S., ... Lee, T.H. (2019). Development of Robot Platform for Autonomous Underwater Intervention. *Journal of Ocean Engineering and Technology*, 33(2), 168-177. <https://doi.org/10.26748/KSOE.2019.021>

Author ORCIDs and Contributions

Author name	ORCID	Contributions
Chae, Junbo	0000-0003-1400-7660	①②③④
Yeu, Taekyeong	0000-0003-2742-3284	②④
Lee, Yeongjun	0000-0002-3808-8349	②
Lee, Yoongeon	0000-0003-2275-6186	②
Yoon, Suk-Min	0000-0002-3523-3221	④⑤

- ① Conceived of the presented idea or developed the theory
 ② Carried out the experiment or collected the data
 ③ Performed the analytic calculations or numerical simulations
 ④ Wrote the manuscript
 ⑤ Supervised the findings of this study

Experimental Study of Load Characteristics of Buried and Exposed Large-Diameter Pipelines Using Fiber-Optic Strain Sensor

Joseph Chul Chung¹, Michael Myung-Sub Lee² and Sung Ho Kang³

¹R&D manager, IT convergence Laboratory, CyTroniQ Co. Ltd., Cheon-an, Korea

²General manager, Department of Business Development, CyTroniQ Co. Ltd., Cheon-an, Korea

³Researcher, IT convergence Laboratory, CyTroniQ Co. Ltd., Cheon-an, Korea

KEY WORDS: Fiber optic, Sensor, Strain, Pipeline load, Monitoring

ABSTRACT: In this study, an optical-fiber sensor was used to measure loads that could act in an environment similar to the loading conditions that exist in an actual pipe. The structure and the installation method of the optical-fiber strain sensor were applied considering the actual large pipe and the buried pipe environment. Load tests were performed using a displacement sensor and sandbags to determine the deflection of the pipe according to the external load, and the linear measurement results were verified. Considering the conditions that could exist in the actual pipe, the test method was presented, and the strain of the buried pipe generated at this time was measured.

1. Introduction

Among the optical sensors that have recently gained attention across various fields, fiber-optic strain sensors, which involve the use of optical fibers, have been classified as intensity, interferometric, and fiber Bragg grating (FBG) sensors based on the measurement method. The distributed sensing technology has recently been developed through the popularization of optical components (Culshaw et al., 2008). Developments in fiber-optic sensor technology advanced with the commencement of research on FBG sensors in the 1990s (Meltz et al., 1989; Hill and Meltz, 1997).

Fiber-optic sensors have the following advantages owing to their structural characteristics: they are unaffected by external electromagnetic waves, can transmit signals over long distances, and enable multiplexing, making it convenient to connect numerous sensors. They also have remarkable durability, with a durability life of 20 years. In civil engineering, FBG sensors have been used to monitor large civil engineering structures, such as bridges and tunnels, and they have recently been applied in mechanical engineering. An FBG creates a permanent refractive index modulation on the core in the longitudinal direction of the optical fiber and uses this modulation as a sensor. Fig. 1 shows a schematic of an FBG structure. When a periodic refractive index modulation is made, a coupling is generated between

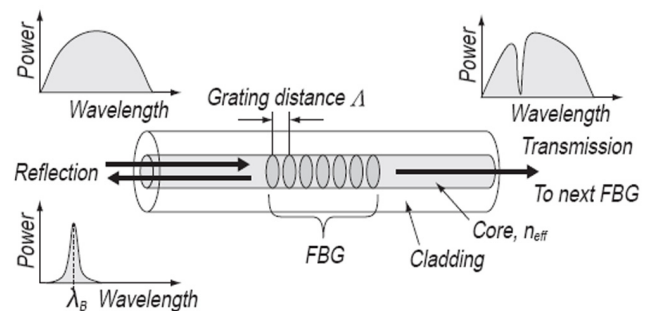


Fig. 1 Characteristics and structure of fiber bragg grating

the propagation mode and the reflection mode, and thus, reflects a particular wavelength.

The wavelength reflected by FBG is determined by the spacing and refractive index modulation of the core. Eq. (1) is used to describe this property:

$$\lambda_B = 2n_{eff}A \quad (1)$$

where λ_B is the Bragg reflection wavelength, n_{eff} is the effective refractive index of the core, and A is the grating spacing that generates the refractive index modulation.

The half-wavelength of the FBG is influenced by external

Received 12 February 2020, revised 27 April 2020, accepted 25 May 2020

Corresponding author Joseph Chul Chung: +82-41-522-3253, cytrnd@cytroniq.com

© 2020, The Korean Society of Ocean Engineers

This is an open access article distributed under the terms of the creative commons attribution non-commercial license (<http://creativecommons.org/licenses/by-nc/4.0>) which permits unrestricted non-commercial use, distribution, and reproduction in any medium, provided the original work is properly cited.

temperature and stress. The refractive index of the core varies with temperature, hence, changing the reflection wavelength. Moreover, the grating spacing changes with stress and consequently changes the reflection wavelength. These changes are described using the following equation:

$$\frac{\Delta\lambda_B}{\lambda_B} = (1 + P_e) \cdot \varepsilon + \xi \cdot \Delta T \quad (2)$$

where P_e is the effective photo-elastic coefficient, ε is the applied stress, ξ is the thermo-optic coefficient, and ΔT is the relative temperature change.

Generally, the effective photo-elastic coefficient of a single-mode optical fiber is 0.22. The Bragg center wavelength modification owing to the stress applied in the axial direction of an FBG made from a single-mode optical fiber is generally adopted as 1.4 pm/microstrain in a 1,550 nm band. Additionally, the Bragg center wavelength shift because of temperature change is 10 pm/°C.

A photosensitive single-mode optical fiber that responds to light in the ultraviolet region is used to produce an FBG. Photosensitivity is increased by injecting hydrogen into the core at high pressures or by doping Ge. A phase mask is used to create a periodic refractive index modulation in an optical fiber with increased photosensitivity. The phase mask generates a periodic interference shape through the

diffraction effect of light. As shown in Fig. 2, an excimer that generates light within the range of 190–250 nm, and an Argon laser with a frequency multiplier, are used to generate ultraviolet light, which is transmitted through the phase mask on the photosensitive optical fiber. The pattern with periodic intervals passing through the phase mask generates a periodic refractive index modulation in the optical fiber, thus, producing the FBG. Fig. 3 shows the wavelength characteristics of the FBG.

As shown in Fig. 3, the light reflected by the optical fiber grating is transmitted in the direction of the incident optical fiber. This transmitted light is reflected and returns with the physical quantity information to the point where the FBG is located. The sensors can be multiplexed, assuming that the structure has light sources that can generate various light types and that gratings with different Bragg center wavelengths are connected in series. Therefore, the FBG can be structured with multiple sensors connected in series to one optical fiber, which can be advantageous depending on the application. A highly effective method for achieving integration in the structure is to use several serialized sensors without additional parallel connections. Because the sensor signal is transmitted to the optical fiber, an amplifier is unnecessary for a distance up to several kilometers. The FBG can be used in various temperature ranges owing to its wide operating temperature range.

In this study, the technique for measuring the load generated in a pipe was applied by adding a sensor assuming that humans can access buried pipes. This dynamic technique can be used for taking up to 100 samples per second by measuring in a specific area where the sensor is installed. Regarding previous studies, for a monitoring method that is used to confirm the related reaction according to load that can act externally (Jeong et al., 2017; Lee et al., 2016), a fiber-optic sensor-based method using a Brillouin distributed sensor through a scattering system capable of strain and temperature measurements was used. Although this method can be used to measure the entire section, several seconds of analysis time are required during the measurement. In addition, pipes buried underground are continuously impacted by external loads, such as soil pressure, vehicles, and ground settlement. In particular, pipes buried in the soft ground are known to be significantly influenced by ground settlement (Hong et al., 2006). Based on measurements using an electric strain sensor, the soft ground has complex characteristics owing to its engineering properties, and when the ground has low strength and an extended depth, large deformation (such as settlement) occurs. Loads acting on pipes include primary loads (such as internal pressure, pipe self-weight, soil pressure, vehicles, and trains) and longitudinal loads (such as wind, snow, temperature variations, earthquakes, and third-party construction loads). The stresses acting on pipes include circumferential stress, axial stress, and synthetic stress.

In this study, the stress and deformation behavior of buried pipes were examined, considering the loading position. Based on the findings of referenced studies, a test method was proposed considering the displacement and stress tests of the buried pipe using fundamental

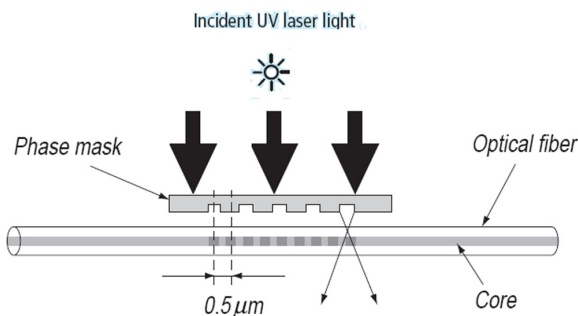


Fig. 2 Fiber bragg grating fabrication method using UV laser and phase mask

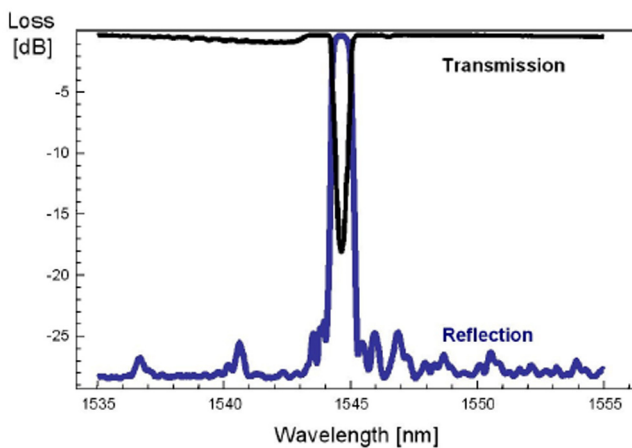


Fig. 3 Reflection and transmission spectrum of fiber bragg gratings

data. Tests of the basic design and characteristics, as well as tests on pipes with similar conditions to actual pipes, were performed, and their results were analyzed.

2. Review of Theoretical Loads on Buried Pipes

Ryu et al. (2017) conducted a numerical analysis to evaluate the effects of applied surface loads near and at the upper part of a buried pipe. Based on the results, the maximum displacement of the buried pipe decreased almost linearly as the loading position became farther away, regardless of the size of the buried pipe for the same buried depth. Moreover, the maximum stresses generated in the buried pipe were similar irrespective of the variations in diameter for the same pipe thickness, and for low thicknesses, the changing pattern varied with the loading position. Hence, the stress behavior of the buried pipe according to the loading position was found to be dependent on the pipe thickness. Next, the maximum displacement of the buried pipe with respect to the loading position was generated when the line of action of the distributed load coincided with the centerline of the buried pipe. When the distributed load acted on the upper part of the buried pipe, the degree of change in the displacement was not significant, even when the loading position was changed partially. Furthermore, when the distributed load was not applied to the vertical upper part of the buried pipe, the stress value decreased as the loading position increased. At extended buried depths, the loading position

scarcely showed any impact. Finally, the maximum stress of the buried pipe was generated in the section with the surface load on the upper part of the buried pipe. However, compared with when the centerline of the buried pipe coincided with the resultant line of action of the surface load, the stress increased by approximately 10% or more when eccentric loading was applied. In this study, the stress and deformation behaviors of buried pipes were investigated considering the loading position, and a test method was presented considering displacement and stress tests of the buried pipe with fundamental data based on the findings of referenced studies.

3. Load Test Using Displacement Sensor and Fiber-optic Strain Sensor in Exposed Pipe

The 1,550 nm FBG sensor measurement equipment and the 100 mm strain sensor using the fiber-optic sensor related to this study were designed and developed by Cytroniq (Lee and Kim, 2011) and were used for the tests. The developed strain sensor was verified according to IEC 61757-1-1 standards (International Electrotechnical Commission, 2016). The fiber-optic sensor property of enabling connection in series was utilized, and the fiber-optic sensor was designed and manufactured to suit the test objectives. First, as the deflection displacement could be measured in the exposed pipe, the load test of the pipe was performed using the fiber-optic sensor (Fig. 4). The fiber-optic sensor and the displacement sensor were used to record the generated displacement in

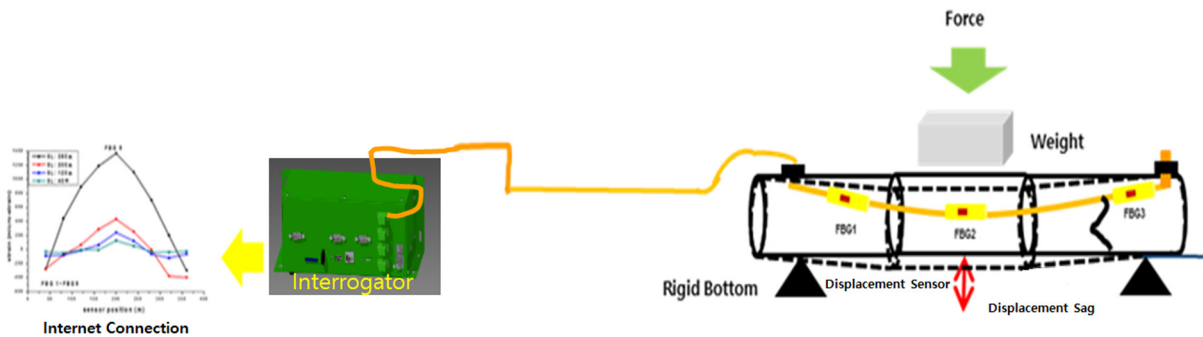


Fig. 4 Block diagram of load testing and monitoring system for fiber strain sensor at exposed pipeline

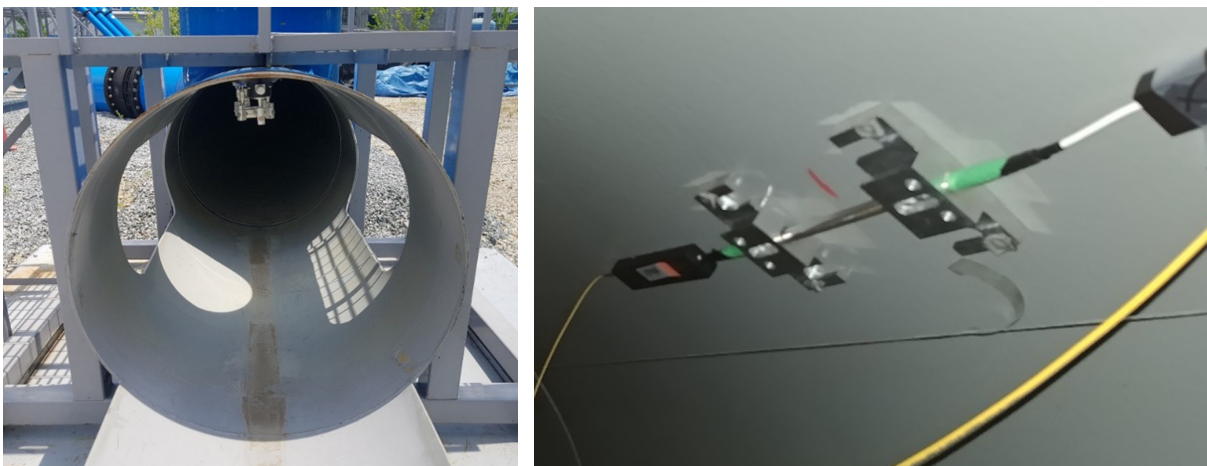


Fig. 5 picture of installation for fiber optic strain sensor at internal pipeline



Fig. 6 picture of Load testing using sandbag and monitoring system using displacement sensor at exposed pipeline

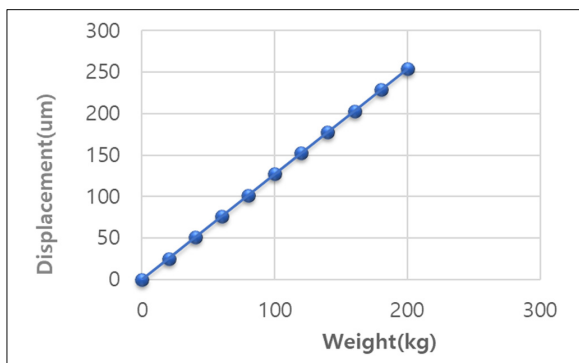


Fig. 7 result of weight versus displacement sensor

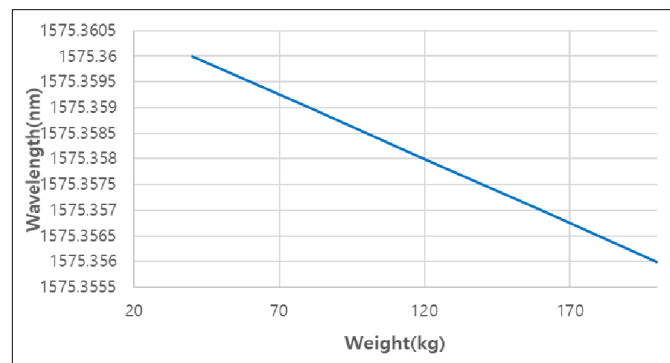


Fig. 8 result of weight versus wavelength shift

the pipe after applying incremental loads to determine the pipe displacement according to the load acting in the gravity direction of the pipe.

As shown in Fig. 5, the equipment was designed, considering the overall conditions in the pipe such that the fiber-optic strain sensor could be installed inside a 1 m diameter pipe (1,000 mm diameter steel-coated pipe for water supply (KSD 3578)). Tests were conducted to measure the deflection displacements of the exposed pipe. The fiber-optic sensor was installed inside the pipe, the span between the supports of the pipe was fixed, and the changes in stress owing to increased load were measured. Fiber-optic strain sensor and displacement sensor-installed tests were carried out to determine the changes in the strain and displacement generated in the pipe. A fiber-optic strain sensor was installed at the upper center of the 1 m diameter pipe, and the span of the pipe supports was maximized.

Incremental measurements were performed to generate external loads at the upper part of the pipe using 10 sandbags weighing 20 kg each. A displacement sensor was installed at the lower part of the center to determine the deflection due to loading. Fig. 6 shows the displacement sensor installed at the lower part of the pipe.

From the measurements, as shown in Fig. 7, when a 200 kg load was applied to the center, a deflection of 254 μ m occurred, which changed sequentially as the load was increased in steps of 20 kg.

The following are the strain results of the fiber-optic sensor internally installed at the upper part when the same load was applied. They describe the results for incrementally applied and removed 20 kg sandbags at the upper center of the exposed pipe. As shown in Fig. 8, when a 200 kg load was applied, a 5 pm change in wavelength occurred. As shown in Fig. 4, because the installation direction of the strain sensor was towards the upper part of the pipe, the strain varied owing to bending at the upper part of the pipe when a load was applied. Additionally, the behavior in which the space between the sensors narrowed according to the degree of bending was observed. Thus, the wavelength, which indicated the strain, was expressed as the change from the reference wavelength to the short wavelength. These test results confirmed that a maximum of 3.5 microstrains was generated, compared to when no load was applied.

4. Load Test Using Fiber-optic Strain Sensor in Buried Pipe

As depicted in Fig. 9, a strain sensor was installed inside the buried pipe to measure the stress in the buried pipe, and the load received when 8-ton heavy equipment (truck) moved on the surface was measured. First, the heavy equipment performed four sets of forward, stop, and reverse operations, and the strain was measured using a

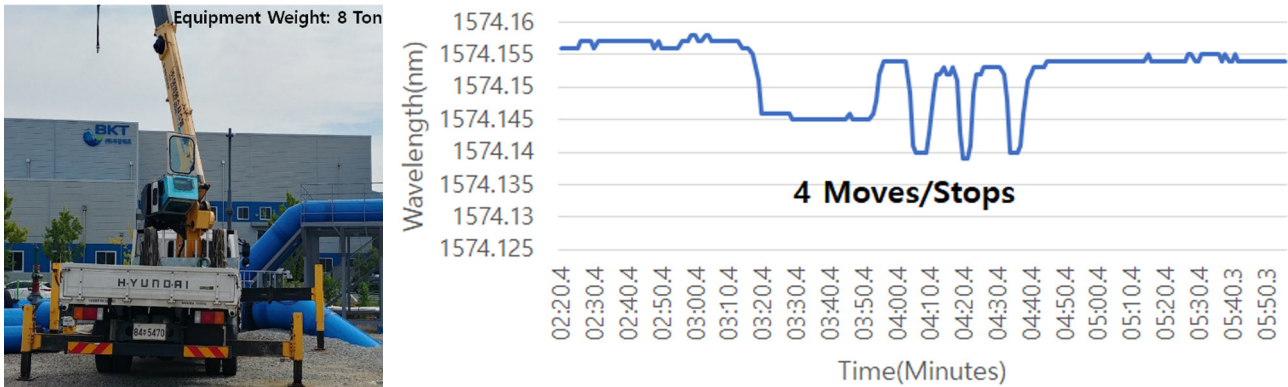


Fig. 9 picture and test result of load testing using weight of 8 t truck at buried pipe

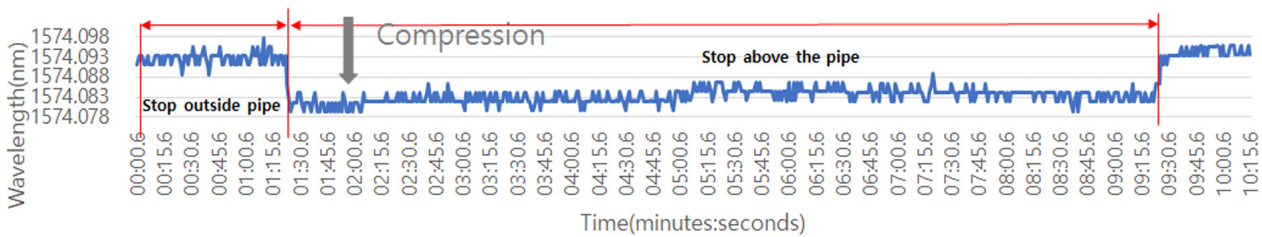


Fig. 10 test result of load and unload testing using weight of 5.88 t pork crane (Excavator) at buried pipe

fiber-optic strain gauge. A 15 pm optical strain was measured on the inside, which corresponded to 10 microstrains.

As depicted in Fig. 10, the load received by the buried pipe installed with a strain sensor when an excavator moved on the surface was measured to determine the stress in the buried pipe. The excavator was stopped outside the pipe, started, stopped on the pipe, and then moved, and the fiber-optic strain gauge was used to measure the strain before and after the excavator operations. The excavator performed a set of movement operations, and the strain was measured using the fiber-optic strain gauge. A 10 pm optical strain was measured on the inside, which corresponded to 7 microstrains. This result was determined based on the compressive force.

Fig. 11 shows a photograph of the 5.88-ton excavator used for the experimental tests, and the diagram indicates the movement direction of the excavator on the buried pipe. The excavator was moved such that eccentricity existed at a direction of 45° of the buried pipe

installed with the strain sensor. A strain sensor was installed inside the buried pipe to obtain the stress in the buried pipe, and the load received when the 5.88-ton excavator moved on the surface was measured.

This Fig. 11 shows the measurement environment where the excavator was moved on the part of the buried pipe installed with the strain sensor to measure the buried pipe stress.

As shown in Fig. 12, a 12 pm optical strain was measured inside the pipe using the fiber-optic strain gauge, which corresponded to 8 microstrains. This result was measured as a tensile force in Fig. 12. The previous test results in Fig.10 showed that when the load was applied, due to the behavior in which the strain changes because of bending and the shorting of the space between the sensor based on the 45° of bending in Fig. 11, the wavelength was expressed as the change from the reference wavelength to the short wavelength and was measured as a compression value. For the test results in case of Fig. 12, however, it was measured from the reference wavelength to the



Fig. 11 test result of unbalanced load (45° direction) testing using weight of 5.88 t pork crane at buried pipe

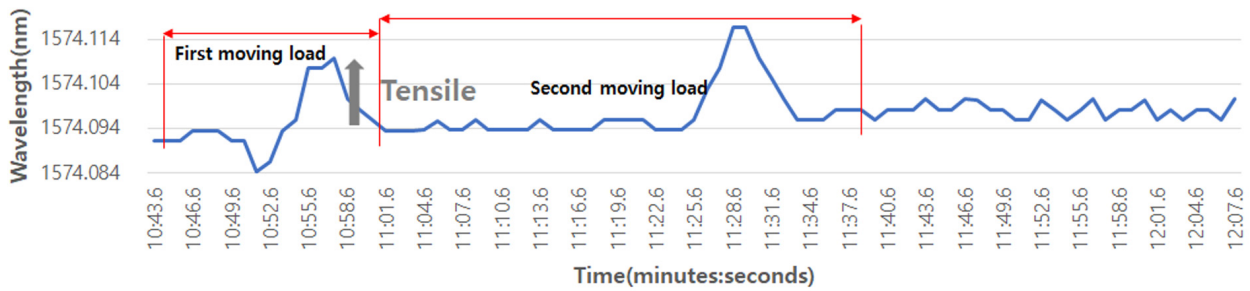


Fig. 12 Results of shift / stop unbalanced (45-degree direction) load testing of buried pipelines



Fig. 13 Test of moved impact load on buried pipelines

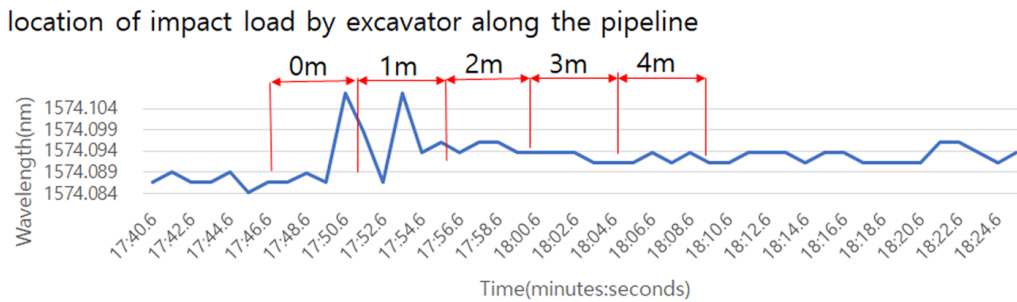


Fig. 14 result of moved impact load by excavator on buried pipeline

long wavelength, which resulted in more extended tension than the reference wavelength.

Fig. 13 shows the measurement environment where the excavator was moved on the part of the buried pipe installed with the strain sensor. In this case, digging operations were performed to determine the influence of third-party construction on the buried pipe. The excavator performed one set of movement operations and moved in 1 m increments away, including the vertical pipe centerline. After incrementally operating the excavator while moving up to 4 m, it performed three digging operations for each position, and the fiber-optic strain gauge was used to measure the strain at each position.

Fig. 13 depicts the 5.88-ton excavator used for the experiment, and the diagram indicates the movement direction of the excavator on the buried pipe and three digging operations. Fig. 14 is a graph of the measurements of the fiber-optic strain sensor installed in the buried pipe section. In terms of the maximum value measured inside the pipe, when three digging operations were performed on the vertical central

axis of the pipe, an optical strain of 20 pm occurred, which corresponded to 14 microstrains. This result was determined as a tensile force. When digging was performed 1 m from the central axis of the buried pipe, the magnitude slightly decreased. Subsequently, because of the sharp decrease in the signal from a 2 m distance, it was difficult to identify the impact of the load. Based on the test results, as the strain caused by the digging increased, it was measured from the reference wavelength to the long wavelength. As this was longer than the reference wavelength, tensile forces were generated.

5. Conclusions and Future Research

Buried pipes are continuously impacted by external loads, such as soil pressure, vehicles, and ground settlement; in particular, pipes buried in the soft ground are known to be significantly influenced by ground settlement. Soft grounds have complex characteristics owing to their engineering properties, and when the ground has low strength and

Table 1 Test results summary of exposed and buried pipeline for load test using fiber optic strain sensor

	Exposed pipeline	Buried pipeline	note
Pipeline dimension	1,000 mm diameter, carbon steel pipes with coated for water works (KS D 3578)		
Installed sensor type	Fiber optic strain and displacement sensor	Fiber optic strain sensor	No installed buried pipeline with displacement sensor
Measurement speed	1 Hz (Static)	100 Hz (Dynamic)	Static/Dynamic load Testing
Testing condition	Static load	Static load / Moving load / Impact load by excavator	
Testing load	20 ~ 200 kg [10 step]	8 t, 5.88 t [2 type]	
Wavelength shift (strain) of static testing result	5 pm @ 200 kg (about 3.5 micro strain)	15 pm @ 8 t (about 10 micro strain)	
Wavelength shift (strain) of dynamic testing result	-	20 pm @ within 1 m location (about 14 micro strain) Detected impact load at buried pipeline around about 2 m	

extended depth, large deformations occur, e.g., settlements. In this study, tests were performed using fiber-optic strain sensors and measurement devices installed in actual-scale pipes to investigate the characteristics of the ground and to identify the presence of abnormalities in the pipes. Table 1 lists a summary of the results of the load tests for large exposed and buried pipes using a fiber-optic strain sensor.

Fiber-optic sensors were used in this study to measure loads that may occur in an environment similar to loading conditions that act on actual pipes. The installation method and the structure of the fiber-optic strain sensor were applied, considering the piping environment of buried pipes and large pipes in actual use. Load tests were performed using a displacement sensor and sandbags, and linear measurement results were obtained. A test method was presented considering the conditions that may occur in actual pipes, and the strains generated in the buried pipes were measured. Tests were conducted to simulate actual pipe conditions by using a truck and an excavator to perform operations, such as movement and digging, with loads of 8 and 5.88 tons. The results of each test confirmed the phenomena that represent the characteristics that may occur in the field.

By comparing the optical strain of 10 pm measured under a load condition of 5.88 tons above buried pipe ground with an optical strain of 5 pm measured under a load condition of 200 kg on the exposed pipe and the load characteristics, a difference of approximately 15 times was obtained. Through these tests, the resolution of the fiber-optic strain sensor installed in the pipe could perform measurements of 3.5 microstrains or less. These results indicate that this technique can be used to identify the presence of abnormalities in pipes that occur during transportation in various application fields.

Regarding the future research directions, particularly in digging construction including buried pipes and third-party construction, the technique can be developed to detect variations in pipes in caved-in roads owing to leakage and to examine the characteristics of Siberian

pipelines, where there is soft ground in a swampy environment because of seasonal changes in summer and winter. In addition, the technique can be applied to pipes in the oil and gas industry that are difficult to access and pipes that change due to the continuously changing characteristics of the ground after the completion of casing work in drilling.

Acknowledgments

This study was funded by Korea Ministry of Environment (MOE) as Service Program for Demand-Responsive Water Supply. (grant No. 127589)

References

- Culshaw, B., & Kersey, A. (2008). Fiber-Optic Sensing: A Historical Perspective. *Journal of Lightwave Technology*, 26(9), 1064-1078.
- Meltz, G., Morey, W.W., & Glenn, W.H. (1989). Formation of Bragg Gratings in Optical Fibers by Transverse Holographic Method. *Optics Letters*, 14(15), 823-825. <https://doi.org/10.1364/OL.14.000823>
- Hill, K.O., & Meltz, G. (1997). Fiber Bragg Grating Technology Fundamentals and Overview. *Journal of Lightwave Technology*, 15(8), 1263-1276. <https://doi.org/10.1109/50.618320>
- Jeong, S.Y., Hong, S.K., & Choi, W.M. (2017). Monitoring for Buried Gas Pipelines Using Optical Fiber Sensor under Roller Vibration. *Proceeding of Korean Society of Civil Engineers*, 2017. 13-14.
- Lee, J.H., & Kim, D.H. (2016). Application of Fiber Optic Sensors for Monitoring Deflection and Deformation of a Pipeline. *Journal of the Korean Society for Nondestructive Testing*, 36(6), 460-465. <https://doi.org/10.7779/JKSNT.2016.36.6.460>
- Hong, S.K., Kim, J.H., & Jeong, S.Y. (2006). Stress Monitoring System for Buried Gas Pipeline in Poor Ground. *Journal of the Korean Society of Safety*, 21(1), 41-47.

- Ryu, Y.S., Cho, H.M., & Kim, Y.B. (2017). Evaluation of Structural Behavior of Buried Pipes Considering Location of Surcharge Load and Buried Depth. *Journal of the Korean Society of Hazard Mitigation*, 17(2), 231-236. <https://doi.org/10.9798/KOSHAM.2017.17.2.231>
- Lee, M., & Kim, H. (2011). Latest Development Status of FBG Sensors & Interrogator from Korea & Other Countries. *Journal of Korean Society of Civil Engineers*, 59(2), 84-90.
- International Electrotechnical Commission. (2016). *Fibre Optic Sensors - Part 1-1: Strain Measurement-Strain Sensors Based on Fibre Bragg Gratings (IEC 61757-1-1)*.

Author ORCIDs and Contributions

Author name	ORCID	Contributions
Chung, Joseph Chul	0000-0003-3240-0407	①③④
Lee, Michael Myung-Sub	0000-0001-6483-7895	⑤
Kang, Sung Ho	0000-0002-5817-0024	②

- ① Conceived of the presented idea or developed the theory
- ② Carried out the experiment or collected the data
- ③ Performed the analytic calculations or numerical simulations
- ④ Wrote the manuscript
- ⑤ Supervised the findings of this study

Estimation of Penetration Depth Using Acceleration Signal Analysis for Underwater Free Fall Cone Penetration Tester

Jung-min Seo¹, Changjoo Shin², OSoon Kwon³, In Sung Jang⁴,
 Hyoun Kang⁵ and Sung Gyu Won⁶

¹Full-time Research Specialist, Korea Institute of Ocean Science & Technology, Busan, Korea

²Senior Research Scientist, Korea Institute of Ocean Science & Technology, Busan, Korea

³Principal Research Scientist, Korea Institute of Ocean Science & Technology, Busan, Korea

⁴Principal Research Scientist, Korea Institute of Ocean Science & Technology, Busan, Korea

⁵Full-time Research Specialist, Korea Institute of Ocean Science & Technology, Busan, Korea

⁶Technical Director, Vibroacoustics Total Solution, Busan, Korea

KEY WORDS: Free fall cone penetration tester, Geotechnical properties, Penetration depth, Acceleration, Acceleration integration

ABSTRACT: A track-type underwater construction robot (URI-R) was developed by the Korea Institute of Ocean Science & Technology. Because URI-R uses tracks to move on the seabed, insufficient ground strength may hinder its movement. For smooth operation of URI-R on the seabed, it is important to determine the geotechnical properties of the seabed.

To determine these properties, standard penetration test (SPT), cone penetration test (CPT), and sampling are used on land. However, these tests cannot be applied on the seabed due to a high cost owing to the vessel, crane, sampler, and analysis time. To overcome these problems, a free fall cone penetration tester (FFCPT) is being developed.

The FFCPT is a device that acquires the geotechnical properties during impact/penetration/finish phases by free fall in water. Depth information is crucial during soil data acquisition. As the FFCPT cannot measure the penetration depth directly, it is estimated indirectly using acceleration. The estimated penetration depth was verified by results of real tests conducted on land.

1. Introduction

The Korea Institute of Ocean Science & Technology has developed the track-type underwater construction robot, URI-R. As shown in Fig. 1, the URI-R is a track-type equipment that moves and excavates on the seabed and can be used up to a maximum depth of 500 m. It can trench up to depth of 2.5 m and width of 0.6 m. The weights of the URI-R in air and water are 38 t and 32 t, respectively. Insufficient ground strength of the seabed can make it difficult to move or trenching work. Therefore, it is critical to obtain the geotechnical properties of the seabed for the smooth operation of the URI-R.

On land, in-situ or lab tests are performed using samples to determine the geotechnical properties (Jang, 2015). For in-situ tests, standard penetration tests (SPTs) or cone penetration test (CPTs) are mainly used. The SPT determines the geotechnical properties by measuring the hit count required to cause the penetration of a rod to a



Fig. 1 Underwater construction robot URI-R

depth of 30 cm through the repeated falling of a hammer (standard weight of 63.5 kg) from a height of 76 cm from the knocking head, which is the hitting point (Lee, 2008). A CPT measures the tip resistance, sleeve friction, and pore pressure while continuously penetrating a cone probe sensor into the ground at a constant rate of 20 mm/s. The test is terminated when penetration becomes impossible due to contact with a hard layer (Rogers, 2011). When sampling is required, samples are acquired from the test site using a sampler and then analyzed in the

Received 27 August 2019, revised 20 March 2020, accepted 9 April 2020

Corresponding author Changjoo Shin: +82-51-664-3563, cjshin@kiost.ac.kr

© 2020, The Korean Society of Ocean Engineers

This is an open access article distributed under the terms of the creative commons attribution non-commercial license (<http://creativecommons.org/licenses/by-nc/4.0>) which permits unrestricted non-commercial use, distribution, and reproduction in any medium, provided the original work is properly cited.

laboratory. When the above-mentioned methods, which are conventionally used on land, are used to determine the geotechnical properties of the seabed a high cost is incurred because of the use of a vessel, crane, and sampler and a longer analysis time. Moreover, various issues such as the applicable depth also need to be considered.

To overcome these problems, Marum (Stegmann et al., 2006) and Rolls-Royce (Brown et al., 2010), among others, have produced free fall cone penetration testers (FFCPTs). The FFCPT is a device that was developed by applying the CPT for land; it determines the geotechnical properties during impact/penetration/finish phases by free fall in water. The mobility of the URI-R can be determined instantly because the FFCPT and its ancillary equipment are smaller than the equipment used on land, the measurement data can be acquired on site and the geotechnical properties can be analyzed after recovering the device from the seabed to the ship. Furthermore, when a FFCPT for deep water can be conveniently used to acquire the non-drained shear strength, which is required for the design of deep sea offshore plant structures (Woor et al., 2018). Therefore, the Korea Institute of Ocean Science & Technology is developing a FFCPT to determine the possibility of stable operation of URI-R in the field.

To determine geotechnical properties, various ground data by the penetration depth is required. On land, the penetration depth and ground data can be obtained using various methods such as encoder, linear variable differential transformer (LVDT), and so on. However, it is difficult for the FFCPT to directly obtain the ground data synchronized with the penetration depth. Therefore, the penetration depth was indirectly estimated using acceleration signals, and the performance was verified by comparing the measurement and estimated depths through a land experiment.

2. Ground Penetration Behavior Characteristics of FFCPT According to Acceleration Changes

FFCPT is a device that determines geotechnical properties of the seabed by penetration depth, and it is critical to penetrate as deeply as possible and derive the penetrated depth. To achieve the maximum possible penetration depth of the FFCPT so as to maximize the falling inertia, it is advantageous to exclude components that interfere with free fall except the recovery wire (Shin et al., 2019). Furthermore, since it is difficult to directly measure the penetration depth of the FFCPT that collided with the seabed, we estimated it indirectly using the acceleration that acts in perpendicular direction to the ground. The acceleration $a(t)$ generated by the FFCPT behavior can be converted to velocity $v(t)$ and displacement $s(t)$ through integration (Yang et al., 2016) as follows:

$$v(t) = v_0 + \int_0^{t_f} a(t) dt \quad (1)$$

$$s(t) = s_0 + \int_0^{t_f} v(t) dt \quad (2)$$

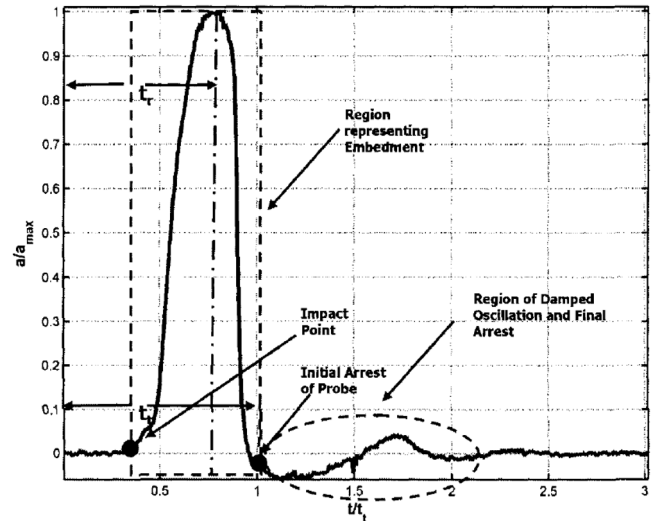


Fig. 2 Acceleration event cases before & after impact

where v_0 is the initial velocity, s_0 is the initial displacement, and t_f is the final arrested time.

The time points for the integral section can be selected by 0 as at the moment of impact and t_f as the final arrested time. In addition, when the selected acceleration integral section is reversed and integrated, v_0 can be assumed to be a stopped state after penetration ($v_0 = 0$) and $v(t_f)$ as the penetration velocity when the FFCPT hits the ground. When the calculated $v(t)$ is reversed and integrated again, s_0 can be assumed to be the depth at the moment when the FFCPT hits the ground and penetration starts ($s_0 = 0$), and $s(t_f)$ as the final penetration depth after the penetration behavior finishes.

McCarty examined the ideal acceleration trend that occurs when an object collides with a random medium as shown in Fig. 2 (McCarty and Carden, 1962). The behavior of the object colliding with a medium appears in five phases: impact, penetration, initial finish, reaction, and final finish. In Fig. 2, the point where the acceleration slope changes sharply is the impact (phase 1). After impact, penetration (phase 2) starts, and the penetration velocity sharply decreases until the maximum acceleration occurs. In the section from the maximum acceleration to the initial finish, the penetration velocity decreases relatively slowly compared to that of the previous section; then, the initial finish (phase 3) occurs. After that, the object moves in reverse direction by the reaction (phase 4). After the first reaction, the object behavior can be changed depending on the properties of the medium, and lastly, the final finish (phase 5) occurs. The FFCPT (object) developed in this study penetrates (impacts) the seabed (medium) and finishes in the ground and can be expected to behave similarly to that shown in Fig. 2.

3. FFCPT Configuration

3.1 Mechanical Part

As shown in Fig. 3, the FFCPT is composed of an electronic part for data measurement and storage, a cone probe which is a sensor for

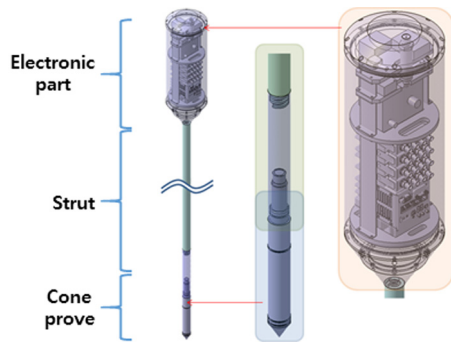


Fig. 3 Configuration of FFCPT

measuring the geotechnical properties, and a strut which acts as a structure support interconnecting the electronic part and the cone probe. The strut can be extended in 1 m units and ranges from 1 m to 3 m.

The electronic part is composed of a data acquisition (DAQ) device for signal measurement and data storage, a sensor and conditioner for measuring acceleration signals, a power battery, and a pressure sensor. Fig. 4(a) shows the assembly inside the electronic part. The pressure-resistant container in which the electronic part is mounted acts as a buoyancy material in the water. The buoyancy center of the total structure is designed to be higher than the center of gravity to achieve stability during the fall in the water. The distance between the buoyancy center and the center of gravity is 21 cm when the strut is 1 m, and 60 cm when the strut is 3 m. Fig. 4(b) shows the upper link, an intermediate structure that interconnects the electronic part at the top and the strut at the bottom. The upper link is a cone with a bottom diameter of 3.6 cm and a top diameter of 18 cm. The impact from the strut is dispersed in the pressure resistant container. Fig. 4(c) and (d)

show the strut and lower link, respectively. The strut is a hollow rod structure with a 1 m screw thread with a hole on the side of the rod so that the inside of the strut will be filled with water while immersed in the water. Once the strut is filled with water, the buoyancy change of the total structure can be minimized even if the strut length is changed. The lower link is an intermediate structure that interconnects the strut and cone probe, which have different thread shapes. The cone probe at the bottom is connected with the electronic part via a cable, and it also prevents the cable from breaking away under impact.

3.2 Electronic Part

Sensors and the DAQ system were composed as shown in Fig. 5 to determine the geotechnical properties data as the FFCPT penetrated the seabed. The cone probe is a sensor complex for collecting geotechnical properties data and can simultaneously measure the cone tip resistance value, main surface frictional resistance, penetration gap water pressure, and slope. NI cRIO-9033 was used for the DAQ, PCB 3711B1150G for the acceleration sensor, and Omega PX409-750G10V for pressure sensor to measure the depth. To capture the accurate acceleration signals, an analog digital convertor (ADC) with 24 bit resolution was used, and a sampling frequency between 1.6 and 51.2 kHz was selected by the user. It can be used continuously for 8 h when fully charged using a 10,000 mAh battery.

4. Experiment and Results Analysis

The estimated penetration depth performance of the FFCPT using acceleration signals was verified through a land experiment. There are two main differences between underwater and land experiments. First,

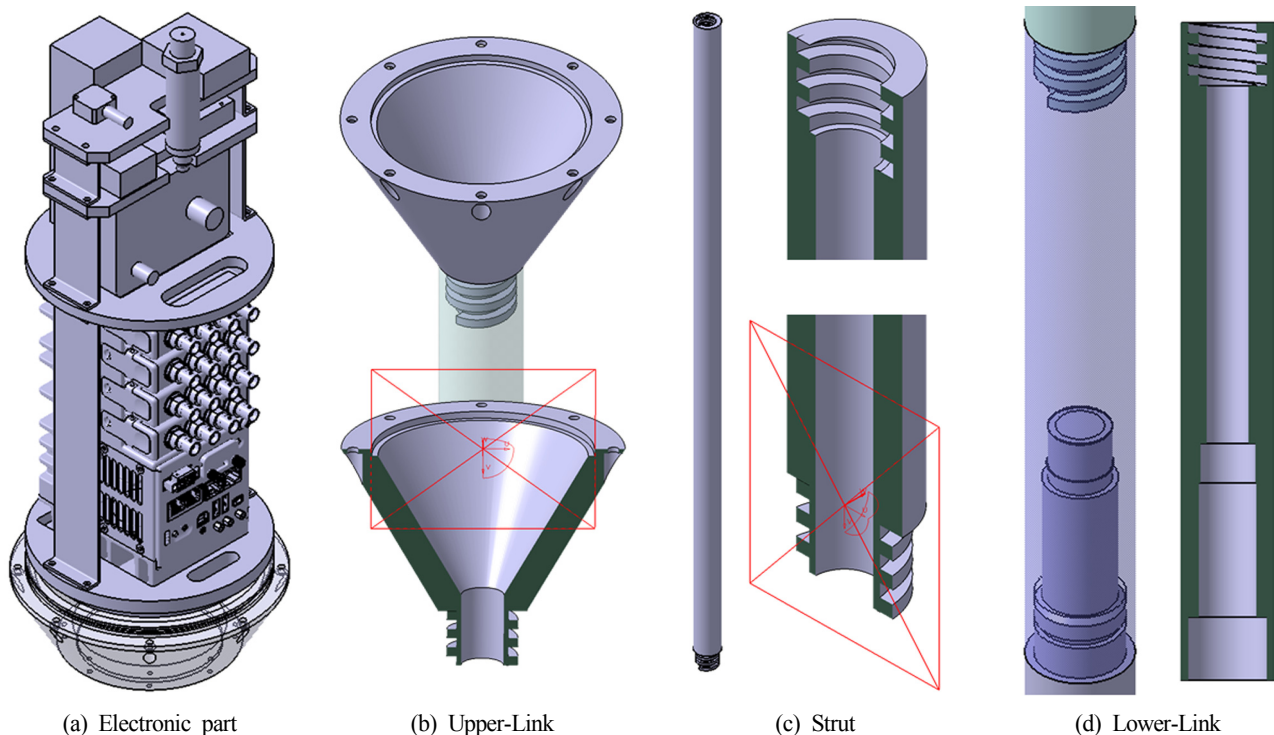
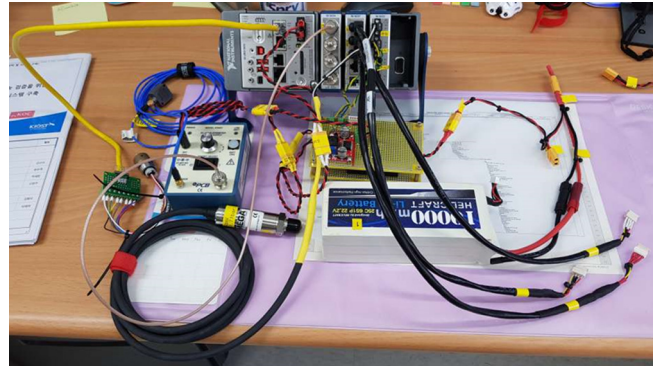


Fig. 4 Detailed design of each components



(a) Cone probe sensor



(b) DAQ system

Fig. 5 Sensors and DAQ system

a difference in the FFCPT terminal speed value occurs during the fall due to a difference in fluid density, which leads to a difference in penetration depth. However, the penetration process of the FFCPT after hitting the ground is identical to the process on land. Second, a strong horizontal force can be applied to the FFCPT during falling due to algae, etc. To verify this, an inclinometer was mounted in the FFCPT. Therefore, the slope of the FFCPT caused by a lateral force can be measured and the penetration depth can be estimated by reflecting it. To improve the precision of the experiment in this study, the FFCPT is set to discard the slope values exceeding $\pm 5^\circ$ during ground penetration. The dominant behaviors of the FFCPT, however, are almost identical between performance on land and underwater. Therefore, the penetration depth can be estimated through land experiment before underground experiment. The experiment was performed on a landfill ground near the Pohang Underwater Construction Robot Complex Demonstration Center. As shown in Fig. 6, using a crane the FFCPT moved by a certain distance from the ground, after then it fell freely. The penetration depth was measured when the behavior of the FFCPT was finally stabilized after it hit the ground. Then, the FFCPT was pulled out from the ground and the data stored in the DAQ was sent to the computer and analyzed. The data analysis program was created using NI Labview and the behaviors of the FFCPT were analyzed using acceleration signals.

The acceleration signals captured from the penetration experiment of the FFCPT at 1 m height are shown in Fig. 7. The FFCPT started falling from 24.513 s and the acceleration was -9.8 m/s^2 . The impact started at 24.988 s, and the FFCPT penetrated the ground, showing a sharply increasing acceleration curve. The maximum acceleration recorded in this penetration experiment was 152 m/s^2 , after which the acceleration showed a decreasing trend. The acceleration rising pattern appears at 25.013 s and 25.033 s, which occurs when the FFCPT hits a hard object in the ground during penetration. The initial finish occurred at 25.053 s and a reaction occurred simultaneously, thus changing the sign of the acceleration signals. The final finish of the FFCPT occurred at 25.103 s; however, the second impact of approximately 10 m/s^2 occurred at 25.133 s due to the gaps generated the assembly of the internal electric parts.



(a) FFCPT



(b) Before test

(c) After test

Fig. 6 Estimation of penetrated depth test

Based on the acceleration trend analysis in Fig. 2, the behavior section by impact was set to 24.988 – 25.103 s, and the calculation results estimated using Eqs. (1) and (2) were an initial penetration velocity of 4.6 m/s and a penetration depth of 0.163 m as shown in Fig. 8. The penetration depth measured in the field was 0.15 m, showing an error of 8.7%.

As shown in Table 1, measurements were performed at the falling heights of 1, 3, and 6 m and the results were compared with the estimated penetration depths. When the FFCPT was fell from a height of 6 m or higher, over-ranged acceleration signals were continuously captured. This was due to the landfill, which consisted of sandy soil from the surface to a depth of approximately 0.3 m and gravel below a

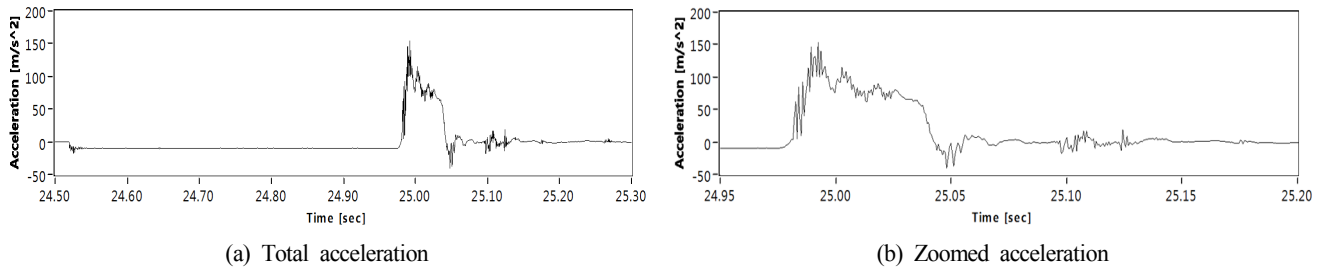


Fig. 7 Obtained acceleration signal during impact test

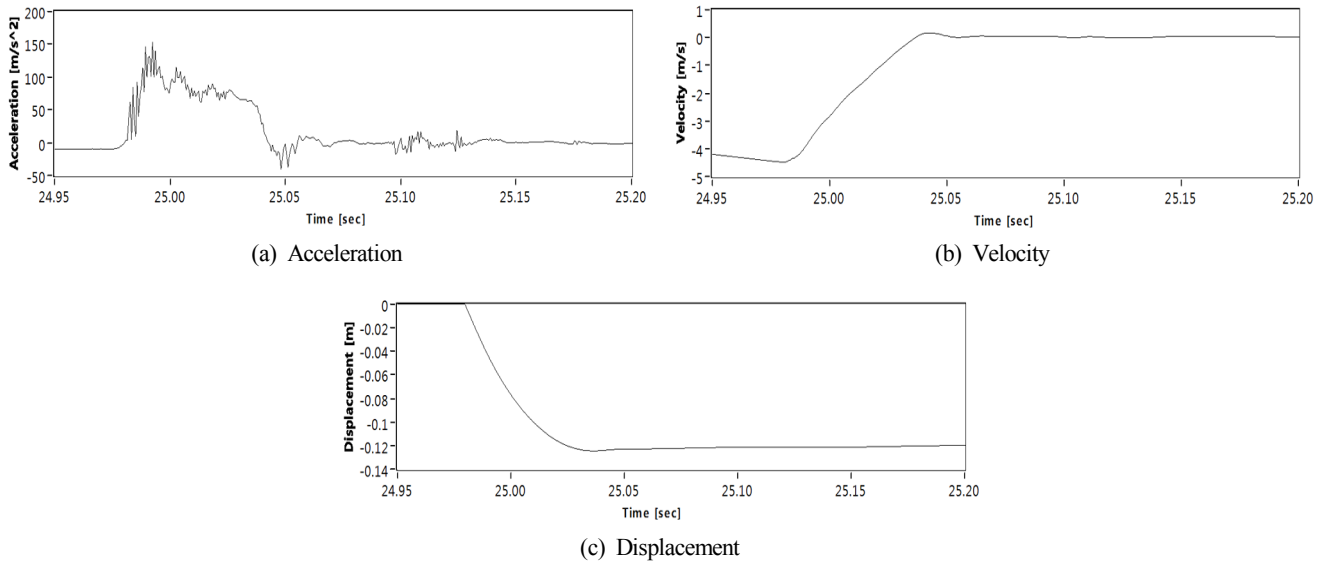


Fig. 8 Estimated results using selected acceleration

Table 1 Comparison of penetration depth results

Drop height (m)	Measured penetration depth (m)	Estimated penetration depth (m)	Inclination difference between Max. and Min. (degree)	Error (%)
1	0.150	0.163	0.9	8.7
3	0.230	0.235	1.4	2.2
3	0.250	0.248	1.1	0.8
6	0.270	0.267	2.2	1.1
6	0.275	0.280	0.6	1.8

depth of 0.3 m. When the FFCPT was fallen from a 6 m height, the maximum measured penetration depth was 0.275 m, and hence fall experiments could not be performed at higher heights. Effective values could be obtained because the ground penetration slope during the fall experiment was within the range of $\pm 5^\circ$. The error of the penetration depth estimated through this experiment relative to the measurement was 2.9% on average.

5. Conclusion

The estimated penetration depth of the FFCPT under development to determine the geotechnical properties of the seabed was examined. The developed device estimated the penetration depth by integrating

acceleration signals. It was experimentally verified that the acceleration signals generated when the FFCPT hits the ground show the pattern of 5 phases: impact, penetration, initial finish, reaction, and final finish. Repeated fall ing tests were performed at different falling heights in the land experiment. The measured values and estimated values of the penetration depth were compared in this experiment, and the error of the estimated penetration depth relative to the measurement was 2.9% on average.

Acknowledgement

This study was supported by research grants from Korea Institute of Ocean Science and Technology(PE99832).

References

- Brown, C.J., Smyth, S., Furlong, A., King, G., Costello, G., Potter, P., & Melton, J.S. (2010). A Synergistic Approach to Improve Multibeam Backscatter Classification Methods for Geological/Habitat Mapping. Proceedings of the Hydro 2010 Conference, Rostock, Warnemunde, Germany.
- Jang, I.S. (2015). Global Trend about Seabed Type Drilling Robots. Korea Institute of Ocean Science and Technology. Retrieved July 2019 from https://kiost.ac.kr/cop/bbs/BBSMSTR_00000000331/selectBoardArticle.do;jsessionid=D21E3C7B49083C686D308CE7F1C3B7A8?nttId=16282&pageIndex=4&searchCnd=&searchWrd=
- Lee, S.-C. (2008). A study on the Estimation on Undrained Shear Strength and Preconsolidation Pressure Using N-Value Obtained from Standard Penetration Test. Graduate School of Korea Maritime University.
- McCarty, J.L., & Carden, H.D. (1962). Impact Characteristics of Various Materials Obtained by an Acceleration-time-history Technique Applicable to Evaluating Remote Targets. NASA Technical Report(NASA-TN-D-1269), University of Texas at Austin.
- Rogers, D. J. (2011). Fundamental of Cone Penetrometer Test (CPT) Soundings. Missouri University of Science and Technology. Retrieved July 2020 from <https://web.mst.edu/~rogersda/umrcourses/ge441/CPT-Soundings.pdf>
- Shin, C.J., Won, S.G., Kwon, O.S., Jang, I.S., Seo, J.M., & Kang, H. (2019). Estimation of Ground Penetration Depth for Underwater Free Fall Cone Penetration Tester. Proceeding of Korean Marine Robot Technology Society, Seoul, Korea, 62-64.
- Stegmann, S., Mörz, T. & Kopf, A. (2006). Initial Results of a New Free Fall-Cone Penetrometer (FF-CPT) for Geotechnical in Situ Characterisation of Soft Marine Sediments. Norwegian Journal of Geology, 86(3), 199-208.
- Woor, S.H., Lee, K., & Choung, J. (2018). Basic Design of Subsea Manifold Suction Bucket. Journal of the Society of Naval Architects of Korea, 55(2), 161-168. <https://doi.org/10.3744/SNAK.2018.55.2.161>
- Yang, Y., Zhao, & Y., Kang, D. (2016). Integration on Acceleration Signals by Adjusting with Envelopes. Journal of Measurements in Engineering, 4(2), 117-121.

Author ORCIDs and Contributions

Author name	ORCID	Contributions
Seo, Jung-min	0000-0001-6323-7783	②④
Shin, Changjoo	0000-0003-3370-8702	①③④⑤
Kwon, OSoon	0000-0003-2091-761X	①⑤
Jang, In Sung	0000-0001-5668-4315	⑤
Kang, Hyoun	0000-0003-3405-646X	②
Won, Sung Gyu	0000-0003-0995-8373	③

- ① Conceived of the presented idea or developed the theory
- ② Carried out the experiment or collected the data
- ③ Performed the analytic calculations or numerical simulations
- ④ Wrote the manuscript
- ⑤ Supervised the findings of this study

A Review of IOSS Design Standardization Technology for Aluminum Alloy Handrail of Offshore Platform

Yeon-Ho Kim^{1,5}, Joo-Shin Park², Hyun-Chang Shin³, Sung-Jun Kim⁴,
Dae-Kyeom Park⁸, Yeon-Chul Ha^{6,9} and Jung-Kwan Seo^{7,10}

¹Senior Manager, Offshore Topside Engineering Team, Samsung Heavy Industry Co. Ltd., Geoje, Korea

²General Manager, Ship and Offshore Research Institute, Samsung Heavy Industry Co. Ltd., Geoje, Korea

³Principal Engineer, DNV-GL Busan, Korea

⁴General Manager, GHI, Yeung-am, Korea

⁵Ph.d Student, Department of Naval Architecture and Ocean Engineering, Pusan National University, Busan, Korea

⁶Associate Professor, Department of Naval Architecture and Ocean Engineering, Pusan National University, Busan, Korea

⁷Professor, Department of Naval Architecture and Ocean Engineering, Pusan National University, Busan, Korea

⁸Senior Researcher, The Korea Ship and Offshore Research Institute, Pusan National University, Busan, Korea

⁹Associate Professor, The Korea Ship and Offshore Research Institute, Pusan National University, Busan, Korea

¹⁰Professor, The Korea Ship and Offshore Research Institute, Pusan National University, Busan, Korea

KEY WORDS: Liquefied natural gas, Integrated offshore standardization specification, Offshore standardization, Bulk material, Aluminum alloy tertiary Structure, Handrail, Joint industry project (JIP)

ABSTRACT: The Integrated Offshore Standard Specification (IOSS) involves Korean shipyards, classification societies, research institutes, the Korean industrial society, engineering companies, and oil companies with the objective of reducing costs and risks without compromising safety in international offshore engineering procurement construction (EPC) projects using new standardized bulk components and qualification procedures. The activities of the IOSS include the analysis of the existing rules and regulations to achieve the best standardization, which is reflected in the best practices, and minimize the variables in regulations and rules. In addition, a standard inventory of shapes and dimensions, referred to as specifications, is proposed in the IOSS. In this paper, the aluminum tertiary standardization part (IOSS S102-1/2 S104: Specification for Structural Tertiary Design) is presented with the details of the procedures, background reviews, and cost-benefit analyses of the design and verification methods for standard designs in the IOSS standardization items. Based on the cost-benefit analysis, the application of standardized aluminum tertiary items to offshore projects has significant advantages in terms of maintenance and repair compared to the carbon steel tertiary items utilized in current industrial practices.

1. Introduction

The demand for liquefied natural gas (LNG) is continuously rising owing to stricter environmental regulations and unstable oil prices. To satisfy this demand, various types of LNG production facilities are being built. LNG storage facilities must be able to process cryogenic/high-pressure and liquefied gas; as such, diverse safety designs are being reviewed, including not only the structural strength in extreme operating environments but also the application of risk-based design techniques concerning life, environment, and property.

In floating LNG production facilities in particular, unlike facilities on land, the weight of the upper structure is limited considering the storage capacity and buoyancy of the lower floating structure. Researchers are making various attempts to reduce weight. However, in the case of the primary and secondary members that require strength and toughness to withstand a variety of extreme environments and operating conditions, precise material and strength design standards must be applied for structural safety, and there are difficulties for achieving innovative weight reduction. As the tertiary member is a non-strength member, aluminum alloy steel, stainless steel, nickel ore, and composite materials are being investigated as effective

Received 6 January 2020, revised 9 April 2020, accepted 21 April 2020

Corresponding author Jung-Kwan Seo: +82-51-510-2415, seojk@pusan.ac.kr

© 2020, The Korean Society of Ocean Engineers

This is an open access article distributed under the terms of the creative commons attribution non-commercial license (<http://creativecommons.org/licenses/by-nc/4.0>) which permits unrestricted non-commercial use, distribution, and reproduction in any medium, provided the original work is properly cited.

alternatives to carbon steel in terms of functional requirements and large-scale use.

Among these materials, aluminum alloy is widely known as an eco-friendly material with a high weight-to-strength ratio and excellent corrosion resistance and workability. Its strength has been enhanced, gradually increasing its applicability as a structural material. However, aluminum tertiary members lack standardized product production and design criteria and quantitative comparisons with carbon steel members. Consequently, owing to differences in manufacturers' product designs, there are many difficulties in applications to actual projects, and the application cases are extremely limited.

Accordingly, to strengthen the shipbuilding industry's technological competitiveness and gain market advantages, researchers have expressed the need for a systematic design standardization, identifying the trends and devising response strategies regarding international standardization, and developing standards for eco-friendly ships in the future (Cha, 2009; Kim et al., 2009). In addition, the studies have identified the major factors that weaken the price competitiveness. They are the low localization rate of key equipment and materials caused by limited business models, an industrial structure focused on offshore platforms, and inadequate technical capabilities such as in front-end engineering design (FEED). These have been consistent issues in the Korean offshore facility industry.

In terms of technology policies for strengthening the offshore facility industry's competitiveness, there are efforts to secure FEED engineering technology and source technology for key equipment and materials, cultivate talent, and develop supply and diffusion business models. For this purpose, it is necessary to create a new market for domestic shipbuilding and marine equipment companies in cooperation with the International Standards Organization (ISO) in connection with the International Maritime Organization (IMO), which is becoming a topic of international discussion, and to increase overseas marketing to enhance export competitiveness (Oh, 2017).

Accordingly, as part of the Integrated Offshore Standard Specification (IOSS) derived through a joint industrial research of the unified offshore standardization bulk package used by offshore facilities, this article presents the contents of the aluminum tertiary member design specifications (IOSS, 2019) and the results of the conducted applicability analysis.

2. Standardization of Aluminum Alloy Tertiary Member

2.1 IOSS Standardization Process

More than 200 shipbuilding-related items are registered as international standards (ISO); however, offshore structures have relatively few registered standards (ISO-TC67 / SC7) compared to other areas, and none are registered in the Korean Standard (KS). This is because the design standards for offshore platforms must apply project specifications that integrate not only the requirements of the installation area but also international standards and ordering

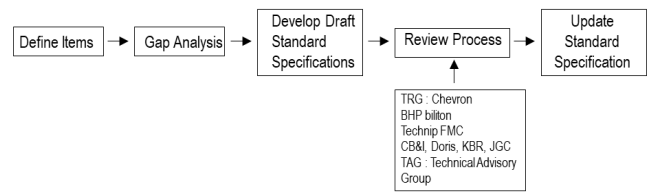


Fig. 1 IOSS Process

company/class requirements. Moreover, even for structures being operated in the same area with the same ordering company, different specifications are applied due to complex and inconsistent project requirements.

Therefore, in spite of standardization attempts applying various designs, there are difficulties in establishing standardizations owing to inconsistency between the standardization leader's goals and the direction of the participating companies. Accordingly, as shown in Fig. 1, this article presents a design standard plan, which is the result of establishing rational design standards through revision and reflection of the standards, defining the standardization items, and analyzing the differences in the rules and regulations applied to each item. It also presents an analysis-based standard proposal and a review of the technical review group/technical advice group (TRG/TAG) standards (Ellingsen et al., 2018).

2.2 Review of Standardized Items and Regulations

First, this study selected the items requiring standardization for the bulk materials used in offshore platforms considering the following three aspects: (1) possibility of cross-use through standardization, (2) possibility to solve problems that chronically arise in projects, and (3) comprehensive satisfaction of various rules and regulations. Based on these three aspects, the priority for development was set as presented in Table 1.

Table 1 Priority of development for IOSS activity

No	Item	Definition	Priority
1	Stair tower	DC5	1
2	Stair	DC5	1
3	Ladder	DC5	1
4	Grating	DC5	1
5	Access platform	DC5	1
6	Ramp way	DC5	3
7	Bridge	DC5	3
8	Handrail	DC5	1
9	Crane boom rest	DC5	Strength, Hardness
10	Green water protection	DC5	2
11	Dropped object protection	DC5	2
12	Radiation shield	DC5	Melting temp
13	Coaming	DC5	Chemical resistance
14	Drain box	DC5	Chemical resistance
15	Equipment support	DC5	Strength, Hardness
16	Radar master	DC5	2
17	Bollard	DC5	Strength, Hardness

Table 2 Identified standards

Name	Handrail	Stair	Vertical ladder
EN ISO	14122-3-2001/4/	14122-1-2001/2/ 14122-3:2001	14122-3-2001/5/
ANSI	A1264.1-2007/6/ S-002 2004, Rev4/8/	A1264.1-2007 S-002 2004, Rev4	A14.3-2008/7/ S-002 2004, Rev4
NORSOK	C-002 2006, Edition 3/9/	C-002 2006, Edition 3	C-002 2006, Edition 3/9/
AS	1657-2013/10/	1657-2013/	1657-2013

Table 3 Identified regulations

Name	Handrail	Stair	Vertical ladder
NMA	856/87 11/ 2318/86	856/87 11/ 2318/86	856/87 11/ 2318/86
PSA	PSA Facilities/12/	PSA Facilities	PSA Facilities
HSE	OTO 2001-069/13	OTO 2001-069	OTO 2001-069
OSHA	1910.23/14/	1910.21 1910.24	1910.26 1910.27

Second, in relation to the items requiring standardization, this study examined and analyzed various rules and regulations of the tertiary members applied to large offshore platforms manufactured within the past decade. Among the tertiary members of offshore platforms, four essential items used in large quantities for safety and convenience are handrails, stairs, vertical ladders, and gratings.

Furthermore, the relevant rules and regulations applying to these four items were classified in accordance with the international rules and regional regulations listed in Tables 2-3 (ISO, 2001a; ISO, 2001b; ISO, 2001c; ISO, 2004; NORSOK Standards, 2004; NORSOK Standards, 2006; ANSI/ASSE, 2007; ANSI, 2000; Australian Standard, 2013).

Therefore, to secure the persuasiveness of the integrated standard and a correct direction for the standard, this study performed a more detailed analysis of the related regulations and rules. Key design factors in terms of function and work safety were derived based on each rule and regulation, as presented in Tables 2 and 3, and the essential evaluation items for design are included in Table 4 with a detailed analysis.

According to the detailed specification analysis, in general, the classified rules and regulations did not differ significantly. Regarding

Table 4 Evaluation of requirements for handrails (continuation)

Parameter	Requirements in standard	Evaluation aspects	Recommended requirement
Height	EN ISO: Min. 1,100 mm ANSI: Min. 42" (1,100 mm) NORSOK: Min. 1,100 mm AS: Min. 900 mm	Sufficient height of handrails on platforms to prevent a fall from heights. NORSOK is an offshore standard as opposed to ANSI which is applied for general industries.	EN ISO NORSOK Min. 1,100 mm
Height on stair	EN ISO: 900-1,000 mm ANSI: 34"-38" (863-965 mm) NORSOK: Min. 1,000	Sufficient height of handrails on stairways to prevent a fall from heights NORSOK is an offshore standard as opposed to ANSI which is applied for general industries.	EN ISO NORSOK Min. 1,000 mm
Vertical opening	EN ISO: Max. 500 mm ANSI: Max. 21" (550 mm) NORSOK: Max. 380 mm AS: Max. 450 mm	Sufficiently narrow space to prevent a fall from height between rails The space of lowest course (between toe board and lowest Intermediate kneerail) should be less than upper space in order to reduce the risk for fall from heights through the lowest course.	NORSOK Max. 380 mm
Number of intermediate kneerail	EN ISO: Min. 1 ANSI: Min. 1 NORSOK: Min. 2 AS: Min. 1	Sufficiently narrow space to prevent a fall from heights through between rails. Additional Intermediate knee rail is also recommended to attach equipment on the top kneerail such as lighting, junction box. Attaching such equipment on the top rail is not allowed due to prevent accidental passage of a body part and attachment on the lower knee rails is also not allowed since this position is too low.	NORSOK Min. 2
Diameter	EN ISO: 25-50 mm ANSI: 1.25"-2" (32-51 mm) NORSOK: 25-50 mm AS: Max. 50 mm	Ergonomic design for holding hand to handrail.	EN ISO, NORSOK, AS ANSI (partly) 25-50 mm
Distance vertical stanchions	EN ISO: Max. 1,500 mm ANSI: Max. 8" (2,438 mm) NORSOK: Max. 1,500 mm	Maximum distance between vertical stanchions should be limited based on the stanchion anchoring strength and the fixing devices.	EN ISO, ANSI, NORSOK, NMA Max. 1,500 mm
Height of toe plate	EN ISO: Min. 100 mm ANSI: Min. 3.5" (89 mm) NORSOK: Min. 100 mm AS: Min. 100 mm	The solid toe plate at the bottom should be provided to prevent fall of minor objects.	EN ISO, NORSOK, ANSI, AS Min. 100 mm

Table 4 Evaluation of requirements for handrails

Parameter	Requirements in standard	Evaluation aspects	Recommended requirement
Vertical clearance btw. toe plate and floor level	EN ISO: Max. 10 mm ANSI: 0.25" (6 mm) NORSOK: Max. 10 mm AS: Max. 10 mm	The gap between the toe plate and the bottom should be minimized to prevent the fall of minor objects.	EN ISO, NORSOK, AS Max. 10 mm
Horizontal clearance btw. toe plates	ANSI: Max 1" NORSOK: continuous type AS: continuous type	The gap between the toe plates should be minimized to prevent fall of minor objects. However, the construction efforts to obtain no gap according to NORSOK are significant and considered disproportionate compared to the safety benefit.	NORSOK, AS, ANSI Continuous type or Max. 10 mm
Space btw two segments	EN ISO: 75-120 mm NORSOK: 75-120 mm	To prevent that hand is trapped in the clearing space between the segments.	EN ISO, NORSOK 75-120 mm
Sharp edges	EN ISO: Not allowed ANSI: Not allowed NORSOK: Not allowed AS: Not allowed	The ends of the handrail shall be designed to eliminate any risk of harm caused by sharp edges of the product or by catching of the user's clothing.	EN ISO, NORSOK, AS Not allowed

Table 5 Comparison of requirements of standards and regulations for handrail

Parameter	Standard (mm)				Regulation (mm)		
	EN ISO	ANSI	NORSOK	AS	PSA	NMA	OSHA
Handrail height	Min. 1,100	Min. 1,067	Min. 1,100	Min. 900 (1,100)	Ref. Norsok	1,000	1,067
Stair height	900 ~ 1,000	864 ~ 965	Min. 1,000		Ref. Norsok		762 ~ 863
Number of intermediate kneerail	Min. 1	Min. 1	Min. 2	Min. 1	Ref. Norsok	Min. 2	Min. 1
Vertical opening	Max. 500	Max 550	Max. 380	Max. 450	Ref. Norsok	Max. 380	Max. 534
Diameter	25 ~ 50	32 ~ 51	25 ~ 50	50	Ref. Norsok		Min. 38
Distance btw. stanchions	Max. 1,500	Max. 2,440	Max. 1,500		Ref. Norsok	Max. 1,500	2,440
Height toe plate	Min. 100	Min. 89	Min. 100 mm	Min. 100	Ref. Norsok		102
Toe plate vertical clearance	Max. 10	Max. 6	Max. 10	Max. 10	Ref. Norsok		6
Toe plate horizontal clearance		Max. 25.4	Continuous type	Continuous type	Ref. Norsok		Max. 25.4
Space btw. segments	75 ~ 120		75 ~ 120		Ref. Norsok		

Table 6 Recommended dimensions for handrails

Parameter	Guideline	Commendation and limitations
Height	Min. 1,100 mm	
Height on stair	Min. 1,000 mm	Not in compliance with ANSI: Min. 34° ~ Max. 38° (863-965 mm)
Vertical opening	Max. 380 mm, Max. 230 mm (Lower course)	
Intermediate knee rail	Min. 2 knee rails	
Diameter	Min. 25 mm ~ Max. 5 mm	Only partly in compliance with ANSI: 1.25" ~ 2" (32 ~ 51 mm)
Distance btw. vertical stanchions	Max. 1,500 mm	
Height of toe plate	Min. 100 mm	
Thickness of toe plate	6 ~ 10 mm	
Vertical clearance btw. toe plate and floor level	Max. 10 mm	Not in compliance with ANSI: Max. 0.25" (6 mm)
Horizontal clearance btw. toe plates	Continuous type (or Max. 10 mm)	NORSOK does not allow any gap
Radius of rounding	150 R	
Length of end segment from vertical stanchion	Max. 600 mm	
Space btw. two segments	Min 75 mm ~ Max 120 mm	
Sharp edges	Not allowed	

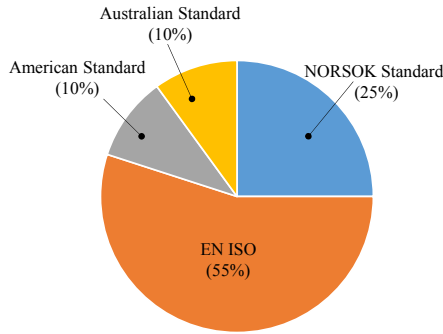


Fig. 2 Statistics of percentage to apply standards for offshore projects during last five years

handrails, which have the highest proportion of use and directly impact safety, there were some differences in the applied rules and regulations, as presented in Table 5, including handrail height, quantity of the intermediate kneerails, and toe plate height. This is primarily because the existing design methods were applied or special additional conditions of the project were applied based on international standards (ISO) (Ellingsen et al., 2018).

As shown in Fig. 2, the application rate within the past five years of the rules and regulations commonly used in offshore platform construction was simultaneously reviewed, and the handrail height was determined to be 1,100 mm considering the worker’s safety and work convenience. Table 6 presents a planned standard that comprehensively satisfies the existing related regulations of NORSOK S-002 (NORSOK Standards, 2004) and ISO 14122-1-4 (ISO, 2001a; ISO, 2001b; ISO, 2001c; ISO, 2004).

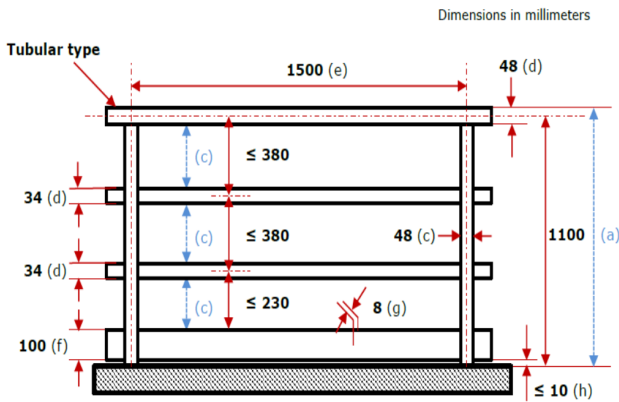


Fig. 3 Specification for handrail design

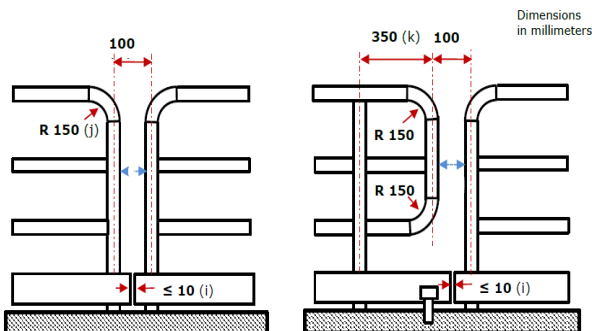


Fig. 4 Specification for handrail design

To minimize analytical errors in design and production by engineering companies, oil companies, and classification societies, which mainly arise when applying the rules and regulations, the standard was devised to avoid confusion during design, manufacturing, and inspection by providing accurate recommended guidelines and reference designs, as those shown in Figs. 3 and 4 (IOSS, 2019).

2.3 Design Applicability Analysis

In the third step, to examine the applicability of the standardized design based on the results of applications, this study reviewed the practical applicability of the verified standards in groups selected as TRG/TAG standards. The new standard established and implemented a systematic review process that minimizes risks such as delivery delays and deficits in real projects, as shown in Fig. 5, thus enhancing its completeness.

Each review process is divided into the proposal of the standard by the W/G members that comprise the classification societies, associations, and shipyards participating in the standard; a primary review by the W/G internal TAG members; and a secondary review by the major oil and engineering companies that are TAG members, thereby improving the quality of the devised standard and maximizing its integration.

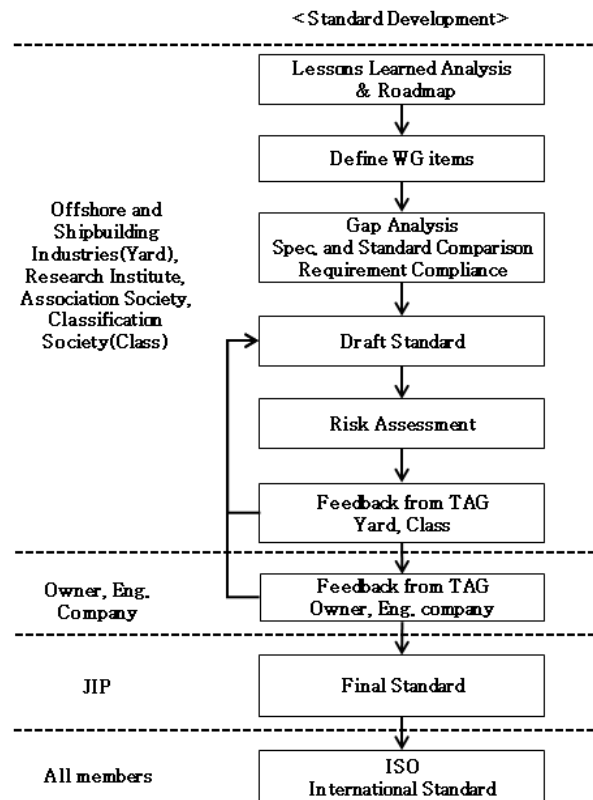


Fig. 5 IOSS standardization review process

2.4 Experimental Analysis of Handrail Standardization

To investigate the adequacy of the devised handrail design standard, this study performed an empirical experiment related to the test certification procedure of the product. In IOSS, the “Top mounted

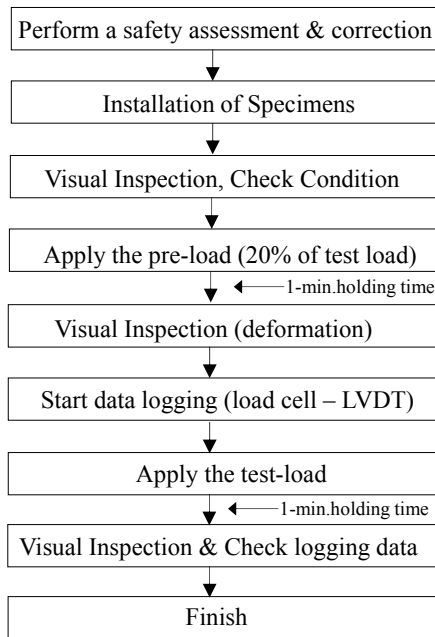


Fig. 6 Experimental test procedure

Table 7 Test condition of handrail

No.	Loading direction	Loading type	Load (kN)
Loading case 1		Distributed load	2.925
Loading case 2	Horizontal		
Loading case 3		Point load	1.3
Loading case 4	Vertical		

Note: Distributed load: $1.5 \text{ kN/m} \times \text{Rail length (Max. 1.5 m)} \times 1.3$ (Load factor) = Max. 2.925 kN, Point load: $1.0 \text{ kN} \times 1.3$ (Load factor) = 1.3 kN

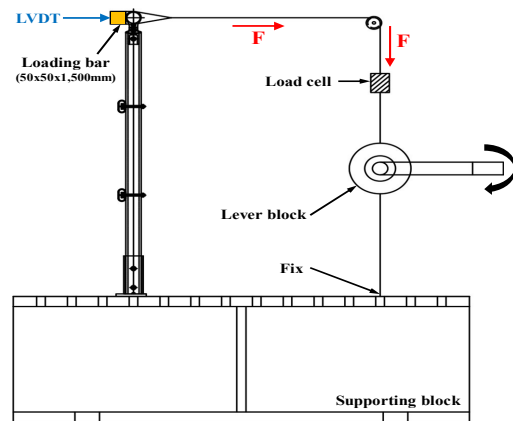
handrail in the case of inside coaming” was selected considering both the strength test procedure and strength characteristics required by the related regulations, and the applied load was determined considering the load conditions and safety factor defined in ISO and NORSOK.

Furthermore, an experimental test procedure was developed in which the experimental conditions for each member constituting the handrail were varied to investigate the structural safety that satisfies the use objective of the handrail, as shown in Fig. 6.

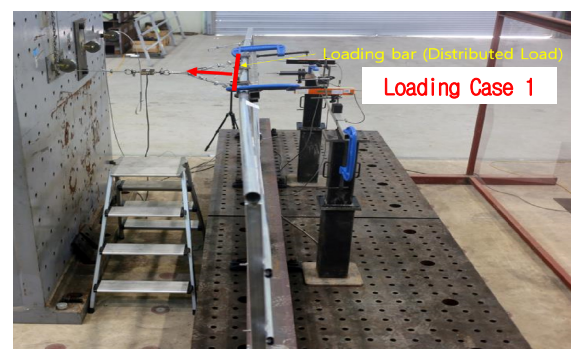
As shown in Figs. 7-9, the distribution and concentration loads were applied to the top-rail, Stanchion and mid-rail of the specimen by connecting the load cell and the lever/chain block. This test were reflected in the standard test procedure through schematics of the specimen top-rail, stanchion, and mid-rail.

As presented in Table 8, in terms of the test criteria, the occurrence of permanent deformation and cracking is not allowed and a maximum deformation of 30 mm under the test load conditions were proposed as the evaluation criteria, with reference to the maximum allowable strain and permanent strain defined in ISO and NORSOK.

For the experimental analysis of the standardization product, this study conducted an empirical verification of the handrail tertiary member standard, as shown in Figs. 8(b)-9(b). In particular, for

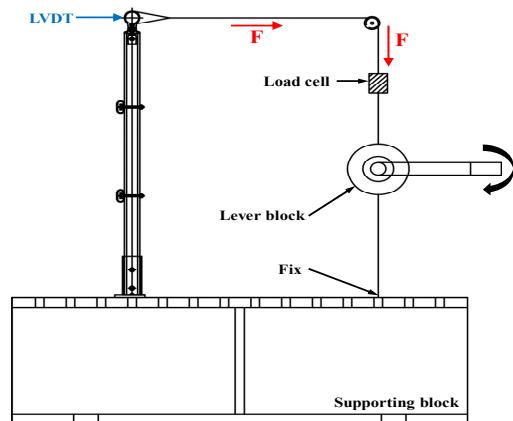


(a) Schematic test condition



(b) Experimental test condition

Fig. 7 Distributed load at a stanchion (Loading Case 1)



(a) Schematic test condition



(b) Experimental test condition

Fig. 8 Horizontal load at a stanchion (Loading Case 2 and 3)

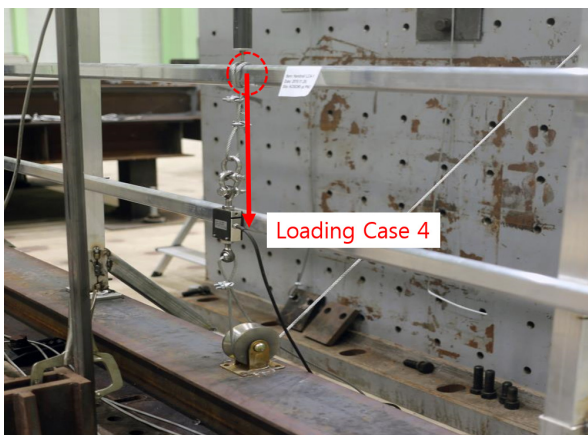
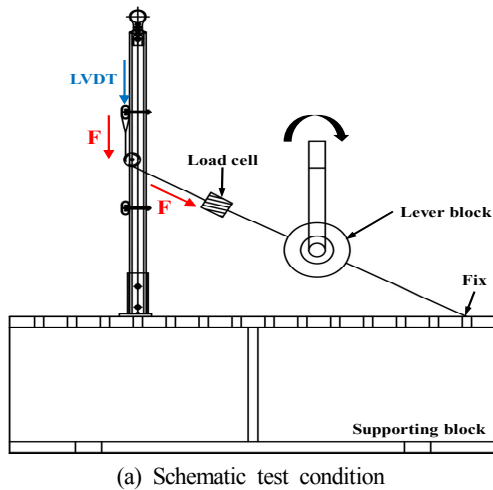


Fig. 9 Vertical load at a midpoint of handrail (Loading Case 4)

Table 8 Allowable criteria of the handrail under test condition

Items	Allowable criteria
Maximum deflection	30 mm
Permanent deflection	Not Allowed
Crack	Not visible cracks

products designed based on the manufacturer's numerical analysis, improvement plans reflecting the on-site installation environment and various manufacturing defects are being derived through experimental verification and are under review to be reflected in the standard.

In addition, regarding ISO and NORSOK standards based on the existing carbon steel, in the case of Loading Case 4, it was impossible to meet the different requirements of each project ordering company (e.g., safety chain fastening conditions for workers) through the existing individual design standards. However, it will be possible to effectively meet the design/production company requirements by reflecting them in the standardization product through the clear comparison and analysis of this experimental analysis method.

Accordingly, based on the standard test procedure and empirical test results, evaluation methods not only of the handrail but also of tertiary member item products derived from the JIP (Joint industry

project) are being reviewed and reflected in the IOSS design standards. This series of processes will serve as an important base technology for the technical completeness of new standards, improvements in product reliability, and enhanced technological competitiveness of manufacturers.

3. Cost-effectiveness Analysis

The developed standardization was applied to an actual project to verify its effectiveness regarding project cost reduction and whether it secured competitiveness. To this end, a large offshore platform manufactured and delivered in Korea was analyzed. Accordingly, a comparative analysis of the weight reduction effect and cost (material cost, manufacturing cost, maintenance cost) was conducted assuming that the IOSS aluminum standard was applied to the carbon steel handrail, stairs, and vertical ladders used in the project.

For comparison of the aluminum and carbon steel tertiary members, the carbon steel and aluminum unit weights were calculated as listed in Tables 9 and 10. Regarding the criteria, the handrail was calculated assuming it was continuous, with three rails, and excluding the stiffener weight, the vertical ladder was calculated without distinguishing between cage and non-cage ladders, and the stair was calculated based on the tread (38 × 5, pitch 30), excluding the handrail weight.

For the maintenance costs of the aluminum tertiary members, the baseline data, the manufacturing/maintenance costs of the aluminum and carbon steel tertiary members were calculated based on an

Table 9 Carbon tertiary items total/unit weight

Parameter	Total weight (t)			Unit weight (kg/m)		
	"S"	"E"	"P"	"S"	"E"	"P"
Handrail	536.2	179.4	254.9	21.0	20.4	21.1
Ladder	120.3	45.5	22.1	21.3	37.5	38.0
Stair	151.2	47.3	146.3	144.7	136.0	127.8

Table 10 Summary of the unit weight for aluminum tertiary items

Items	Unit weight (kg/m)
Handrail	13.73
Ladder	13.53
Stair	104.08

Table 11 A comparison of the carbon and aluminum cost according to outfitting items

Item	Component	Cost (KRW/kg)	
		Carbon	Aluminum
Handrail	Investment cost	40,616	72,397
Ladder		17,063	13,827
Stair		31,218	31,538
Maintenance	Maintenance cost	4,40	1,100

Table 12 A comparison of the carbon and aluminum weight according to outfitting items

Items	Aluminum weight (kg/m)	Carbon weight (kg/m)	Comparison seight
Handrail	13.73	20.8	66%
Ladder	13.53	32.3	42%
Stair	104.08	136.2	76%

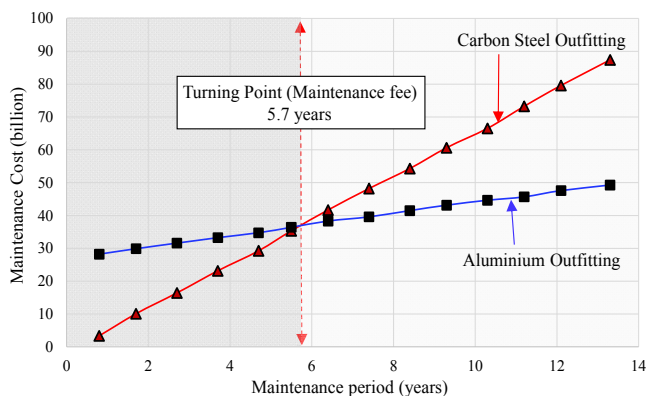


Fig. 10 A relationships of between cost and maintenance period according to materials (carbon steel and aluminum)

precedent research (Muzathik et al., 2012), as shown in Table 11, and compared.

Table 9 shows the comparison of the total and unit weight for the handrail, ladder, and stair applied in three large projects “S,” “E,” and “P.” Given the shape of the aluminum tertiary members, as aluminum is lighter than carbon steel and minimizes welding, the weight was reduced by an average of 40%, as presented in Table 12.

Table 11 compares the cost per unit weight of the aluminum production cost and the cost of the carbon steel tertiary member material + manufacturing cost + hot-dip galvanization cost. Although the initial material cost for aluminum exceeds that of carbon steel, as aluminum does not require hot-dip galvanization and welding, when compared by item, the cost of the aluminum tertiary members was similar to that of carbon steel members, or even lower. Moreover, considering the maintenance period, as shown in Fig. 10, aluminum is more cost-effective than carbon steel after an average of 5.7 years.

A comprehensive analysis of the above results demonstrated that the aluminum tertiary members designed and manufactured using the technical standard can be an alternative to the existing carbon steel tertiary members in offshore platforms.

4. Conclusion and Discussion

As part of the IOSS obtained through a joint industrial research of the unified offshore standardization bulk package used by offshore facilities, this article presents the contents of the aluminum tertiary member design specifications (IOSS S102-1/2 S104) (ISSO, 2019) and the results of a design standardization and applicability analysis

based on the handrail, a tertiary member that uses aluminum alloy. The following detailed conclusions were drawn.

- (1) The major contents of the international tertiary member standardization can be confirmed, which should serve as useful data for similar future projects by specifying the effect of application.
- (2) The devised aluminum tertiary member standard design was applied to a recently manufactured large offshore project and analyzed. According to the results, the material cost of aluminum was more than twice that of carbon steel, raising concerns about increased project costs. However, when calculating the actual tertiary member costs by unit weight and incorporating the material, welding, and hot-dip galvanization costs, the cost of aluminum was equal to or less than that of carbon steel.
- (3) In comparison to carbon steel, aluminum barely has maintenance costs, and it does not require paint. Thus, aluminum showed lower costs than carbon steel after an average of 5.7 years, giving it sufficiently high applicability.

Through the participation of relevant Korean equipment companies in the standardization process, this will serve as an important base technology not only for the technical completeness of new standards, but also for improvement in product reliability and enhanced technological competitiveness of manufacturers.

In addition, the IOSS is being applied primarily in shipyards for real projects, and preparations are underway for its reflection in international standards for offshore structures. Finally, a working committee under ISO TC67 was newly established, and a draft international standard (DIS) for reflection in ISO is currently in progress.

Acknowledgements

This article utilized some content from UBS JIP and is the result of a research conducted under the Encouragement Program for the Industries of Economic Cooperation Region of the Ministry of Trade, Industry and Energy and the Korea Institute for Advancement of Technology (Task No.: P0002308).

References

ANSI/ASSE. (2007). Safety Requirements for Workplace Walking/ Working Surfaces and Their Access; Workplace, Floor, Wall and Roof Openings; Stairs and Guardrails Systems (ANSI/ASSE A1264.1-2007).

ANSI. (2000). Ladders – Fixed – Safety Requirements (ANSI Standard A14.3-2000),

Australian Standard. (2013). Fixed Platforms, Walkways Stairways and Ladders - Design, Construction and Installation (AS 1657:2013).

Cha, J.H., 2009. Development Direction of Standardization of

- Shipbuilding Equipment, Bulletin of the Society of Naval Architects of Korea, 46(2), 10-16.
- Ellingsen, H.P., Lim, Y.K., Shin, H.C., Singh, K., Kang, S.Y., Kim, Y.H., ... Ok, D. (2018). First Set of Bulk Standard Specifications Set to Reduce Cost and Delays in Offshore Oil & Gas Projects. Proceedings of Offshore Technology Conference, Houston, Texas, USA.
- International Organization for Standardization (ISO). (2001a). Safety of Machinery – Permanent Means of Access to Machinery – Part 1: Choice of Fixed Means of Access between Two Levels (EN ISO 14122-1:2001).
- International Organization for Standardization (ISO). (2001b). Safety of Machinery – Permanent Means of Access to Machinery – Part 2: Working Platforms and Walkways (EN ISO 14122-2:2001).
- International Organization for Standardization (ISO). (2001c). Safety of Machinery – Permanent Means of Access to Machinery – Part 3: Stairs, Stepladders and Guard-rails (EN ISO 14122-3:2001).
- International Organization for Standardization (ISO). (2004). Safety of Machinery – Permanent Means of Access to Machinery – Part 4: Fixed Ladders (EN ISO 14122-4:2004).
- Integrated Offshore Standard Specification (IOSS). (2019). Specification for Structural Tertiary Design (IOSS S102-1/2 S104). Unified Offshore Standardization JIP, Bulk Package-Phase IV., Korea.
- NORSOK Standards. (2004). Working Environment. Rev. 4 (NORSOK S-002).
- NORSOK Standards. (2006). Architectural Components and Equipmen (3th ed.) (NORSOK C-002).
- Kim, C.Y., Lee, S.C., Choi, & B.C. (2009). The Study on the Trend of International Standards and the Domestic Plan. Bulletin of the Society of Naval Architects of Korea, 46(2), 3-9.
- Oh, S.Y. (2017). Shipbuilding & Offshore Industry Status & Standardization Trend, KATS Technical Report, No.98, 1-15.
- Muzathik, A.M., Ferry, M., Chan, M.Y., Samo, K.B., & Noor C.W.M. (2012). Comparison of Aluminum Alloy and Steel Materials as Deckhouses for Offshore Support. Proceedings of International Conference on Marine Technology, Kuala Terengganu, Malaysia.

Author ORCIDs and Contributions

Author name	ORCID	Contributions
Kim, Yeon-Ho	0000-0001-8621-5608	①②③④
Park, Joo-Shin	0000-0001-5335-8151	②③④
Shin, Hyun-Chang	0000-0003-2876-0709	①②③
Kim, Sung-Jun	0000-0003-4849-2334	②③
Park, Dae-Kyeom	0000-0002-9833-0352	②⑤
Ha, Yeon-Chu	0000-0003-3591-8471	③
Seo, Jung-Kwan	0000-0002-3721-2432	①④⑤

- ① Conceived of the presented idea or developed the theory
- ② Carried out the experiment or collected the data
- ③ Performed the analytic calculations or numerical simulations
- ④ Wrote the manuscript
- ⑤ Supervised the findings of this study

Study on System Support for Offshore Plant Piping Process Using 3D Simulator

Hyun-Cheol Kim¹ and Gyu-Hong Lee²

¹Associate professor, Faculty of Mechanical Engineering, Ulsan College, Ulsan, Korea

²Research director, TIM Solution, Ulsan, Korea

KEY WORDS: Offshore plant, Piping process, 3D simulator 3D, Working efficiency, Installation drawing

ABSTRACT: An offshore plant is an offshore platform that can process oil and gas resources in rough seas with a poor working environment. Moreover, it is a complex structure with different types of offshore facilities and a large amount of outfitting that connects different offshore installations. In particular, an enormous amount of various piping materials is installed in a relatively narrow space, and thus, the difficulty of working is relatively high compared to working in ships or ground plants. Generally, when the 3D detailed design is completed, an offshore plant piping process is carried out at the shipyard with ISO 2D fabrication drawings and ISO 2D installation drawings. If a worker wants to understand the three-dimensional piping composition in the working area, he can only use three-dimensional viewers that provide limited functionality. As offshore plant construction progresses, correlating work with predecessors becomes more complicated and rework occurs because of frequent design changes. This viewer function makes it difficult to identify the 3D piping structure of the urgently needed part. This study deals with the process support method based on a system using a 3D simulator to improve the efficiency of the piping process. The 3D simulator is based on the Unity3D engine and can be simulated by considering the classification and priority of 3D models by the piping process in the system. Further, it makes it possible to visualize progress information of the process. In addition, the punch content can be displayed on the 3D model after the pipe inspection. Finally, in supporting the data in relation to the piping process, it is considered that 3D-simulator-supported piping installing could improve the work efficiency by more than 99% compared to the existing method.

1. Introduction

Pipe installation work in offshore plant construction is a major construction process that accounts for more than 40% of the total construction by work type (Kim and Shin, 2014). Previous studies have continuously minimized the loss and cost of work by efficiently managing the production and installation processes of numerous pipes made of various materials according to the characteristics of work on offshore plants (Ham et al., 2016). To examine the contents of major studies, Ham et al. (2016) attempted to minimize the inefficiency of delayed pipe delivery by designing a regression analysis predictive model for pipe production and installation. This study demonstrated the possibility of more accurate pipe lead time prediction if high-quality data are acquired and appropriate variables are selected as a result of the nature of regression analysis. Wei and Nienhyuis (2012) applied an assembly sequence algorithm for fittings to the pipe installation plan and examined the possibility of interference and

processing. They implemented a system that derives an automatic assembly sequence by reflecting constraints in the actual assembly; however, there were partial limitations in improving the entire piping process. DSME (2015) suggested an automatic method for cross-verification of 2D drawings and 3D models in 2D and 3D pipe systems using the ISO 15926 xml file format. Furthermore, SHI (2015) proposed a piping work management system composed of a unit for pipe information extraction from pipe design information, a work difficulty setting unit, an individual work ratio setting unit, a performance management unit, and a performance database. It manages only the engineering information, excluding the 3D computer-aided design (CAD) model. Park and Woo (2018) proposed a data structure for an integrated piping process management system by defining items that need to be improved for each process of offshore plant piping materials. Oh et al. (2018) presented a method for predicting the required amount of pipe materials for offshore structures based on big data analysis for more accurate material

Received 18 November 2019, revised 8 March 2020, accepted 9 April 2020

Corresponding author Hyun-Cheol Kim: +82-52-279-3103, hckim@uc.ac.kr

© 2020, The Korean Society of Ocean Engineers

This is an open access article distributed under the terms of the creative commons attribution non-commercial license (<http://creativecommons.org/licenses/by-nc/4.0>) which permits unrestricted non-commercial use, distribution, and reproduction in any medium, provided the original work is properly cited.

demand planning and purchasing for designers. Park et al. (2019b) addressed a management method based on the connection relationships between installation pipe fitting items acquired from CAD information for prior management of the offshore plant installation readiness. Park et al. (2019a) performed process visualization, bottleneck process analysis, and partner performance analysis-based process mining with log data generated in the pipe materials supply process.

The aforementioned studies focused predominantly on pipe design, process plan, and piping process management system configuration methods. However, incorrect working and reworking occur frequently because workers do not identify the three-dimensional structure of the work area during field piping work, even if the pipe design and process plan and management are performed systematically. Offshore plants undergo frequent design changes during the construction period. To perform field work by accurately reflecting the design intent, we need 3D development information as well as isometric (ISO) 2D installation drawings. Furthermore, the 3D CAD pipe model requires identification of the three-dimensional pipe structure considering relationships with the previous task and the interrelationships of tasks by classifying the tasks by material, spool, and size according to the characteristics of the tasks. However, a process management system without a 3D simulator feature cannot meet these requirements, and a 3D viewer with limited functions is used or an additional 3D CAD pipe simulation work is performed according to the workers' demands.

With this background, our study proposes a system support method using a 3D simulator for easy and efficient identification of the on-site piping process work structure. The implemented 3D simulator can perform 3D simulation for the piping process in the system through a lightweight 3D CAD model based on the Unity3D engine and can visualize the process by interconnecting every process progress information in the system. Furthermore, the post-processing status after the pipe inspection can be referenced by indicating the punch details on the 3D model. In addition, the degree of work efficiency improvement compared to the existing method was examined for a 3D simulator-based system used through three work scenarios.

2. Items Analysis for Supporting Offshore Plant Piping Process

The piping of an offshore plant is arranged and installed considering the relationship with the previous task and the interrelationships of tasks in a limited local space with the components of Architecture; Structure; Equipment; heating, ventilation, and air conditioning (HVAV) system; and Electric as shown in Fig. 1. To perform the pipe installation work efficiently considering these offshore plant components, the following information support is required for the workers in general.

(1) Installation status of components: The piping must be installed

without interferences for connections between different facilities or internal structures. Hence, the worker must be aware of the installation status of components related to the piping.

(2) Pipe installation priorities: The pipe installation priorities are determined according to the physical characteristics such as the spool diameter, thickness, and material; the installed block; and the deadline. Furthermore, in general, the following piping work is performed in consideration of interference with surrounding structures after large pipes are installed on the site. Therefore, the subsequent piping work cannot be performed unless the worker is already aware of the priorities, and the piping must be installed again in serious cases. Hence, the worker must always be aware of the priorities of tasks.

(3) Isometric 2D drawing by work type: In the piping work and inspection stage, the worker or inspector may need to identify the isometric 2D drawing by material, size, spool, and package, or the 3D piping structure model. In this case, the sorting function of the 3D CAD pipe model needs to be provided in this field work.

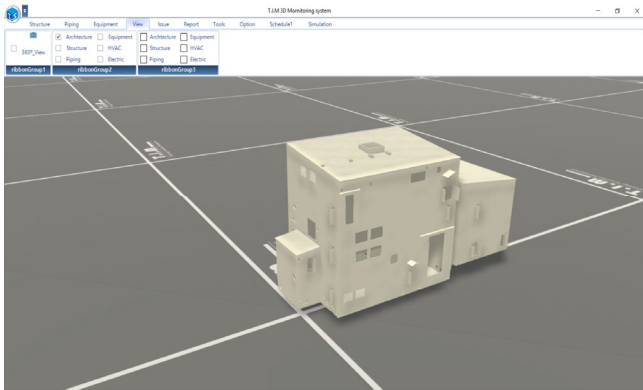
(4) 3D working internal space: To better understand the working internal structure in which components are arranged in a complex manner, we need to identify the 3D piping structure model by combining only the partially required components. In this case, the 3D CAD model must allow disassembly and assembly. In addition, a partial modeling feature should be provided to allow identification of the internal connection status by expanding or shrinking only a part of the workspace.

(5) Punch: Punch refers to the writing of the problems and processing requirements together with the inspection date and location after piping inspection. In general, the site creates isometric 2D drawings or takes pictures and provides them to the shipyard. Therefore, for specific reworks, the 3D CAD model related to the punch must be identified.

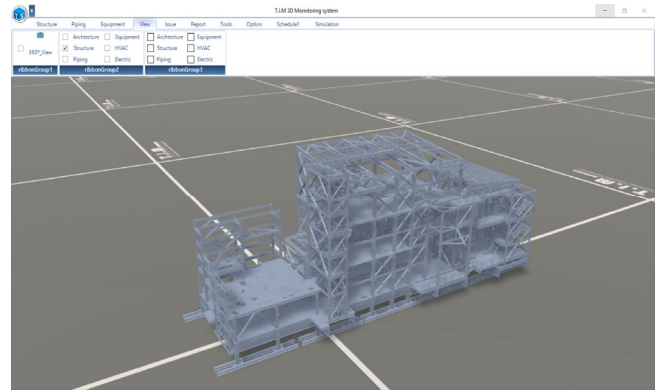
3. Development of Offshore Plant Piping Process Support System Using 3D Simulator

3.1 Composition of 3D-simulator-based System

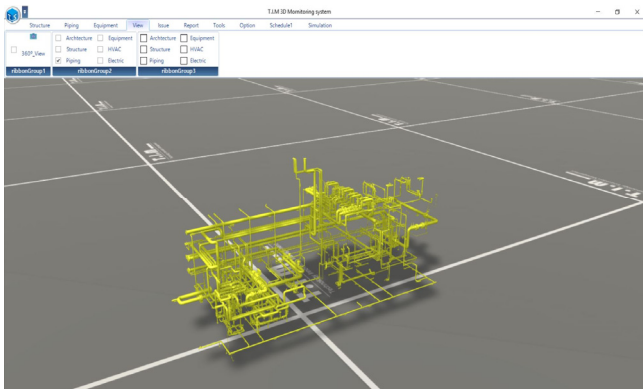
To minimize incorrect working in field work and to improve work efficiency, the worker must be aware of the installation and arrangement of structures and various fittings, including piping, in the workspace during the progress of work in three dimensions. Therefore, in this study, we designed a system to visualize the work situation in three dimensions by connecting the offshore plant process with a 3D CAD model and to enable 3D simulation of the internal structure according to the demands of the worker or inspector. Fig. 2 shows the correlation between the internal information and the system configuration based on the working progress and engineering data of the 3D CAD model shape information and the manufacturing resource planning (MRP) system of an offshore plant production design. The 3D simulator of this system shares and interconnects the process and engineering data in the database and various ISO 2D drawings.



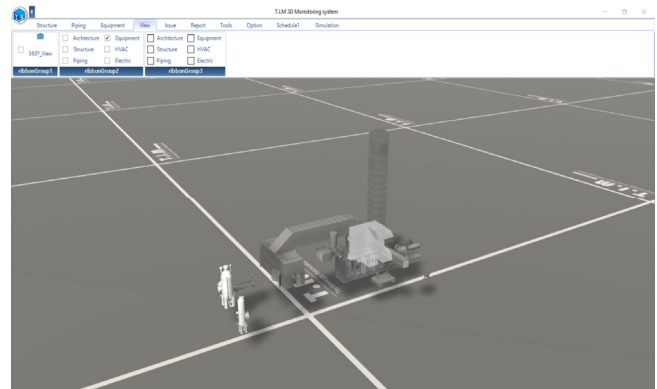
(a) Architecture



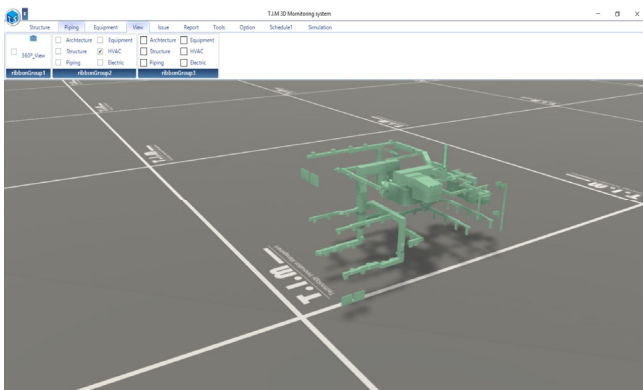
(b) Structure



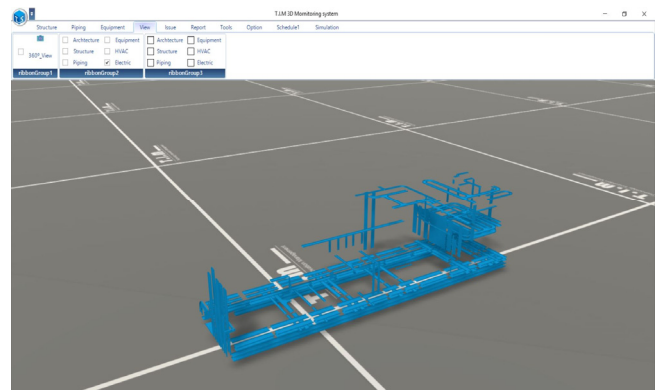
(c) Piping



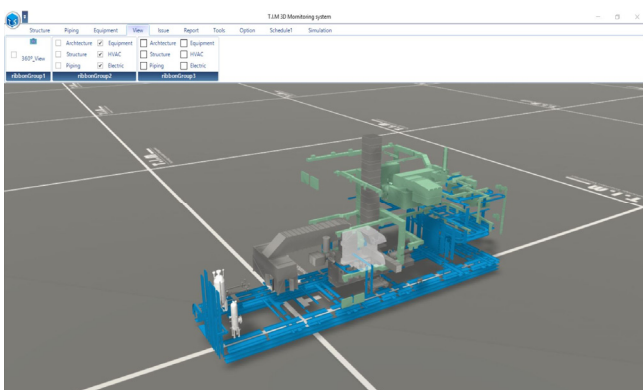
(d) Equipment



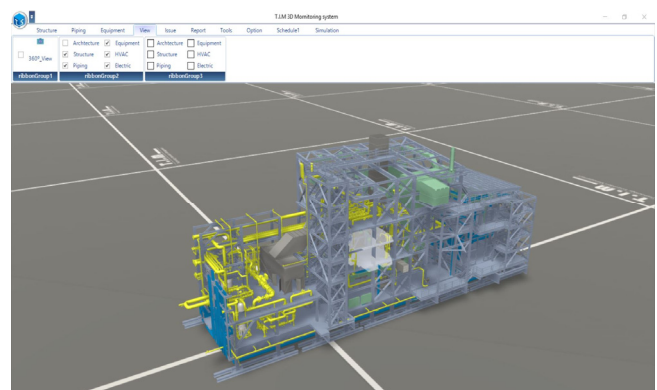
(e) HVAC



(f) Electric



(g) Equipment+HVAC+Electric



(h) Structure+Piping+Equipment+HVAC+Electric

Fig. 1 Constitution of a part in offshore plant: water injection module

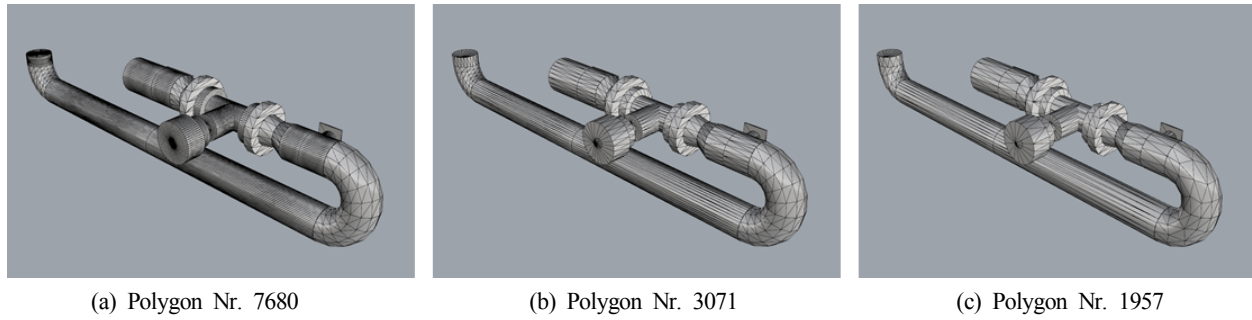


Fig. 4 An example of simplification for 3D CAD pipe model

arranged in a complex manner together with structures and facilities. Thus, the workers and process managers need to visually check the current situation of the process. In particular, it will assist in improving the process work efficiency if the installation of equipment, facilities, and structures, as well as the receipt, installation preparation, and installation completion of the pipes can be checked before, during, and after the work.

3.3.1 Representation of piping process status based on 3D CAD model

Most shipyards operate a proprietary system to manage the working process from manufacturing to the receipt and installation of materials. Therefore, the 3D simulator in this system was implemented in association with the database of a process management system. Fig. 5 shows an example of the receipt of piping materials (white), installation preparation (gray), and installation completion (black) in association with the 3D simulator. Fig. 5 (a) numerically shows the receipt, installation completion, and installation completion of the piping materials in Working Process Summary, and the progress of work is displayed in terms of percentage. Furthermore, Fig. 5 (b) displays the status from receipt to installation completion of the piping

materials corresponding to the working process in the 3D CAD pipe model. When a worker registers the work result to the MRP system from the site, the working process situation is expressed in color (white, gray, and black) in the 3D CAD pipe model from the shared database, which allows the worker to intuitively see the working progress.

3.3.2 Identification of 3D pipe location and structure by work type

During pipe installation, it is necessary to identify the piping work status by block, size, material, and system, and to identify the location and structure of the 3D pipe during pipe inspection according to the purpose such as line inspection, flushing, hydro test, pneumatic test, and reinstatement. Fig. 6 (a) indicates a 6-inch-diameter pipe by contour lines in the 3D CAD pipe model. Fig. 6 (b) shows the representation of the pipes with contour lines for pipes in the package—the smallest unit—during pipe flushing using air or water to remove foreign substances from inside the pipes. Besides, the 3D simulator in the system can distinguish a pipe package for line inspection, pipe package for inspection of water pressure of the weld using water pressure, and pipe package indicating completion of reinstatement as shown in Fig. 6.

2019년 11월		2019년 12월									
일	월	수	목	금	토	일	월	수	목	금	토
27	28	29	30	31	1	2					
3	4	5	6	7	8	9	1	2	3	4	5
10	11	12	13	14	15	16	8	9	10	11	12
17	18	19	20	21	22	23	15	16	17	18	19
24	25	26	27	28	29	30	22	23	24	25	26
							29	30	31	1	2

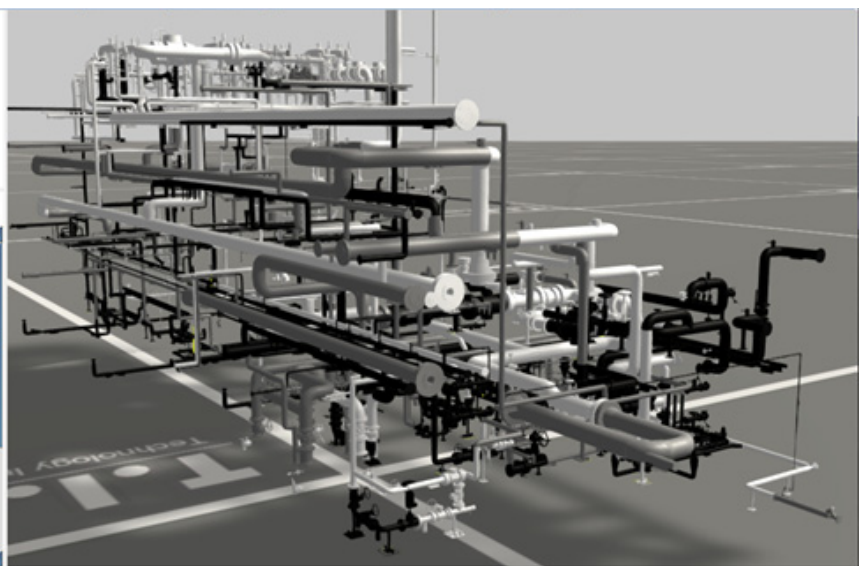
오늘: 2019-11-07

Date : 2019-11-07

Summary

DECKNO	Qty	HOVer	Load	Today	Inst	Perc	Remain
1 CA11	4					0%	4
2 CA21	1	1	1			0%	1
3 CD11	119	110	110		91	73%	28
4 CD21	45	33	33		20	44%	25
5 CH11	3	3	3			0%	3
6 CP11	56	41	41		23	41%	33
7 CP12	57	40	40		18	31%	39
8 CT11	37	29	29		16	43%	21
9 CT12	20	10	10		4	20%	16
10 CT21	87	13	13		9	10%	78
11 CV11	2					0%	2
12 CV21	12	6	6			0%	12
13 CX11	12					0%	12
14 M21A	2					0%	2
15 M21B	2					0%	2

(a) Working process summary



(b) Display of piping installation state on 3D CAD model

Fig. 5 Working process displaying on 3D CAD pipe model



(a) 3D CAD pipe model with identical 6-inch diameter



(b) 3D CAD pipe model with identical package for pipe flushing

Fig. 6 Example of working process state displaying on 3D CAD pipe model

3.3.3 Pipe inspection result displaying in 3D CAD model

Punch means to indicate the pipe inspection date and the details and locations of problems (processing or otherwise), directly in the corresponding work area. In general, the punch details are directly indicated on the ISO 2D installation drawing, or pictures are taken and stored separately in the process management department. Therefore, it

is time-consuming to find and refer to the related information through the package number to check the punch location and processing. The punch function of this system indicates the problems directly in the 3D CAD model, which are linked to the MRP information and are provided to users. Consequently, the worker can identify more accurately the location of the punch and whether or not the punch has

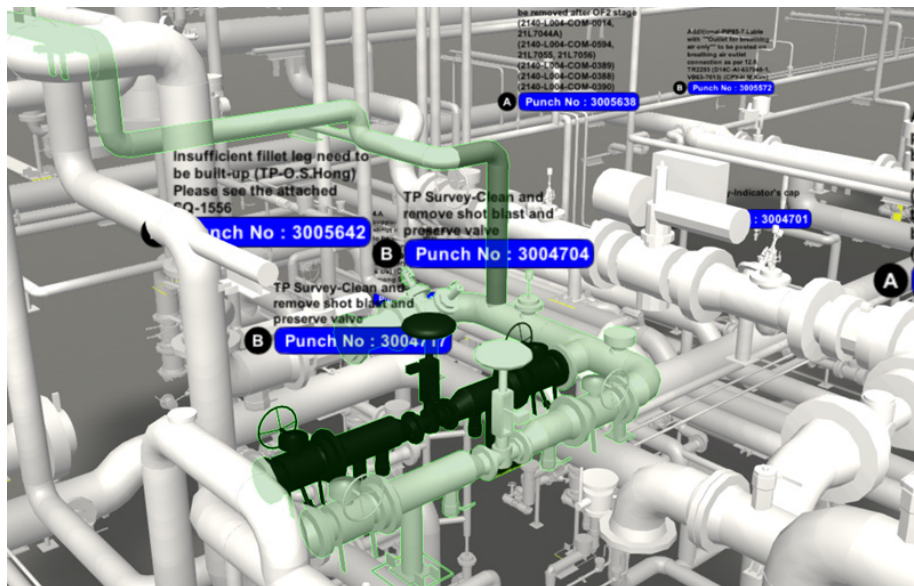


Fig. 7 Example of punch displaying on 3D CAD pipe model

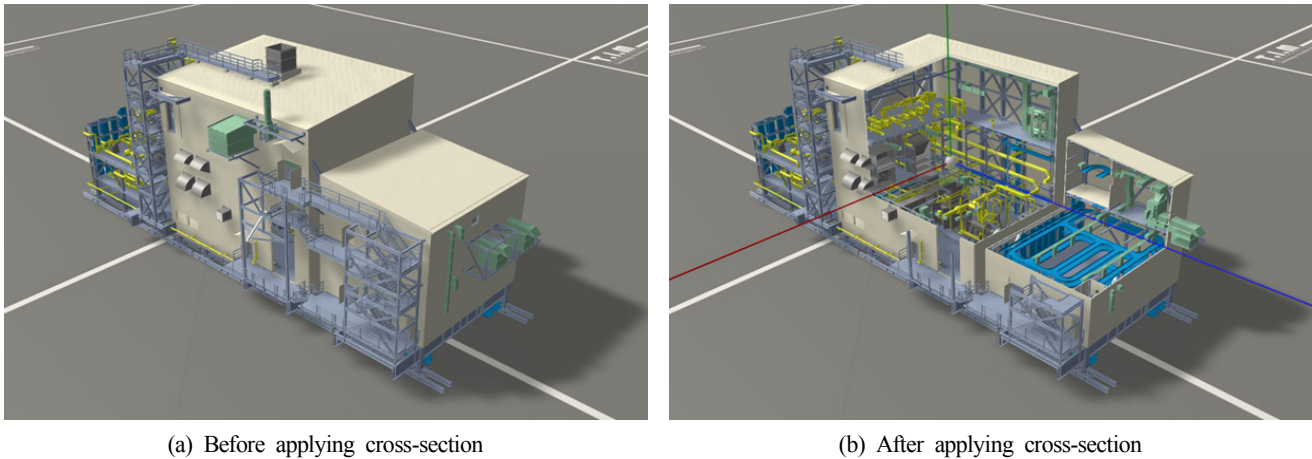


Fig. 8 Example of cross section function on 3D CAD structure model

been processed. Fig. 7 shows an example of a punch indicating a problem together with an expression of the corresponding package in the 3D CAD model.

3.3.4 3D simulation displaying the internal plant structure

The offshore plant piping process is performed considering the interferences between related structures and various facilities and fittings. Therefore, if a worker has identified the relevant 3D work structure in the workspace together with the ISO 2D installation drawing, it can assist in not only preventing incorrect working but also improving work efficiency. To this end, this system enables partial visualization of the disassembly and assembly between offshore plant structures and the internal structure. Fig. 1 (a)–(f) show simulation examples of each component of the offshore plant module. Fig. 1 (g) and (h) show simulation examples that combine only the necessary components. Furthermore, Fig. 8 shows cross-sections of partial simulation examples of the arrangements of structures, facilities, pipes, and other fittings to be installed inside the relevant work space. Fig. 8 (a) shows the 3D CAD model of the entire offshore plant modules before applying the cross-section. Fig. 8 (b) shows the internal structure of an offshore plant by removing the necessary parts by applying the cross-section feature.

4. Work Efficiency Analysis

To examine the work efficiency of the offshore plant process support system based on the 3D simulator, we composed three simulation work scenarios for the water injection module in Fig. 1.

Table 1 Piping components applied to offshore plant module of Fig. 1

Item	Symbol	Unit	Value
Spool	SPL	EA	434
Package	PKG	EA	85
Punch	-	EA	21

Table 1 lists the pipe spool, package, and number of punches used in the offshore plant. Here, spool is the smallest unit of pipe work, package refers to the minimum unit of piping structure, and punch denotes the recording of modifications or problems in work finishing after piping inspection.

The first work scenario represents a case where the worker demands the simulation result of an installed 3D pipe structure in order to identify the working progress status. To verify efficiency, we compared the time required for the 3D spool simulation until 434 spools by using the MRP system and the 3D simulation-based system, which are currently used. The MRP system does not include ISO 2D installation drawing and the 3D CAD model. Hence, the 3D CAD pipe model must be found and simulated from the pipe spool number in the MRP system, and the higher the number of spools, the longer the simulation time. However, the 3D-simulation-based system is linked to the database of the MRP system, and this is directly reflected in the 3D CAD model; the installed piping work status can be simulated in real time. Therefore, as shown in Fig. 9, an approximately 99% or higher work efficiency improvement can be expected.

The second work scenario requires the simulation result of the 3D pipe structure by package for the pipe-inspection status, which is required to intuitively identify the inspection report preparation or progress status. Fig. 10 compares the time required for 3D pipe simulation until 85 packages using the MRP system and 3D simulation-based system. The 3D-simulation-based system allows real-time simulation because it can reflect the process working status in the 3D CAD model by package. However, the MRP system must perform simulation by finding the individual 3D CAD pipe model corresponding to the package number. Hence, as shown in Fig. 9, the simulation time increases in proportion to the number of packages and there is a difference in work efficiency of approximately 99% or higher.

The third work scenario is the case in which the punch details are indicated in the 3D CAD model after piping inspection. With the existing method, when the punch details are prepared in an isometric 2D drawing and then submitted, and the process manager or designer finds the relevant 3D CAD model and enters the punch details to

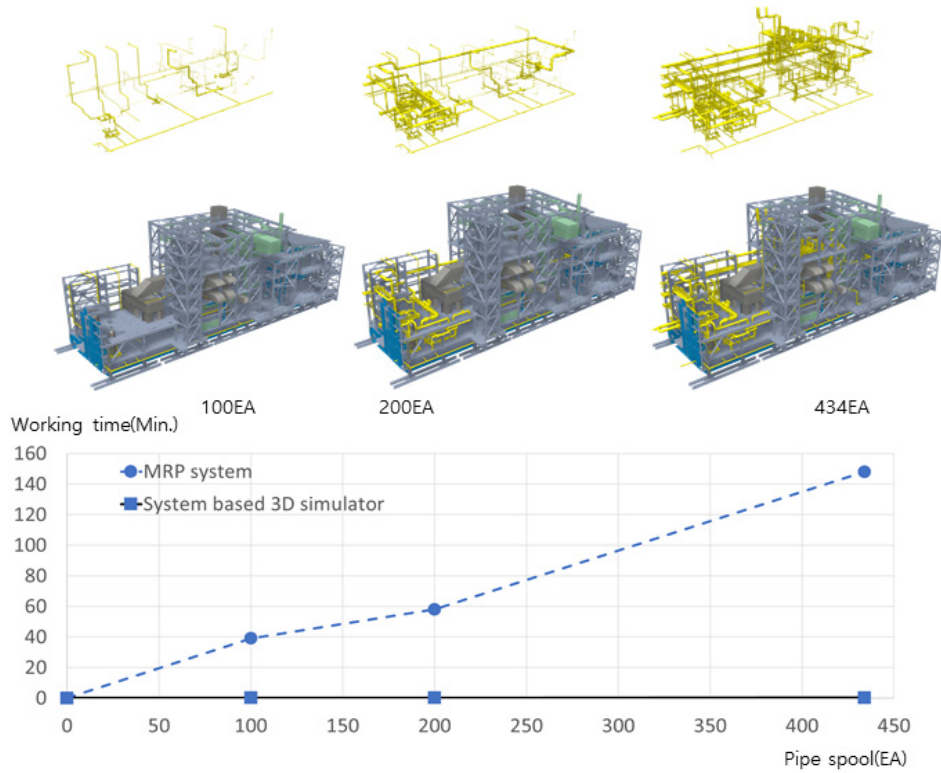


Fig. 9 Comparison of 3D simulation on the installed pipe spools between MRP system and system in this study

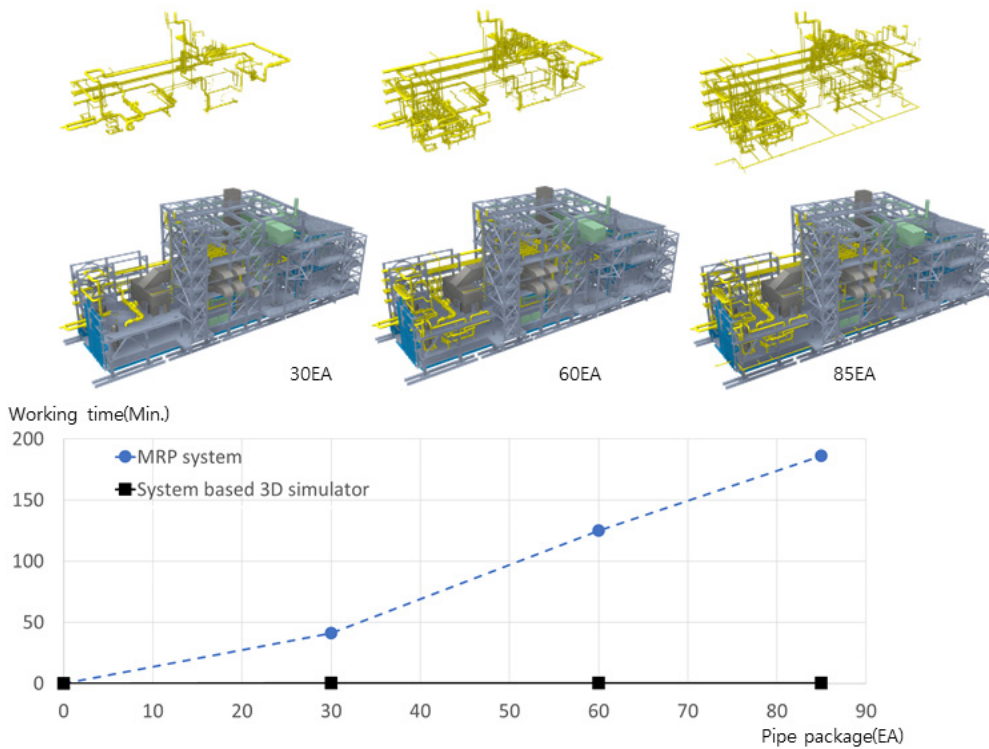


Fig. 10 Comparison of 3D simulation on the inspected pipe packages between MRP system and system in this paper

provide the 3D CAD information to the workers. Therefore, it takes some time to acquire information for rework. As shown in Table 1, it took 56 min to input the details of 21 punches in the 3D CAD model. However, in our system, the punch details are input to the 3D CAD

model in real time; hence, the punch details in the 3D CAD model can be directly output and used. Fig. 11 shows an example of inputting the 21 punch details in Table 1 in the 3D CAD model. As with the previous results, the work efficiency is approximately 99% or higher.

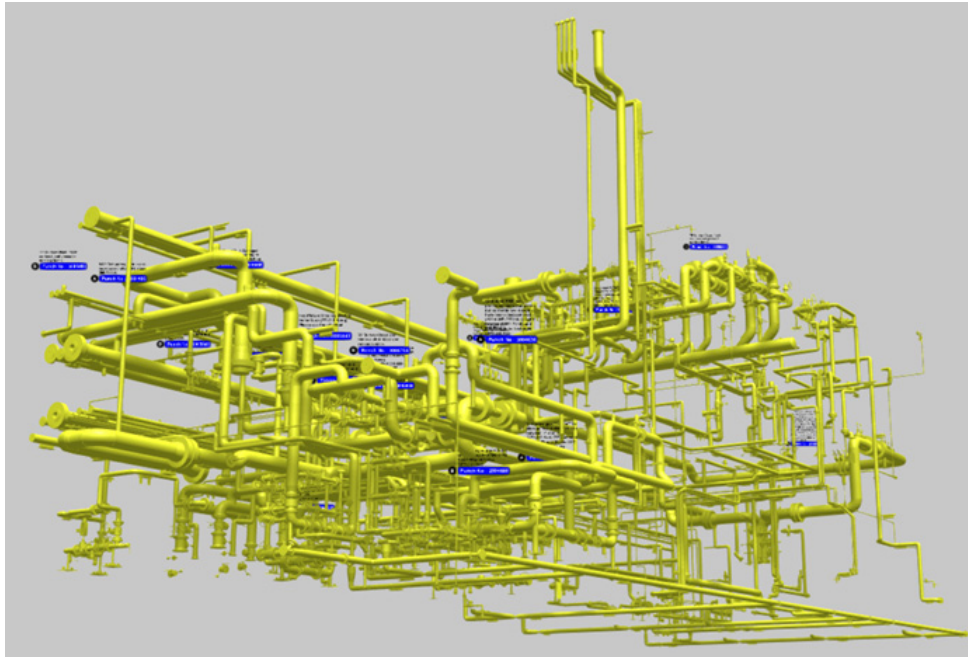


Fig. 11 Example of punch comments registered on 3D CAD pipe model

5. Conclusion

The 3D simulator enables a virtual simulation test of a real offshore plant in which offshore structures, facilities, and various fittings are arranged in a complex manner for easy and accurate identification of workspace information prior to actual work. In the present study, we introduced a method of linking this 3D simulator with the offshore plant piping process for system support. We compared the work efficiency improvement of the proposed system through three simulation-related work scenarios with the existing method.

The results of this study can be summarized as follows.

First, the offshore plant model designed with 3D CAD was simplified while maintaining the 3D shape and was implemented in the system— including the boundary curve—through the simplification process of the offshore plant model designed with 3D CAD.

Second, the offshore plant working process was visualized in a 3D CAD model by linking the process work result to the 3D simulator in real time.

Third, the 3D CAD pipe model corresponding to the same work type was distinguished by spool and package to allow the worker and inspector to check the work status in 3D pipe structure model.

Fourth, the cross-section feature can be used to divide or combine only the work areas for simulation to identify the complex internal and external structures of the offshore plant.

Fifth, the punch details can be directly input to the 3D CAD model after piping inspection, thus allowing the simultaneous visualization of the rework and working progress of the punch details.

Sixth, it was verified using work scenarios that the 3D-simulator-based support system for offshore plant process management can contribute toward the improvement of work efficiency.

The 3D-simulator-based process support system introduced in this paper was developed so that a systematically designed 3D CAD model can provide 3D shape information that meets the requirements of the production site while contributing to an improvement in efficiency of the process work. If the worker can intuitively and easily recognize 3D shapes together with isometric 2D drawings in the field with frequent design changes, it can minimize incorrect working and greatly contribute to an improvement in work efficiency. In this vein, the offshore plant process support system based on the 3D simulator is a critical research field that should be developed continuously with keen interest in the future.

References

- Daewoo Shipbuilding & Marine Engineering (DSME). (2015). Method of Validation Check for Piping 2D & 3D Information. Patent Application Number 10-2015-0012344, Korean Intellectual Property Office.
- Ham, D.K., Back, M.G., Park, J.G., & Woo, J.H. (2016). A Study of Piping Leadtime Forecast in Offshore Plant's Outfittings Procurement Management. *Journal of the Society of Naval Architects of Korea*, 53(1), 29-36. <https://doi.org/10.3744/SNAK.2016.53.1.29>
- Kim, J.S., & Shin, Y.T. (2014). Development Portable Pipe Spool Location-confirm System Based UHF RFID. *KIPS Transactions on Computer and Communication Systems*, 3(10), 329-336. <https://doi.org/10.3745/KTCCS.2014.3.10.329>
- Oh, M.J., Roh, M.L., Park, S.W., & Kim, S.H. (2018). Estimation of Material Requirement of Piping Materials in an Offshore Structure using Big Data Analysis. *Journal of the Society of Naval Architects*

- of Korea, 55(3), 243-251. <https://doi.org/10.3744/SNAK.2018.55.3.243>
- Park, J.G., Kim, M.G., & Woo, J.H. (2019a). A Study on Process Management Method of Offshore Plant Piping Material using Process Mining Technique. *Journal of the Society of Naval Architects of Korea*, 56(2), 143-151. <https://doi.org/10.3744/SNAK.2019.56.2.143>
- Park, J.G., Kim, H.J., Kim, M.G., & Park, J.C. (2019b). A Study on the Installation Readiness Management Method of Offshore Plant using CAD Information. *Journal of the Society of Naval Architects of Korea*, 56(2), 152-160. <https://doi.org/10.3744/SNAK.2019.56.2.152>
- Park, J.G., & Woo, J.H. (2018). A Study on Process Management Method of Offshore Plant Piping Material. *Journal of the Society of Naval Architects of Korea*, 55(2), 124-135. <https://doi.org/10.3744/SNAK.2018.55.2.124>
- Samsung Heavy Industries (SHI). (2015). Piping Work Management System and Method. Patent Application Number 10-2015-0087612, Korean Intellectual Property Office.
- Wei, Y., & Nienhuis, U. (2012). Automatic Generation of Assembly Sequence for the Planning of Outfitting Processes in Shipbuilding. *Journal of Ship Production and Design*, 28(2), 49-59. <https://doi.org/10.5957/JSPD.28.2.120002>

Author ORCIDs and Contributions

Author name	ORCID	Contributions
Kim, Hyun-Cheol	0000-0001-9631-5645	①③④⑤
Lee, Gyu-Hong	0000-0003-4242-5827	②③

- ① Conceived of the presented idea or developed the theory
- ② Carried out the experiment or collected the data
- ③ Performed the analytic calculations or numerical simulations
- ④ Wrote the manuscript
- ⑤ Supervised the findings of this study

Underwater Acoustic Research Trends with Machine Learning: Passive SONAR Applications

Haesang Yang¹, Keunhwa Lee², Youngmin Choo³ and Kookhyun Kim⁴

¹Research Professor, Department of Naval Architecture & Ocean Engineering, Seoul National University, Seoul, Korea

²Associate Professor, Department of Defense System Engineering, Sejong University, Seoul, Korea

³Assistant Professor, Department of Defense System Engineering, Sejong University, Seoul, Korea

⁴Associate Professor, School of Naval Architecture & Ocean Engineering, Tongmyong University, Busan, Korea

KEY WORDS: Underwater acoustics, Passive SONAR system, Machine learning, Deep learning, Signal processing, Passive target classification, Passive source localization

ABSTRACT: Underwater acoustics, which is the domain that addresses phenomena related to the generation, propagation, and reception of sound waves in water, has been applied mainly in the research on the use of sound navigation and ranging (SONAR) systems for underwater communication, target detection, investigation of marine resources and environment mapping, and measurement and analysis of sound sources in water. The main objective of remote sensing based on underwater acoustics is to indirectly acquire information on underwater targets of interest using acoustic data. Meanwhile, highly advanced data-driven machine-learning techniques are being used in various ways in the processes of acquiring information from acoustic data. The related theoretical background is introduced in the first part of this paper (Yang et al., 2020). This paper reviews machine-learning applications in passive SONAR signal-processing tasks including target detection/identification and localization.

1. Introduction

Underwater acoustics is a scientific domain that involves the study of the phenomena of sound waves in water, including their generation, propagation, and reception. Specifically, the sound navigation and ranging (SONAR) system is utilized to investigate underwater communication and target detection and to study marine resources and the environment; further, it is utilized to measure and analyze sound sources in water. The main objective of underwater acoustics-based remote sensing is the indirect acquisition of information on underwater targets of interest using acoustic data. At present, highly advanced data-driven machine-learning techniques are being applied in various ways for extracting information from acoustic data. The techniques closely related to these applications are introduced in the first part of this paper (Yang et al., 2020). This paper presents a detailed review of the applications of machine learning in underwater acoustics and passive SONAR signal processing.

2. Passive SONAR Signal Processing

2.1 Passive Target Detection and Identification

Signals measured by a passive SONAR system exhibit fluctuations owing to irregular noises in the ocean. This hinders target signal detection. The conventional signal processing method for detecting target signals is based on the Neyman-Pearson criterion (Nielsen, 1991). As the probability distribution of the received signals, including the target signals, differs from that of the noise signals, the probability ratio that is set according to the presence of the target signal at the time of observation is compared with a preset value. This helps determine whether the target signal is included in the observed time period. This technique can be expanded to detect the target signal by comprehensively analyzing all the signals measured in the time domain of interest as well as signals observed at a specific time.

In general, techniques for detecting a target signal through comparison with a threshold value have a disadvantage: false alarms can occur frequently, particularly in the scenario of a low signal-

Received 2 March 2020, revised 11 April 2020, accepted 13 April 2020

Corresponding author Youngmin Choo: +82-2-6935-2532, ychoo@sejong.ac.kr

© 2020, The Korean Society of Ocean Engineers

This is an open access article distributed under the terms of the creative commons attribution non-commercial license (<http://creativecommons.org/licenses/by-nc/4.0>) which permits unrestricted non-commercial use, distribution, and reproduction in any medium, provided the original work is properly cited.

to-noise ratio. To overcome this problem, Komari Alaie and Farsi (2018) combined the time and frequency domain information of the measurement signals to derive an adaptive threshold for such signals. They used this threshold value to determine whether the target signal is included in the corresponding observed interval.

However, in passive SONAR, the use of a threshold to identify a target as described earlier is a detection technique that uses only the size-related features of the target signal. Shin and Kil (1996) developed a target identifier that defined and utilized the multifaceted features of a target signal in terms of various aspects to increase the accuracy of target detection. In the conventional target detection technique based on the signal size described earlier, the tendencies exhibited in the spectrogram of the observed signal are simplified, and the sum of the signal sizes corresponding to the frequency domain of interest in each time frame is used. In the study conducted by Shin and Kil, apart from these fundamental features, other features such as those related to the size/frequency statistics of the observed signal and the frequency of the target signal were integrated to utilize these as input vectors for several machine learning algorithms including neural networks. In conventional target detection, a process is required for identifying the detected target signal. However, in target identifiers that use multiple features of the target signal as mentioned in the aforementioned technique, target classification is achieved before detection (classify-before-detect method). The technique proposed by Shin and Kil delivered superior performance, compared to the performance of the conventional technique, particularly in low signal-to-noise ratio conditions.

The aforementioned studies have mainly used passive SONAR (binary classification) to determine whether the target signal is included in the observed interval. This type of classification can be extended further to the classification of various types of signals present in the ocean. Hemminger and Pao (1994) proposed a classifier that used neural networks to distinguish between six types of marine noises. In the process of detection or identification of a signal by a SONAR operator, a technique such as a short-time Fourier transform (STFT) that displays the temporal frequency variations of a signal of interest is often used in conjunction with the auditory information. With reference to this, the study conducted by Hemminger and Pao defined the features that reflected the visual information of the STFT, as follows. When the spectrum that constituted the STFT of the observed signal was compared in relation to the trend exhibited by the preceding cluster in each time frame, the STFT could be represented as a list of prototype numbers. The prototype numbers listed in this manner constituted the input vectors of the neural network. A classifier was developed according to the type of noise source to be classified. The type of noise source included in the test data was determined using a classifier that yielded the highest value among different classifier results.

While detecting a target signal using passive SONAR, a transient sound is detected for a period of time. This could be emitted by various sources such as biological sound or machinery noise. In general, a

skilled SONAR operator is capable of classifying these transient sounds according to the source. Tucker and Brown (2005) extracted various features including human auditory characteristics reflected from timbre (Fig. 1) and proposed a transient sound classifier using these features. For the classification, timbre-related features that helped classify various types of sounds were selected based on the results of a classification experiment that classified various transient sounds present in underwater environments including biological and mechanical sounds. In addition, factors related to the material of the sound-generating target were explored and used as features. Finally, the features reflecting sound variability were calculated using a rhythmogram that reflected the temporal variability of transient sound (related to repeatability in the time domain). The feature vectors derived from the combination of features defined in various domains have a higher dimension than the specified data size. Among these vectors, the features that help identify the type of sound source are selected. As their study distinguished sounds included in a specific class from those in other classes, different features were selected according to the sound to be classified. These input feature vectors with reduced dimensions were combined with the k-nearest neighbors (KNN) algorithm to classify the type of sound. The classification performance obtained by combining and using features derived from various domains (including human sound perception) was superior to that obtained using statistical features of frequency variations

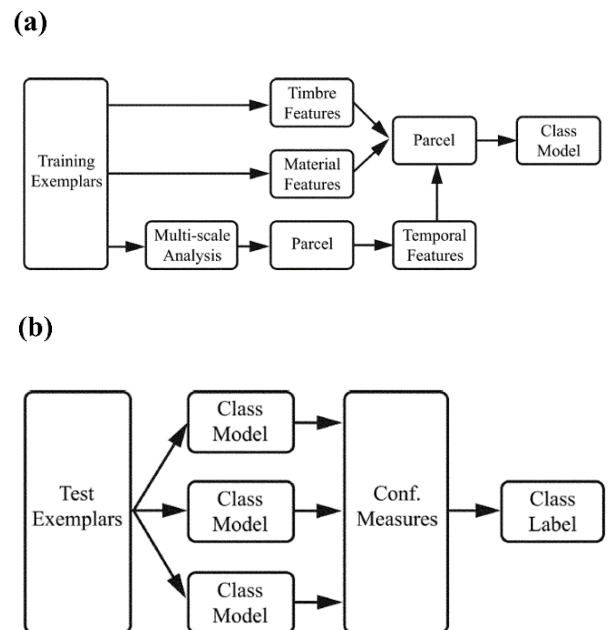


Fig. 1 Overview of the training (a) and testing (b) procedures. During training, three kinds of features are computed for each example in the training set. During testing, the feature vectors for each transient class are computed, and a classifier is used to determine the confidence value for each class model. The class with the highest confidence value is considered as the label of the test example (Tucker and Brown, 2005).

over time that were obtained from frequency features or spectrograms of the observed signals. This was demonstrated by comparing the receiver-operating-characteristics (ROC) curve of the identifier using each feature. Finally, they concluded the following. To identify the type of transient sounds, it was most advantageous to select and use a feature that was suitable for the research purpose by integrating the sound perception features, frequency features, and statistical features.

To distinguish the types of noise sources by using machine learning, the classifiers need to learn a large amount of data. However, in practice, there is a deficiency of passive SONAR data classified by the type of noise source. Meanwhile, passive SONAR data without classification are relatively abundant. Yang et al. (2018) and Ke et al. (2018) have conducted studies utilizing unclassified SONAR data for pre-training to increase the efficiency of supervised learning. Yang et al. (2018) used the values of the final hidden layer of the competitive deep-belief network (CDBF) (designed by them) as classifier inputs. This was unlike other existing methods that use passively defined feature vectors based on the experience of experts. A large amount of data is required to automatically extract features from the input vector (e.g. spectrum) that are effective for classification. Unclassified SONAR data are used for this purpose. In CDBF, a restricted Boltzmann machine (RBM) is trained on the probability distribution of the input data. This is a type of unsupervised learning that is performed using data without class labels. Then, using the classified data, the degree of sensitivity of the unit in the hidden layer of the RBM can be calculated according to the type of the noise source. Based on this, the units of the hidden layer can be clustered. The competitive layer is placed at the rear of the hidden layer, and training is performed to

increase the distinction between the clustered classes. Finally, the unit value of the competitive layer is used as the input vector of the support vector machine (SVM) to distinguish between types of ships for classification. This method has delivered a classification performance that is superior to those of methods using the Mel-frequency cepstral coefficient (MFCC), waveform, wavelet, or feature vectors based on auditory model.

Ke et al. (2018) also used unclassified passive data to improve the accuracy of learning performed with marginal amounts of classified passive SONAR data. In their study, the following four steps were used for classifying ships: (1) pre-processing, (2) pre-training, (3) fine-tuning, and (4) classification (Fig. 2). In the pre-processing step, only the effective components for data classification were extracted from the measured time-series acoustic data through the wavelet transform. These extracted components were transformed to the frequency domain and used as a pre-training input for the subsequent step. In the pre-training step, a multi-layered autoencoder was used. High-level features for noise source classification were extracted from this encoder. In the fine-tuning step, the trained autoencoder was applied to a marginal amount of classified SONAR data. Furthermore, the training was performed such that the high-level feature vectors extracted through the feature-separation layer increased the spatial distance according to the class. The result of the fine-tuning step was used as the input to the support vector machine (SVM) in the classification step. This method delivered a better classification performance than those of the existing methods that use MFCC as the input.

Wang et al. (2019b) fused features extracted from multiple domains to identify the types of marine noise sources (four types of ship noises, marine mammal sounds, and background noise). Furthermore, they combined these with a deep neural network (DNN). Typically, MFCC is used to identify noise sources. However, it was verified in this study that the Gammatone frequency cepstral coefficient (GFCC) is more advantageous for marine noise source classification. Furthermore, the GFCC was used as a part of the feature vectors. Modified empirical mode decomposition was applied to extract the feature vectors incorporating diverse information related to complex marine noise sources, from time-series signals. At this time, the features were calculated based on the magnitude of the decomposed signals and frequency variation, which were fused with the GFCC and used as the input vectors of the DNN. The DNN had a Gaussian mixture model (GMM) in the first layer and extracted the statistical features of the feature vector rather than those of the overfit feature vector. These were used to conduct supervised learning. The performance was improved significantly compared to the results obtained from the existing noise source classification methods that combine MFCC with limited information by using a simple classifier such as a GMM.

As mentioned earlier, it has been established that the performance of a skilled SONAR operator is superior to that of the target detection process based on the traditional SONAR signal processing technique. For example, an echo signal from a metal object has a timbre that is

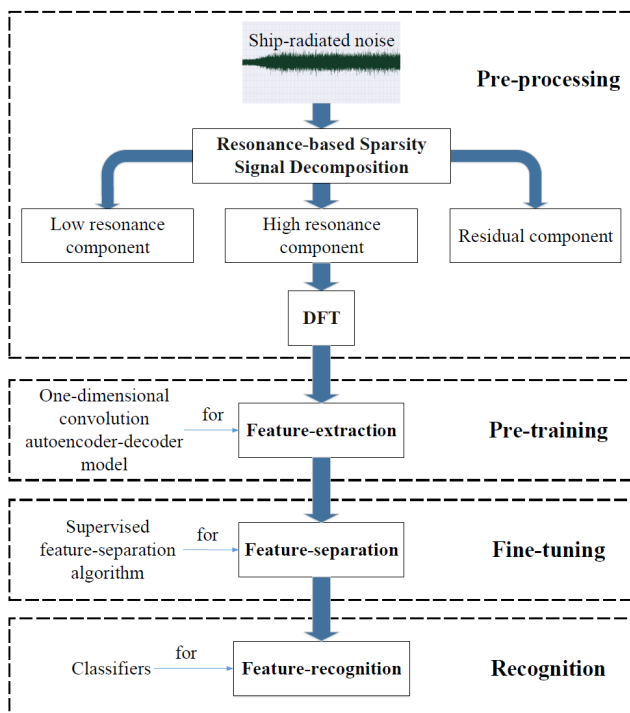


Fig. 2 The process of underwater acoustic target recognition (Ke et al., 2018).

different from that of an echo signal from a natural object, such as a rock, and humans can recognize this difference. In this regard, studies have been conducted to identify target signals from echo signals having different timbres depending on the material of the target object using active SONAR (Allen et al., 2011; Murphy and Hines, 2014; Young and Hines, 2007). Similar to these studies, Yang and Chen (2015) conducted a study wherein they tested the human capability to distinguish between artificially generated sounds and naturally occurring sounds using passive SONAR. Furthermore, they analyzed strategies for humans to recognize sounds according to the sound sources to improve the performance of the automatic identifier. In their study, experiments were performed to understand the human capabilities of auditory perception for identifying and distinguishing between artificial sounds (such as those of large ships, torpedoes, and underwater vehicles) and natural sounds (such as those from dolphins or rain), between sounds of surface ships and submarines, and between sounds from three ships. For the sound identification method used by the participants in this experiment, the following were defined and extracted from the observed signals: harmonic spectrum features associated with the tonal component of the noise source, equivalent rectangular bandwidth spectrum features associated with the timbre, and auditory cortical features associated with frequency variation characteristics over time. The features extracted over multiple domains had a high dimension. In each domain, principal component analysis (PCA) was used to reduce the dimension and then combine the features to be used as input values for machine learning. In this study, a logistic regression-based classifier was trained using the training data prepared for each class, and the performance of the classifier trained for each objective was evaluated using the test data. It was verified that the automatic target classifier was superior to the human participants in all the tasks. In particular, the performance of the automatic target classifier with feature vectors of lower dimension was better when sounds were more similar within a class or when the sounds significantly differed across classes. The automatic target classifier delivered the most inferior performance in the classification of artificial noise and natural noise and the most superior performance in the classification of noise from the three ships. In addition, they proposed a method of combining the classification experience of the human participant with the automatic target classifier for the task of artificial/natural noise classification in which the classifier delivered the most inferior classification performance. Furthermore, they verified that the classification performance of the automatic target classifier could be improved through similar combinations.

2.2 Passive Target Localization

2.2.1 Passive target arrival angle estimation

In general, a vertical/horizontal line array consisting of multiple sensors is used for target localization in underwater acoustics. In particular, when the target is located remotely, the elevation angle or the azimuthal angle (depending on the type of line array) of the target can be estimated using the time difference of arrival of the target noise

incident on the line array. Hereinafter, in this review paper, the elevation angle and azimuthal angle of the target are collectively referred to as the target arrival angle. In the conventional approach for underwater acoustics, the similarity between the acoustic field actually measured in the line array and the replica field simulated according to the arrival angle with the plane wave assumption is assessed to estimate the arrival angle of the target. This angle can be estimated using the replica field that displays high similarity with the measured field (Jensen et al., 2011). This technique is highly robust against noise. However, it has a disadvantage, wherein a long line array is required to estimate the target azimuthal angle with high resolution. An adaptive beamforming method has been proposed to overcome this disadvantage. However, the adaptive beamforming method using a covariance matrix of a measured field has a disadvantage: the performance deteriorates when correlated target signals are estimated (Jensen et al., 2011).

Several techniques have recently been proposed for estimating the target arrival angle with high resolution using a limited-length line array in an environment with correlated target signals. Among these, a representative technique is compressive beamforming (Edelmann and Gaumond, 2011; Xenaki et al., 2014; Xenaki and Gerstoft, 2015). It is based on compressive sensing, which is designed to derive the solution of a (non-deterministic) linear system. In compressive sensing, the sparsest solution among the many solutions that satisfy the linear system is determined by minimizing the l_0 norm of signal x (Donoho, 2006). The target arrival angle in underwater acoustics can be estimated as a linear system problem. It is advantageous as the arrival angle can be estimated with high resolution using limited observation by applying compressive sensing. However, in compressive sensing with compressive beamforming, there is a trade-off between the observed data proximity and the sparsity of the estimated solution. Therefore, there is a disadvantage: the hyperparameters that determine the priority between the sparsity and data-fitting of the solution need to be adjusted passively to derive the solution that is appropriate for each scenario (Park et al., 2017). Sparse Bayesian learning (SBL), an algorithm based on machine learning, is drawing attention as an effective method to address this problem (Tipping, 2001).

SBL has been proposed for the regression of a specified data trend or classification using Bayesian inference (Tipping, 2001). Similar to compressive sensing, SBL is applied when the measured data can be represented as a linear combination of specified bases (linear system problem). In this case, it is assumed that the base size and noise in the measured data follow a normal distribution. Unlike compressive sensing (in which x is directly and deterministically derived), in SBL, x is derived by first estimating the probability distribution and then using the distribution. As mentioned earlier, the problem of evaluating the arrival angle of an underwater target can also be established as a linear system: $y = Ax + n$. Here, y denotes the measured data, and n denotes the noise included in each acoustic sensor of the line array. When estimating the target arrival angle using SBL, the probability distributions of x and n (i.e., the signal size and noise variance) can be

extracted from the measured data. The arrival angle of the target signal incident on the line array can be evaluated using probability distribution. While performing beamforming based on SBL, the signal size and noise variance are repeatedly updated using the expectation-maximization algorithm (Tipping, 2001). The update rule used at this time is one of the key parts of SBL. However, in this review paper, rather than detailing the algorithm of SBL, we review the SBL modification method that is used to estimate the target arrival angle more robustly.

When measuring an acoustic signal in an actual experiment, the target signal is continuously recorded on the line array. Multiple measurements or multi-snapshots in the time domain can be used to obtain a reliable estimation of the arrival angle of the target signal. In particular, the target in an adjacent signal can be regarded as stationary in the underwater environments where the speed of sound waves is significantly higher than the target speed. Gerstoft et al. (2016) extended the existing SBL to utilize the stationary target signal recorded at the adjacent time. In this manner, the single measurement signal y and the corresponding target signal size x of the existing SBL were substituted with the adjacent multiple measurement signals $Y=[y_1, y_2, \dots, y_L]$ and corresponding target signal size $X=[x_1, x_2, \dots, x_L]$, respectively. Here, y_1 is a signal measured at a line array at a specific time, and x_1 is the corresponding target signal. In addition, in the study mentioned earlier, it was assumed that the noise had the same variance regardless of the sensor and measurement time. Gerstoft et al. (2019) extended the SBL such that these noises could have different magnitudes depending on the sensor and measurement time. In addition, they verified through a simulation that the extension was capable of robustly estimating the target arrival angle, compared to the existing method. In addition, Nannuru et al. (2019) extended the conventional SBL to account for the scenario with different matrices A_f according to different frequencies. They verified the effectiveness of the extension method based on actual measurement data (SWellEx-96).

For estimating the arrival angle of a target, SBL has the advantage of automatically deriving values without the need to adjust hyperparameters separately, unlike in the case of compressive sensing. However, as the linear relationship used in SBL utilizes a replica field for a preset target signal arrival angle, a basis mismatch occurs as in compressive beamforming. This lowers its performance. To address this problem, Das (2017) proposed two methods for the off-grid sparse Bayesian arrival angle estimation algorithm and analyzed the error of each method based on the Cramer–Rao lower bound (CRLB). The first method is based on the fact that a randomly incident target signal can be expressed by the Taylor series of a replica field having the arrival angle set at equal intervals. The difference is calculated between the actual arrival angle derived using the Taylor expansion process for the incident angle and the preset arrival angle. After adding this to the estimated variable of the SBL and updating it, the proposed method is more robust against a basis mismatch than the existing method. In the second method, it is assumed that the target signal incident on the

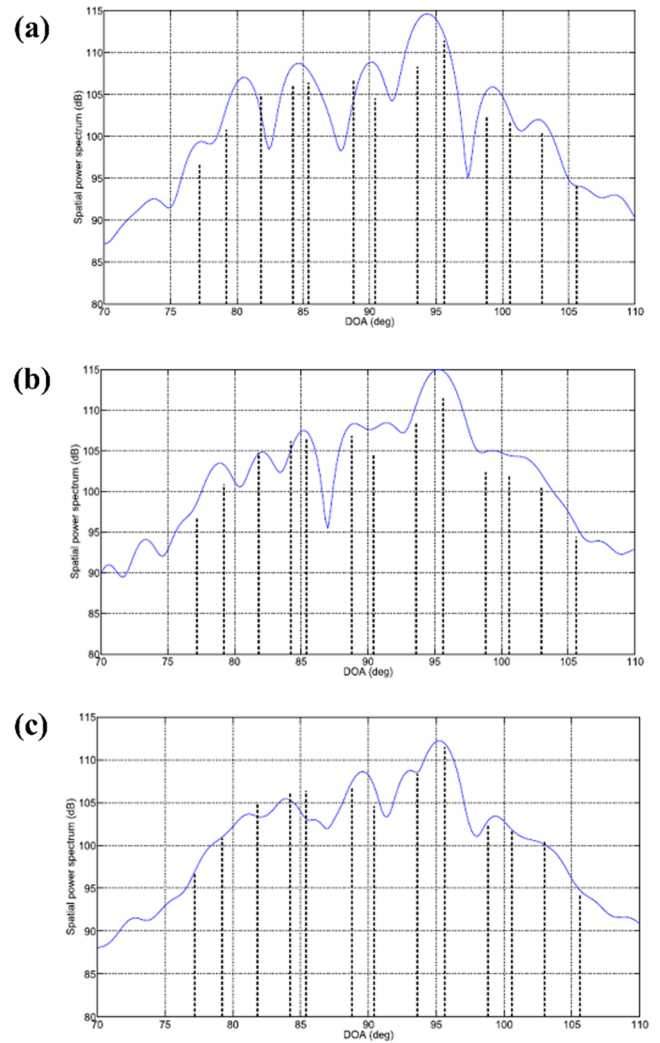


Fig. 3 Comparing the conventional beamforming (CBF) spectra (denoted in blue) from two frequency bins [(a) 2625 Hz and (b) 2725 Hz] and the incoherent average of the CBF spectra from all frequency bins (c) with the estimated spectrum [denoted in dotted black in (a), (b), and (c)] by the proposed wideband direction-of-arrival estimation algorithm (Das and Sejnowski, 2017).

line array at an arbitrary angle can be expressed through linear interpolation of the replica field with respect to a preset arrival angle in the vicinity. The weights of the replica fields distributed at uniform angle intervals, which are used for linear interpolation, are additionally estimated by the SBL. The second method is more robust against basis mismatch than the existing SBL method. However, its performance is inferior to that of the first method. Subsequently, Das and Sejnowski (2017) extended the Taylor series-based off-grid sparse Bayesian arrival angle estimation method to include the broadband signals. This method was applied to the measured data. As shown in Fig. 3, a more reliable estimation of the target arrival angle was achieved by utilizing the common incident angle information of the target signal having various frequency components rather than using individual incident angle information.

In the case of an SBL-based beamforming technique using multiple measurements over time, the arrival angle of a target is estimated without considering the correlation of adjacent measurements. Zhang and Rao (Zhang and Rao, 2011; Zhang and Rao, 2013) extended the existing SBL technique to consider the temporal correlation of the target signal observed in the line array signal at the adjacent time. They verified that this method outperformed the other techniques.

Furthermore, in one of the techniques for estimating the target arrival angle in air, the images obtained by combining the STFT of the acoustic signal measured using the microphone array and the phase component according to the frequency in a specific time frame were used as input values for a convolutional neural network (CNN) (Chakrabarty and Habets, 2017). This technique was able to estimate the arrival angle of a signal without generating a replica field based on an understanding of the physical properties. It can also be applied to signals measured with a line array that is installed underwater. However, to date, the estimation methods of the arrival angle of an underwater target using machine learning have been developed by modifying the update rule used in SBL according to the particular scenario, with SBL as the basic framework, as described in the examples of previous studies. This is because it is challenging to obtain the underwater measurement signals necessary for learning, unlike in the case of air. However, further research is likely to be conducted in the future on the automatic extraction of the arrival angle estimation rule from the data with higher availability of the signal data necessary for learning.

2.2.2 Passive target localization

In target localization, the wave propagation phenomenon in the underwater waveguide considering the sound speed profile, properties of the seafloor, and bathymetry are reflected. Furthermore, the replica field on the line array is calculated according to the location of the potential sound source. The results are compared with those of the measured field. This is called matched field processing (MFP). The research on MFP has grown rapidly because of the development of an acoustic propagation model that can simulate a real sound field in a specified marine environment. MFP is still used as a method of localizing underwater sound sources. However, there is a limitation in its use: the accuracy of the replica field is lowered when inaccurate marine environment information or an inappropriate acoustic propagation model is used (Jensen et al., 2011).

The application of machine learning to underwater sound source localization is known to have started in approximately the early 1990s (Ozard et al., 1991; Zion et al., 1991). These studies trained highly shallow feedforward neural networks (FNN) with simulation or measurement data and differentiated the range and depth information of underwater sound sources. The machine learning model used in these studies was a very simple model that considered the sum of linear weights as an output. Furthermore, in that period, there was limited understanding of how the optimal weight can be obtained using a nonlinear algorithm. This limited the amount of computation. With the

development of machine learning, more advanced and improved models (compared to the initial ones) are being applied. Furthermore, an increasing number of studies are being published on the localization of underwater sound sources using data obtained directly from more complex marine environments or data simulated by models. Lefort et al. (2017) applied a regression-based localization technique for the tank experiment data and simulation data to examine whether underwater sound source localization was possible with a machine learning technique in a varying underwater channel environment. They reported on a few potential applications. In a study using in-situ measurement data, Niu et al. (2017a) directly trained the ship range estimation function with data obtained by a line array (The Santa Barbara Channel Experiment). In their study, the sound field measured by the line array and path of the ship sailing along a certain route were used as the training data, as shown in Fig. 4(a). At this time, several ships were operating on the same route, and specific ship noise and the corresponding route were used for training. Other ship noises were used for testing the performance of the proposed machine learning-based ship range estimation technique. In particular, ship noise had multiple frequency components in the low frequency band. Furthermore, the extracted vectors for each frequency were concatenated and used as the final input vector such that all the frequency components of the ship noise could be used for ship range estimation. As mentioned earlier, the GPS-based ship route was specified according to the sound field measurement time such that the range between the ship and line array for each input vector could be determined. In the case of MFP using a replica field, the performance rapidly deteriorated as the range of the ship increased. However, the machine learning-based classifier delivered superior performance even for the distant ships (Fig. 4(b)). Subsequently, Niu et al. (2017b) applied the proposed algorithm for other data (Noise09 experiment). They investigated the performance of the machine learning-based ship range estimator according to the frequency

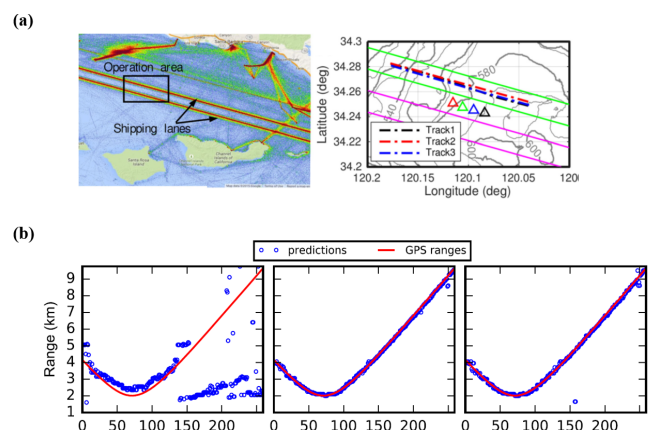


Fig. 4 (a) Operation area and two shipping lanes in Santa Barbara Basin and the experiment geometry with three cargo ships transiting the operation area. The vertical line arrays are denoted by triangles. (b) Localization results with frequency band 53-200 Hz by Bartlett MFP (left); SVM classifier (middle); and FNN classifier (right) (Niu et al., 2017a).

bandwidth of the ship noise or the supervised learning method (classification and regression). The method of classification with the use of multiple frequencies delivered superior results.

Furthermore, occasionally, in cases such as the operation of a passive SONAR system for military purposes, it is more important to accurately evaluate specific information, such as the depth of the target, rather than its overall spatial information. This is because the surface vessel and submarine can be distinguished according to the depth. This is another example where a simulated sound field based on an acoustic propagation model is mainly used (Conan et al., 2016; Conan et al., 2017; Liang et al., 2018). In particular, Conan et al. (Conan et al., 2017) conducted a study to distinguish the depth of a sound source by using the propagation characteristics of sound waves in a specified environment. In their study, the normal mode method was used, which is one of the representative acoustic propagation models. The depth of the sound source was extracted by converting the measurement sound field into the mode space. They verified that the sound source depth can be estimated with higher accuracy using this approach based on binary classification, compared to using MFP. In contrast, Choi et al. (Choi et al., 2019) conducted a study to formulate a rule for estimating the depth of a sound source directly from the measured data using machine learning without a physical understanding of the propagation characteristics of the waves (Choi et al., 2019). In their study, the covariance matrix of the sound field measured in the vertical line array (VLA) and the mode space covariance matrix were used as the input values for machine learning. The mode space covariance matrix is the covariance of the space vector, which is a transformation of the sound field measured in the line array into the mode space based on the normal mode method. They derived a binary classification function for classifying surface vessel and submarine noises through representative machine-learning algorithms such as random forest, SVM, FNN, and CNN. In particular, most of the combinations using real/imaginary parts of the covariance matrix as input values exhibited high accuracy. For these studies on the sound source depth classification based on machine learning, a line array measurement field was required for learning. In their study, to overcome the challenge of acquiring a sufficient amount of actual measurement acoustic data necessary for learning in an underwater environment, simulation sound field results were used that had been obtained using the normal mode method in a specified marine environment. At this time, simulated sound fields were used for training and testing that had been generated in various scenarios by varying the range and depth of the source and signal-to-noise ratio.

While estimating the ship range using a machine-learning technique, such as FNN, the classifier may be overfitted to the training data as the learning process is repeated. This may not yield superior performance on the test data. Chi et al. (2019) prevented the classifier from being overfitted to the training data by adding regularization to the test data while training on ship range estimation. As the input, they used the covariance matrix of a vectorized sound field proposed by Niu et al. (2017a). In their study, with reference to the line array, the linear relationship between the range of a ship sailing at constant speed and

the measurement time was optimized for each learning process. By using the optimized linear relationship and estimated range error as a regularization of the cost function, the study verified that the method prevented the classifier from being overfitted to the training data. It also verified that the classifier exhibited superior generality, compared to the MFP or the overfitted classifier.

While estimating the location of a sound source by applying FNN, it is necessary to train the weight and bias of all the layers connecting the input and output values based on the specified learning data. Wang and Peng (2018) extracted a spread factor that determined the probability distribution of data using a generalized regression neural network based on the data and performed localization of a sound source. In this case, as in the previous study, the normalized covariance matrix of the sound field measured by a VLA was used as the input value. In addition, a supervised learning method was applied that assigned range information to all the sound fields at the training stage. Thus, their study derived an algorithm that could estimate the location of a sound source by determining a spread factor that could provide the best probabilistic description of the training data with the class information. The proposed algorithm was applied to the Swellex-96 experiment data. This revealed that the method was superior to sound source localization using FNN or MFP.

In practice, the neural network-based sound source range estimation algorithm in underwater acoustics has a limitation: the weight and bias must be trained using a limited number of sound fields because of the deficiency of data. To address this problem, Wang et al. (2019a) proposed a deep transfer learning method. In their study, a simulated sound field was generated using an acoustic propagation model under various ocean environments where the ship range was to be estimated. Then, the simulated sound field was normalized according to the line array sensor, and the frequency and sound source range was estimated based on a CNN that used the normalized field as the input image for training. In addition, a limited amount of in-situ measurement data was used to fine-tune the weight and bias of the CNN that first underwent training through a simulated sound field. This deep transfer learning method was applied to the data measured in the deep-sea environment near China. The results verified that the method outperformed the existing MFP or CNN approaches based on deep learning.

Meanwhile, the underwater MFP works similar to the beamforming technique in terms of signal processing. The exception is that in the former, the replica field calculated for the line array according to the location of the sound source is generated by reflecting the sound wave propagation in the underwater waveguide. Gemba et al. (2019) used SBL, a machine-learning algorithm, to estimate sound-source location with high resolution (depth and range from the line array). They applied the SBL-based MFP to both the simulated and actually measured sound fields and demonstrated its effectiveness. In addition, Huang et al. (2018) used a different type of DNN for the localization of a sound source. The crucial difference between the two proposed DNNs is in the presence of a direct design of features to be used for learning. In the first method using the directly designed features, the

eigenvalues of the covariance matrix of the sound field observed with the line array were defined as the features, and these were combined with the neural network to localize the sound source. In particular, a time delay neural network was used to consider the temporal relationship of the measured field. Hence, the past and future (predicted) sound fields were used as the input values to estimate the present position of the measured field. In their study, regression-based supervised learning was used because the location information of the sound field used at the training stage was known, and the location of the sound source in a continuous space was derived. Accordingly, the objective function of this machine-learning technique was defined based on the distance between the estimated and actual sound-source locations. In the second method, the time-series signals measured by various sensors in the line array were used as the input values. Similar to a CNN, the filter for the sound source localization was automatically trained based on data. Furthermore, the features according to the purpose were automatically extracted and combined with an FNN to localize the sound source. Their study verified that this DNN-based sound source-localization algorithm outperformed the conventional MFP. In particular, the first method using directly designed features delivered the most superior performance, and the performance was evaluated under many scenarios. The performance of the sound source-localization algorithm based on machine learning was lowered when the ocean environment of the training data was different from that of the test data (e.g. difference in the bathymetry). This performance degradation can be reduced by training with data acquired from various environments.

As described earlier, underwater sound-source localization based on conventional MFP or machine learning uses spatially sampled sound pressure such as sound fields measured by a line array. Meanwhile, a study investigated the source localization by using the sound pressure measured by a sensor and utilizing broadband source signals with a machine-learning algorithm (Niu et al., 2019). In their study, the absolute vector of the sound pressure for each frequency was normalized and used to utilize the sound pressure measured in various frequency bands. In addition, when the magnitude of the sound source was frequency dependent, to reduce the effect of the sound source magnitude on the sound source localization, the above process was repeated at predetermined frequency-band intervals. This information was derived from the measured sound pressure and then applied to a DNN. The training for range information exploration was conducted by dividing into two stages depending on the range interval. Furthermore, an acoustic propagation model was used to generate large amount of acoustic data that was necessary for the training in two stages. This sound source-localization algorithm was applied to the data measured in the Yellow Sea. It delivered superior localization performance, compared to the performance of MFP.

3. Conclusion

In this paper, we have reviewed the history and evolution of passive

SONAR applications from the studies employing conventional techniques to the research employing recent machine-learning techniques for target detection, classification, and localization.

In a passive SONAR system, target detection/classification uses and integrates multiple features from time, frequency, and other domains to overcome the limitations of the probability distribution analysis and threshold comparison-based techniques for signals that contain both the target signal and noise. The information of the target is extracted from the measured signals. The target identifier models are of various types in terms of use, ranging from simple binary classifiers to models imitating human sound perception capabilities and deep learning models capable of multiple classifications. These models are combined with conventional theoretical models. In addition, these complement each other in terms of the sound sources, environmental characteristics, and research objectives for continuous development. Various techniques are used for localization in passive SONAR systems, ranging from the conventional localization techniques represented by array signal processing and MFP to classification and regression models using compressive sensing, SBL, and machine-learning techniques based on measurement data. However, the satisfactory performance of these machine-learning techniques can be ensured only when sufficient quality data are secured. Therefore, methods are applied for simultaneously using the actual measurement data and data generated from the acoustic models. Although this paper describes techniques for utilizing machine learning only for passive SONAR systems, these techniques can be directly applied to active SONAR systems. This aspect as well as the passive SONAR system for detecting and classifying target signals will be discussed in the future.

References

- Allen, N., Hines, P.C., & Young, V.W. (2011). Performances of Human Listeners and an Automatic Aural Classifier in Discriminating between Sonar Target Echoes and Clutter. *The Journal of the Acoustical Society of America*, 130(3), 1287-1298. <https://doi.org/10.1121/1.3614549>
- Chakrabarty, S., & Habets, E.A. (2017). Broadband DOA Estimation Using Convolutional Neural Networks Trained with Noise Signals. Paper Presented at the 2017 IEEE Workshop on Applications of Signal Processing to Audio and Acoustics (WASPAA). <https://doi.org/10.1109/WASPAA.2017.8170010>
- Chi, J., Li, X., Wang, H., Gao, D., & Gerstoft, P. (2019). Sound Source Ranging Using a Feed-forward Neural Network with Fitting-based Early Stopping. *The Journal of the Acoustical Society of America*, 146(3), EL258-EL264. <https://doi.org/10.1121/1.5126115>
- Choi, J., Choo, Y., & Lee, K. (2019). Acoustic Classification of Surface and Underwater Vessels in the Ocean Using Supervised Machine Learning. *Sensors*, 19(16), 3492. <https://doi.org/10.3390/s19163492>
- Conan, E., Bonnel, J., Chonavel, T., & Nicolas, B. (2016). Source Depth

- Discrimination with a Vertical Line Array. *The Journal of the Acoustical Society of America*, 140(5), EL434-EL440. <https://doi.org/10.1121/1.4967506>
- Conan, E., Bonnel, J., Nicolas, B., & Chonavel, T. (2017). Using the Trapped Energy Ratio for Source Depth Discrimination with a Horizontal Line Array: Theory and Experimental Results. *The Journal of the Acoustical Society of America*, 142(5), 2776-2786. <https://doi.org/10.1121/1.5009449>
- Das, A. (2017). Theoretical and Experimental Comparison of Off-grid Sparse Bayesian Direction-of-arrival Estimation Algorithms. *IEEE Access*, 5, 18075-18087. <https://doi.org/10.1109/ACCESS.2017.2747153>
- Das, A., & Sejnowski, T.J. (2017). Narrowband and Wideband Off-grid Direction-of-arrival Estimation via Sparse Bayesian Learning. *IEEE Journal of Oceanic Engineering*, 43(1), 108-118. <https://doi.org/10.1109/JOE.2017.2660278>
- Donoho, D.L. (2006). Compressed Sensing. *IEEE Transactions on Information theory*, 52(4), 1289-1306. <https://doi.org/10.1109/TIT.2006.871582>
- Edelmann, G.F., & Gaumont, C.F. (2011). Beamforming Using Compressive Sensing. *The Journal of the Acoustical Society of America*, 130(4), EL232-EL237. <https://doi.org/10.1121/1.3632046>
- Gemba, K.L., Nannuru, S., & Gerstoft, P. (2019). Robust Ocean Acoustic Localization with Sparse Bayesian Learning. *IEEE Journal of Selected Topics in Signal Processing*, 13(1), 49-60. <https://doi.org/10.1109/JSTSP.2019.2900912>
- Gerstoft, P., Mecklenbräuker, C.F., Xenaki, A., & Nannuru, S. (2016). Multisnapshot Sparse Bayesian Learning for DOA. *IEEE Signal Processing Letters*, 23(10), 1469-1473. <https://doi.org/10.1109/LSP.2016.2598550>
- Gerstoft, P., Nannuru, S., Mecklenbräuker, C.F., & Leus, G. (2019). DOA Estimation in Heteroscedastic Noise. *Signal Processing*, 161, 63-73. <https://doi.org/10.1016/j.sigpro.2019.03.014>
- Hemming, T.L., & Pao, Y.-H. (1994). Detection and Classification of Underwater Acoustic Transients Using Neural Networks. *IEEE Transactions on Neural Networks*, 5(5), 712-718. <https://doi.org/10.1109/72.317723>
- Huang, Z., Xu, J., Gong, Z., Wang, H., & Yan, Y. (2018). Source Localization Using Deep Neural Networks in a Shallow Water Environment. *The Journal of the Acoustical Society of America*, 143(5), 2922-2932. <https://doi.org/10.1121/1.5036725>
- Jensen, F.B., Kuperman, W.A., Porter, M.B., & Schmidt, H. (2011). *Computational Ocean Acoustics*. Springer Science & Business Media.
- Ke, X., Yuan, F., & Cheng, E. (2018). Underwater Acoustic Target Recognition Based on Supervised Feature-Separation Algorithm. *Sensors*, 18(12), 4318. <https://doi.org/10.3390/s18124318>
- Komari Alaie, H., & Farsi, H. (2018). Passive Sonar Target Detection Using Statistical Classifier and Adaptive Threshold. *Applied Sciences*, 8(1), 61. <https://doi.org/10.3390/app8010061>
- Lefort, R., Real, G., & Dreameau A. (2017). Direct Regressions for Underwater Acoustic Source Localization in Fluctuating Oceans. *Applied Acoustics*, 116, 303-310. <https://doi.org/10.1016/j.apacoust.2016.10.005>
- Liang, G., Zhang, Y., Zhang, G., Feng, J., & Zheng, C. (2018). Depth Discrimination for Low-Frequency Sources Using a Horizontal Line Array of Acoustic Vector Sensors Based on Mode Extraction. *Sensors*, 18(11), 3692. <https://doi.org/10.3390/s18113692>
- Murphy, S.M., & Hines, P.C. (2014). Examining the Robustness of Automated Aural Classification of Active Sonar Echoes. *The Journal of the Acoustical Society of America*, 135(2), 626-636. <https://doi.org/10.1121/1.4861922>
- Nannuru, S., Gemba, K.L., Gerstoft, P., Hodgkiss, W.S., & Mecklenbräuker, C.F. (2019). Sparse Bayesian Learning with Multiple Dictionaries. *Signal Processing*, 159, 159-170. <https://doi.org/10.1016/j.sigpro.2019.02.003>
- Nielsen, R.O. (1991). *Sonar Signal Processing*. Artech House.
- Niu, H., Gong, Z., Ozanich, E., Gerstoft, P., Wang, H., & Li, Z. (2019). Deep-learning Source Localization Using Multi-Frequency Magnitude-only Data. *The Journal of the Acoustical Society of America*, 146(1), 211-222. <https://doi.org/10.1121/1.5116016>
- Niu, H., Ozanich, E., & Gerstoft, P. (2017a). Ship Localization in Santa Barbara Channel Using Machine Learning Classifiers. *The Journal of the Acoustical Society of America*, 142(5), EL455-EL460. <https://doi.org/10.1121/1.5010064>
- Niu, H., Reeves, E., & Gerstoft, P. (2017b). Source Localization in an Ocean Waveguide Using Supervised Machine Learning. *The Journal of the Acoustical Society of America*, 142(3), 1176-1188. <https://doi.org/10.1121/1.5000165>
- Ozard, J.M., Zakarauskas, P., & Ko, P. (1991). An Artificial Neural Network for Range and Depth Discrimination in Matched Field Processing. *The Journal of the Acoustical Society of America*, 90(5), 2658-2663. <https://doi.org/10.1121/1.401860>
- Park, Y., Seong, W., & Choo, Y. (2017). Compressive Time Delay Estimation off the Grid. *The Journal of the Acoustical Society of America*, 141(6), EL585-EL591. <https://doi.org/10.1121/1.4985612>
- Shin, F.B., & Kil, D.H. (1996). Full-spectrum Signal Processing Using a Classify-before-detect Paradigm. *The Journal of the Acoustical Society of America*, 99(4), 2188-2197. <https://doi.org/10.1121/1.415407>
- Tipping, M.E. (2001). Sparse Bayesian Learning and the Relevance Vector Machine. *Journal of Machine Learning Research*, 1(Jun), 211-244.
- Tucker, S., & Brown, G.J. (2005). Classification of Transient Sonar Sounds Using Perceptually Motivated Features. *IEEE Journal of Oceanic Engineering*, 30(3), 588-600. <https://doi.org/10.1109/JOE.2005.850910>
- Wang, W., Ni, H., Su, L., Hu, T., Ren, Q., Gerstoft, P., & Ma, L. (2019a). Deep Transfer Learning for Source Ranging: Deep-sea Experiment Results. *The Journal of the Acoustical Society of America*, 146(4), EL317-EL322. <https://doi.org/10.1121/1.5126923>
- Wang, X., Liu, A., Zhang, Y., & Xue, F. (2019b). Underwater Acoustic

- Target Recognition: A Combination of Multi-Dimensional Fusion Features and Modified Deep Neural Network. *Remote Sensing*, 11(16), 1888. <https://doi.org/10.3390/rs11161888>
- Wang, Y., & Peng, H. (2018). Underwater Acoustic Source Localization Using Generalized Regression Neural Network. *The Journal of the Acoustical Society of America*, 143(4), 2321-2331. <https://doi.org/10.1121/1.5032311>
- Xenaki, A., & Gerstoft, P. (2015). Grid-free Compressive Beamforming. *The Journal of the Acoustical Society of America*, 137(4), 1923-1935. <https://doi.org/10.1121/1.4916269>
- Xenaki, A., Gerstoft, P., & Mosegaard, K. (2014). Compressive Beamforming. *The Journal of the Acoustical Society of America*, 136(1), 260-271. <https://doi.org/10.1121/1.4883360>
- Yang, H., Lee, K., Choo, Y., Kim, K. (2020). Underwater Acoustic Research Trends with Machine Learning: General Background. *Journal of Ocean Engineering and Technology*, 34(2), 147-154. <https://doi.org/10.26748/2020.015>
- Yang, H., Shen, S., Yao, X., Sheng, M., & Wang, C. (2018). Competitive Deep-belief Networks for Underwater Acoustic Target recognition. *Sensors*, 18(4), 952. <https://doi.org/10.3390/s18040952>
- Yang, L., & Chen, K. (2015). Performance and Strategy Comparisons of Human Listeners and Logistic Regression in Discriminating Underwater Targets. *The Journal of the Acoustical Society of America*, 138(5), 3138-3147. <https://doi.org/10.1121/1.4935390>
- Young, V.W., & Hines, P.C. (2007). Perception-based Automatic Classification of Impulsive-source Active Sonar Echoes. *The Journal of the Acoustical Society of America*, 122(3), 1502-1517. <https://doi.org/10.1121/1.2767001>
- Zhang, Z., & Rao, B.D. (2011). Sparse Signal Recovery with Temporally Correlated Source Vectors Using Sparse Bayesian Learning. *IEEE Journal of Selected Topics in Signal Processing*, 5(5), 912-926. <https://doi.org/10.1109/JSTSP.2011.2159773>
- Zhang, Z., & Rao, B.D. (2013). Extension of SBL Algorithms for the Recovery of Block Sparse Signals with Intra-block Correlation. *IEEE Transactions on Signal Processing*, 61(8), 2009-2015. <https://doi.org/10.1109/TSP.2013.2241055>
- Zion, B., Beran, M., Chin, S., & Howard, J.J. (1991). A Neural Network Approach to Source Localization. *The Journal of the Acoustical Society of America*, 90(4), 2081-2090. <https://doi.org/10.1121/1.401635>

Author ORCIDs and Contributions

Author name	ORCID	Contributions
Yang, Haesang	0000-0001-7101-5195	②④
Lee, Keunhwa	0000-0003-4827-3983	②⑤
Choo, Youngmin	0000-0002-9100-9494	②④⑤
Kim, Kookhyun	0000-0002-4214-4673	②⑤

- ① Conceived of the presented idea or developed the theory
- ② Carried out the experiment or collected the data
- ③ Performed the analytic calculations or numerical simulations
- ④ Wrote the manuscript
- ⑤ Supervised the findings of this study



Title of Article

Firstname Lastname¹, Firstname Lastname² and Firstname Lastname³

¹Professor, Department of OO, OO School, OO University, Busan, Korea

²Graduate Student, Department of OO, OO University, Seoul, Korea

³Senior Researcher, Department of OO, OO Engineering. Corp., Seoul, Korea

KEY WORDS: Lumped mass line model, Explicit method, Steel lazy wave riser (Immediately after the abstract, provide a maximum of 5 or 6 keywords.)

ABSTRACT: A concise and factual abstract is required. The abstract should state briefly the purpose of the research, the principal results and major conclusions. An abstract should be written in around 300 words and is often presented separately from the article, so it must be able to stand alone. For this reason, References should be avoided, but if essential, then cite the author(s) and year(s). Also, non-standard or uncommon abbreviations should be avoided, but if essential they must be defined at their first mention in the abstract itself.

Nomenclature

<i>I</i> TOC	Increment of total operating cost (\$/yr)
<i>L</i> HV	Lower heating value (kJ/kg)
<i>P</i> w	Power (kW)
<i>T</i>	Temperature (K)
<i>V</i>	Volume (m ³)
ρ	Density (kg/m ³)

1. Introduction

The introduction should briefly place the study in a broad context and highlight why it is important. It should define the purpose of the work and its significance. The current state of the research field should be reviewed carefully and key publications cited. Please highlight controversial and diverging hypotheses when necessary. Finally, briefly mention the main aim of the work and highlight the principal conclusions. As far as possible, please keep the introduction comprehensible to scientists outside your particular field of research.

2. General Information for Authors

2.1 Requirement for Membership

One of the authors who submits a paper or papers should be member of

The Korea Society of Ocean Engineers (KSOE), except a case that editorial board provides special admission of submission.

2.2 Publication type

Manuscript is made up of scholarly monographs, technical reports and data. The paper should have not been submitted to other academic journal. Conference papers, research reports, dissertations and review articles can be submitted to Journal Of Ocean Engineering and Technology (JOET). When part or whole of a paper was already published to conference papers, research reports, dissertations, and review articles, then corresponding author should note it clearly in the manuscript. After published to JOET, the copyright of manuscript belongs to KSOE.

(example) It is noted that this paper is revised edition based on proceedings of KAOST 2100 in Jeju.

2.3 Manuscript submission

Manuscript should be submitted through the on-line manuscript website (<http://www.joet.org>). The date that corresponding author submits a paper through on-line website is official date of submission. Other correspondences can be sent by an email to the Editor in Chief. The manuscript must be accompanied by a signed statement that it has been neither published nor currently submitted for publication elsewhere. The manuscript should be written in English or Korean and a

Received 00 February 2100, revised 00 October 2100, accepted 00 October 2100

Corresponding author Firstname Lastname: +82-51-759-0656, e-mail@e-mail.com

It is a recommended paper from the proceedings of 2019 spring symposium of the Korea Marine Robot Technology (KMRTS).

© 2100, The Korean Society of Ocean Engineers

This is an open access article distributed under the terms of the creative commons attribution non-commercial license (<http://creativecommons.org/licenses/by-nc/4.0>) which permits unrestricted non-commercial use, distribution, and reproduction in any medium, provided the original work is properly cited.

minimum standard of the proficiency in the English or Korean language should be met before submission to the editorial office.

Ensure that online submission or submission by e-mail text files are in a standard word processing format (Hangul or MS Word are preferred). Ensure that graphics are high-resolution. Be sure all necessary files have been uploaded/attached.

2.3.1 Author's checklist and Transfer of copyright

Author's checklist and Transfer of copyright can be found in submission homepage (<http://www.joet.org>).

2.4 Research and Publication Ethics

Authorship should be limited to those who have made a significant contribution to the conception, design, execution, or interpretation of the reported study. All those who have made significant contributions should be listed as co-authors. Where there are others who have participated in certain substantive aspects of the research project, they should be acknowledged or listed as contributors.

The corresponding author should ensure that all appropriate co-authors and no inappropriate co-authors are included on the paper, and that all co-authors have seen and approved the final version of the paper and have agreed to its submission for publication.

If the work involves chemicals, procedures or equipment that have any unusual hazards inherent in their use, the author must clearly identify these in the manuscript. If the work involves the use of animal or human subjects, the author should ensure that the manuscript contains a statement that all procedures were performed in compliance with relevant laws and institutional guidelines and that the appropriate institutional committee(s) has approved them. Authors should include a statement in the manuscript that informed consent was obtained for experimentation with human subjects. The privacy rights of human subjects must always be observed.

When an author discovers a significant error or inaccuracy in his/her own published work, it is the author's obligation to promptly notify the journal editor or publisher and cooperate with the editor to retract or correct the paper. If the editor or the publisher learns from a third party that a published work contains a significant error, it is the obligation of the author to promptly retract or correct the paper or provide evidence to the editor of the correctness of the original paper.

3. Manuscript

Manuscript must consist of as follow: (1) Title, (2) Author's information (include title), (3) Key word, (4) Abstract, (5) Nomenclature description, (6) Introduction, (7) Body (analysis, test, results and discussion), (8) Conclusion, (9) Acknowledgements, (10) Reference, (11) Appendix, etc.

3.1 Unit

Use the international system units(SI). If other units are mentioned, please give their equivalent in SI.

3.2 Equations

All mathematical equations should be clearly printed/typed using well accepted explanation. Superscripts and subscripts should be typed clearly above or below the base line. Equation numbers should be given in Arabic numerals enclosed in parentheses on the right-hand margin. They should be cited in the text as, for example, Eq. (1), or Eqs. (1)-(3).

$$G_{GEV}(x;\mu,\sigma,\xi) = \begin{cases} \exp[-(1+\xi(x-\mu)/\sigma)^{-1/\xi}] & \xi \neq 0 \\ \exp[-\exp(-(x-\mu)/\sigma)] & \xi = 0 \end{cases} \quad (1)$$

in which μ , σ , and ξ represent the location ("Shift" in figures), scale, and shape parameters, respectively.

3.3 Tables

Tables should be numbered consecutively with Arabic numerals. Each table should be typed on a separate sheet of paper and be fully titled. All tables should be referred to in the text.

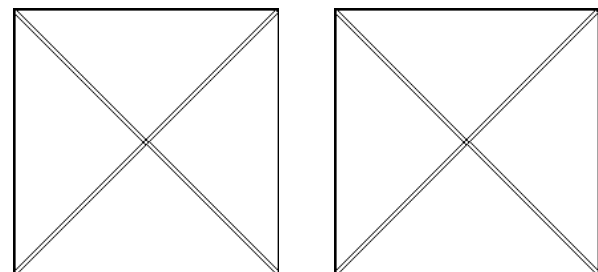
Table 1 Tables should be placed in the main text near to the first time they are cited

Item	Buoyancy riser
Segment length ¹ (m)	370
Outer diameter (m)	1.137
Inner diameter (m)	0.406
Dry weight (kg/m)	697
Bending rigidity (N·m ²)	1.66E8
Axial stiffness (N)	7.098E9
Inner flow density (kg·m ³)	881
Seabed stiffness (N/m ²)	6,000

¹Tables may have a footer.

3.4 Figures

All the illustrations should be of high quality meeting with the publishing requirement with legible symbols and legends. In preparing the illustrations, authors should consider a size reduction during the



(a) Description of what is contained in the first panel

(b) Description of what is contained in the first panel

Fig. 1 Schemes follow the same formatting. If there are multiple panels, they should be listed as: (a) Description of what is contained in the first panel; (b) Description of what is contained in the second panel. Figures should be placed in the main text near to the first time they are cited

printing process to have acceptable line clarity and character sizes. All figures should have captions which should be supplied on a separate sheet. They should be referred to in the text as, for example, Fig. 1, or Figs. 1-3.

3.5 How to describe the references in main texts

All references should be listed at the end of the manuscripts, arranged in order of Alphabet. The exemplary form of listed references is as follows:

- Single author: (Kim, 1998) or Kim (1998)
- Two authors: (Kim and Lee, 2000) or Kim and Lee (2000)
- Three or more authors: (Kim et al., 1997) or Kim et al. (1997)
- Two or more papers: (Lee, 1995a; Lee, 1995b; Ryu et al., 1998)
- Year unknown: (Kim, n.d.) or Kim (n.d.)

4. Conclusions

.....

Acknowledgments

Please add: "This research was funded by Name of Funder, grant number XXX" and "The OOO was funded by XXX". Check carefully that the details given are accurate and use the standard spelling of funding agency names at <https://search.crossref.org/funding>

In this section you can acknowledge any support given which is not covered by the author contribution or funding sections. This may include administrative and technical support, or donations in kind (e.g., materials used for experiments).

References

- Journal name should not be abbreviated.
- A private report with limited access or download availability can not be a reference.
- Include the digital object identifier DOI or URL for all references where available.

Referring to journal publications:

- Author, A.A., Author, B.B., & Author, C.C. (Year). Title of Article. Journal Title, vol(no), pp-pp. <https://doi.org/xx.xxxx/xxxxxx>
- Author, A.A., Author, B.B., Author, C.C. (accepted; in press). Title of Article. Title of Periodical. Retrieved from <http://xx.xxx/x.pdf>
- Lee, T.K., Kim, T.W., Rim, C.W., & Kim, S.C. (2013). A Study on Calculation of Local Ice Pressures for ARAON Based on Data Measured at Arctic Sea. Journal of Ocean Engineering and Technology, 27(5), 88-92. <https://doi.org/10.5574/KSOE.2013.27.5.088>
- Lee, T.K., Kim, T.W., Rim, C.W., & Kim, S.C. (accepted; in press). A Study on Calculation of Local Ice Pressures for ARAON Based on Data Measured at Arctic Sea. Journal of Ocean Engineering and Technology, Retrieved from <http://xxx.xxx/xxx.pdf>

Referring to conference proceedings:

- Author, A.A., Author, B.B., & Author, C.C. (Year). Title of Article. Proceeding Title, City, Country, pp-pp. <https://doi.org/xx.xxxx>
- Aoki, S., Liu, H., & Sawaragi, T. (1994). Wave Transformation and Wave Forces on Submerged Vertical Membrane. Proceedings of International Symposium Waves - Physical and Numerical Modeling, Vancouver, Canada, 1287-1296.
- Tsukamoto, C.L., Lee, W., Yuh, J., Choi, S.K., & Lorentz, J. (1997). Comparison Study on Advanced Thruster Control of Underwater Robots. Proceedings of International Conference on Robotics and Automation, 1845-1850. <https://doi.org/110.1109/ROBOT.1997.619056>

Referring to books:

- Author, A.A. (Year). Title of Book (xx ed.). Location: Publisher.
- Strunk, W., & White, E.B. (2000). The Elements of Style (4th ed.). New York, USA: Longman.
- Schlichting, H. (1968). Boundary Layer Theory (6th ed.). New York, USA: McGraw-Hill.

Referring to theses or dissertations:

- Author, A.A. (Year). Title of Doctoral Dissertation or Master's thesis (Doctoral Dissertation or Master's thesis). Name of Institution, City, Country.
- Giovanni, I. (1998). Modelling and Identification of Underwater Robotic Systems (Ph.D. Thesis). University of Genova, Genova, Italy.

Referring to technical reports, rules, or guidelines:

- Author, A.A. (Year). Title of report (Reprot No. xxx), Location: Publisher.
- Likhomanov, V. (2010). Full-Scale Ice Trials of the Korean Research Icebreaker ARAON. Daejeon, Korea: Arctic and Antarctic Research Institute (AARI).
- ABS. (2011). Guide for Ice Loads Monitoring Systems. Houston, USA: American Bureau of Shipping.
- Lloyd's Register. (2011). FDA ICE Fatigue Induced by Ice Loading, ShipRight Design and construction - Fatigue Design Assesment. London, United Kingdom: Lloyd's Register.
- Larson, M., & Kraus, N.C. (1989). SBEACH: Numerical Model for Simulating Storm-Induced Beach Change - Report 1 Empirical Foundation and Model Development (Technicla Report CERC-89-9). Coastal Engineering research center Vicksburg Ms.

Referring to patents:

- Righsholder, A.A. (Year). Title of Patent. Patent number, Patent office with country.
- Dawoo Shipbulding & Maringe Engineering (DSME). (2013). Distance Length Standardization Method for Preventing Interference at the time of Uploading Cell Guide of Container Ship. Unexamined Patent Publication 1020130044635, Korean Interlllectual Property Office.

Referring to websites:

- Righsholder, A.A. (Year). Title of webpage. Retrieved Month Year from <http://xxxx>
- International Association of Classification Societies (IACS). (2010a).

Common Structural Rules for Bulk Carriers. Retrieved July 2010 from <http://www.iacs-data.org.uk>

US Congressional Hearing. (2009). Strategic Importance of the Arctic in Us Policy. Retrieved June 2019 from <https://fas.org/irp/arctic.pdf>

Dawoo Shipbuilding & Maringe Engineering (DSME). (2013). Distance Length Standardization Method for Preventing Interference at the time of Uploading Cell Guide of Container Ship. Retrieved June 2019 from <https://patentimages.storage./pdfs/792.pdf>

Referring to software:

Righsholder, A.A. (Year). Title of Software. Downloaded Month Year from <http://xxxx>

Referring to some exceptional cases:

- when authors are missing, institution can replace authors

National Oceanic and Atmospheric Administration (NOAA). (2015). Deep-ocean Assessment and Reporting of Tsunamis (DART). Retrieved December 2019 from <https://nctr.pmel.noaa.gov/Dart/>

- when dates or years are missing, it is replaced with "n.d."

National Oceanic and Atmospheric Administration (NOAA). (n.d.). Deep-ocean Assessment and Reporting of Tsunamis (DART).

- when more than seven authors, first 6 authors ... last author.

Yeu, T., Choi, H.T., Lee, Y., Chae, J., Lee, Y., Kim, S.S., ... Lee, T.H. (2019). Development of Robot Platform for Autonomous Underwater Intervention. *Journal of Ocean Engineering and Technology*, 33(2), 168-177. <https://doi.org/10.26748/KSOE.2019.021>

Appendix

The appendix is an optional section that can contain details and data supplemental to the main text. For example, explanations of experimental details that would disrupt the flow of the main text, but nonetheless remain crucial to understanding and reproducing the research shown; figures of replicates for experiments of which representative data is shown in the main text can be added here if brief, or as Supplementary data. Mathematical proofs of results not central to the paper can be added as an appendix.

All appendix sections must be cited in the main text. In the appendixes, Figures, Tables, etc. should be labeled starting with 'A', e.g., Fig. A1, Fig. A2, etc.

Examples:

<https://doi.org/10.26748/KSOE.2019.022>

<https://doi.org/10.26748/KSOE.2018.4.32.2.095>

Author ORCIDs and Contributions

Author name	ORCID	Contributions
So, Hee	0000-0000-000-00X	①②③
Park, Hye-Il	0000-0000-000-00X	④
Yoo, All	0000-0000-000-00X	⑤
Jung, Jewelry	0000-0000-000-00X	⑤

- ① Conceived of the presented idea or developed the theory
- ② Carried out the experiment or collected the data
- ③ Performed the analytic calculations or numerical simulations
- ④ Wrote the manuscript
- ⑤ Supervised the findings of this study

Authors' Information

Requirement for membership

One of the authors who submits a paper or papers should be member of the Korean Society of Ocean Engineers (KSOE), except a case that editorial board provides special admission of submission.

Publication type

Article types include scholarly monographs (original research articles), technical articles (technical reports and data), and review articles. The paper should have not been submitted to other academic journal. When part or whole of a manuscript was already published to conference papers, research reports, and dissertations, then the corresponding author should note it clearly in the manuscript.

Copyright

After published to JOET, the copyright of manuscripts should belong to KSOE. A transfer of copyright (publishing agreement) form can be found in submission website (<http://www.joet.org>).

Manuscript submission

Manuscript should be submitted through the on-line submission website (<http://www.joet.org>). The date that corresponding author submits a paper through on-line website is the official date of submission. Other correspondences can be sent by an email to the Editor in Chief or secretariat. The manuscript must be accompanied by a signed statement that it has been neither published nor currently submitted for publication elsewhere. The manuscript should be written in English or Korean. Ensure that online submission are in a standard word processing format (Hangul or MS Word are accepted). Ensure that graphics are high-resolution. Be sure all necessary files have been uploaded/attached.

Authors' checklist

Please refer to "Authors' Checklist" for details.

Article structure

Manuscript must be edited in the following order: (1) Title, (2) Authors' names and affiliations, (3) Keywords, (4) Abstract, (5) Nomenclature (optional), (6) Introduction, (7) Main body (analyses, tests, results, and discussions), (8) Conclusions, (9) Acknowledgements (optional), (10) References, (11) Appendices (optional).

Abstract

A concise and factual abstract is required. The abstract should state briefly the purpose of the research, the principal results and major conclusions. An abstract should be written in around 300 words. References are not cited in abstract whenever possible. Also, non-standard or uncommon abbreviations should be avoided, but if essential they must be defined at their first mention in the abstract itself.

Keywords

Immediately after the abstract, provide a maximum of 5 or 6 keywords.

Equations

All mathematical equations should be clearly printed/typed using well accepted explanation. Superscripts and subscripts should be typed clearly above or below the base line. Equation numbers should be given in Arabic numerals enclosed in parentheses on the right-hand margin.

Tables

Tables should be numbered consecutively with Arabic numerals. Each table should be fully titled. All tables should be referred to in the texts.

Figures

Figures should be numbered consecutively with Arabic numerals. Each figure should be fully titled. All figures should be referred to in the texts. All the illustrations should be of high quality meeting with the publishing requirement with legible symbols and legends.

References in text

References in texts follow the APA style. Authors can also see how references appear in manuscript text through the 'Template'.

Reference list

Reference list follows the APA style. Authors can see how references should be given in reference section through the 'Template'.

Appendices

The appendix is an optional section that can contain details and data supplemental to the main text. If there is more than an appendix, they should be identified as A, B, C, etc. Formulae and equations in appendices should be given separate numbering: Eq. (A.1), Eq. (A.2), etc.; in a subsequent appendix, Eq. (B.1) and so on. Similarly for tables and figures: Table A.1; Fig. A.1, etc.

Peer reviews

Every manuscript received is circulated to two or more peer reviewers. The author's name and affiliation is disclosed during review process to reviewers. The review process can be repeated till the revision requests are suggested by reviewers.

Revised manuscript

Manuscript reviewed should be revised and submitted with responses to the reviewers' comments in three months. Otherwise, the submission is finished with decision of reject.

Proof reading

The accepted manuscript will be sent for the proof reading for

the consistency of text format and the completeness of references. The manuscript may be revised according to the opinion of the manuscript editor.

Galley proof will be provided as a PDF file to the author. Attention of authors should be directed to the instructions which accompany the galley proof, especially the requirement that all corrections, revisions, and additions be entered on the galley proof. The galley proof with the corrections should be returned to the KSOE Secretariat by e-mail within a week. In principal, substantial changes in an article at this stage may not permitted.

Article processing charge

Payment due

Article processing charge (APC) covers the range of publishing services JOET provides. This includes provision of online tools for editors and authors, article production and hosting, and customer services. Upon editorial acceptance of an article for the regular review

service and upon submission of an article for the fast review service, the corresponding author will be notified that payment is due.

APC

The APC up to 6 pages is ₩200,000 (or \$200) for the regular review service and ₩550,000 (or \$550) for the fast review service. For papers longer than 6 pages, an extra APC of \$30 per page is charged. No taxes are included in this charge.

Payment methods

Credit card payment can be made online using a secure payment form as soon as the manuscript has been editorially accepted. We will we send a receipt by email once payment has been processed. Please note that payment by credit card carries a surcharge of 10% of the total APC.

Invoice payment is due within 7 days of the manuscript receiving editorial acceptance. Receipts are available on request.

Authors' Checklist

The following list will be useful during the final checking of an article prior to sending it to Journal of Ocean Engineering and Technology for review. Please submit this checklist to the KSOE when you submit your article.

< Editing checklist >

- I checked my manuscript has been 'spell-checked' and 'grammar-checked'.
나의 원고에 오타 및 문법적 오류가 있는지 확인하였습니다.
- One author has been designated as the corresponding author with contact details such as
 - E-mail address
 - Phone numbers저자 중 한명의 저자는 교신저자로 지정되었으며, 다음의 연락처가 표기되었습니다.
 - 이메일 주소
 - 전화 번호
- I checked abstract 1) stated briefly the purpose of the research, the principal results and major conclusions, 2) was written in around 300 words, and 3) did not contain references (but if essential, then cite the author(s) and year(s)).
나는 초록이 1) 연구의 목적, 주요 결과 및 결론을 포함하고 있음을 확인하였으며, 2) 300단어 내외의 단어로 구성되었음을 확인하였으며, 3) 참고문헌을 포함하고 있지 않음을 확인하였습니다.(꼭 필요시 참고문헌 삽입 가능).
- I provided 5 or 6 keywords.
나는 5-6개의 키워드를 사용하였습니다.
- I checked manuscript consisted of as follow: (1) Title, (2) Authors' names and affiliations, (3) Keywords, (4) Abstract, (5) Nomenclature (optional), (6) Introduction, (7) Main body (analyses, tests, results, and discussions), (8) Conclusions, (9) Acknowledgements (optional), (10) References, (11) Appendices (optional).
나는 원고가 다음의 순서로 구성되었음을 확인하였습니다: (1) 제목, (2) 저자명/소속기관, (3) 키워드, (4) 초록, (5) 기호 (옵션), (6) 서론, (7) 본문 (해석, 실험, 결과, 검토), (8) 결론, (9) 후기 (옵션), (10) 참고문헌, (11) 부록.
- I confirmed that I used clear pictures to make every picture legible.
나는 모든 그림이 가독될 수 있도록 선명한 그림을 사용하였음을 확인하였습니다.
- I checked all table and figure captions were written in English.
나는 원고의 모든 표 제목과 그림 제목은 영문으로 작성되었음을 확인하였습니다.
- I checked all table and figure numbered consecutively in accordance with their appearance in the text.
나는 본문에서 나타나는 순서대로 표 번호 및 그림 번호가 지정되었음을 확인하였습니다.
- I checked abbreviations were defined at their first mention there and used with consistency throughout the article.
나는 영문 약자를 원고의 첫 번째 사용에서 정의하였으며, 이후 원고에서는 동일한 약자를 사용하였음을 확인하였습니다.
- I checked that references were in the correct format for the journal (See 'Authors' Information' for details).
나는 모든 참고문헌이 본 저널의 참고문헌 표기법(저자 가이드 참조)에 따라서 작성되었음을 확인하였습니다.
- I checked all references mentioned in the Reference list were cited in the text, and vice versa.
나는 'References'에 존재하는 모든 참고문헌은 원고 본문에서 언급되었으며, 반대로 원고 본문에 언급된 모든 참고문헌은 'References'에 표기되었음을 확인하였습니다.
- I checked I used the international system units (SI) or SI-equivalent engineering units.
나는 SI 단위계 또는 공학적으로 인정되어지는 단위계를 사용하였음을 확인하였습니다.

< Ethical checklist >

- I checked the work described has not been published previously (except in the form of an abstract or as a part of a published lecture or academic thesis).
나는 본 원고의 내용이 초록, 단행본, 학위논문 등을 제외한 타 저널 등에 게재된 사실이 없음을 확인하였습니다.
- I checked when the work described has been published previously in other proceedings without copyright, it has clearly noted in the text.
나는 본 원고의 내용이 판권이 없는 프로시딩에 게재되었던 경우 이를 원고에서 명시하였음을 확인하였습니다.
- I checked permission has been obtained for use of copyrighted material from other sources including the Web.
나는 웹을 포함하여 판권이 있는 자료의 사용 허가를 득했습니다.
- I have processed Plagiarism Prevention Check through reliable web sites such as www.kci.go.kr, <http://www.ithenticate.com/>, or <https://www.copykiller.org/> for my submission.
나는 논문 표절 유사도 검사를 마친 후 투고하였습니다.
- I agree that final decision for my final manuscript can be changed according to results of Plagiarism Prevention Check by JOET administrator.
나의 최종본 논문에 대한 JOET 자체적인 논문 표절 유사도 검토 결과에 따라 최종 판정이 변경될 수 있다는 사실에 동의합니다.
- I checked one author at least is member of the Korean Society of Ocean Engineers.
나는 저자 중 1인 이상이 한국해양공학회 회원임을 확인하였습니다.
- I agreed all policies related to 'Ethical Code of Research' and 'Research and Publication Ethics' of the Korean Society of Ocean Engineers.
나는 연구출판정책과 연구윤리규정을 확인했으며, 준수할 것을 서약합니다.
- I agreed to transfer copyright to the publisher as part of a journal publishing agreement and this article will not be published elsewhere including electronically in the same form, in English or in any other language, without the written consent of the copyright-holder.
나는 한국해양공회지의 저작권 정책에 동의하며, 저작권 위임동의서를 제출하겠습니다.
- I have read and agree to the terms of Authors' Checklist.
나는 저자 체크리스트 모든 조항을 검토하였으며, 모든 조항에 동의합니다.

Title of article :

Date of submission : DD/MM/YYYY

Corresponding author :

signature

Email address :

※ E-mail this with your signature to ksoehj@ksoe.or.kr

Publishing Agreement

ARTICLE DETAILS

Title of article :
Corresponding author :
E-mail address :
DOI : <https://doi.org/10.26748/KSOE.2XXX.XXX>

YOUR STATUS

I am one author signing on behalf of all co-authors of the manuscript.

ASSIGNMENT OF COPYRIGHT

I hereby assign to the Korean Society of Ocean Engineers, the copyright in the manuscript identified above and any tables, illustrations or other material submitted for publication as part of the manuscript (the "Article"). This assignment of rights means that I have granted to Korean Society of Ocean Engineers the exclusive right to publish and reproduce the Article, or any part of the Article, in print, electronic and all other media (whether now known or later developed), in any form, in all languages, throughout the world, for the full term of copyright, and the right to license others to do the same, effective when the Article is accepted for publication. This includes the right to enforce the rights granted hereunder against third parties.

SCHOLARLY COMMUNICATION RIGHTS

I understand that no rights in patents, trademarks or other intellectual property rights are transferred to the Journal owner. As the author of the Article, I understand that I shall have: (i) the same rights to reuse the Article as those allowed to third party users of the Article under the CC-BY-NC License, as well as (ii) the right to use the Article in a subsequent compilation of my works or to extend the Article to book length form, to include the Article in a thesis or

dissertation, or otherwise to use or re-use portions or excerpts in other works, for both commercial and non-commercial purposes. Except for such uses, I understand that the assignment of copyright to the Journal owner gives the Journal owner the exclusive right to make or sub-license commercial use.

USER RIGHTS

The publisher will apply the Creative Commons Attribution-Noncommercial Works 4.0 International License (CC-BY-NC) to the Article where it publishes the Article in the journal on its online platforms on an Open Access basis.

The CC-BY-NC license allows users to copy and distribute the Article, provided this is not done for commercial purposes and further does not permit distribution of the Article if it is changed or edited in any way, and provided the user gives appropriate credit (with a link to the formal publication through the relevant DOI), provides a link to the license, and that the licensor is not represented as endorsing the use made of the work. The full details of the license are available at <http://creativecommons.org/licenses/by-nc/4.0/legalcode>.

REVERSION OF RIGHTS

Articles may sometimes be accepted for publication but later rejected in the publication process, even in some cases after public posting in "Articles in Press" form, in which case all rights will revert to the author.

I have read and agree to the terms of the Journal Publishing Agreement.

Corresponding author:

name

signature

※ E-mail this with your signature to ksoehj@ksoe.or.kr (Papers will not be published unless this form is signed and returned)

Ethical Codes of Research

The Korean Society of Ocean Engineers [1, Nov. 2008 amended]

All members of The Korean Society of Ocean Engineers, by observing the following codes of conduct and regulations regarding research in the field, will contribute to the development of ocean engineering and the security and prosperity of the society and the nation, thus holding our honesty, reputation and authority in the highest standards.

A. Foundational Spirit

1. We make a contribution to mutual prosperity of mankind through ocean development, using the knowledge and technique in the field of ocean engineering.
2. We contribute to fostering the good spirit of citizenship by conducting responsible research.
3. We make efforts to enhance our authority and competitiveness as experts in ocean engineering.

B. Fundamental Canons

1. We consider the public security and welfare as a top priority and conform to the principle of sustainable use of ocean in conducting our research.
2. We promote professional development through performing proper research and provide young researchers with the opportunities to develop professionally.
3. We respect the public values such as honesty, accuracy, efficiency and objectivity in offering services such as providing expertise or disclosing research results.
4. We do not have unfair competitions with others and solve problems with objective information and processes when there is a clash of interests.
5. We raise common issues only through objective and fair methods.

C. Practical Platforms

1. We consider the public security and welfare as a top priority and conform to the principle of sustainable use of ocean in conducting our research.
 - (a) We must acknowledge the fact that the life, security, health and welfare of the public have an absolute reliance over our products such as structures, equipments and machines that are given thought to and made into decision by engineers.
 - (b) We must not propose or approve research plans which cause harm to the public health and welfare.
 - (c) We must conform to the principle of sustainable use of ocean to enhance the quality of the public life and endeavor to improve the ocean environment.
2. We promote professional development through performing proper research and provide young researchers with the opportunities to develop professionally.

- (a) As we build our career, we must continue to acquire new knowledge and promote intellectual development by keeping track of research results, organizing research methods and raising necessary issues voluntarily.
 - (b) We must be thoroughly honest to the contributions from cooperators, competitors and predecessors and utilize them for our professional development.
 - (c) We, as administrators, must supervise young researchers in a fair manner and, as their advisors, must assist them sincerely to grow into socially recognized members.
3. We respect the public values such as honesty, accuracy, efficiency and objectivity in offering services such as providing expertise or disclosing research results.
 - (a) When we offer service under our responsibility that involves providing professional knowledge, we must act according to professionalism as a commissioner, trying to prevent waste of resources and reporting objective facts, trustworthy data and accurate research results.
 - (b) We prohibit any fraudulent acts in conducting research such as fabrications, forgeries and plagiarism.
 - (c) We must admit our mistakes or errors when they are verified and must not try to justify them by distorting facts or data.
 4. We do not have unfair competitions with others and solve problems with objective information and processes when there is a clash of interests.
 - (a) We must not distort the professional, academical qualifications of ourselves and coworkers. We must not fabricate or exaggerate our positions or authorities of the past achievements.
 - (b) Our papers must contain facts and no exaggeration that are contributed to media sources. When publishing a paper or a report which involves multiple researchers, we must allocate authors based on their levels of contributions and mention every person and institution that is concerned and provided assistance.
 - (c) We must not criticise others' achievements in an irresponsible manner by intentionally distorting their professional reputation, prospects and character in both direct and indirect ways.
 - (d) When a clash of interests occur, we must organize a committee composed of authoritative experts in the field and fairly solve the problem based on objective facts and data.
 5. We raise common issues only through objective and fair methods.
 - (a) We must be thoroughly objective and honest when submitting expert reports or policy proposals and include relevant, sufficient and appropriate information.
 - (b) When addressing public issues through open debates or forums, we must provide opinions based on objective facts

and data and must not cause harm to the public interest by making groundless argument or being involved in private interests with others.

- (c) We must be honest when explaining our business and its advantages, and must not try to meet our interests by damaging professional honor and coordination with coworkers.
6. All members of The Korean Society of Ocean Engineers must abide by the ethical codes of research stated above.

D. The Scope of Manuscript

1. Manuscripts include papers, technical reports and commentaries, and papers must be the ones that are not released in other journals.
2. "Journals" are the ones that have an appropriate screening of submitted theses and that are published on a regular basis.
3. All manuscripts other than the ones stated in the previous clause can be submitted such as conference papers, research reports, diploma papers and academic articles, provided that their sources are stated according to the 3rd clause of The Regulations on Paper Submission in The Journal of the Korean Society of Ocean Engineers.

E. The Definitions and Types of Fraudulent Acts in Research

1. "Fraudulent acts in research" include all affairs that violates ethical codes of research: fabrications, forgeries, plagiarism, overlapping publications and unfair marking of writers which may occur in every phase of research process, such as in a proposal, conducting, a report or presentation of research results.
2. "Fabrication and forgeries" refers to an act of distorting the content or outcome of research by making up false data or results.
3. "Plagiarism" refers to an act of unfairly employing all research results, such as others' publications, research proposals, ideas, hypotheses and theories, without a fair approval or quotation.
4. "Overlapping publications" refers to two writings published in different media sources that are totally identical in their contents or share the major contents. It is also the case of overlapping publication where the paper published later contains a slightly different viewpoint, yet contains the same or slightly different analysis on the same data from the previous paper.
5. "Unfair marking of writers" refers to an act of unfairly gaining reputation by pretending to be a real author of a paper without any participation in research.
6. Fraudulent acts also include a behavior of intentionally disturbing investigations regarding assumed misconducts in research or inflicting an injury on an informant.
7. "Other fraudulent acts in research" refers to all affairs that are generally accepted as the violations to ethical codes of research in the academia.

F. Screening System, Processing Criteria and Procedure

1. Screening System
 - (a) Authors must submit a "consent form of delegation of copyright" which necessitates an author's confirmation on

any violations to ethical codes of research.

- (b) When inspectors raise question on any violations to ethical codes of research, The Committee of Ethical Codes of Research determines its/their compliance to the regulations after examining all materials concerned and giving the contributor a chance to defend him/herself.
- (c) When any violations to ethical codes of research are found while screening or editing (after the insertion of a paper in an academic magazine), The Committee of Ethical Codes of Research determines its/their compliance to the regulations after giving the contributor a chance to defend him/herself.
- (d) When any violations to ethical codes of research are called into question after a paper is published, The Committee of Ethical Codes of Research determines its/their compliance to the regulations after giving the contributor a chance to defend him/herself.

2. Processing Criteria

- (a) All processing criteria regarding fraudulent acts in research follow the regulations and detailed rules for operation of The Committee of Ethical Codes of Research of this society.

3. Processing Procedure

- (a) When any affair is determined as a violation to the ethical codes of research in the phase of submission or screening, The Editing Commission should report it to The Committee of Ethical Codes of Research.
- (b) When any affair is determined as a violation to the ethical codes of research after the insertions of a paper in an academic magazine, The Committee of Ethical Codes of Research should immediately cancel its publication and notify the cancellation to the author/s

G. Ethical codes of Editing

1. The editor must a strong sense of ethics regarding the codes of conduct in research and in publication. Also, he/she must not have any personal interests with others in the process of edition.
2. The editor must thoroughly keep security in all matters related to the contribution of manuscripts, screening and publication.
3. The editor must be well-informed about the violations to ethical codes of research and make a neutral and impersonal judgement when he/she found any violations.

Supplementary Provisions

1. Regulations stated above are enacted after 1 Nov. 2008. For the manuscripts contributed in academic magazines before 1, Nov. 2008, the 3rd clause in "D" is not applied. Also, they are not interpreted as violations to the ethical codes of research even if they did not stated their source in the journal of this society.
2. Also, for the papers applicable to the clause "D" or "E", the writer/s can take measures such as "cancellation of a paper" based on their judgement, or "rejection of screening" if the paper is under screening.

Research and Publication Ethics

Authorship of the paper

Authorship should be limited to those who have made a significant contribution to the conception, design, execution, or interpretation of the reported study. All those who have made significant contributions should be listed as co-authors. Where there are others who have participated in certain substantive aspects of the research project, they should be acknowledged or listed as contributors.

The corresponding author should ensure that all appropriate co-authors and no inappropriate co-authors are included on the paper, and that all co-authors have seen and approved the final version of the paper and have agreed to its submission for publication.

Hazards and human or animal subjects

If the work involves chemicals, procedures or equipment that have any unusual hazards inherent in their use, the author must clearly identify these in the manuscript. If the work involves the use of animal or human subjects, the author should ensure that the manuscript contains a statement that all procedures were performed in compliance with relevant laws and institutional guidelines and that the appropriate institutional committee(s) has approved them. Authors should include a statement in the manuscript that informed

consent was obtained for experimentation with human subjects. The privacy rights of human subjects must always be observed.

Ensure correct use of the terms sex (when reporting biological factors) and gender (identity, psychosocial or cultural factors), and, unless inappropriate, report the sex and/or gender of study participants, the sex of animals or cells, and describe the methods used to determine sex and gender. If the study was done involving an exclusive population, for example in only one sex, authors should justify why, except in obvious cases. Authors should define how they determined race or ethnicity and justify their relevance

Fundamental errors in published works

When an author discovers a significant error or inaccuracy in his/her own published work, it is the author's obligation to promptly notify the journal editor or publisher and cooperate with the editor to retract or correct the paper. If the editor or the publisher learns from a third party that a published work contains a significant error, it is the obligation of the author to promptly retract or correct the paper or provide evidence to the editor of the correctness of the original paper.



The Korean Society of Ocean Engineers